



HAL
open science

Development and in-depth characterization of biodegradable polymeric nanoparticles as drug delivery systems

Merve Seray Ural

► **To cite this version:**

Merve Seray Ural. Development and in-depth characterization of biodegradable polymeric nanoparticles as drug delivery systems. Material chemistry. Université Paris-Saclay, 2021. English. NNT : 2021UPASF028 . tel-03806721

HAL Id: tel-03806721

<https://theses.hal.science/tel-03806721>

Submitted on 8 Oct 2022

HAL is a multi-disciplinary open access archive for the deposit and dissemination of scientific research documents, whether they are published or not. The documents may come from teaching and research institutions in France or abroad, or from public or private research centers.

L'archive ouverte pluridisciplinaire **HAL**, est destinée au dépôt et à la diffusion de documents scientifiques de niveau recherche, publiés ou non, émanant des établissements d'enseignement et de recherche français ou étrangers, des laboratoires publics ou privés.

Development and In-Depth
Characterization of Biodegradable
Polymeric Nanoparticles as Drug Delivery
Systems

*Développement et caractérisation approfondie de
nanoparticules en polymères biodégradables
pour l'administration de molécules actives*

Thèse de doctorat de l'université Paris-Saclay

École doctorale n° 571 sciences chimiques : molécules, matériaux,
instrumentations et biosystèmes (2MIB)

Spécialité de doctorat: Chimie

Unité de recherche : Université Paris-Saclay, CNRS, Institut des Sciences Moléculaires
d'Orsay, 91405

Référent : Faculté des Sciences d'Orsay

Thèse présentée et soutenue à Orsay le 07 Juillet 2021 par

Merve Seray URAL

Composition du Jury

Hynd REMITA

Directeur de Recherche, CNRS, Université Paris Saclay

Présidente

Niko HILDEBRANDT

Professeur, Université de Rouen Normandie

Rapporteur & Examineur

Sergii RUDIUK

Chargé de recherche, Ecole Normale Supérieure

Rapporteur & Examineur

Eric BUSSERON

R&D Manager, Pharma Polymer Unit, Seqens Aramon

Examineur

Direction de la thèse

Ruxandra GREF

Directeur de Recherche CNRS, Université Paris Saclay

Directrice de thèse

Claire SMADJA

Professeur, CNRS, Université Paris Saclay

Co-directrice de thèse

Titre : Développement et caractérisation approfondie de nanoparticules en polymères biodégradables pour l'administration de molécules actives

Mots clés : PLGA; PLA; encapsulation; analyse individuelle des nanoparticules ; couronne de protéines

Résumé : Les nanomédicaments présentent de grands avantages pour l'administration ciblée et la libération contrôlée d'agents thérapeutiques. Ainsi, les nanoparticules (NPs) permettent de franchir des barrières biologiques et d'augmenter la biodisponibilité des molécules actives. Les (co)polymères biodégradables poly(acide lactique) (PLA) et poly(acide lactique-co-glycolique) (PLGA), dont la biocompatibilité est bien connue, restent les matériaux les plus utilisés pour préparer des NPs chargées en médicaments. Cependant, certaines limitations affectent le développement clinique de ces NPs: i) les charges en principe actif (DL) sont parfois insuffisantes réduisant l'efficacité thérapeutique des NPs; ii) le manque de méthodologies pour caractériser les NP individuellement pour un contrôle de qualité accru ; iii) des études approfondies des interactions nano-bio. Par conséquent, l'objectif du présent travail de thèse était de préparer une série de NPs de PLA et de PLGA pour obtenir des DL élevés et de les caractériser en profondeur.

La vancomycine (VCM) est un antibiotique de dernier recours utilisé pour traiter les infections bactériennes graves. L'encapsulation de la VCM au sein de NPs est une stratégie de choix pour accroître sa biodisponibilité et pour réduire les doses et effets secondaires. Les NPs-VCM ont été préparées en utilisant une série de (co)polymères PLA et PLGA. Les formulations ont été optimisées pour obtenir des DLs proches de 25 % en poids et une libération sensible au pH. Les interactions médicament-polymère ont été révélées par RMN du solide. Le médicament se situe dans des compartiments internes où il exerce de fortes interactions électrostatiques avec les groupes terminaux des (co)polymères. Un ensemble de microscopies électroniques ont été utilisées pour élucider les structures des NPs. Des compartiments internes ont été trouvés dans les NPs chargées en VCM, mais pas dans celles non chargées. Ces études ouvrent la voie à l'obtention de NP avec une faible libération de VCM dans conditions physiologiques

et une libération déclenchée à un pH acide, qui est parfois associée à des sites d'infection.

Les NP individuelles ont été caractérisées dans le but de localiser le médicament (chapitre II) grâce à des techniques de pointe combinant la visualisation des NP individuelles (microscopie à haute résolution) et l'analyse chimique par spectroscopies. Les techniques SEM-EDX, STEM-EDX et AFM-IR ont permis d'identifier et de localiser chaque composant d'une NP.

Pour aller plus loin, nous avons établi une méthode de quantification qui permet de mesurer la DL localement sur une seule NP. Pour ce faire, une série de films et de NPs ont été préparés à partir de mélanges de PLA et d'un médicament anticancéreux à base de Re. Ces deux matériaux possèdent des empreintes IR intenses répondant au mieux aux besoins de l'étude. Le chapitre III présente une preuve de concept de quantification réalisée par l'AFM-IR qui offre deux modes d'acquisition : i) cartographie chimique à des absorptions IR sélectionnées et ii) enregistrement d'un spectre IR local avec la résolution de l'AFM (10-15 nm). Tout d'abord, une courbe d'étalonnage a été obtenue par microspectroscopie IR et a servi de base pour la quantification par AFM-IR. Les NPs individuelles présentent des DL disparates, ce qui souligne l'utilité de notre approche.

Enfin, une étude complète a été menée pour étudier les interactions nano-bio. Les NPs en PLGA ont été étudiées comparativement avec les nanoMOFs. Ces NPs ont été PEGylées, pour moduler leurs interactions avec une protéine modèle. La méthodologie proposée dans le chapitre IV comprend des études fines de la couronne protéique. En combinant des approches quantitatives et qualitatives, l'étude donne un aperçu des altérations que certaines NPs peuvent induire sur la structure et la stabilité des protéines avec lesquelles elles entrent en contact. Ces interactions pourraient affecter le devenir in vivo des NPs.

Title : Development and in-depth characterization of biodegradable polymeric nanoparticles as drug delivery systems

Keywords : PLGA; PLA; drug loading; individual nanoparticle analysis; protein corona

Abstract : Drug delivery systems based on nanoparticles (NPs) are engineered technologies with great advantages of targeted delivery and controlled release of therapeutic agents, overcoming biological barriers and limitations of free therapeutics. Biodegradable poly (lactic acid) (PLA), poly (lactic-co-glycolic acid) (PLGA) (co)polymers with well-known biocompatible profile remain the most employed materials to prepare drug nanocarriers. However, some limitations remain affecting mainly their transition into clinics: i) insufficient drug loadings (DLs) lowering the therapeutic efficiency of the NPs ii) lack of methodologies to characterize individual NP for high quality control of the formulations; iii) in depth studies of the nano-bio interactions and in particular of protein fate in contact with the NPs. Therefore, the aim of the current work was to prepare a series of PLA and PLGA NPs to achieve high DLs and to further characterize them deeply.

Vancomycin (VCM) is a last resort antibiotic used to treat serious bacterial infections that are resistant to other drugs. VCM loading into NPs is a good strategy to overcome its low bioavailability and to decrease the administered doses and associated side effects. NPs were prepared using a series of PLA and PLGA (co)polymers. Formulations were optimized to achieve drug loadings close to 25 wt% and pH-responsive release. Drug-polymer interactions were revealed by solid state NMR investigations. The drug located in inner compartments where it experienced strong electrostatic interactions with the (co)polymer end groups. Various electron microscopies were employed to unravel the NPs' structures. Remarkably, the inner compartments were found in VCM-loaded NPs, and not in the unloaded ones. These studies pave the way to achieve stable NPs with low drug release at physiological conditions and triggered release at acidic pH, which sometimes is associated infected sites or intracellular compartments.

A systematic study was carried on individual NP

characterization with the aim to localize the drug (chapter II). This challenging task was achieved through a range of techniques combining visualization of individual NPs (high resolution microscopy) with simultaneous chemical analysis of the NP (spectroscopic analysis). By using state-of-the-art techniques (SEM-EDX, STEM-EDX and AFM-IR), the NPs components were chemically identified, drug location and homogeneity of the DL into the NPs were successfully investigated.

To go a step further, we established a quantification method that enables to measure local DL on a single NP basis. To do so, a series of films and NPs were prepared from mixtures of PLA and a hydrophobic [Re] anticancer drug. These two materials possess intense IR fingerprints meeting the needs of the study at best. Chapter III presents a proof of concept of quantification achieved by AFM-IR that offers two acquisition modes: i) chemical mapping at selected IR absorptions and ii) recording a local IR spectrum with AFM resolution (10-15 nanometers). First, a calibration curve was obtained by IR-microspectroscopy which provided the accurate quantitative information to build the grounds of quantification by AFM-IR. A high discrepancy was obtained in terms of loadings of individual NPs highlighting the usefulness of our approach.

Finally, a comprehensive study was carried on to investigate nano-bio interactions. PLGA NPs were studied together with nanoMOFs, possessing different characteristics, and compared with their PEGylated counterparts as PEG has been shown to shield nano-bio interactions, thus increase NPs' blood circulation time. The methodology proposed in chapter IV includes protein corona investigations. By combining quantitative and qualitative approaches it gives insights on NPs' in vivo fate as well as the NP induced alterations on protein's structure and stability that might affect its functionality.

*Science is the supreme guide for civilisation, for life, for success
in the world. To search for a guide other than science
is absurdity, ignorance and heresy.
Mustafa Kemal Atatürk*

This thesis is dedicated first of all to Atatürk who encouraged me to search for the truth of life, to all my mentors who enlightened me with science, to my family who liberated me from any borders, finally to Paris, embraced me with art, science and civilization.

Table of content

Abbreviations.....
General introduction.....	1
Chapter I.....	11
Introduction	12
1. Nanomedicine.....	12
1.1.Nanotechnology based drug delivery systems	13
1.1.1. Nanoparticles (NPs)	15
1.1.1.1. Polymeric NPs.....	19
1.1.1.2. Preparation methods of drug loaded polymeric NPs.....	24
1.1.1.2.1. Nanoprecipitation.....	26
1.1.1.2.2. Emulsions.....	27
2. An introduction to NP characterization	29
2.1.Characterization parameters and techniques for polymeric nanoparticles.....	30
2.1.1. Particle size and surface charge.....	30
2.1.2. Spectromicroscopies.....	32
2.1.3. Drug loading and release.....	35
2.2.Current challenges in polymeric NP characterization.....	36
2.3.State-of-the-art characterization.....	39
2.3.1. Scanning transmission electron microscopy - energy dispersive X-ray spectroscopy	39
2.3.2. Atomic force microscopy - infrared spectroscopy	39
3. Characterization of Nano-bio interactions.....	42
3.1.Capillary electrophoresis.....	48
3.2.Circular dichroism spectroscopy	49
3.2.1. Synchrotron radiation - circular dichroism spectroscopy.....	50
4. Conclusion.....	51
5. References.....	54

Chapter II	54
Compartmentalized Polymeric Nanoparticles Deliver Vancomycin in a pH-Responsive Manner.....	55
Chapter III	104
AFM-IR Allows Determining How Much Drug Each Polymeric Nanoparticle Contains	105
Chapter IV	148
A Comprehensive Investigation of the Interactions of Human Serum Albumin with Polymeric and Hybrid Nanoparticles.....	149
General Discussion and Perspectives	197
General Conclusion	208

Abbreviations

AFM	Atomic Force Microscopy
ATR	Attenuated Total Reflexion
BCA	Bicinchoninic acid
CaF ₂	Calcium Fluoride
CD	Circular Dichroism
CDx	Cyclodextrin
CE	Capillary Electrophoresis
Cryo-TEM	Cryogenic Transmission Electron Microscopy
DCM	Dichloromethane
DDS	Drug Delivery Systems
DL	Drug Loading
DLS	Dynamic Light Scattering
DMSO	Dimethyl Sulfoxide
DNA	Deoxyribonucleic Acid
EDX	Energy Dispersive X-Ray
EE	Encapsulation efficiency
EM	Electron Microscopy
F	Film
FDA	Food and Drug Administration
FTIR	Fourier-Transform Infrared
G	Glycolic Acid
HSA	Human Serum Albumin
ISO	International Organization of Standardization
ITC	Isothermal Titration Calorimetry
HAADF	High-Angle Annular Dark-Field Imaging
HPLC	High Performance Liquid Chromatography
IR	Infrared

L	Lactic Acid
LC-MS-MS	Liquid Chromatography Mass Spectrometry
MAS	Magic-Angle Spinning
MRSA	Methicillin-Resistant <i>Staphylococcus Aureus</i>
MOF	Metal Organic Frameworks
Mw	Molecular Weight
NaCl	Sodium Chloride
NaOH	Sodium Hydroxide
NMR	Nuclear Magnetic Resonance spectroscopy
NP	Nanoparticle
O/W	Oil in Water
O/W/O	Oil in Water in Oil
PB	Phosphate Buffer
PBS	Phosphate Buffer Saline
PCL	Poly (ϵ -caprolactone)
PDI	Polydispersity Index
PEG	Poly (Ethylene Glycol)
PGA	Poly (Glycolic Acid)
PLA	Poly (Lactic Acid)
PLGA	Poly (Lactic-co-Glycolic Acid)
PVA	Poly (Vinyl Alcohol)
Re	Rhenium
RNA	Ribonucleic Acid
QCL	Quantum Cascade Laser
S. aureus	Staphylococcus aureus
SAXS	Small Angle X-ray Scattering
SD	Standard Deviation
SEM	Scanning Electron Microscopy

SR	Synchrotron Radiation
SR-CD	Synchrotron Radiation Circular Dichroism
STEM	Scanning Transition Electron Microscopy
TEM	Transmission Electron Microscopy
VCM	Vancomycin
wt	Weight

General Introduction



Introduction générale

Synthèse en français

Les nanomédicaments ont apporté des solutions à de nombreux problèmes non résolus de la médecine moderne. La taille "nano" définit les bases de la nanomédecine et fait référence aux propriétés uniques des nanomatériaux, différentes de celles des matériaux ayant servi à leur élaboration. Parmi eux, les nanoparticules (NPs) utilisées comme systèmes d'administration de médicaments (nanomédicaments) ont attiré une attention toute particulière^{1, 2}. Avec plus de quarante ans de développement, les NsP en polymère biocompatible sont devenues l'un des systèmes nanoparticulaire les plus étudiés³. Ils offrent des avantages certains par rapport aux traitements conventionnels avec des molécules actives libres. Des études ont mis en évidence les capacités des nanomédicaments à : i) contrôler le profil pharmacocinétique et de distribution du médicament ; ii) protéger le médicament de la dégradation ou de l'inactivation; iii) améliorer l'absorption du médicament et sa pénétration intracellulaire; iv) délivrer le médicament au niveau d'un site spécifique ; v) libérer le médicament de manière contrôlée^{4, 5}.

Etant donné qu'ils sont approuvés par la Food and Drug Administration, les (co)polymères biodégradables de poly(acide lactique) (PLA) et de poly(acide lactique-co-glycolique) (PLGA) ont été les polymères les plus utilisés car ils permettent de délivrer une large gamme de médicaments (hydrophiles, hydrophobes et amphiphiles) *via* plusieurs voies d'administration^{6, 7}. Leurs propriétés physicochimiques modulables (masse molaire, nature des groupements terminaux, hydrophilie, etc.) permettent un contrôle précis des caractéristiques des NPs telles que leur stabilité, charge de surface, réactivité, contenu en médicament et cinétique de libération⁸. Les scientifiques ont également fonctionnalisé leurs surfaces avec des polymères tels que le poly(éthylène glycol) (PEG) et des ligands spécifiques afin d'obtenir des propriétés "furtives" et un temps de circulation sanguine plus long^{9, 10}.

Bien que des recherches approfondies aient été menées sur le développement et la caractérisation des NPs à base de PLA et de PLGA, leur évaluation clinique est étonnamment faible. Cependant, cela n'est pas le cas pour les microparticules à base de PLA et de PLGA, et cela pourrait s'expliquer étant donné les défis spécifiques liés à la taille nanométrique :

i) Contenu insuffisant en médicaments,

Alors qu'une charge médicamenteuse insuffisante a un effet direct sur l'efficacité thérapeutique des NPs, la taille réduite des NPs limite la charge médicamenteuse, en particulier pour les médicaments hydrophiles appartenant à des familles importantes telles que les antibiotiques, les protéines, les médicaments anticancéreux¹¹.

ii) Manque de méthodologies pour la caractérisation des NP à l'échelle individuelle,

La caractérisation individuelle des NP est indispensable pour comprendre les hétérogénéités entre les NPs d'un même lot et éviter ainsi des activités thérapeutiques surestimées ou sous-estimées.

iii) Interactions nano-bio,

Les interactions nano-bio font référence à l'étude des interactions entre un nanomatériau et un système biologique. Ces interactions déterminent l'identité biologique des nanomatériaux et peuvent modifier leurs propriétés en termes de toxicité, d'efficacité, de ciblage, de biodistribution ou d'interaction cellulaire^{12, 13}.

Pour relever ces défis, le présent travail se concentre sur le développement et la caractérisation approfondie d'une série de NPs de PLA et PLGA et est divisé en quatre chapitres principaux.

Le premier chapitre est une introduction axée sur une étude bibliographique. Parmi les systèmes d'administration de médicaments basés sur les nanotechnologies, les NP sont représentées avec l'accent sur celles de PLA et de PLGA. Les méthodes de préparation des NPs chargées en médicaments sont présentées, montrant les stratégies principales pour augmenter les charges en médicaments et l'évaluation de l'homogénéité des NPs. Une brève introduction à la caractérisation des NPs en polymère est ensuite donnée, suivie d'une présentation des techniques pertinentes de caractérisation. Les défis actuels de la caractérisation des NP polymériques sont abordés. Ensuite, nous présentons chaque technique de pointe qui nous a permis d'effectuer une analyse individuelle des NP tout au long de cette thèse (chapitres II et III). Enfin, les problématiques croissantes dues aux interactions nano-bio sont présentés et ensuite la position de la recherche actuelle et les techniques disponibles sont résumées. Les limites des techniques actuelles sont détaillées. Les techniques de caractérisation avancées utilisées dans la méthodologie proposée au chapitre IV sont présentées.

Le deuxième chapitre est consacré à la préparation et à la caractérisation de NPs de PLA et de PLGA dans le but d'encapsuler une molécule active importante, la vancomycine (VCM). Cet antibiotique très efficace a cependant tendance à former des agrégats et possède également une faible biodisponibilité en raison de son hydrophilie élevée¹⁴. Après un examen détaillé des facteurs (expérimentaux et physico-chimiques) ayant un impact sur l'incorporation du VCM dans une série de

(co)polymères PLA et PLGA qui diffèrent par leur poids moléculaire, leur groupement terminal et leur hydrophobie, le mécanisme d'incorporation du médicament a été élucidé. De manière remarquable, cela a permis de concevoir des NPs avec des charges élevées de VCM et une libération contrôlée.

Une caractérisation approfondie des NPs chargées de médicaments a été effectuée en mettant l'accent sur la localisation du médicament dans chaque NP individuelle. Les NPs compartimentées ont été étudiées à l'aide de microscopies électroniques couplées à l'analyse chimique par spectroscopie de rayons X à dispersion d'énergie. La localisation du médicament à l'intérieur des NPs a été clairement identifiée. Les résultats ont été confirmés par une autre technique versatile, l'AFM-IR, qui permet à la fois la visualisation des NPs par microscopie à force atomique (AFM) et leur analyse chimique par spectroscopie infrarouge (IR).

Le troisième chapitre présente une étude innovante sur l'analyse des NPs individuelles. Elle vise à apporter la preuve de concept de la quantification des charges en molécules actives au niveau de NPs individuelles, un aspect important en nanomédecine qui n'a pas encore été abordé. Un principe actif présentant des propriétés anticancéreuses a été utilisé comme molécule de choix en raison de ses propriétés physicochimiques, afin d'établir la preuve du concept. Avant d'employer l'AFM-IR pour étudier les NPs en PLA chargés en molécules anticancéreuses, nous avons vérifié la linéarité du signal IR par rapport à l'épaisseur de l'échantillon.

Tout d'abord, une étude de preuve de concept est réalisée sur des films en PLA. Une courbe d'étalonnage a été établie en utilisant la microspectroscopie IR, permettant ainsi une analyse quantitative par AFM-IR. Une fois la méthode établie, elle a été appliquée dans le cas des NPs chargées de médicaments. Des hétérogénéités importantes ont été trouvées en termes de composition, soulignant l'utilité de notre approche originale.

Dans le quatrième chapitre, une étude approfondie est menée pour étudier les interactions nano-bio d'une série de NPs, car il a été clairement démontré que celles-ci pouvaient modifier leur effet thérapeutique. Pour ce faire, les NPs de PLGA ont été élaborées avec et sans un recouvrement de PEG "en brosse". De plus, des NPs hybrides organiques-inorganiques (nanoMOFs), PEGylées ou non, ont été utilisées à titre de comparaison.

Le PEG est un revêtement hydrophile bien étudié qui peut adopter une structure en forme de brosse, et dont il a été démontré qu'il protège l'interaction des NPs avec diverses biomolécules et augmente leur temps de circulation dans le sang. La "couronne de protéines", un phénomène couramment observé lorsque les NPs pénètrent dans la circulation sanguine, est définie comme la couche dynamique constituée de protéines adsorbées à la surface des NPs et donne un aperçu de leur

devenir *in vivo*. En outre, un aspect original de cette étude a été d'examiner qualitativement l'interaction d'une protéine modèle, l'albumine de sérum humain, qui entre en contact avec les NPs sans s'adsorber à leur surface, phénomène très peu étudié de nos jours. Bien qu'il existe de nombreuses techniques disponibles pour l'étude de la couronne protéique, chacune d'entre elles se concentre sur un aspect spécifique et ne donne pas une image complète des interactions complexes entre les NP et les protéines. Par conséquent, l'une des nouveautés de cette étude est la combinaison stratégique de méthodes orthogonales afin de parvenir à une compréhension plus approfondie de ces interactions en combinant les aspects quantitatifs et qualitatifs de la couronne protéique. Notre compréhension a été encore améliorée par l'analyse comparative de différents recouvrements, ainsi que des compositions chimiques de NPs.

Enfin, les principaux résultats sont résumés et les perspectives sont présentées.

General Introduction

Nanomedicines have been providing solutions to many of unsolved problems in modern medicine. "Nano-" size sets the grounds in nanomedicine and refers to the unique properties of the nanomaterials, different from those of the bulk. Among them, nanoparticles (NPs) used as drug delivery systems was foreseen as the nanomedicines most likely to bring input in healthcare and improvements in drug administration^{1, 2}. With over forty-years of development, biocompatible polymer NPs have become one of the most widely studied nanoparticulate delivery system³. They generally offer new avenues over the conventional treatments with free drugs. Studies have highlighted their capability on: i) controlling the pharmacokinetic and drug distribution profile; ii) protecting the drug from degradation or inactivation; iii) enhancing drug absorption & improvement of intracellular penetration; iv) site-specific delivery; v) drug release in controlled manner^{4, 5}.

As they are approved by the Food and drug administration, biodegradable poly (lactic acid) (PLA) and poly (lactic-co-glycolic acid) (PLGA) (co)polymers have been the most employed polymers as they offer to deliver a wide range of drugs (hydrophilic, hydrophobic and amphiphilic) via several routes of administration^{6, 7}. Their tuneable physicochemical properties (molecular weight, end group, hydrophilicity etc.) allow a precise control of the NP features such as stability, surface charge, responsivity, drug loading, and release kinetics⁸. Scientists also engineered their surfaces with polymers such as poly(ethylene glycol) (PEG) and ligands to achieve "stealth" properties and longer blood circulation time^{9, 10}.

Although there has been an extensive research on the development and characterization of PLA and PLGA based NPs, their transition into clinics is surprisingly low. Considering this is not the case for PLA and PLGA based microparticles, we have identified one of the main reasons resulting in this transitional gap from bench to bedside. These nano-size induced novel challenges are;

- i) Insufficient drug loadings,

While insufficient drug loading has a direct effect on the therapeutic efficacy of NPs, the tiny size of the NPs restricts the drug loading especially for hydrophilic drugs belonging to important families such as antibiotics, proteins, anticancer drugs¹¹.

- ii) Lack of methodologies for individual NP characterization,

Individual NP characterization is a must to understand heterogeneities among the NPs of same batch thus to avoid over or underestimated therapeutic activities.

iii) Nano-bio interactions,

Nano-bio interactions refers to the study of interactions between a nanomaterial and a biological system. Such interactions dictates NPs' biological identity and might alter their properties in terms of toxicity, efficacy, targeting, biodistribution or cellular uptake^{12, 13}.

To address these challenges, the present work focuses on developing and fully characterizing a series of PLA and PLGA NPs and is divided into four main chapter.

The first chapter is the introduction focusing on a bibliographic survey. Among nanotechnology-based drug delivery systems, NPs are represented with a special interest on PLA and PLGA NPs. The methods to prepare drug loaded NPs are introduced, showing strategies to increase drug loadings and NPs' homogeneity. A brief introduction on polymeric NP characterization is then given followed by introducing the characterization parameters and the relevant techniques. Current challenges in polymeric NP characterization is discussed briefly before the transition to state-of-the-art characterization. There, we introduce each technique that allowed us to make individual NP analysis throughout this thesis (Chapter II and III). Finally, the rising concerns due to nano-bio interactions are asserted and thereafter the position of current research and available techniques are summarized. Limitations of the current techniques on obtaining different aspects of nano-bio interactions are further detailed. The advanced characterization techniques used in the methodology proposed in Chapter IV is introduced.

The second chapter is dedicated to preparation and characterization of PLA and PLGA NPs with the interest of encapsulating an important drug, vancomycin (VCM). VCM is a powerful antibiotic but prone to form aggregates. It also possess a low bioavailability due to its high hydrophilicity¹⁴. After a detailed examination of the factors (experimental and physicochemical) impacting VCM incorporation into a series of PLA and PLGA (co)polymers that differ in molecular weight, end group and hydrophobicity, the drug loading mechanism is unravelled. Remarkably, this further allowed to engineer NPs with high VCM loadings as well as controlled release. An in-depth characterization of drug loaded NPs is carried on emphasizing the location of the drug in each individual NP. Compartmentalized NPs are identified using electron microscopies together with chemical analysis by energy-dispersive X-ray spectroscopy. Drug localization is identified visibly inside the NPs. Results are confirmed with another versatile technique, AFM-IR, that enables both visualization of the NPs by atomic force microscopy (AFM) and their chemical analysis with infrared (IR) spectroscopy.

The third chapter presents a breakthrough study on individual NP analysis. It aims to advance quantification on individual NPs and achieve local drug loadings, an important aspect in drug delivery and yet to be addressed. A Re-based drug presenting anticancer properties, is used as molecules of choice in reason of its physicochemical properties, in order to establish the proof of concept. AFM-IR is chosen to perform this challenging task on drug loaded PLA NPs. Several parameters were set up to ensure the efficient IR analysis. This includes homogeneity of the sample, linearity of the IR signal against sample thickness and linearity of concentration against thickness. First, a proof-of-concept study is carried on PLA films. A calibration curve is plotted using IR microspectroscopy (giving quantitative data) in order to establish a comparability between the two techniques, thus allowing quantitative analysis by AFM-IR. Once the method established, it is applied on drug-loaded NPs. Important heterogeneities are found in terms of composition, highlighting the usefulness of our innovative approach which could find potential applications towards the clinical applications of polymeric NPs.

In the fourth chapter, a comprehensive study is carried on investigating nano-bio interactions of a series of NPs, as these have been shown to alter their therapeutic effect. To do so, PLGA NPs are engineered with and without a “brush” PEG shell. Besides, for comparison reasons and to gain better understandings, hybrid organic-inorganic NPs (nanoMOFs) are used. They are also PEGylated or not. By this way the respective influences of both NPs’ shells and cores could be investigated.

PEG is a well-studied hydrophilic coating which can adopt a brush-like structure, and which has been shown to shield the NPs interaction with various biomolecules and increase their blood circulation time. “Protein corona”, a phenomenon commonly observed when NPs enter to the bloodstream, is defined as the dynamic layer consisting of proteins adsorbed on the surface of NPs. Quantitative protein corona investigations answer how much protein gets absorbed on the NP surface. This gives clear insights on the NPs’ *in vivo* fate. In addition to that, one original aspect here was to investigate qualitatively the fate of a protein that gets in contact with NPs without adsorbing onto their surface. Indeed, this interaction could induce dramatic effects on the protein structure as well as on its stability, function or signalling. However nowadays scarce studies deal with these aspects. A model protein, human serum albumin, is used in our investigations and the core-shell NPs do not contain drugs, for simplicity reasons. Although there are numerous techniques available for the protein corona investigations, each one focuses on one specific aspect and do not give a whole picture of the complex NP-protein interactions. Therefore, one novelty of this study is the strategic combination of orthogonal methods in order to achieve a deeper understanding of these interactions combining quantitative and qualitative aspects of

protein corona. Our understanding is further enhanced by the comparative analysis of different NP surfaces and morphologies.

Finally, the main results are summarized, and the perspectives are presented.

References

1. Madkour, L. H. Nanoparticle and polymeric nanoparticle-based targeted drug delivery systems. in *Nucleic Acids as Gene Anticancer Drug Delivery Therapy* 191–240 (Elsevier, 2019). doi:10.1016/b978-0-12-819777-6.00013-5.
2. Bayda, S., Adeel, M., Tuccinardi, T., Cordani, M. & Rizzolio, F. The history of nanoscience and nanotechnology: From chemical-physical applications to nanomedicine. *Molecules* vol. 25 112 (2020).
3. Peltonen, L., Singhal, M. & Hirvonen, J. Principles of nanosized drug delivery systems. in *Nanoengineered Biomaterials for Advanced Drug Delivery* 3–25 (Elsevier, 2020). doi:10.1016/b978-0-08-102985-5.00001-2.
4. Rempel, G. L. Introduction of Polymer Nanoparticles for Drug Delivery Applications. *Nanotechnol. Nanomedicine&Nanobiotechnology* **2**, 1–6 (2015).
5. Patra, J. K. *et al.* Nano based drug delivery systems: recent developments and future prospects. *J. Nanobiotechnology* **16**, 71 (2018).
6. Astete, C. E. & Sabliov, C. M. Synthesis and characterization of PLGA nanoparticles. *J. Biomater. Sci. Polym. Ed.* **17**, 247–289 (2006).
7. Mir, M., Ahmed, N. & Rehman, A. ur. Recent applications of PLGA based nanostructures in drug delivery. *Colloids and Surfaces B: Biointerfaces* vol. 159 217–231 (2017).
8. Ahlin Grabnar, P. & Kristl, J. The manufacturing techniques of drug-loaded polymeric nanoparticles from preformed polymers. *J. Microencapsul.* **28**, 323–335 (2011).
9. Gref, R. *et al.* 'Stealth' corona-core nanoparticles surface modified by polyethylene glycol (PEG): Influences of the corona (PEG chain length and surface density) and of the core composition on phagocytic uptake and plasma protein adsorption. *Colloids Surfaces B Biointerfaces* **18**, 301–313 (2000).
10. Gref, R. *et al.* Biodegradable long-circulating polymeric nanospheres. *Science*

- (80-.). **263**, 1600–1603 (1994).
11. Jain, A. K. & Thareja, S. In vitro and in vivo characterization of pharmaceutical nanocarriers used for drug delivery. *Artif. Cells, Nanomedicine Biotechnol.* **47**, 524–539 (2019).
 12. Saptarshi, S. R., Duschl, A. & Lopata, A. L. Interaction of nanoparticles with proteins: Relation to bio-reactivity of the nanoparticle. *J. Nanobiotechnology* **11**, 1 (2013).
 13. Owens, D. E. & Peppas, N. A. Opsonization, biodistribution, and pharmacokinetics of polymeric nanoparticles. *Int. J. Pharm.* **307**, 93–102 (2006).
 14. Abed, N. & Couvreur, P. Nanocarriers for antibiotics: A promising solution to treat intracellular bacterial infections. *International Journal of Antimicrobial Agents* vol. 43 485–496 (2014).

Chapter I

Introduction

Introduction

This chapter will first focus on nanomaterials used for engineering drug delivery systems (DDS). Polymer based nanoparticles (NPs) are of main interest as they offer delivery platforms for wide variety of drugs, with versatile release properties. The second part of this chapter will introduce the techniques that are commonly used for the characterization of the NPs and define the current challenges in the field concerning polymeric NPs. To address these issues, we propose here a state-of-the-art methodology based on an individual NP characterization, together with a detailed description of the techniques which were used in the course of this thesis. Finally, a new methodology was also proposed with the aim to investigate the interactions of the developed NP formulations with a model protein, albumin. The current trends will be analyzed according to different aspects of the protein corona investigations.

1. Nanomedicine

Within the past few decades nanotechnology has broadened the areas of science and its application to healthcare has been termed as nanomedicine by The European Science Foundation. Nanotechnology-enabled medicine, nanomedicine, involves the use of nanoscale materials for diagnosis, treatment and prevention of diseases.¹ While the prefix nano originates from the Greek word *nannos* meaning "dwarf", a nanometer (nm) represents a billionth of a meter (10^{-9} m) and nanoscale is characterized by the dimensions of order of 1000 nm or less.^{2 3 4} In 2011, the European Commission (EC) adopted a 'Recommendation on the Definition of a Nanomaterial', which defines 'nanomaterial' as: "*A natural, incidental or manufactured material containing particles, in an unbound state or as an aggregate or as an agglomerate and where, for 50 % or more of the particles in the number size distribution, one or more external dimensions is in the size range 1 nm - 100 nm.*"⁵ The EC also emphasized on the importance of **gaining a deep knowledge on the**

physicochemical characterization of the NPs and on their interactions with the biological media. These topics will constitute the core of this thesis and novel methodologies will be proposed here.

Nanometric size induces unique properties to nanomaterials as compared to their bulk counterparts mainly because of the naturally occurring quantum effects and expanded surface area that is inversely proportional to particle size. Such materials having unique surface to volume ratios present increased reactive surface areas with a wider range of biological targets. They can greatly penetrate into tissues and generally promote higher cellular uptake than particles with sizes larger than 1 μm .^{6 7} Substantially, nanotechnology allows scientists to engineer nanomaterials while tailoring their physical, chemical, mechanical and optical properties that directly have influence on biological interactions.

1.1. Nanotechnology based drug delivery systems (DDSs)

One of the most exciting concepts in nanomedical research is the design and the development of nanotechnology-based drug delivery systems that combine diagnostic and therapeutic agents with enhanced activity and improved safety. The drugs incorporated in nanocarriers can be targeted to their appropriate site of action, and released in a controlled way to produce the expected therapeutic effect. Novel drug delivery technologies such as targeted delivery, triggered release, timed release aim to ensure patient compliance, improve drug bioavailability, cell permeability, minimize undesirable side effects and diminish toxicity.⁸ **(Fig. 1)** The encapsulated drug is not only protected from possible enzymatic degradation and/or inactivation but also overcomes the biological barriers such as intestinal barrier, blood brain barrier etc.⁶ Nanocarriers also provide the delivery of poorly soluble drugs considering the fact that low aqueous solubility is one of the major problem for the

development of new therapeutics. Consequently, lower doses are given to the patient with higher efficacy that dramatically minimizes undesirable side effects and toxicity. Targeted delivery systems can be used especially to treat cancer more effectively and a wide range of other diseases which call for drugs of high potency.⁹ The route of administration is systematically tailored to achieve the desired benefits. While the oral and intravenous administration are the most commonly used, NP delivery through pulmonary, nasal, ocular and transdermal routes have been creating new opportunities.¹⁰ **(Fig. 1)** Nanocarriers should be designed to be suitable for intravenous delivery considering the fact that the smallest capillaries in the body are 5-6 μm in diameter. The size of the nanocarrier being distributed into bloodstream must be significantly smaller than 5 μm to avoid embolism in case the formulation forms aggregates.¹¹

The physicochemical properties of a nanocarrier have an important role in its biodistribution. Indeed, the components of a nanocarrier should be cautiously chosen depending on their i) biocompatibility, preferably biodegradability in the case of polymers; ii) immunotoxicity; non-toxic and ideally materials with known safety profiles, iii) stability and iv) capacity to solubilize/incorporate the drug cargo of interest.¹² **(Fig. 1)**

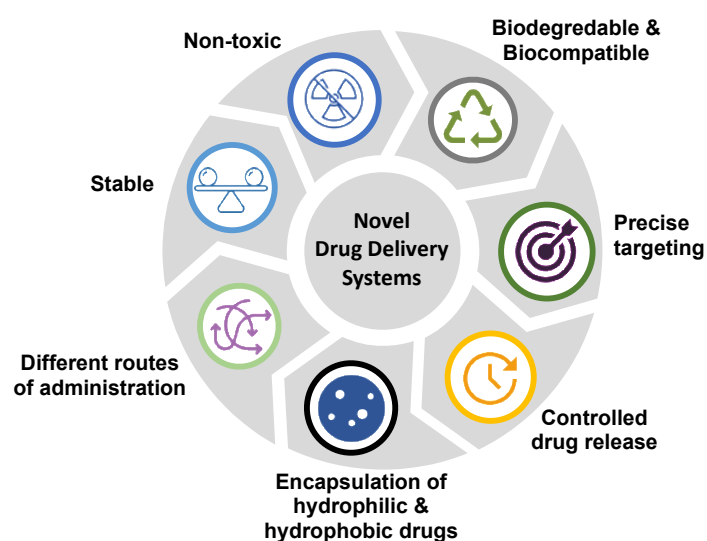


Figure 1. Advantages of nanotechnology-based DDSs

An “ideal” drug nanocarrier should have good encapsulation efficiency (EE, percentage of successfully entrapped drug), exhibit drug loadings (DL, mass ratio of entrapped drug to the nanocarrier) of at least 10 wt% and trigger the release of their payload in controlled manner. Controlled release systems offer prolonged release at a predetermined and controllable rate. Release can last for days to years while maintaining the drug concentration within the effective therapeutic range thus reducing the number of required doses and maintaining the drug concentrations in the therapeutic window.¹³

1.1.1. Nanoparticles

While the history of NPs can be traced back to 9th century where the artisans used silver and copper NPs to generate glitter effects, in 1959 Feynman had pointed out the big potential of NPs that is hidden in the smallest dimensions of the matter.¹⁴ The clever use of NPs has revolutionized how drugs are formulated and delivered.

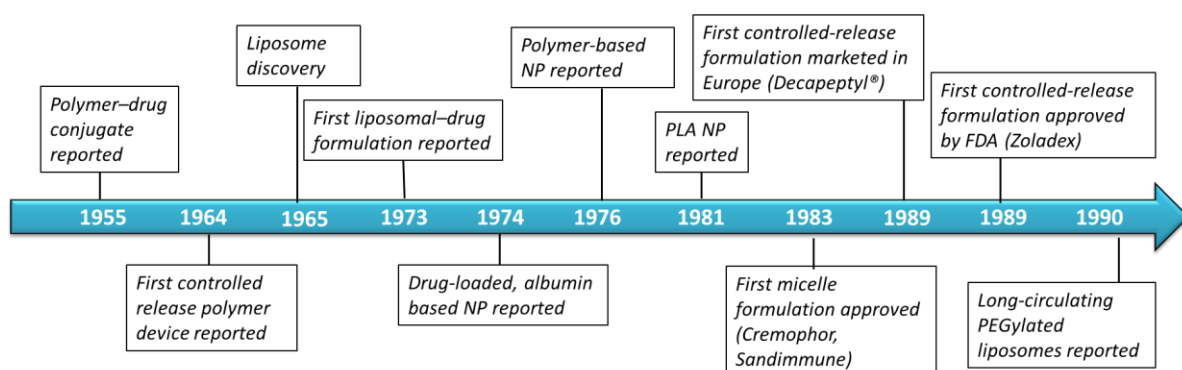


Figure 2: Timeline representing key moments in the nano drug delivery systems.¹² PLA and PEG refers to biodegradable polymers; poly(lactic acid) and poly(ethylene glycol) respectively.

Polymer–drug conjugates and liposomes mark the birth of the field of the nanotechnology based DDS and represents together the most marketed therapeutics of DDSs (**Fig. 2**). The very first generation of NPs introduced in 1965 that are now FDA-approved liposomes, are formed by one or more lipid bilayers surrounding an aqueous cavity (**Fig. 3**). A wide variety of molecules can be encapsulated within liposomes since both encapsulation within the aqueous cavity and lipid layers are possible.¹⁵ By the supramolecular organization of hydrophilic and hydrophobic regions, different structures such as lipospheres, lipid NPs or micelles can be obtained.¹⁶

One recent example of lipid NPs that are formulated to encapsulate the vaccine component, messenger RNA (mRNA), became the first approved vaccine against coronavirus 2 (SARS-CoV-2) hitting clinical use. This virus caused more than 2 million deaths and the World Health Organization declared a global pandemic on March 2020. The new class of DNA- and RNA-based vaccines deliver the genetic sequence of specific viral proteins to the host cells using nanotechnology platforms.¹⁷

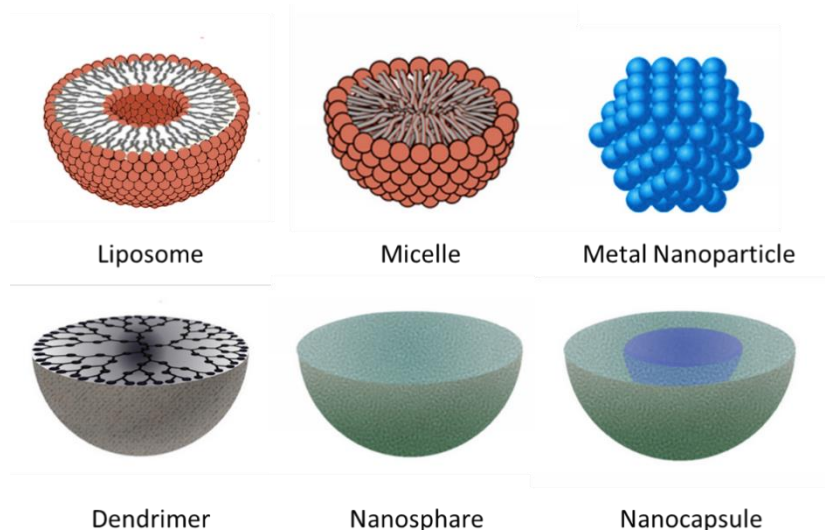


Figure 3: Schematic representation of the main types of nanocarriers

During the period 1973–76, Speiser's research group has employed emulsion polymerization techniques for the preparation of drug-loaded NPs.¹⁸ During the same period albumin-based NPs were also reported with the capability to specifically target cells.¹⁹ **(Fig. 2)** Subsequently, a wide variety of nanocarriers have been developed by using different organic (polymers and lipids) and inorganic materials (silica and metals). Organic materials are often biocompatible and have the advantages to build specific interactions with biomolecules. Although they might suffer from swelling or low mechanical properties, they have found most of the applications in DDSs. On the other hand, inorganic materials have better mechanical properties, however their affinity for molecules of interest are generally lower.

The classification of NPs regarding to their composition is as following:

i) metallic NPs are composed of metals, commonly gold, iron, silver or metal oxides such as [iron(II, III)oxide (Fe_3O_4), gadolinium(III) oxide (Gd_2O_3), or titanium dioxide (TiO_2)]. **(Fig. 3)** Although they have found diverse applications in daily life, there is still lack of knowledge and big concerns about their safety and toxicity, and therefore on their impacts to the human health.²⁰

ii) Hybrid NPs are made by the association of different materials combining the characteristics and advantages of both organic and inorganic materials. Recently, biodegradable metal organic frameworks (MOFs) consisting of metal nodes connected to organic bridging ligands have been proposed as DDSs.²¹ They showed a great potential to entrap high payloads of a large variety of drugs within their open porosity. Their degradation mechanism is peculiar and related to the stability of the coordination bonds between the organic ligands and the metal nodes, in contrast to the organic NPs where degradation occurs through breaking strong chemical bonds.²²

iii) organic NPs are mainly prepared using polymers and polysaccharides. Polymeric NPs are generally engineered using synthetic polymers, such as poly(lactic-co-glycolic acid) (PLGA), PLA, PEG, methoxy poly(ethylene glycol), poly(vinyl alcohol) (PVA), and poly(vinyl acetate). Amphipathic polymers promote the formation of polymeric micelles. Dendrimers are also based on polymers such as poly(propylene imine) and they are composed of repetitive branches. **(Fig 3)**

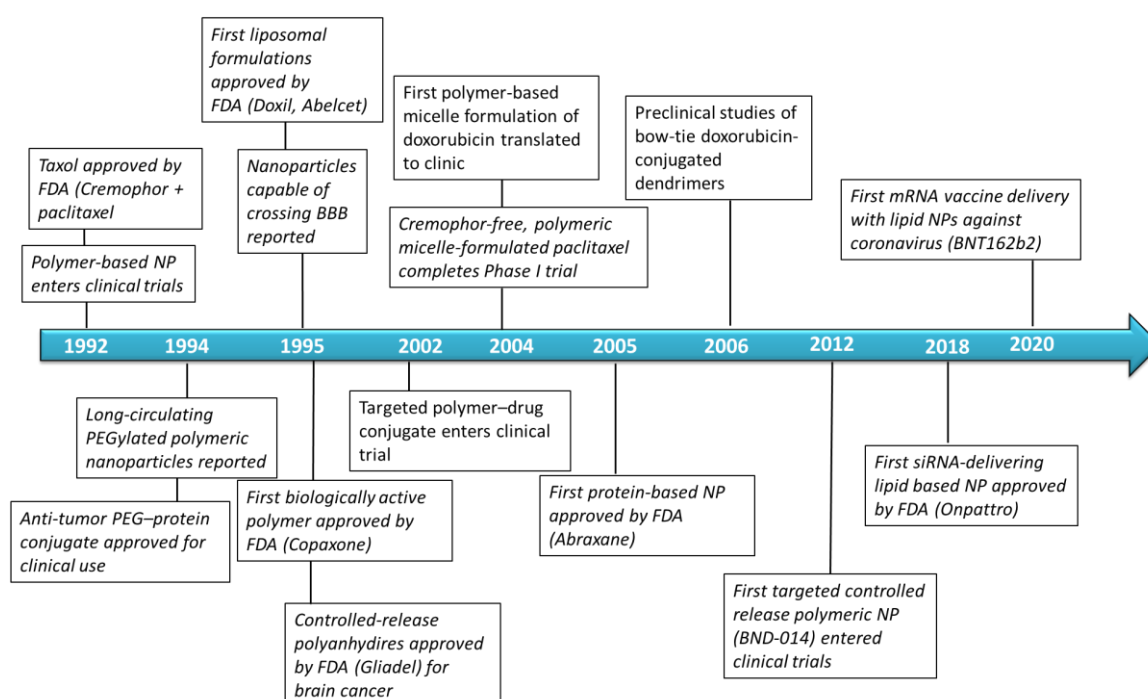


Figure 4. Timeline representing key moments in the nano drug delivery systems. ^{12 17 23}

As represented in **Fig. 2,4**, after their first report, the polymer-based NPs have gained a tremendous attention as colloidal DDSs and they assisted the progress of new discoveries. While the number of research conducted on various kind of NPs as drug delivery vehicles have been expanding notably since the first decade of the 21st century, polymer based nanoparticulate DDSs represent a substantial part of this research field. **(Fig. 5)**

Remarkably, Langer's research group pioneered the controlled release of drugs from degradable/non-degradable polymer matrices. ²⁴ In the

following section and the rest of this thesis, we will focus on polymeric NPs which is a growing field as assessed by the number of publications.

(Fig 5)

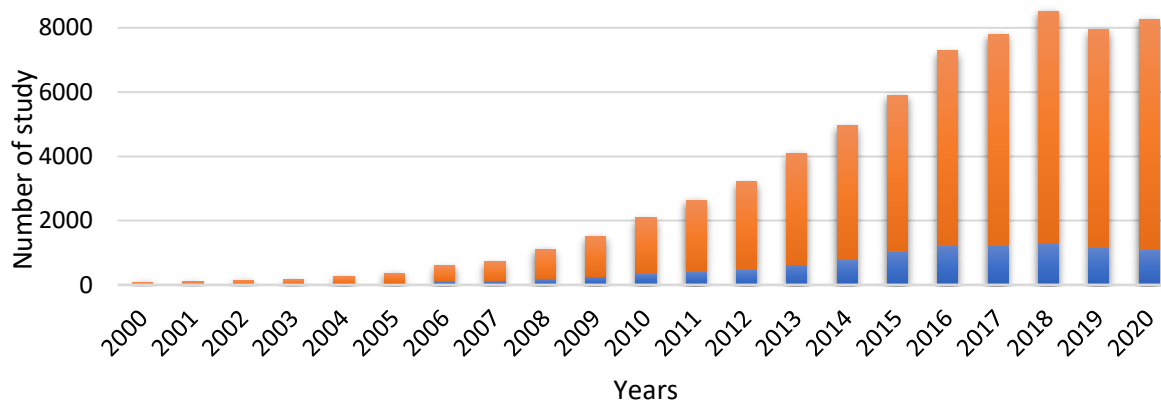


Figure 5. Number of studies that have been published on “nanoparticles & drug delivery” (orange) and “polymeric nanoparticles & drug delivery” (blue) since 2000. Source: Web of science

1.1.1.1. Polymeric Nanoparticles

Owing to their versatility and wide range of properties, NPs consisting of polymeric materials have been thoroughly studied for delivery and controlled release of drugs. Unlike liposomes, polymer-based NPs present greater encapsulation efficiencies and also better protection of the drug from external environment.^{25 26} Studies also showed better stabilities and cellular uptake for polymeric NPs.²⁷ Furthermore, compared to metal NPs that are generally prepared with more costly and potentially hazardous materials, polymeric NPs are less toxic and can be produced by simpler methods.²⁸ Biodegradation of polymeric NPs at specific sites and time is their main advantage as drug carriers. Indeed, controlled release is acquired basically by the balance between the rate of polymer degradation and/or the drug diffusion through the polymer matrix. Therefore to achieve targeted delivery, controlled release and drug-

loading capabilities of DDSs, both synthetic and natural polymers have been developed through advanced polymer chemistry and engineering.²⁹ Structures such as multivalent polymers, branched polymers, graft polymers, dendrimers, dendronized polymers, block copolymers, star-like polymers and hybrid glyco- and peptide polymeric derivatives take advantage of well-defined and tailored chemical compositions,³⁰ On the other hand, natural polymers differ in purity and variations from batch-to-batch. Complexities associated with their purification and immunogenicity have been shown. They also impose possibilities of disease transmission from their source organisms to humans. Additionally, they often require cross linking that might potentially denature the encapsulated drug. Therefore, natural polymers have been used less broadly in DDSs.³¹

Biodegradable polymers in DDSs

Although in general the polymers in earlier stage were mainly used in non-biological purposes, the invention of synthetic biodegradable polymers in the 1960s has flourished the drug delivery thanks to the pioneered works of luminary researchers, including Folkman, Langer, Higuchi, Peppas, Heller, Ringsdorf, and Speiser.²⁹ Biodegradable polymers with the greatest advantage of breaking down into naturally occurring metabolites and removal from the body with normal metabolic pathways allow scientists to develop safer, non-toxic and biocompatible NPs. Moreover, synthetic biodegradable hydrophobic polymers in contrast to natural hydrophilic polymers have advantage of releasing the incorporated drug over a period of days to several weeks facilitating improvements in the therapeutic index of drugs.³² Using the concepts of targeted and controlled release, successful *in vitro* and *in-vivo* investigations established the ground for human testing and ongoing phase II clinical trials for polymeric NPs.³³

Drug delivery vehicles based on polyanhydrides were approved in 1996 with a great degree of control in the polymer degradation rate (which can

vary over six orders of magnitude) and surface erosion allowing precise tuning of drug release. Polyanhydrides have been used to deliver anti-cancer drugs, antibiotics, vaccines and proteins.³⁴ Polycaprolactone (PCL) is an example of biodegradable semi-crystalline aliphatic polyester that is Food and Drug Administration approved and used as carrier for sustained delivery of several drugs such as ibuprofen, docetaxel, Cyclosporin A.³⁵ However due to its long *in vivo* degradation time (two to three years) it has mainly found applications as a long term implant delivery devices, such as Capronor® which is a subdermal contraceptive that releases levonorgestrel over a year. PCL is often blended or copolymerized with other polymers to afford better overall NP erosion.³⁴ Indeed polyesters such as PLA and PLGA (**Fig. 6**) are the most widely studied synthetic biodegradable polymers. Together with their ease of synthesis (via ring opening or condensation polymerization) and commercial availability,³⁴ their status of Food and Drug Administration (FDA) approval for human uses makes them highly potent to use as novel DDSs. Their hydrolysable backbones make these polyesters great candidates for drug nanocarriers, taking into account their tunable degradability in aqueous environments such as body fluids. For these reasons, the PLGA/PLA family was used in this work, and the physicochemical characteristics of these biodegradable polymers will be detailed in the next sections.

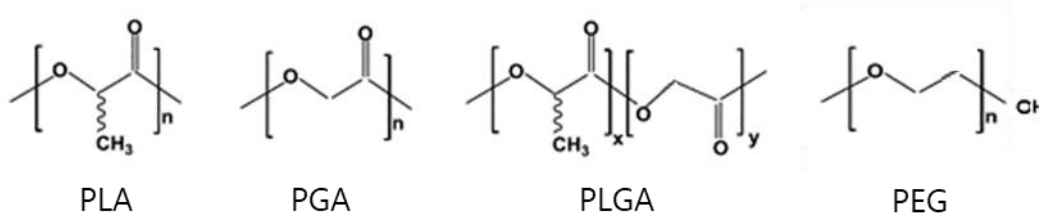


Figure 6. Chemical structure of FDA approved PLA, PGA, PLGA and PEG.

PLA & PLGA copolymers and PLA-PEG & PLGA-PEG diblock copolymers

Poly(lactic acid) or polylactide is an aliphatic polyester produced by direct condensation of lactic acid (low molecular weight (Mw) PLAs, Mw < 3000 g/mol) or by ring opening polymerization of lactide (high Mw PLAs). Lactic acid (LA) is obtained from the fermentation of agricultural byproducts such as corn starch or sugar canes. PLA, being a chiral molecule, exists in two optically active configurations; D(-)-lactic acid and L(+)-lactic acid which are partially crystalline, while the racemic poly(D,L-lactic acid) is amorphous.³⁶

Poly(glycolic acid) (PGA) marketed under the name of Dexon was the first totally biodegradable polymer ever investigated for biomedical use. However, with its fast degradation profile and insolubility issues in many common solvents, PGA use for drug delivery purposes is limited.³⁷ Consequently, PLGA copolymers were developed that are easily prepared by polycondensation reactions with lactic acid and glycolic acid and by ring-opening polymerization of lactide and glycolide. Both PLAs and PLGAs are soluble in various organic solvents including acetone, chlorinated or fluorinated solvents, dioxane and furane, but insoluble in water and common alcohols like methanol and ethanol.

A wide variety of mechanical properties and degradation rates can be tailored by varying the Mw, opening perspectives for different applications.³⁸ For instance, while PLA with high Mw is often used as augmentation devices for orthopedics, low PLA molecular weight is preferred as drug carrier. PLA and PLGA often undergo hydrolytic degradation leading to a bulk erosion. Advantageously, the degradation product is nothing more than the non-toxic lactic acid (L) and/or glycolic acid (G).³⁹ It is worth mentioning that polymers presented here are

approved by FDA and found to have great biodegradability and biocompatibility for human clinical applications.⁴⁰

Since PLA and PGA have distinctive individual properties, by varying the number and composition of the lactic and glycolic acid units, PLGA copolymers can be synthesized with significantly different physicochemical profiles (hydrophilicity, crystallinity, inherent viscosity, glass transition temperatures etc.) offering to engineer NPs with distinct properties. For instance, with specific L:G ratios, the degradation times of 50:50 PLGA, 75:25 PLGA, and 85:15 PLGA were reported to be 1–2 months, 4–5 months and 5–6 months, respectively. In general, PLGA NPs made of low L:G ratio, low Mw and uncapped PLGA polymers is expected to show high drug release rates that is associated with increased water uptake, accelerated hydrolysis and erosion of the polymer.

PLA and PLGA copolymers are available with different end groups (carboxylic acid or ester) that provide not only numerous chemical interactions with the drug molecules and the surrounding media, but also allow end group functionalization.

Biodegradable diblock copolymers PLA-PEG and PLGA-PEG are synthesized with covalently linked PEG to PLGA or PLA. They are of great interest to develop NPs with a hydrophilic PEG “brush” at their surface which acts as a barrier avoiding the adsorption of opsonins from the biological media. Indeed, the hydrophilic PEG chains migrate towards the NP surface during the NP formation forming a steric and hydrated barrier for the repulsion of foreign molecules.⁴¹ Gref et al. introduced for the first time PEGylated polymeric NPs, based on PLGA and showed increased the circulation half-life of NPs as well as reduced liver uptake compared to bare PLGA NPs⁴². This pioneering study led to the future clinical development of PEGylated NP formulations. Unique opportunity of targeting tumors upon systematic administration was achieved by the enhanced permeability and retention (EPR) effect.⁴³

Nowadays, several companies propose PLA PLGA and PLGA-PEG (co)polymers with well-defined properties. Among them, we have used here the Expansorb[®] portfolio manufactured in Aramon, France by the Seqens company. They offer the advantages of long-term storage below -15°C, under dry inert atmosphere. The manufacturing units operate according to ICHQ7 and cGMP guidelines and have large scale capacities (FDA inspected sites) up to industrial scale.

As previously mentioned, polymeric NPs can be engineered to encapsulate both hydrophilic and hydrophobic drugs to treat severe diseases such as cancer and resistant infections. In this work, we focused on a challenging aspect, the treatment of intracellular infections, where pathogens "hidden" inside cells cannot be eradicated by drugs which do not bypass the cell membranes barriers. Indeed, the intracellular bacteria can shield the immune response of the host but also escape from the killing effect of most of the antibiotics.⁴⁴ Addressing this challenge is one of our main interest and the approach will be developed in the second chapter of this thesis. The following section will deal with the preparation methods of drug loaded polymeric NPs, which is a fundamental aspect to achieve high drug payloads and controlled release.

1.1.1.2. Preparation methods of drug loaded polymeric NPs

Several methods have been employed to prepare polymeric NPs. The selection of the convenient methodology is crucial to engineer the nanomaterial according to the clinical needs. The NPs fabrication route is chosen depending on the physicochemical properties of the drug molecules, along with NP size and loading requirements. NPs can be prepared synthetically mainly by a polymer self-assembly approach or by monomers polymerization. The self-assembly approach is preferred, as it

employs well-characterized preformed polymers. Indeed, NP preparation by polymerization presents several drawbacks such as the resulting potentially toxic side-products, and the difficulties to remove unreacted monomers, as well as the possible unwanted chemical reactions with the loaded drugs.

Depending on the preparation method, nanocapsules or nanospheres can be obtained. Nanocapsules are vesicles with core-shell structures in which the drug is confined in the compartments which is surrounded by a polymer membrane, whereas nanospheres are dense matrices formed by intermingled polymer chains. **(Fig. 7)**

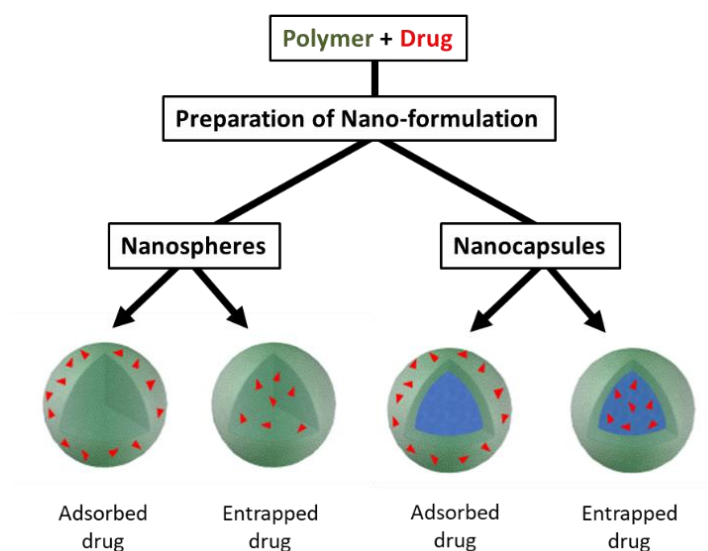


Figure 7. Schematic representation of different types of drug loaded polymer-based nanoparticles.

In general, in these structures, the drug of interest can be: i) directly attached to the NP matrix by degradable or nondegradable covalent bonds or ii) physically entrapped into the nanomatrix or iii) adsorbed onto the NP surface through non-covalent interactions. The latter case should be avoided in order to prevent the phenomenon known as “burst release”. The “burst effect” is characterized by a rapid drug release once the NPs

are exposed to an aqueous environment. Such a “burst” release is an obstacle to achieve optimal controlled release kinetics and might result in a major loss of the drug cargo before the NP reaches its biological target.

Polymeric NPs can be used to deliver both water soluble and insoluble drugs using adapted preparation methods. Polymeric NPs have been developed with a great diversity of shapes, sizes, and components, enabling them to be engineered for specific applications. Some of the main polymeric NPs preparation methods are developed in the next section.

1.1.1.2.1. Nanoprecipitation

The most common method to prepare polymeric NPs is nanoprecipitation, also called solvent displacement or interfacial deposition, since it is based on the displacement of a solvent (organic phase) with a non-solvent (aqueous phase). Nanoprecipitation was discovered and patented by Fessi et al. in 1989 and it was mostly employed for hydrophobic drugs. An essential prerequisite for this method is the miscibility of the organic and aqueous solvents. The organic phase (usually the polymer and the drug dissolved in acetone) is introduced into the aqueous phase (usually dropwise) ensuring a good mixing.

When the two phases are mixed, due to the differences in the surface tensions, interfacial turbulence occurs. By a rapid desolvation of the polymer, immediate nanoprecipitation takes place involving instantaneous drug entrapment. NPs are obtained with or without using a surfactant and the organic phase can subsequently be removed completely from the aqueous suspension by evaporation. Key variables that determine the size of the NPs are associated with the organic phase injection rate, aqueous phase stirring rate, the method of organic phase addition and the organic phase/aqueous phase ratio. The presence of

surfactant and the concentration of the components also play a role in the final characteristics of the NP. Nanoprecipitation has main advantages as being simple, fast, reproducible and easy to scale up. It requires volatile solvents with low toxicities such as acetone and requires only mild stirring under minimal shear stress. Smaller NPs are usually obtained by this method as opposed to other methods using same polymers. However, it has significant limitations to encapsulate hydrophilic drugs which tend to diffuse out in the suspension media and to form concentrated NP suspensions.

1.1.1.2.2. Emulsions

Unlike nanoprecipitation, other polymeric NP preparation methods generally consist of two main steps: the preparation of an emulsified system and polymer precipitation leading to NP formation. Nano-emulsions (oil droplets typically of 40-500 nm) are generally formulated through the so-called "high-energy" methods that require the use of specific devices applying mechanical energy (homogenizers and/or probe sonicators). The aim of using such devices is to provide energy that breaks up macroscopic phases or turn larger droplets into submicronic droplets by increasing the water/oil interfacial area. From a thermodynamic point of view, nano-emulsions are in a non-equilibrium state that cannot be formed spontaneously. However, the kinetics of destabilization of nano-emulsions is slow so that they are considered kinetically stable during the timeframe of NP formation. This is mainly due to their very small size, resulting in the prevention of droplet flocculation and coalescence".

Emulsification-based approaches differ based on the properties of the polymer and drug, as well as on the miscibility of the organic solvent (oil) with the aqueous phase. Some methods utilizing hydrophobic polymers

involve volatile and water-immiscible solvents that can be removed by simple evaporation leading to polymer precipitation (emulsification-solvent evaporation method). Others use a partially or fully water miscible solvent and controlled diffusion processes take place resulting in polymer precipitation (salting-out or emulsion-diffusion methods). **(Fig. 8)**

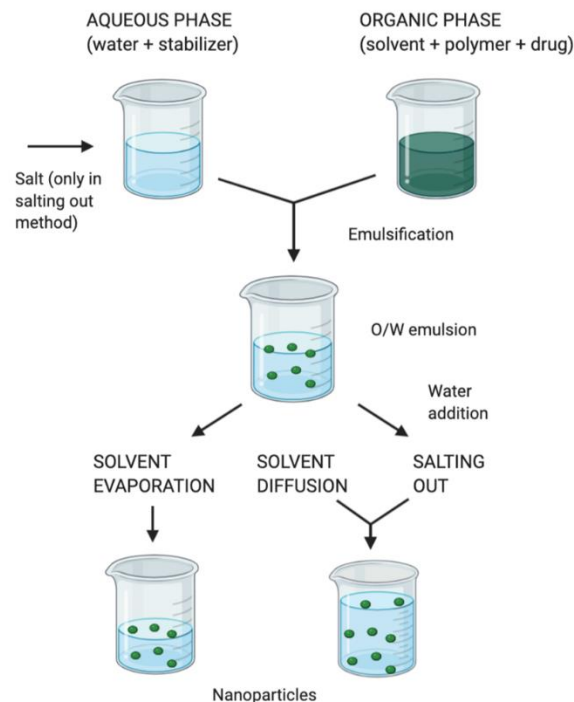


Figure 8. Emulsification-solvent evaporation (1), emulsification-solvent diffusion (2) and salting-out method (3).

The methods that involve organic solvent diffusion to formulate PLGA or PLA NPs generally use low polymer concentrations in order to obtain nanometric particles.

At higher polymer concentrations, the salting out method is preferable, but it necessitates additional purification steps and can pose problems of incompatibility between the salts and the drug. The methods involving solvent evaporation are less sensitive to polymer concentration than nanoprecipitation ones. They were widely used to entrap both type of

drugs i.e. hydrophilic (multiple emulsions) and hydrophobic (oil in water emulsions).⁴⁵

2. An introduction to NP characterization

In comparison to small molecule drugs, investigations on NP's quality, safety and efficacy profiles demands to analyze some extra parameters such as average particle sizes, polydispersity, particle shape, surface charge, drug loading and release, surface coating and chemical composition. Characterization of these parameters associated with the physicochemical properties of NPs is very crucial as they critically determine the physiological interactions, *in vivo* distribution, therapeutic efficacy and/or diagnostic accuracy of NPs. Their extensive characterization is an important pre-requisite for preclinical development.

⁴⁶

Up to date, a wide variety of NP characterization techniques questioning different aspects of NP properties were developed. Since none of them can reveal an entire characterization of the nanomaterial, combining different techniques is key to reach satisfactory results. Besides that, each technique has its strong and weak points and some could lead to ambiguities and result misinterpretations.⁴⁷ Therefore, to ensure the correct assessment of a characterization parameter, evaluation with at least two techniques preferably based on different working principles is suggested.

In the following section, we will firstly focus on the main characteristics of polymeric NPs including stability, size, charge, shape and morphology while introducing the corresponding characterization techniques that are commonly used. Common strategies to investigate the drug loading and release properties will also be presented. After we state the current

challenges for the polymeric NP characterization, in the second part of this section, some advanced characterization techniques that have been used in the course of this thesis will be introduced with a special interest on the chemical identity of drug loaded NPs. More precisely, the challenges will be focused on the localization and quantification of the drug on an individual NP basis. Finally, characterizations of nano-bio interactions will be introduced stressing on NP-protein interactions. It has been emphasized that nano-bio interactions play a main role on the toxicity and biodistribution of the NPs thus its characterization is a key element to enhance polymeric NPs' translation from bench to bedside.⁴⁸

2.1. Characterization parameters and techniques for polymeric nanoparticles

2.1.1. Particle size and surface charge

To take advantage of the unique properties of NPs, size needs to be optimized as it differentiates NPs from their bulk materials and other delivery platforms. Being one of the key physicochemical parameters, NP size has a vital role determining NPs' penetration across the physiological barriers, circulation and navigation in the bloodstream, targeting and cellular uptake. In terms of drug loading, it has been showed that larger particles can accommodate larger quantities of drugs.⁴⁹ Drug release on the other hand, can be associated with both diffusion and polymer degradation, so that it is affected by the size of the NPs. Larger NPs are expected to present slower release rates.⁵⁰

Surface charge expressed as **Zeta potential** is a key indicator of the NP stability. High zeta potentials either positive or negative (more than +30 mV or less than -30 mV), usually result in colloidally stable particles since

repulsion between particles reduce the possibility of particle aggregation.

⁵¹ Zeta potential is evaluated by light scattering techniques. In an electrolyte solution where the mobile charges in the solution are attracted by the static charges on NP surface, the Zeta potential (measured in milliVolts) corresponds to the potential difference between stationary layer of charges surrounding the particles and the solution. In addition to the effect of molecules adsorbed on NP surface, pH and ionic strength of the solution (conductivity, concentration or type of the salt) as well as the concentration of NP components (e.g. polymer or surfactant) can have an impact on their Zeta potential. ⁵²

Besides Zeta potential analysis, dynamic light scattering (**DLS**) is one of the most commonly used technique for a rapid size distribution evaluation. It measures the temporal fluctuations of the light scattered due to Brownian motion of the particles *in situ* thus the average hydrodynamic size is obtained over tens of thousands of NPs. ⁵³ DLS is used to investigate the stability of formulations and to estimate the presence of aggregation or agglomeration as well as the polydispersity index (PDI). Homogeneity of size distribution is expressed by **PDI** that is being a dimensionless parameter which can vary between 0 and 1. Values lower than 0.2 correspond to narrow size distributions, meaning monodisperse NP suspensions. On the other hand, a PDI value higher than 0.5 signifies broader size distribution referring to polydisperse or multimodal NPs. ⁵⁴

Although DLS provides fast, precise (for monodisperse samples) and reproducible results with little amount of samples without damaging it, it is noteworthy to mention its drawbacks such as being sensitive to dust or small NP aggregates, being restricted to spherical, transparent and monodisperse samples. Since DLS data treatment assumes NPs are spherical, this assumption should be validated *via* microscopic examination.

Nanoparticle tracking analysis (**NTA**) is also based on Brownian motion and visualise trajectories of individual particles scattering light. This particle-by-particle analysis strategy provides a suitable analysis for highly polydisperse samples and is complementary to DLS. Analytical ultracentrifugation (**AUC**) is a commonly preferred technique for the characterization of small polymeric NPs (1-10 nm). It employs separation of populations according to their sedimentation characteristics based on their sizes with a diverse availability of detectors (fluorescents, absorbance, interference).⁵⁵

Among the X-ray based techniques, X-ray Diffraction (**XRD**) has become a cornerstone technique to analyze the crystal structure and the crystalline grain size by the scattered X-rays that gives rise to definite diffraction patterns. It is one of the most convenient characterization technique for polymer nanocomposites, however it gives poor information when the NPs are amorphous.⁵⁶ Small Angle X-ray Scattering (**SAXS**) measures the X-rays scattered due to the elastic collision between X-rays and the sample.

2.1.2.Spectromicroscopies

Particles with similar compositions and sizes might behave drastically different as a result of differences in their morphology. While NP degradation is highly dependent on shape, biological responses such as surface binding capability, targeting, cellular uptake, retention in tissues and organs are also affected by their morphology.

Electron microscopies (**EMs**) have been used to reveal the NP size and morphology. As opposed to DLS, EM offers to measure individual particles' size and shape through visualization with sub-nanometer resolution. EMs use highly focused electron beams that are scanned across the specimen. The electron beam is scattered and some electrons collide

with the sample atoms, while electromagnetic lenses focus the electrons.⁵⁷ In order to avoid electron scattering by air, measurements should be done under vacuum and samples should be dried or analyzed in a frozen state. Therefore, size measured by EM techniques represents the dried NPs mean diameter, therefore smaller particle sizes are expected in comparison to DLS. Scanning electron microscopy (**SEM**) and transmission electron microscopy (**TEM**) are the most common EMs. While TEM uses high energies between 80-300 keV with small beam size, SEM uses much smaller electron energies that are typically between 1-30 keV with a larger beam size, thus lower spatial resolution (around 5nm). High voltage electron beam in TEM allows to determine the structure and internal properties of the NPs (e.g. pores, core-shell structure) whereas SEM is used to characterize surface morphology due to its limited penetration depth. Scanning TEM (**STEM**) is an extension to classical TEM where a highly focused electron beam is scanned across the sample as similar to SEM. The transmitted electrons at high scattering angle are collected to form high-resolution, chemically sensitive, atomic number (Z-) contrast images. High atomic number elements with greater electron densities give higher contrast. The contrast can be enhanced by staining reagents, typically osmium tetroxide.⁵⁸

These EMs can be coupled with a number of analytical techniques such as energy loss spectroscopy (**EELS**) or energy-dispersive X-ray spectroscopy (**EDS**) to acquire additional information such as chemical analysis. These techniques will be detailed in section 2.3.1.

Unlike DLS, EMs often fail to provide statistical analysis of NP size distribution and mean size because of particle segregation on the grid and incapacity to analyze numerous NPs. Besides, the high energy electron beam in TEM might cause sample destruction especially for polymer NPs. Sample preparation approaches might include drying, fixation, dehydration and cutting. Drying tends to cause aggregates and sample

shrinking and might introduce artifacts. These issues can be addressed by using transmission electron cryomicroscopy (**CryoTEM**), where the samples are analyzed at the cryogenic temperatures allowing imaging of the flash frozen sample that allow to maintain their initial structure.⁴⁶

Atomic force microscopy (**AFM**) is one of the scanning probe technique that has revolutionised the characterization of NPs since its invention in 1986.⁵⁹ AFM was employed mainly for imaging and studying NP morphology and size, and results were generally in close agreement with DLS and EM.⁶⁰ Surface properties, topography and stiffness could be also assayed. Sample preparation in AFM is straightforward and does not require any staining nor metal coating. It allows to observe almost any kind of material (conducting, non-conducting, biological, polymer or inorganic in ambient environments or submersed in liquids or in contact with cells.^{61 62} AFM uses a pyramidal, very sharp tip attached to a flexible cantilever (referred as probe) which determines the resolution of the image. The cantilever moves across the sample either across (x, y-plane) or perpendicular (z-plane) to the surface of interest. Deflection of the cantilever upon interaction with the surface is detected by a focused laser beam. During scanning across the surface, known as contact mode, the forces between the sample and the tip are constant and the detected z-movements correspond to height changes on the surface, thus revealing its topography. In this mode, due to lateral forces, artefacts might appear such as moving the loosely adhered samples or damaging soft or delicate structures such as polymers or biological material. On the other hand, in tapping mode, the cantilever oscillates perpendicular to the surface and comes in contact with the sample intermittently. Therefore it allows to work with very soft or delicate samples or living cells.⁶³

2.1.2.1. NMR spectroscopy

Among the characterization techniques, NMR spectroscopy retains in the leading place for structural analysis being highly sensitive to structural and

dynamical details of molecules. Although NMR allows to work both in liquid and/or in solid state, due to their size and short nuclear T_2 relaxation times, NPs are often not applicable for liquid state NMR. However, a few studies highlight the interest of liquid NMR to detect the PEG shells on polymeric NPs.⁶⁴

Solid-state NMR is of particular interest since it is one of the few techniques that provides analysis on non-crystalline solid materials. Spinning the sample at the so-called "magic angle" (54.74° relative to the static magnetic field) at a rate of few thousand hertz provides that sample rotation (kHz) is greater than the magnitude of chemical shift anisotropy CSA (kHz) which thus removes the spectral broadening caused by CSA.⁶⁵

⁶⁶ Solid state NMR allows investigating the molecular structures, inter- and intra-molecular interactions, as well as the physical state of the encapsulated drug(s). Besides, the technique can be used to investigate drug release.⁶⁷

2.1.3. Drug loading and drug release

Drug loading and encapsulation efficiency are the two important parameters that offer quantitative information about drug loading process and its efficiency. During NP preparation, drugs are either loaded inside the NPs or adsorbed on their surface. Unloaded drugs remain in the NP suspension in their free form. In order to determine the drug amount associated with the NPs, the free fraction of drug is separated from the NPs commonly by ultracentrifugation. The quantity of drug encapsulated in the NPs can be determined either by analysing the incorporated drug found in NP pellet (sediment) after ultracentrifugation or the non-incorporated drug found in the supernatants (liquid above the NP sediments). To do so, standard analytical techniques such as spectrophotometry, fluorescence spectroscopy or UV spectroscopy can be used. High-performance liquid chromatography (HPLC) quantifies the drug using detectors, based on the drug's spectral properties. While UV–

Vis or fluorescence detectors are often used, mass spectrometry, evaporative light scattering detector (ELSD), and charged aerosol detector (CAD) can also be employed to increase sensitivity.⁶⁸ Similar approaches are applied to estimate the concentration of the drug released from the NPs under physiological conditions and more specifically in accordance to relevant media, pH, temperature and sampling time.

Advantageously, a NP system with maximal drug loading and high entrapment efficiency can reduce the amount of NP required for the administration of sufficient amount of active compound. It will also allow reducing drug waste during NP manufacturing. Establishing or promoting interactions between drug and the polymer matrix could enhance drug incorporation. This could be a good strategy especially to achieve sufficient loadings of water soluble drugs into hydrophobic polymeric NPs. Such strategies will be used in this thesis for the entrapment of hydrophilic antibiotics.

Besides, various release profiles of the drug can be obtained by tuning the drug-polymer interactions and by playing with factors such as the pH. To sum up, understanding the nature of drug-polymer interactions allow scientists to improve drug content, develop new DDS as well as to establish desired release profile of the drug.

2.2. Current challenges in polymeric NP characterization

After discussing the general aspects and traditional methods for polymeric NP characterization, this session will bring several emerging challenges. Although there has been a significant effort on the development and characterization of polymeric NPs, some aspects of NP characterization have not been addressed yet. This overarching consideration is associated with the complex structure of the multifunctional NPs which indeed tremendously complicates their characterization. NPs are often not

identical due to the complex steps involved in their preparation (several physical mechanisms such as phase separation and kinetic supramolecular assembling). Within a same batch, NPs can exhibit different physicochemical properties. **(Fig. 9)** Heterogeneity can be classified i) at the suspension level refers to subpopulation of particles within the same batch exhibiting different properties and/or chemistry; ii) at the individual NP level, this means nonhomogeneous distribution of physicochemical properties of a single particle. **(Fig. 9)** Such heterogeneities at different levels contribute to non-linear effects upon formulation optimization and scale up processes. Eventually, NPs within the same batch behave differently in terms of the therapeutic efficacy and cause unexpected biological outcomes as well as over or under estimated activities.⁶⁹ To sum up, heterogeneity has a strong effect on the NPs' *in vitro/in vivo* fate and possesses a fundamental challenge in their clinical translation.⁶⁹

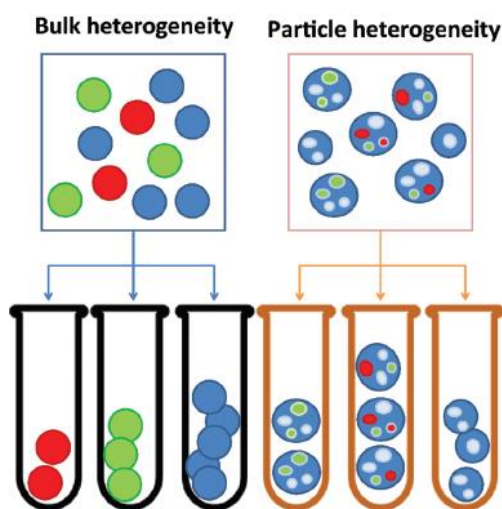


Figure 9. Schematic representation of the heterogeneity at the suspension level (left) and at the single particle level (right).⁶⁹

Heterogeneities should be examined both according to NP size distribution and also NP composition. Although characterization of size distributions and polydispersity of polymeric NPs have become routine laboratory tests, characterizations of chemical composition of individual

NPs still have not been addressed. In this context, the team of Dr. Gref in Institute of Molecular Sciences of Orsay (ISMO) focusses the efforts on an individual NP characterization.

Indeed, mapping the chemical composition of individual NPs reveals to be one of the most noteworthy parameters in DDSs to be unraveled. Crucial information could be obtained on the location of the NP components, including drug(s), targeting ligands, coating and surfactant, as well as on the homogeneity of their distribution. Moreover, the determination of drug location (encapsulated into the core or absorbed on the surface) is critically important to estimate the therapeutic efficacy and to apprehend the drug release mechanism (diffusion or degradation or desorption). Besides, the presence and location of targeting ligands, coatings and surfactants are crucial to identify the nano-bio interactions, thus the *in vivo* fate of the NPs.⁷⁰

To address these challenges, complementary characterization techniques that combine high resolution imaging (microscopies) with chemical characterization (spectroscopies) are powerful tools to affirm the structure of individual NPs.⁷¹ In this regard, high resolution microscopes are well suited to visualise the NPs. However, challenges arise in terms of chemical analysis since it requires chemical labelling. Chemical labelling of drug and/or NP might result in significant alterations of the formulations properties and therefore lead to misinterpretations which do not represent the reality.⁷²

From another standpoint, NP characterization appears to be employed commonly on behalf of qualitative information and quantitative data are collected generally from the bulk suspensions (drug loading, chemical composition etc.). Therefore, quantitative analysis of NP components (drugs, shells, ligands) on an individual NP basis remains a major challenge.

In the next session, we will introduce the state-of-the-art techniques used in this thesis in order to address the challenges mentioned above with a special focus on energy dispersive X-ray spectroscopy (EDX) and atomic force microscopy infrared spectroscopy (AFM-IR).

2.3. State-of-the-art characterization

2.3.1.S(T)EM EDX

EDX (also called XEDS or EDS) is an analytical technique employed for the chemical composition relies on the interaction of X-rays with a sample. The X-ray emissions are analysed by an energy dispersive detector. The unique atomic structure of each element allows obtaining a specific set of peaks ("fingerprint") on the X-ray emission spectrum. Combination of electron microscopies (SEM or TEM) with EDX allows particle by particle chemical composition analysis. Depending on the energy of the electrons, EDX in combination with SEM gives information on components located in the NPs top layers, whereas TEM provides information on the internal structural features.⁷³ Scanning TEM (STEM) was also coupled to EDX providing high resolution chemical composition detection. Qualitative analysis can be operated to estimate relative abundance of the elements (energies of the X-rays emitted from the area which is excited). Quantitative analysis is also conducted to determine the amounts of the elements by measuring the intensities of the X-ray peaks. The method can also provide mapping that shows spatial variation of the elements in the sample.⁷⁴

2.3.2.Atomic force microscopy infrared spectroscopy (AFM-IR)

IR spectroscopy is one of the most widely used techniques for chemical analysis. The pattern of vibrational absorption spectra in the mid IR range serves as a fingerprint by which chemical species can be identified. Spatially resolved chemical analysis can be conducted by IR

microspectroscopy which is the IR spectroscopy coupled with a microscope. However spatial resolution is limited to 2-10 μm due to diffraction.⁷⁵ Combination of IR with AFM⁷⁶ is a breakthrough since it breaks the diffraction limit of light and provides nanoscale spatial resolution with a chemical imaging. The sample is placed in contact with the tip of an AFM probe. When the IR radiation (laser) illuminates the sample (with an region of around 40 μm), photothermal expansion occurs in the parts of the sample that absorb the irradiation, which pushes the cantilever tip whose movements are recorded.⁷⁷ A direct relation of the amplitude of the cantilever oscillations with local absorption was proven.⁷⁸ As a result, local absorption spectra are revealed at a location of the AFM tip by sweeping the laser wavelength. Moreover, by illuminating the sample at a fixed wavelength, IR chemical maps can be obtained through scanning the tip over the sample. **(Fig. 10)**⁷⁹

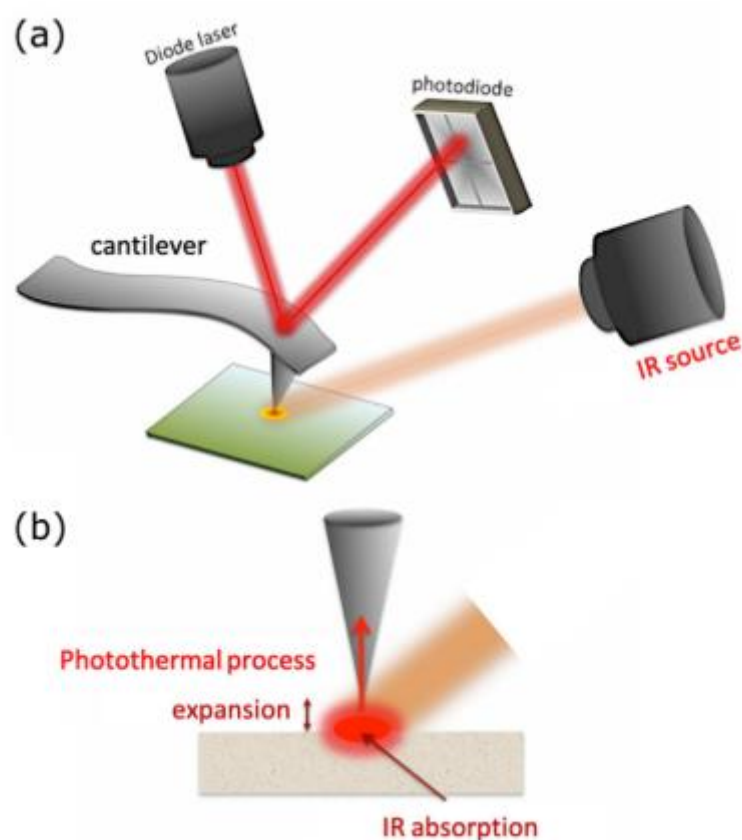


Figure 10. (a) Schematic view of an AFM-IR setup in the contact mode. The IR irradiation is set from the top (b). Sketch illustrates the photothermal expansion process.⁷⁷

Pancani et al. recorded correlative images of PLA NPs within cells by comparing AFM-IR and confocal microscopy experiments. **(Fig.11)**⁷² AFM-IR was thus revealed to be a powerful, reliable tool for chemical characterization and polymeric NPs component localization, by taking advantage of the IR fingerprint of the constitutive PLA polymer. In particular, AFM-IR requires no labelling of the complex NP structures nor of their components.

The recent implementation of the tapping mode to AFM-IR enabled chemical characterisation of polymeric NPs (PLA NPs) with an improved resolution (below 10 nm) and revealed the core shell structure of NPs.⁸⁰ In the study by Mathurin et al., the drug was detected preferentially in the NPs shell, although it was expected to be located in the core. This was well correlated with the “burst release” of the drug. In conclusion, the study shed light on the significance of chemical characterization of individual NPs.

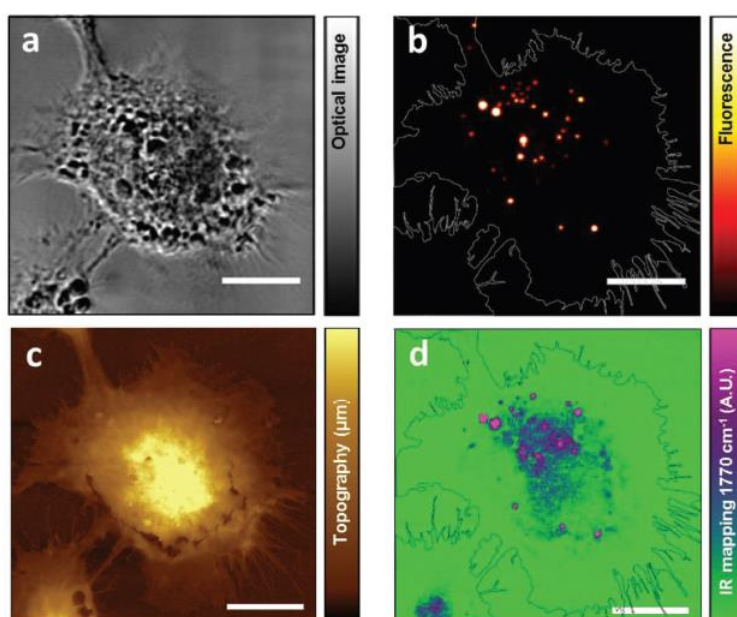


Figure 11. Visualization of fluorescently labelled PLA NPs internalized in macrophages using confocal microscopy and AFM-IR. Confocal microscopy: a) transmission image and b) Z- projection of averaged fluorescence intensity of internalized NPs. The pixel size of fluorescence image is 160×160 nm while voxel depth is 98.8 nm. The same cell, once dehydrated, was imaged by AFM-IR: c) AFM topography d) IR map at 1770 cm^{-1} (detection of NPs). Scale bars represent $10 \mu\text{m}$.⁷²

The next important challenge is to localize the drug inside the NPs as well as to determine its local quantity within individual NPs. These findings could be a breakthrough in the quality control of drug delivery systems. The second and the third chapter of this thesis will be dedicated to addressing these issues. Before moving to the next part, we intent to further highlight that the combination of analytical techniques has been the main strategy to address the challenges upon NP characterization. This strategy will be applied as well in the following part of this introduction that aims to present an original methodology for the characterization of nano-bio interactions, also based on a set of complementary methods.

3. Characterization of Nano-bio interactions

Engineered NPs designed to be administered into bloodstream are prone to bind with biomolecules, mainly with serum/plasma proteins. NPs upon contact with proteins could immediately be coated by proteins that leads a change in the biological identity of the surface of the NPs.⁸¹ This coating layer was termed as “protein corona” by Dawson in 2007. Up to date, investigations on protein corona has been filling the gaps between bench investigations and clinical applications of NPs through a deep understanding of the biological effects triggered by protein corona *in vivo*.⁸² Since protein corona dictates NPs’ biological identity, it might result into the failure of a nanocarrier in terms of toxicity, efficacy, targeting,

biodistribution or cellular uptake. Additionally, the adsorption of some specific proteins acting as opsonins might result into a fast removal of the NPs from the bloodstream as a result of inflammatory responses.^{83 84} Studies also showed that NP interaction with proteins can induce a structural rearrangement (conformational changes) in the protein and lead to protein aggregation, inappropriate signaling and/or functional alterations.⁸⁵ Therefore, to achieve a safe use of nanotechnology and have the control to manipulate protein binding on NPs, scientist must gain a comprehensive knowledge not only on which proteins are attached to the NPs, but also on the kinetics, affinities, and stoichiometries of these interactions.⁸⁶

Strategies to prevent protein adsorption on polymeric NPs have been developed. Numerous studies have demonstrated that opsonisation rates are low and/or slow in case of using neutral NPs and/or hydrophilic NPs.⁸⁷ Therefore, one of the main approaches is to engineer NP surface by using non-ionic surfactants and/or hydrophilic polymer chains (conjugated, grafted or surface adsorbed). This potentially could act as a shield between NP and proteins by blocking the electrostatic and hydrophobic interactions.⁸⁴ Among of all proposed shielding macromolecules (polysaccharides, polyacrylamide, poly(vinyl alcohol), poly(N-vinyl-2-pyrrolidone), poloxamers, poloxamines, polysorbates), poly(ethylene glycol) (PEG), PEG containing copolymers have had so far the biggest success in terms of effectivity and biocompatibility. Molecular weight of the PEG chains is a main criteria since it dictates the thickness of the coating layer, whereas PEG density is also a crucial factor ensuring good protein repulsion and NP "stealth" character.⁸⁸ The effect of PEG conformation (mushroom, brush, and dense brush) on protein corona formation has also been demonstrated and it is related to the PEG density at the NP surface. With optimized PEG coatings, reduced protein binding and prolonged blood circulation half-lives of PEGylated polymeric NPs have been reported.^{89 90}

Numerous strategies have been developed to characterize protein corona; composition, stability, binding affinity, thickness and conformation, including spectroscopic, electrophoretic and microscopic techniques.

Table 1 presents some of the main techniques.

Table 1. Main techniques to analyse protein corona

Technique	Description	Limitations
Protein identification		
Sodium Dodecyl Sulfate Poly-acrylamide Gel Electrophoresis (SDS-PAGE)	Resolution of proteins depending on a rough estimation of their molecular weight	Sensitivity limitations; possibility to obtain inaccurate results due to mobility variations; used only for comparison; quantitative results are not often possible; might not give the real identity of a protein
Mass spectroscopy	Protein identification; quantification and composition	Low abundance proteins can be masked by the abundant ones; limits in molecular weight (100-3000 Da)
Size, shape, and surface charge		
DLS and Zeta potential	Thickness of the protein corona on the NPs and shifts in the surface charge upon corona formation	Influenced by particle agglomeration; counterion binding; low precision; assumption of NP spherical shape
TEM	Morphology and thickness of protein corona	Staining of protein is needed; sample preparation can cause protein destabilization; sensitivity of NPs to electrons
AFM	Real state surface profile of the NPs	Unable to distinguish hard and/or soft corona formation

Kinetics & Binding capacity		
Isothermal titration calorimetry (ITC)	Thermal changes induced by protein binding; binding constant; protein to NP stoichiometry	High concentrations of samples are needed; analysis is carried with single protein at a time
Surface plasmon resonance (SPR)	kinetics of NP-protein interactions in real time and even under flowing conditions	Interference issues with the solid support of the device
NMR	Binding site by probing individual residues of the protein	needs high amounts of samples; cannot distinguish between different proteins
Quantity		
Protein assays	Amount of adsorbed protein in mass	No information about composition; possible interference of NP components
Conformational changes		
Raman spectroscopy	Relatively simple and rapid (no sample preparation); possible to detect aromatic chains; peptides and sulfur bonds from protein; no interference with water; non-destructive; highly specific	Sensitive to impurities; cannot be used for metals or alloys
Circular dichroism	Observations on structural alterations on protein upon contact with NPs; protein affinity; adapted for a wide range of solutions and temperatures; rapid data	Cannot provide information on individual amino acid residues

collection; small sample
amounts

Study of protein-NP interactions often include at first, the isolation of unbounded entities from the NP-protein complex, usually by ultracentrifugation. While some techniques analyse only unbounded proteins, some isolate the bounded proteins from the NP surface. In this case, detergents like sodium dodecyl sulphate are used since they can break the hydrophilic-hydrophobic interactions and thus can detach the protein layers from the NP surface. Gel electrophoresis (GE) or mass spectrometry (MS) are commonly used characterization methods to identify the proteins based on their molecular weights. Size, shape and surface charge observations give insights about the protein corona formation and its thickness and morphology. DLS must be carefully interpreted since the increases in the NP size might also mean particle aggregation in the presence of proteins or other non-covalent interactions rather than multilayer corona formation. Surface techniques such as EMs are used to visualize physical properties of the dried state of protein corona formation. While dry state do not represent the solubilized system, the need of using staining in proteins for EM can destabilize the protein or lead misinterpretation of the data.⁹¹ AFM can work both in solid and liquid state with high accuracy however it lacks efficiency since it is unable to distinguish hard and/or soft corona formation. **(Table 1)**

Gaining insights on the affinity of proteins towards NPs requires highly specialized techniques. Isothermal titration calorimetry (ITC) gives information about the binding constants as well as the stoichiometry of protein – NP interactions. However, it does not allow to work with multiple proteins at the same time, and thus is not adapted for the study of complex systems.⁹² Another label free technique that analyses the kinetics of association and dissociation of protein corona is surface plasmon

resonance (SPR). It has the advantages of real time analysis and detection of structural alterations (denaturation) of bound proteins. However, since it requires the chemical coupling of NPs or proteins to the solid support of the SPR device, interference problems might appear.⁹³ NMR also provides detailed information about the structures, thermodynamics and binding sites of the proteins with the main advantage of probing individual protein residuals. A wide variety of samples can be analyzed both in liquid and solid state. On the other side, it sometimes fails to detect surface bound proteins.⁹⁴

Net protein adsorption is frequently measured through protein assays that provide quick readouts with accuracy and sensitivity. They often measure the unbound protein (free protein) and the amount of adsorbed protein is then calculated. Bradford, Lowry, bicinchoninic acid (BCA) assays are some common examples of colorimetric detection methods based on optical absorbance of proteins in comparison with external calibration standards. In some cases, NPs' interference could be overcome by creating adequate calibration in the presence of particles.^{92 95}

In a nutshell, each technique has its own advantages and limitations, and the obtained information are specific. Although there is a tremendous available literature on the role of protein corona (altering pharmacokinetics and pharmacodynamics of NPs), analytical characterization methodologies still remain to be developed to give detailed information. Therefore, we focused our efforts to develop new methodologies to investigate the protein corona by combining complementary methods. The techniques that have been selected will be introduced in the following sessions.

3.1. Capillary electrophoresis

CE has emerged as a versatile technique for the physicochemical characterization of various types of samples including proteins and NPs and in particular showed potential to study the nano-bio interactions. Indeed, CE is able to separate, identify, and characterize different objects, from small molecules up to microorganisms. Electrophoresis meaning “to bear electrons” is based on liquid-phase electrokinetic separation in an electric field (up to 30 kV) within a capillary. Separation takes place according to differences in electrophoretic mobilities in a background electrolyte (BGE), consisting of a buffer that creates an electrically conductive medium.⁹⁶ The mobility depends on the particle size, shape and the properties of the BGE.

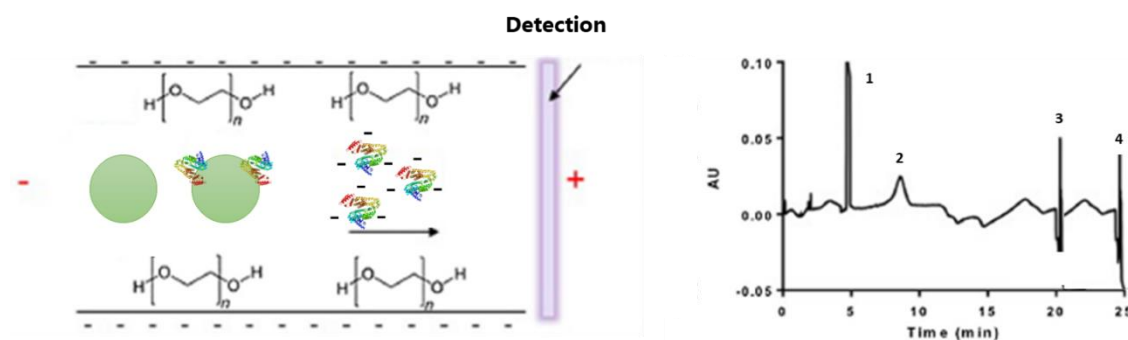


Figure 12. Principles of the separation using CE of a mixture consisting of free proteins (coils), NPs (green circle) and NP-protein complexes. The different species migrate in an electric field (-/+ , indicated in red) in the capillary which is coated by a neutral polymer such as PEG (left); Typical electropherogram migration of the; Peak 1: marker, peak 2: protein, peak 3: NP-protein complex, peak 4: NP. (right) Adapted from⁹⁷. AU = arbitrary unit

The estimation of protein binding is done by measuring the signal of either free or bounded protein or NP in function of their respective concentrations.⁹⁸ Noteworthy, bounded protein to the NP substantially contributes to both the NP’s overall charge and size, thus to the mobility that differentiates the NP-protein complex from the NPs.⁹⁹ **(Fig. 12)**

Furthermore, a quantitative analysis can be performed by using various detectors, such as UV–visible, fluorescence, and electrochemical detectors, and MS CE can provide high-resolution separations. For an accurate estimation, adsorption of the analyte onto the capillary wall should be considered. Wall modifications can be done by either permanent or dynamic coating.¹⁰⁰ **(Fig. 12)**

Moreover, the absence of a stationary phase in the CE capillary as compared to other separation techniques such as HPLC or SPR is an advantage especially for the separation of large entities (NP, proteins).

3.2. Circular Dichroism (CD) spectroscopy

As it has been previously discussed, different chemical environments on the NP surfaces can lead to structural changes in the bound proteins. These unwanted alterations can be tracked by analyzing the secondary structure of the proteins upon contact with NPs. By using circularly polarized light (right and left-handed) CD spectroscopy reveals the interactions of various chemical groups in the vicinity of proteins that are optically active molecules. Actual secondary structure is analyzed by the difference in these lights possessing different spin angular momentums on chiral molecules. Conventional CD works below the 240 nm UV range and peptide bond adsorption and conformational changes of proteins are detected at around 170–240 nm. However, the normalized background signal of the NPs needed to be removed from the protein–NP complex signal to avoid the possible impact of NPs. CD spectroscopy can be used to measure the interactions between NPs and proteins in real time and in the presence of unbound proteins.⁸⁷

3.2.1. Synchrotron radiation circular dichroism (SRCD) spectroscopy

SRCD spectroscopy relies on the very bright light produced by a synchrotron ring, used as the light source, which results in a higher photon flux over a wider wavelength range than in a conventional CD instrument. Advantageously, in the DISCO beamline (Soleil Synchrotron) this high flux covers a wide spectral range and down to 165 nm.¹⁰¹ Limitation to do measurement at even lower wavelengths was addressed by designing micro-sample-cells made of calcium fluoride. This setup has very low absorption in vacuum UV (VUV) range and shorter path length. Hence it requires sample volumes as low as 1 microliter and minimise the amount of solvent in the beam. Therefore highly reproducible spectra can be collected in lower wavelengths.¹⁰² (Fig 13.)

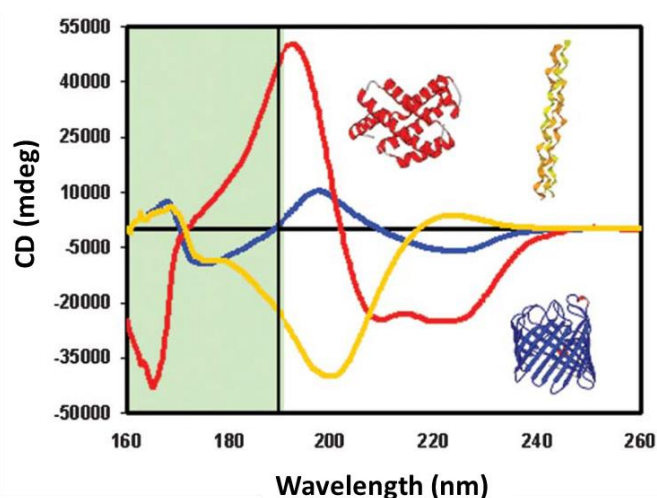


Figure 13. SRCD spectra of a helical protein (red), a beta sheet protein (blue), and a collagen (yellow). The green area represents the low wavelength region that is only accessible by using SRCD.¹⁰³

The absorption bands correspond to different characteristics of the secondary structure components (α -helix, β -sheet etc.). For instance, the

secondary structure features of helical proteins can be probed by two main absorption bands around 190 nm (π - π^* transition) and 210-220 nm (n - π^* transition) that are associated with the peptide backbone chain thus allowing protein conformation determination.

SRCD is also used to monitor folding and unfolding behavior of proteins in association with the protein stability. By gradually increasing the measurement temperature, unfolding of proteins can be followed by the changes in their CD spectra and melting temperature can be obtained after analysis of the CD spectra as a function of temperature.¹⁰⁴ Unfolded protein is denatured and possess a different secondary structure. Upon cooling, if the changes in CD spectra are fully reversible, this suggests that the protein maintained its stability. Therefore, by following melting temperature and thermal unfolding behavior, one can identify the protein stability affected by the physicochemical properties of NPs.¹⁰⁵

In this work, we obtained a working session in Synchrotron Soleil (Proposal: 20180883 (Standard) "VUV spectroscopy of nanoparticle-protein interactions " Main proposer: Dr. Ruxandra GREF, Assigned Local contact: Dr. Frank WIEN) which allowed us performing studies of HSA interaction with polymeric core-shell NPs, which were complementary to CE investigations.

4. Conclusion

In this chapter, we delved into the literature and advances on development of polymeric NPs and their characterization while highlighting the crucial parameters to be studied *in vitro* for their quality control and also for their successful translation into clinics.

A timeline displayed in the beginning of this chapter gave an overview on the key moments of NP development for drug delivery. Biodegradable polymeric NPs were explored as delivery platform for both hydrophilic and

hydrophobic drugs with targeting capabilities and controlled release profiles. The types of polymer-based NPs and their preparation methods were presented with the emphasis on PLA and PLGA based NPs and the trends in drug encapsulation. PLA and PLGA copolymers and their PEGylated counterparts (PLA-PEG and PLGA-PEG) offer to engineer NPs with unique properties. Simply by tuning the molecular weight, L:G ratios or end groups of copolymers, a great control in the NP size, drug loading, stability, surface properties can be achieved. PEGylated formulations have been shown to form hydrophilic brushes at the NP surface thus a barrier for the undesired nano-bio interactions. This has increased the NP circulation half-life and the therapeutic activity.

In the second part, NP characterization was discussed. Although it is often associated with physico-chemical properties of NP's compounds, in the process of developing NPs, in-depth characterization of NPs in bulk and also in individual NP basis provide vital information for the quality control during preclinical and clinical studies. It also allows to optimize NP preparation parameters and characteristics. Therefore, after we first introduced the common characterization parameters and techniques for polymeric nanoparticles that are often performed from bulk, we further stressed out the current challenges. Heterogeneities within the same batch of NPs were of concern.

Due to the complex mechanisms involved in their preparation methods, NPs can exhibit different physicochemical properties within the same batch and can cause strong alterations in their *in vivo* and *in vitro* fate as well as complicates the processes like optimization or scale up. Questions about drug loading, its location in single NP and its local quantity were raised. Therefore, individual NP characterization was on the focus of attention that should achieve both visualization and the chemical analysis on nanoscale. The state-of-the-art techniques such as STEM-EDX and AFM-IR were the methods suggested in this chapter to achieve

identification of the drug location on a single NP. To the best of our knowledge, individual NP analysis on PLA and PLGA NPs conducting chemical analysis for the drug location and quantification has never been reported.

Finally, nano-bio interactions were explored with the aim of establishing a methodology that investigate protein interactions with NPs. These interactions were discussed considering two main aspects, first was the protein corona formation that might cause modifications on the biological identity of NP and/or provoke their recognition by the immune system thus the removal from the body. *In vitro* protein corona investigations with quantitative aspect was of interest to have insights on the abundance of protein corona. In addition to that, CE was explored with the advantage of enabling both an accurate protein quantification and valuable qualitative information on the protein forms. Finally, SR-CD was described as a powerful tool for the secondary structure an analysis of the proteins. SR-CD provides complementary insights on the protein interactions with NPs contributing the qualitative aspect of the analysis.

In a nutshell, polymeric NPs were described as promising candidates for drug delivery. Strategies to engineer these NPs more efficiently were presented focusing on their preparation and advanced characterization.

5. References

1. EMRC, european M. R. C. ESF Forward Look on Nanomedicine 2005. **33**, 52 (2005).
2. Bayda, S., Adeel, M., Tuccinardi, T., Cordani, M. & Rizzolio, F. The history of nanoscience and nanotechnology: From chemical-physical applications to nanomedicine. *Molecules* vol. 25 112 (2020).
3. Committee, S. & Sccp, C. P. Scientific Committee on Consumer Products PRELIMINARY OPINION ON. *In Vivo (Brooklyn)*. **95**, 1–56 (2007).
4. Aminu, N. *et al.* The influence of nanoparticulate drug delivery systems in drug therapy. *Journal of Drug Delivery Science and Technology* vol. 60 101961 (2020).
5. EU Definition of a Nanomaterial.
<https://www.safenano.org/knowledgebase/regulation/substances/eu-definition-of-a-nanomaterial/>.
6. Patra, J. K. *et al.* Nano based drug delivery systems: recent developments and future prospects. *J. Nanobiotechnology* **16**, 71 (2018).
7. Panyam, J. & Labhasetwar, V. Biodegradable nanoparticles for drug and gene delivery to cells and tissue. *Advanced Drug Delivery Reviews* vol. 55 329–347 (2003).
8. Nayak, A. K., Ahmad, S. A., Beg, S., Ara, T. J. & Hasnain, M. S. Drug delivery: Present, past, and future of medicine. in *Applications of Nanocomposite Materials in Drug Delivery* 255–282 (Elsevier, 2018). doi:10.1016/B978-0-12-813741-3.00012-1.
9. Tomellini, R., Faure, U. & Panzer, O. *European Commission European Technology Platform on NanoMedicine-Nanotechnology for Health Luxembourg: Office for Official Publications of the European Communities*.
<http://www.cordis.lu/nanotechnology/nanomedicine.htm>.

10. Shah, N. K., Torrico Guzmán, E. A., Wang, Z. & Meenach, S. A. Routes of administration for nanocarriers. in *Nanoparticles for Biomedical Applications: Fundamental Concepts, Biological Interactions and Clinical Applications* 67–87 (Elsevier, 2019). doi:10.1016/B978-0-12-816662-8.00006-0.
11. Mohapatra, S. S., Ranjan, S., Dasgupta, N., Mishra, R. K. & Thomas, S. *Characterization and Biology of Nanomaterials for Drug Delivery: Nanoscience and Nanotechnology in Drug Delivery*. *Characterization and Biology of Nanomaterials for Drug Delivery: Nanoscience and Nanotechnology in Drug Delivery* (Elsevier, 2018). doi:10.1016/C2017-0-00272-0.
12. Petros, R. A. & Desimone, J. M. Strategies in the design of nanoparticles for therapeutic applications. *Nature Reviews Drug Discovery* vol. 9 615–627 (2010).
13. Abu-Thabit, N. Y. & Makhoul, A. S. H. Historical development of drug delivery systems: From conventional macroscale to controlled, targeted, and responsive nanoscale systems. in *Stimuli Responsive Polymeric Nanocarriers for Drug Delivery Applications: Volume 1: Types and Triggers* 3–41 (Elsevier, 2018). doi:10.1016/B978-0-08-101997-9.00001-1.
14. Sudha, P. N., Sangeetha, K., Vijayalakshmi, K. & Barhoum, A. Nanomaterials history, classification, unique properties, production and market. in *Emerging Applications of Nanoparticles and Architectural Nanostructures: Current Prospects and Future Trends* 341–384 (Elsevier Inc., 2018). doi:10.1016/B978-0-323-51254-1.00012-9.
15. *Rapid Immunotests for Clinical, Food and Environmental Applications*. (2016). doi:10.1016/s0166-526x(16)30095-2.
16. Ageitos, J. M. & Garcia-Fuentes, M. Advances in Drug Delivery Strategies for Microbial Healthcare Products. in 1–38 (2019). doi:10.1007/978-3-030-01881-8_1.

17. Milane, L. & Amiji, · Mansoor. Clinical approval of nanotechnology-based SARS-CoV-2 mRNA vaccines: impact on translational nanomedicine. *Drug Deliv. Transl. Res.* (2021) doi:10.1007/s13346-021-00911-y.
18. Kreuter, J. & Speiser, P. P. New adjuvants on a polymethylmethacrylate base. *Infect. Immun.* **13**, 204–210 (1976).
19. Hassanin, I. & Elzoghby, A. Albumin-based nanoparticles: a promising strategy to overcome cancer drug resistance. *Cancer Drug Resist.* **3**, 930–976 (2020).
20. Khan, S. A. Metal nanoparticles toxicity: Role of physicochemical aspects. in *Metal Nanoparticles for Drug Delivery and Diagnostic Applications* 1–11 (Elsevier Inc., 2019). doi:10.1016/B978-0-12-816960-5.00001-X.
21. Horcajada, P. *et al.* Porous metal-organic-framework nanoscale carriers as a potential platform for drug delivery and imaging. *Nat. Mater.* **9**, 172–178 (2010).
22. Christodoulou, I., Serre, C. & Gref, R. Metal-organic frameworks for drug delivery: Degradation mechanism and in vivo fate. in *Metal-Organic Frameworks for Biomedical Applications* 467–489 (Elsevier, 2020). doi:10.1016/b978-0-12-816984-1.00023-8.
23. Anselmo, A. C. & Mitragotri, S. Nanoparticles in the clinic: An update. *Bioeng. Transl. Med.* **4**, 1–16 (2019).
24. Liechty, W. B., Kryscio, D. R., Slaughter, B. V. & Peppas, N. A. Polymers for drug delivery systems. *Annu. Rev. Chem. Biomol. Eng.* **1**, 149–173 (2010).
25. Nanotechnology-Based Approaches for Targeting and Delivery of Drugs and Genes - 1st Edition.
<https://www.elsevier.com/books/nanotechnology-based-approaches-for-targeting-and-delivery-of-drugs-and-genes/mishra/978-0-12-809717-5>.
26. Martinho, N., Damgé, C. & Reis, C. P. Recent Advances in Drug

- Delivery Systems. *J. Biomater. Nanobiotechnol.* **02**, 510–526 (2011).
27. Kamps, J. A. A. M. & Scherphof, G. L. Biodistribution and uptake of liposomes in vivo. *Methods Enzymol.* **387**, 257–266 (2004).
 28. Harish, K. K., Nagasamy, V., Himangshu, B. & Anuttam, K. Metallic Nanoparticle: A Review. *Biomed J Sci & Tech Res* **4**, (2018).
 29. Kamaly, N., Yameen, B., Wu, J. & Farokhzad, O. C. Degradable controlled-release polymers and polymeric nanoparticles: Mechanisms of controlling drug release. *Chem. Rev.* **116**, 2602–2663 (2016).
 30. Ahlin Grabnar, P. & Kristl, J. The manufacturing techniques of drug-loaded polymeric nanoparticles from preformed polymers. *J. Microencapsul.* **28**, 323–335 (2011).
 31. De Souza, R., Zahedi, P., Allen, C. J. & Piquette-Miller, M. Polymeric drug delivery systems for localized cancer chemotherapy. *Drug Delivery* vol. 17 365–375 (2010).
 32. Langer, R. & Tirrell, D. A. Designing materials for biology and medicine. *Nature* vol. 428 487–492 (2004).
 33. Hrkach, J. *et al.* Preclinical development and clinical translation of a PSMA-targeted docetaxel nanoparticle with a differentiated pharmacological profile. *Sci. Transl. Med.* **4**, (2012).
 34. Ulery, B. D., Nair, L. S. & Laurencin, C. T. Biomedical applications of biodegradable polymers. *Journal of Polymer Science, Part B: Polymer Physics* vol. 49 832–864 (2011).
 35. Ramanujam, R. *et al.* Biodegradable Polycaprolactone Nanoparticles Based Drug Delivery Systems: A Short Review. *Biosci. Biotechnol. Res. Asia* **15**, 679–685 (2018).
 36. Södergård, A. & Stolt, M. Properties of lactic acid based polymers and their correlation with composition. *Progress in Polymer Science (Oxford)* vol. 27 1123–1163 (2002).
 37. Manoukian, O. S. *et al.* Biomaterials for tissue engineering and regenerative medicine. in *Encyclopedia of Biomedical Engineering*

- vols 1–3 462–482 (Elsevier, 2019).
38. Gupta, A. P. & Kumar, V. New emerging trends in synthetic biodegradable polymers - Polylactide: A critique. *European Polymer Journal*/vol. 43 4053–4074 (2007).
 39. Nair, L. S. & Laurencin, C. T. Biodegradable polymers as biomaterials. *Progress in Polymer Science (Oxford)* vol. 32 762–798 (2007).
 40. FDA's Regulatory Science Program for Generic PLA/ PLGA-Based Drug Products | American Pharmaceutical Review - The Review of American Pharmaceutical Business & Technology. <https://www.americanpharmaceuticalreview.com/Featured-Articles/188841-FDA-s-Regulatory-Science-Program-for-Generic-PLA-PLGA-Based-Drug-Products/>.
 41. Suk, J. S., Xu, Q., Kim, N., Hanes, J. & Ensign, L. M. PEGylation as a strategy for improving nanoparticle-based drug and gene delivery HHS Public Access Graphical abstract. *Adv Drug Deliv Rev* **99**, 28–51 (2016).
 42. Gref, R. *et al.* Biodegradable long-circulating polymeric nanospheres. *Science (80-.)*. **263**, 1600–1603 (1994).
 43. Gajbhiye, K. R. & Gajbhiye, J. M. EPR effect based nanocarriers targeting for treatment of cancer. *Int. J. Drug Deliv.* **8**, (2017).
 44. Xiong, M. H., Bao, Y., Yang, X. Z., Zhu, Y. H. & Wang, J. Delivery of antibiotics with polymeric particles. *Adv. Drug Deliv. Rev.* **78**, 63–76 (2014).
 45. Mir, M., Ahmed, N. & Rehman, A. ur. Recent applications of PLGA based nanostructures in drug delivery. *Colloids and Surfaces B: Biointerfaces* vol. 159 217–231 (2017).
 46. Lin, P. C., Lin, S., Wang, P. C. & Sridhar, R. Techniques for physicochemical characterization of nanomaterials. *Biotechnol. Adv.* **32**, 711–726 (2014).
 47. Kumar, G., Shafiq, N. & Malhotra, S. Drug-loaded PLGA

- nanoparticles for oral administration: Fundamental issues and challenges ahead. *Critical Reviews in Therapeutic Drug Carrier Systems* vol. 29 149–182 (2012).
48. Jain, A. K. & Thareja, S. In vitro and in vivo characterization of pharmaceutical nanocarriers used for drug delivery. *Artif. Cells, Nanomedicine Biotechnol.* **47**, 524–539 (2019).
 49. De Jong, W. H. & Borm, P. J. A. Drug delivery and nanoparticles: Applications and hazards. *International Journal of Nanomedicine* vol. 3 133–149 (2008).
 50. Sharma, S., Parmar, A., Kori, S. & Sandhir, R. PLGA-based nanoparticles: A new paradigm in biomedical applications. *TrAC - Trends Anal. Chem.* **80**, 30–40 (2016).
 51. Astete, C. E. & Sabliov, C. M. Synthesis and characterization of PLGA nanoparticles. *J. Biomater. Sci. Polym. Ed.* **17**, 247–289 (2006).
 52. Modena, M. M., Rühle, B., Burg, T. P. & Wuttke, S. Nanoparticle Characterization: What to Measure? *Adv. Mater.* **31**, 1–26 (2019).
 53. Anderson, W., Kozak, D., Coleman, V. A., Jämting, Å. K. & Trau, M. A comparative study of submicron particle sizing platforms: Accuracy, precision and resolution analysis of polydisperse particle size distributions. *J. Colloid Interface Sci.* **405**, 322–330 (2013).
 54. Lu, X. Y., Wu, D. C., Li, Z. J. & Chen, G. Q. Polymer nanoparticles. in *Progress in Molecular Biology and Translational Science* vol. 104 299–323 (Elsevier B.V., 2011).
 55. Diaz, L., Peyrot, C. & Wilkinson, K. J. Characterization of Polymeric Nanomaterials Using Analytical Ultracentrifugation. *Environ. Sci. Technol.* **49**, 7302–7309 (2015).
 56. Rajeswari, A., Jackcina Stobel Christy, E., Gopi, S., Jayaraj, K. & Pius, A. Characterization studies of polymer-based composites related to functionalized filler-matrix interface. in *Interfaces in Particle and Fibre Reinforced Composites: Current Perspectives on Polymer, Ceramic, Metal and Extracellular Matrices* 219–250 (Elsevier, 2019).

- doi:10.1016/B978-0-08-102665-6.00009-1.
57. Ferreira, L. M. B., Kiill, C. P., Pedreiro, L. N., Santos, A. M. & Gremião, M. P. D. *Supramolecular design of hydrophobic and hydrophilic polymeric nanoparticles. Design and Development of New Nanocarriers* (2018). doi:10.1016/b978-0-12-813627-0.00005-3.
 58. Tkachenko, V. *et al.* Characterizing the core-shell architecture of block copolymer nanoparticles with electron microscopy: A multi-technique approach. *Polymers (Basel)*. **12**, 1656 (2020).
 59. Binnig, G., Quate, C. F. & Gerber, C. Atomic force microscope. *Phys. Rev. Lett.* **56**, 930–933 (1986).
 60. Teulon, J. M. *et al.* On the operational aspects of measuring nanoparticle sizes. *Nanomaterials* **9**, (2019).
 61. Smith, J. R., Olusanya, T. O. B. & Lamprou, D. A. Characterization of drug delivery vehicles using atomic force microscopy: current status. *Expert Opinion on Drug Delivery* vol. 15 1211–1221 (2018).
 62. Sitterberg, J., Özçetin, A., Ehrhardt, C. & Bakowsky, U. Utilising atomic force microscopy for the characterisation of nanoscale drug delivery systems. *European Journal of Pharmaceutics and Biopharmaceutics* vol. 74 2–13 (2010).
 63. Maver, U., Velnar, T., Gaberšček, M., Planinšek, O. & Finšgar, M. Recent progressive use of atomic force microscopy in biomedical applications. *TrAC - Trends in Analytical Chemistry* vol. 80 96–111 (2016).
 64. Hrkach, J. S., Peracchia, M. T., Domb, A., Lotan, N. & Langer, R. Nanotechnology for biomaterials engineering: Structural characterization of amphiphilic polymeric nanoparticles by ¹H NMR spectroscopy. *Biomaterials* **18**, 27–30 (1997).
 65. Martínez-Richa, A. & Silvestri, R. L. Developments in Solid-State NMR Spectroscopy of Polymer Systems. in *Spectroscopic Analyses - Developments and Applications* (InTech, 2017). doi:10.5772/intechopen.70116.

66. Bugay, D. E. Solid-State Nuclear Magnetic Resonance Spectroscopy: Theory and Pharmaceutical Applications. *Pharmaceutical Research: An Official Journal of the American Association of Pharmaceutical Scientists* vol. 10 317–327 (1993).
67. Casabianca, L. B. Solid-state nuclear magnetic resonance studies of nanoparticles. *Solid State Nuclear Magnetic Resonance* vol. 107 101664 (2020).
68. Clogston, J. D., Crist, R. M. & Mcneil, S. E. Polymer Nanoparticles for Nanomedicines. *Polym. Nanoparticles Nanomedicines* 187–203 (2016) doi:10.1007/978-3-319-41421-8.
69. Rabanel, J. M. *et al.* Nanoparticle heterogeneity: An emerging structural parameter influencing particle fate in biological media? *Nanoscale* vol. 11 383–406 (2019).
70. M Chaupard, M de Frutos, R Gref. Deciphering the structure and chemical composition of drug nanocarriers : from bulk approaches to individual nanoparticle characterization. *Part. Part. Syst. Charact. Syst. Charact.* (2021).
71. Mathurin, J. *et al.* How to unravel the chemical structure and component localization of individual drug-loaded polymeric nanoparticles by using tapping AFM-IR. *Analyst* **143**, 5940–5949 (2018).
72. Pancani, E. *et al.* High-Resolution Label-Free Detection of Biocompatible Polymeric Nanoparticles in Cells. *Part. Part. Syst. Charact.* **35**, (2018).
73. Yesilkir-Baydar, S., Oztel, O. N., Cakir-Koc, R. & Candayan, A. Evaluation techniques. in *Nanobiomaterials Science, Development and Evaluation* 211–232 (Elsevier Inc., 2017). doi:10.1016/B978-0-08-100963-5.00011-2.
74. Bergström, J. Experimental Characterization Techniques. in *Mechanics of Solid Polymers* 19–114 (Elsevier, 2015). doi:10.1016/b978-0-323-31150-2.00002-9.

75. Gross, E. Challenges and opportunities in IR nanospectroscopy measurements of energy materials. *Nano Research* vol. 12 2200–2210 (2019).
76. Dazzi Dazzi, A., Ullis, L., Policar, C. & Kjoller, K. *United States Patent HIGH FREQUENCY DEFLECTION MEASUREMENT OF ABSORPTION*. (2013).
77. Mathurin, J., Deniset-Besseau, A. & Dazzi, A. Advanced Infrared Nanospectroscopy Using Photothermal Induced Resonance Technique, AFMIR: New Approach Using Tapping Mode. **137**, (2020).
78. Dazzi, A., Glotin, F. & Carminati, R. Theory of infrared nanospectroscopy by photothermal induced resonance. *J. Appl. Phys.* **107**, 124519 (2010).
79. Kurouski, D., Dazzi, A., Zenobi, R. & Centrone, A. Infrared and Raman chemical imaging and spectroscopy at the nanoscale. *Chem. Soc. Rev.* **49**, 3315–3347 (2020).
80. Mathurin, J. *et al.* How to unravel the chemical structure and component localization of individual drug-loaded polymeric nanoparticles by using tapping AFM-IR. *Analyst* **143**, 5940–5949 (2018).
81. Gref, R. *et al.* 'Stealth' corona-core nanoparticles surface modified by polyethylene glycol (PEG): Influences of the corona (PEG chain length and surface density) and of the core composition on phagocytic uptake and plasma protein adsorption. *Colloids Surfaces B Biointerfaces* **18**, 301–313 (2000).
82. Cai, R. & Chen, C. The Crown and the Scepter: Roles of the Protein Corona in Nanomedicine. *Adv. Mater.* **31**, 1–13 (2019).
83. Saptarshi, S. R., Duschl, A. & Lopata, A. L. Interaction of nanoparticles with proteins: Relation to bio-reactivity of the nanoparticle. *J. Nanobiotechnology* **11**, 1 (2013).
84. Owens, D. E. & Peppas, N. A. Opsonization, biodistribution, and

- pharmacokinetics of polymeric nanoparticles. *Int. J. Pharm.* **307**, 93–102 (2006).
85. Satzer, P., Svec, F., Sekot, G. & Jungbauer, A. Protein adsorption onto nanoparticles induces conformational changes: Particle size dependency, kinetics, and mechanisms. *Eng. Life Sci.* **16**, 238–246 (2016).
 86. Aggarwal, P., Hall, J. B., McLeland, C. B., Dobrovolskaia, M. A. & McNeil, S. E. Nanoparticle interaction with plasma proteins as it relates to particle biodistribution, biocompatibility and therapeutic efficacy. *Advanced Drug Delivery Reviews* vol. 61 428–437 (2009).
 87. Baimanov, D., Cai, R. & Chen, C. Understanding the Chemical Nature of Nanoparticle-Protein Interactions. *Bioconjug. Chem.* **30**, 1923–1937 (2019).
 88. Gref, R. *et al.* 'Stealth' corona-core nanoparticles surface modified by polyethylene glycol (PEG): Influences of the corona (PEG chain length and surface density) and of the core composition on phagocytic uptake and plasma protein adsorption. *Colloids Surfaces B Biointerfaces* **18**, 301–313 (2000).
 89. Rezvantab, S. *et al.* PLGA-based nanoparticles in cancer treatment. *Front. Pharmacol.* **9**, 1260 (2018).
 90. Mitchell, M. J. *et al.* Engineering precision nanoparticles for drug delivery. *Nature Reviews Drug Discovery* vol. 20 101–124 (2021).
 91. Pinals, R. L., Chio, L., Ledesma, F. & Landry, M. P. Engineering at the nano-bio interface: Harnessing the protein corona towards nanoparticle design and function. *Analyst* vol. 145 5090–5112 (2020).
 92. Rampado, R., Crotti, S., Caliceti, P., Pucciarelli, S. & Agostini, M. Recent Advances in Understanding the Protein Corona of Nanoparticles and in the Formulation of "Stealthy" Nanomaterials. *Frontiers in Bioengineering and Biotechnology* vol. 8 (2020).
 93. Hühn, J. *et al.* Dissociation coefficients of protein adsorption to

- nanoparticles as quantitative metrics for description of the protein corona: A comparison of experimental techniques and methodological relevance. *Int. J. Biochem. Cell Biol.* **75**, 148–161 (2016).
94. Li, Y. & Lee, J. S. Insights into characterization methods and biomedical applications of nanoparticle-protein corona. *Materials* vol. 13 3093 (2020).
95. Campion, E. M., Loughran, S. T. & Walls, D. Protein quantitation and analysis of purity. in *Methods in Molecular Biology* vol. 1485 225–255 (Humana Press Inc., 2017).
96. Ramírez-García, G., Trapiella-Alfonso, L., D'Orlyé, F. & D'Orlyé, A. Electrophoretic methods for characterizing nanoparticles and evaluating their bio-interactions for their further use as diagnostic, imaging, or therapeutic tools. in *Capillary Electromigration Separation Methods* 397–421 (Elsevier, 2018). doi:10.1016/B978-0-12-809375-7.00019-8.
97. Coty, J. B. *et al.* Characterization of nanomedicines' surface coverage using molecular probes and capillary electrophoresis. *Eur. J. Pharm. Biopharm.* **130**, 48–58 (2018).
98. Trapiella-Alfonso, L., Ramírez-García, G., d'Orlyé, F. & Varenne, A. Electromigration separation methodologies for the characterization of nanoparticles and the evaluation of their behaviour in biological systems. *TrAC - Trends Anal. Chem.* **84**, 121–130 (2016).
99. Aleksenko, S. S., Shmykov, A. Y., Oszwałdowski, S. & Timerbaev, A. R. Interactions of tumour-targeting nanoparticles with proteins: Potential of using capillary electrophoresis as a direct probe. *Metallomics* **4**, 1141–1148 (2012).
100. Boulos, S. P. *et al.* Nanoparticle-protein interactions: A thermodynamic and kinetic study of the adsorption of bovine serum albumin to gold nanoparticle surfaces. *Langmuir* **29**, 14984–14996 (2013).

101. Capomaccio, R. & Rossi, F. Gold nanoparticles increases UV and thermal stability of human serum albumin albumin. **310**, (2017).
102. Wien, F. & Wallace, B. A. Calcium fluoride micro cells for synchrotron radiation circular dichroism spectroscopy. *Appl. Spectrosc.* **59**, 1109–1113 (2005).
103. Miles, A. J. & Wallace, B. A. Synchrotron radiation circular dichroism spectroscopy of proteins and applications in structural and functional genomics. *Chem. Soc. Rev.* **35**, 39–51 (2006).
104. Greenfield, N. J. Using circular dichroism collected as a function of temperature to determine the thermodynamics of protein unfolding and binding interactions. *Nat. Protoc.* **1**, 2527–2535 (2007).
105. Laera, S. *et al.* Measuring protein structure and stability of protein-nanoparticle systems with synchrotron radiation circular dichroism. *Nano Lett.* **11**, 4480–4484 (2011).

Chapter II

*Compartmentalized Polymeric Nanoparticles
Deliver Vancomycin in a pH-Responsive
Manner*

Compartmentalized Polymeric Nanoparticles Deliver Vancomycin in a pH-Responsive manner

M. Seray Ural^a, Mario Menéndez-Miranda^a, Giuseppina Salzano^a, Jérémie Mathurin^b, Ece N. Aybeke^b, Ariane Deniset-Besseau^b, Alexandre Dazzi^b, Marianna Porcino^c, Charlotte Martineau-Corcoss^{c,d}, Ruxandra Gref^{a,}*

a Institut de Sciences Moléculaires d'Orsay (ISMO), CNRS UMR 8214, Université Paris-Sud, Université Paris-Saclay, 91405 Orsay, France

b Institut de Chimie Physique (ICP), CNRS UMR 8000, Université Paris Sud, Université Paris-Saclay, 91405 Orsay, France

c Conditions Extrêmes et Matériaux : Haute Température et Irradiation (CEMHTI), CNRS UPR 3079, Université d'Orléans, 45071 Orléans, France

d Institut Lavoisier de Versailles (ILV), CNRS UMR 8180, Université Paris-Sud, Université Paris-Saclay, 45 avenue des Etats-Unis, 78035 Versailles, France

KEYWORDS

Nanoparticle, biodegradable polymer, vancomycin, controlled release, drug location antibiotic

ABSTRACT

Vancomycin (VCM) is a last resort antibiotic in the treatment of severe gram-positive infections. However, its administration is limited by several drawbacks such as: strong pH-dependent charge, tendency to aggregate, low bioavailability and poor cellular uptake. These drawbacks could be circumvented by engineering pH-responsive nanoparticles (NPs) capable to incorporate a high VCM payload and to deliver it specifically at a slightly acidic pH corresponding to infection sites. Here we show how, taking advantage of the peculiar physicochemical properties of VCM, it was possible to efficiently incorporate it in biodegradable NPs made of poly(lactic-co-glycolic acid) and polylactic acid (co)polymers bearing terminal functional groups. The NPs were prepared by a simple and reproducible method, establishing strong electrostatic interactions between VCM and the (co)polymers' end groups. VCM payloads reached up to 25 wt%. The drug loading mechanism was investigated by solid state nuclear magnetic resonance spectroscopy. The engineered NPs were characterized by a set of advanced physicochemical methods, which allowed examining their morphology, internal structures, and chemical composition on an individual basis. The compartmentalized structure of the NPs was evidenced by cryogenic transmission electronic microscopy, whereas the chemical composition of the NPs' top layers and core was obtained by electron microscopies associated with energy-dispersive X-ray spectroscopy. Noteworthy, atomic force microscopy coupled to infrared spectroscopy allowed mapping the drug location and gave semiquantitative information about the loadings of individual NPs. In addition, the NPs were stable upon storage and did not release the incorporated drug at neutral pH. Interestingly, a slight acidification of the medium induced a rapid VCM release. The compartmentalized NPs could find potential applications for controlled VCM release at an infected site with a local acidic pH.

INTRODUCTION

The glycopeptide antibiotic vancomycin (VCM) represents the last-line defense against infections caused by numerous species of gram-positive bacteria including *Staphylococci*, *Enterococci*, *Streptococci*. Those strains are responsible of the majority of bacterial infections in humans worldwide and represent the main cause of hospital-acquired infections.¹⁻³ VCM is thus a gold standard treatment against *Staphylococcus aureus* (*S. aureus*) and in particular, of the methicillin-resistant *S. aureus* (MRSA) that can invade and survive within different types of cells such as keratinocytes, fibroblasts, enterocytes and osteoblasts⁴⁻⁷ or even alveolar macrophages thus evading the immune system.⁸⁻¹⁰

VCM exerts its biological action by forming key hydrogen bonds with carboxy-terminal peptide moieties of bacterial cell walls.¹¹ Despite its efficacy, VCM suffers from several drawbacks mainly related to its poor bioavailability¹², low tissue penetration and incapacity to bypass cell membranes. Therefore, VCM is mainly administered by the intravenous route as a slow infusion over at least 60 minutes with a frequency of administration of every 8 to 24 hours.¹³ However, the low pH (<4) of the VCM infusion leads to tissue irritation.¹⁴ Moreover, VCM is a large, highly hydrophilic and polar compound, which partially ionizes at physiological pH and does not readily diffuse from blood to tissues.¹⁵ It also strongly binds to plasma proteins¹⁶ and is eliminated *via* renal route.¹⁷ Thus, VCM has to be administered in large doses to reach sufficient therapeutic activity, which in turn leads not only to the emerge of VCM-resistant strains, but also unwanted side effects such as thrombophlebitis, fever, kidney damage, epidermal necrolysis, and a hypersensitivity reaction known as red man syndrome.¹⁸⁻²⁰

In this context, nanotechnology opens new opportunities to improve VCM bioavailability and diminish its adverse effects. Indeed, nanoparticles (NPs) are engineered to protect drugs from degradation and rapid

elimination, to allow controlled release and targeted drug delivery to the infection sites.²¹

Infected tissues are characterized by an acidic pH that can reach to 5.5 due to the accumulation of lactic and acetic acids as a result of low oxygen-triggered anaerobic fermentation.^{22, 23} Therefore, targeted VCM delivery using pH-responsive NPs could be a pertinent strategy upon fighting with Gram-positive infections while avoiding the drawbacks of conventional VCM treatment.²⁴ NPs can also be employed as Trojan horses to track *S. aureus* in its hideouts inside cells.²¹

An "ideal" VCM nanocarrier should: i) be prepared by a simple method, without excipients and using materials with known safety profiles; ii) efficiently incorporate high drug loading (DL); iii) have good stability upon storage and iv) allow a pH-responsive VCM release specifically at acidic pH, but not in physiological conditions. However, the efficient encapsulation of large hydrophilic molecules such as VCM in NPs is challenging, mainly in reason of the drug low affinity for the hydrophobic materials generally used to elaborate NPs.²⁵ Several attempts have been made to incorporate VCM in NPs. Liposomal formulations showed enhanced MRSA eradication, but their encapsulation efficiency was less than 20% wt%.^{8,26,27} Gold and silver NPs combined with VCM showed enhanced antibacterial activities²⁸⁻³² but metal NPs were reported to have toxic side-effects and tendency to aggregation.³³

Among the polymer-based biomaterials, food and drug administration (FDA)-approved polylactic acid (PLA) and poly(lactic-co-glycolic acid) (PLGA) have shown clear potency as drug carriers due to their clinically well-established biocompatibility and low toxicity. PLA and PLGA degrade by hydrolysis, forming lactic and glycolic acid metabolites which are eliminated from the body through natural pathways.³⁴ In previous studies, VCM was incorporated in nano- and microparticles made of PLA and PLGA, followed by a progressive release at physiological pH.³⁵⁻³⁸ For instance, diblock PLGA-poly(ethylene glycol) (PEG) NPs were loaded with VCM up

to 8.9 wt%.³⁷ PLGA NPs designed for oral VCM administration reached payloads of 0.5-7.4 wt% and released the whole VCM cargo within 12h at physiological pH.³⁹

Other research groups attempted to achieve a pH-controlled VCM release by using composite NPs prepared by combining several ingredients (PLGA, chitosan, PEG-PLGA and Eudragit E100)¹⁹, by using chitosan cores and PLGA shells⁴⁰ or by synthesizing PLGA-b-poly(L-histidine)-b-poly(ethylene glycol) derivatives.²³ Switchable surface charge properties were achieved on VCM loaded chitosan/polymer core-shell composite NPs.⁴⁰ However, DLs only reached around 8 wt%, the preparation methods were sophisticated and specific release of VCM in acidic and not in neutral conditions was difficult to be achieved.

In this context, our strategy was to take advantage of the VCM's peculiar physicochemical properties (highly pH-dependent global charge, hydrophilicity, tendency to aggregation) in order to engineer NPs with high drug payloads, no release at neutral pH and rapid release in acidic condition. To do so, we used a series of charged PLA and PLGA (co)polymers able to establish electrostatic interactions with VCM in a pH-dependent manner. As a result, we created compartmentalized NPs, with a loading of around 25 wt%, that spontaneously released the whole VCM cargo upon changes from neutral to acidic conditions.

To decipher the underlying molecular mechanisms, we investigated the effect of polymers' physicochemical properties (molar mass, chemical composition, nature of the end groups) on VCM loading and release. Noteworthy, the pH-dependent VCM release was achieved by avoiding the use of excipients such as pH-responsive materials.

To achieve the best quality control, the VCM-loaded NPs were characterized at the single NP level to determine their morphology, composition and respective location of their components. In this context, transmission electron microscopy (TEM) and cryogenic TEM (cryo-TEM) enabled to investigate the NPs' peculiar internal structures. Electron

microscopies (EMs) associated with energy-dispersive X-ray (EDX) spectroscopy and atomic force microscopy coupled to infrared spectroscopy (AFM-IR) allowed to locate VCM in the NP's compartments. Finally, solid state nuclear magnetic resonance (NMR) spectroscopy brought complementary insights on VCM location in the NPs and pH-dependent interactions between VCM and the NPs.

EXPERIMENTAL SECTION

Materials

(Co)polymers with different lactic acid : glycolic acid ratios (from 50:50 to 100:0), end groups (carboxylic (C) or ester (E)) and molecular weights (M_w) were kindly donated by Sequens (Expansorb, Aramon, France) with the compositions:

PLGA, 50:50, C terminated (M_w : 42-65 KDa, EXPANSORB® 10P001) named PLGA₅₄C, PLGA, 75:25, C terminated (M_w : 37-84 KDa, EXPANSORB® 10P002) named PLGA₆₁C, PLGA, 75:25, C terminated (M_w : 76-130 KDa, EXPANSORB® 10P003) named PLGA₁₁₃C, PLGA, 50:50, C terminated (M_w : 95-130 KDa, EXPANSORB® 10P012) named PLGA₁₁₃C, PLGA, 75:25, C terminated (M_w : 5-20 KDa, EXPANSORB® 10P015) named PLGA₁₃C, PLGA, 50:50, ester terminated (M_w : 72-91 KDa, EXPANSORB® 10P016) named PLGA₈₂E, PLGA, 50:50, C terminated (M_w : 15-40 KDa, EXPANSORB® 10P017) named PLGA₂₈C, PLGA, 50:50, C terminated (M_w : 10-20 KDa, EXPANSORB® 10P019) named PLGA₁₅C, PLGA, 50:50, ester terminated (M_w : 10-20 KDa, EXPANSORB® 10P024) named PLGA₁₅E, PLGA, 45:55, C terminated (M_w : 15-30 KDa, EXPANSORB® 10P032) named PLGA₂₃C, PLA, C terminated (M_w : 10-20 KDa, EXPANSORB® 10P005) named PLA₁₅C, PLA, C terminated (M_w : 6-10 KDa, EXPANSORB® 10P006) named PLA₈C.

VCM (Vancomycin hydrochloride for injection, USP, Sandoz®) was kindly provided by the International Center for Research on Infectious diseases (Lyon, France). Poly (vinyl alcohol) (PVA) (30000-70000 g/mol, 88% hydrolyzed), sodium cholate, anhydrous dichloromethane (DCM),

trifluoroacetic acid (TFA), dimethyl sulfoxide (DMSO), hydrochloric acid (HCl), sodium chloride (NaCl), potassium chloride (KCl), sodium phosphate dibasic (Na_2HPO_4), potassium phosphate monobasic (KH_2PO_4) were all obtained from Sigma-Aldrich. Buffers covering a range of pH from 5.3 to 7.4 were prepared by mixing stock solutions of KH_2PO_4 and Na_2HPO_4 in distilled water. Complete cell culture medium prepared with DMEM (Life Technologies, France) supplemented with 10% v/v decomplexed fetal bovine serum (FBS) (Life Technologies, France) and 1% Penicillin/Streptomycin (Life Technologies, France) was used for release studies. Solvents and reagents were analytical grade and were used without further purification except otherwise stated.

Preparation of VCM Loaded PLA and PLGA NPs

VCM-loaded PLA and PLGA NPs were prepared by a water-in-oil-in-water ($w_1/o/w_2$) emulsion solvent evaporation method using PVA as an emulsifier as represented schematically in **Figure 1**. Briefly, 0.2 mL of an aqueous phase containing VCM (150 mg/mL) in 1 mL of DCM containing PLA or PLGA (75 mg) was sonicated using a probe (Sonopuls HD 2070, Bandelin electronic GmbH & Co, Berlin, Germany) at 40% of power for 15 s. To create a $w_1/o/w_2$ emulsion, 5 mL of 0.5% w/v PVA (or sodium cholate) solution containing or not 1% w/v NaCl was poured to the first emulsion, followed by an immediate sonication for 30 s at 40% of power in an ice bath to avoid overheating. The resulting $w_1/o/w_2$ emulsion was left at room temperature under gentle magnetic stirring until complete evaporation of the organic solvent. Control plain NPs were prepared in the same conditions except that VCM was not added. All formulations were prepared at least in triplicate.

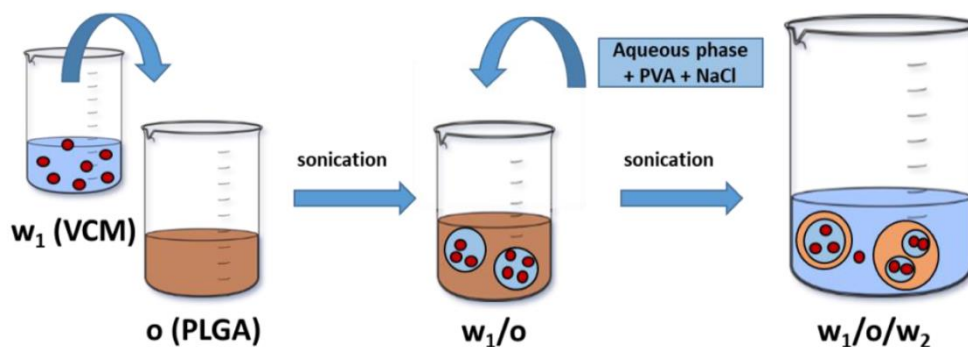


Figure 1. Schematic representation of the preparation of VCM-loaded PLA and PLGA NPs using a double-emulsion ($w_1/o/w_2$) solvent evaporation method. The organic (o) and aqueous (w_1 and w_2) phases are represented in brown and blue, respectively. VCM (•) is solubilized in w_1 .

Drug Quantification

The drug loading (DL) calculated as shown in equation 1 is defined as the mass fraction of a NP that is composed of drug. The entrapment efficiency (EE) (equation 2) is defined as the fraction of drug effectively encapsulated into the NPs compared with the amount of drug that was used to prepare the NPs.

$$DL (\%) = \frac{(mg \text{ of encapsulated drug})}{(mg \text{ of polymer})} \times 100 \quad (1)$$

$$EE (\%) = \frac{(mg \text{ of encapsulated drug})}{(mg \text{ of drug initially added to the formulation})} \times 100 \quad (2)$$

The DL was determined by two methods: i) an indirect method, analyzing the non-incorporated drug in the supernatants after NP centrifugation and ii) a direct method, dissolving the NPs (pellet) and quantifying the extracted drug. The DLs and EEs calculated through both methods were consistent with less than 5% differences, validating the method.

VCM was quantified by reverse-phase liquid chromatography, using a C18 column (Kinetex 5u C18, 100 A, Phenomenex) connected to a HPLC (Agilent 1100, USA) system with a UV-vis detector (wavelength was fixed

at $\lambda = 254$ nm). The chromatographic conditions are detailed in the **Table S1**.

Determination of Residual PVA in The Preparation of PLGA And PLA Particles

The residual PVA in the NPs was quantified by a colorimetric assay based on the formation of a blue complex between PVA and iodine in the presence of boric acid, as detailed in SI.⁴¹ All experiments were prepared in triplicate.

Release Studies

VCM release studies were performed in complete cell culture medium (DMEM supplemented with 10% fetal calf serum (FCS), 1% penicillin/Streptomycin and 1% L-Glutamine) at pH 7.4 and 4.5, and also in PB 100 mM at pH 5.3, 6.4 and 7.4. In all cases, the NP suspensions were diluted ten times with the release media. After incubation at 37°C under stirring, the NP suspensions were centrifuged at 17.000 x g for 15 min and the supernatants were recovered. VCM release was assessed by HPLC-UV-VIS as described in **Table S1** and expressed as % referring to the DL of the formulations. All experiments were carried on at least in triplicate.

Nanoparticle Characterization

NP Size Measurement by Dynamic Light Scattering (DLS) and Zeta Potential Measurements

The NPs' average hydrodynamic diameter was determined by DLS at 25 °C with an equilibration time of 60 s using a Zetasizer® (Nano ZS90, Malvern Instruments, Worcestershire, UK). All formulations were measured at least in triplicate. Mean diameters were reported as Z Average (nm) \pm SE (Standard Error) with the polydispersity index (PDI). The NPs mean diameters were monitored up to three months of storage at 25 °C. The NPs Zeta potential was measured in KCl 1 mM using a Zetasizer.

Solid State NMR Spectroscopy

The ^1H magic-angle spinning (MAS) NMR spectra were recorded at a magnetic field of 20 T, using a Bruker 850 MHz WB NMR spectrometer and using a HXY 1.3 mm probe in double mode. The spectra were acquired using Hahn echo pulse sequence, with a 90° pulse duration of 1.4 μs , an inter-pulse delay synchronized with one rotor period and a spinning rate of 60 kHz. The recycle delay was set to 20 s and 16 transients were recorded for each sample. The ^1H chemical shifts were referenced to tetramethylsilane (TMS). The assignment of VCM protons was made by comparison with liquid NMR spectra.

The ^{13}C cross-polarization (CP) experiments were recorded on a 9.4 T magnet (^1H and ^{13}C Larmor frequency of 400 and 100 MHz, respectively) with a Bruker spectrometer, using a 4 mm double resonance MAS probe. The ^{13}C chemical shifts are referenced to adamantane. The contact time was set to 3.5 ms, the recycle delay was set at 5 s, the initial 90° pulse on ^1H to 3 μs with a Radio Frequency (RF) field of 83 kHz. ^1H SPINAL-64 decoupling was applied during the ^{13}C acquisition. The NMR spectra were acquired using TopSpin 3.5 Bruker Software and processed with DM fit program.⁴²

Size-Exclusion Chromatography (SEC)

The polymer molar masses were determined after release using SEC with THF as eluent (1 mL/ min) at room temperature. SEC was equipped with a refractive index detector (Waters 410) and two mixed-bed ViscoGELTM columns (7.8 x 300 mm, type GMHH R-H) provided by Viscotek.

TEM and Cryo-TEM Investigations

TEM images were acquired on a JEOL electron microscope (JEM 100 CX II, operating at 120 kV) equipped with an US1000 2kx2k camera (Gatan). To do so, 5 μL of samples were deposited onto a 400 mesh carbon-coated copper grid beforehand treated with a glow discharge (easiGlow, Ted Pella

Inc), and dried with a filter paper after 30 sec. Cryo-TEM images were acquired on a JEOL 2200FS energy-filtered (20 eV) field emission gun electron microscope operating at 200 kV. To do so, 5 μL of NPs suspensions were deposited onto a 200 mesh copper grid and flash-frozen in liquid ethane cooled down at liquid nitrogen temperature.

Scanning electron microscopy (SEM)-EDX

SEM-EDX quantitative analysis was performed using a Carl Zeiss Merlin SEM with a field emission gun equipped with secondary electron detectors. SEM was coupled with an EDX equipped with a 50 mm^2 SDD X-Max detector from Oxford Instruments. The characterization of the NPs was performed at 2 keV.

Scanning TEM-EDX

Chemical composition analyses were performed with a scanning TEM (STEM) device (FEI TECNAI F20) fitted to high angle annular dark field (HAADF) imaging. The microscope was equipped with a field emission gun, a scanning device, an EDX detector (EDAX R-TEM Sapphire) and an electron energy loss spectrometer (GIF 2001). Carbon films on 400 Mesh Copper Grids were treated with the PELCO easiGlow™ discharge cleaning system to make the film hydrophilic. 5 μL of samples were deposited onto a carbon-coated copper grid for 1 min, and then the excess of liquid was removed. The characterization of the NPs was performed at 200 keV.

Fourier transform IR (FTIR) spectroscopy

Attenuated total reflection (ATR) FTIR spectra of NPs components were obtained by using a Bruker Vertex 70 FTIR spectrometer (MCT detector, cooled down using liquid nitrogen) and a ATR module (PIKE MIRacle crystal plate diamond ZnSe). Spectra were recorded in the range of 4000–600 cm^{-1} with an accumulation of 100 scans and a resolution of 4 cm^{-1} . Only significant absorptions were listed.

AFM-IR

Aliquots of the NPs samples were deposited on CaF₂ cell windows and left to dry completely over several days. Experiments were performed with either NanoIR-2 or NanoIR-2s (Anasys Instruments) coupled with a multichip QCL source (MIRcat, Daylight Solutions; tunable repetition rate range of 0–2 MHz; spectral resolution of 0.1 cm⁻¹) covering the range from 1900 cm⁻¹ to 900 cm⁻¹ of the mid-IR region with a tunable repetition rate. An Au-coated silicon tapping AFM-IR cantilever (Multi75GB-G, f=75 kHz 3N/m, Budget Sensors) was employed. Gold coating was used to avoid effects linked to IR absorption of the silicon cantilever. Power was set between 22% to 100% with tapping mode frequency around 50-60 kHz. Laser pulse rate was set around 317 kHz with a pulse duration of 200 ns. Topography and IR maps were processed using the Mountains Map 7.3 software and the spectra (sampled at 1 cm⁻¹) were filtered using the Savitzky – Golay algorithm (1rd order polynomial using 11 points).⁴³

RESULTS AND DISCUSSION

NP Preparation

As shown by a set of studies involving NMR spectroscopy, X-Ray crystallography and molecular modeling, VCM exerts its biological action by: i) specific complexation with peptides containing terminal D-alanyl-D-alanine units on the surface of bacterial cell walls leading to stable hydrogen bond interactions⁴⁴ and ii) establishing charge-charge interactions with peptide carboxylate groups.^{45–47} This is in line with a previous study showing that VCM was associated to nanodiamonds only when electrostatic interactions were established, and more particularly, on the surfaces comporting carboxyl groups.⁴⁸ Those observations inspired us to use a series of biodegradable PLGA and PLA (co)polymers possessing carboxyl end groups, to establish electrostatic interactions with VCM. This

will enhance the payloads and help achieving a pH-triggered release. Additionally, (co)polymers, with ester end groups, were used as controls. The (co)polymers are named here PL(G)A_xC or PL(G)A_xE: C and E represent respectively the carboxyl and the ester end groups whereas x represents the mean M_w.

A double-emulsion solvent evaporation method schematically represented in **Figure 1** was employed to prepare the NPs and to maximize the interactions at the interfaces between aqueous and organic phases. The double-emulsion method was used since 1998 to incorporate large hydrophilic macromolecules such as proteins inside NPs⁴⁹ and more recently for VCM incorporation.^{39, 50} Briefly, in our study, an aqueous VCM solution was dispersed in an organic phase containing the PLA or PLGA (co)polymers resulting in the first emulsion. Sonication was employed to efficiently reduce the aqueous droplet size.^{51, 52} The hydrophilic carboxyl chain ends of the (co)polymers tended to migrate towards the inner aqueous phase where VCM was located. Then, a water-in-oil-in-water (w₁/o/w₂) emulsion was prepared forming of oil droplets containing aqueous compartments with VCM, followed by the evaporation of the organic solvent that led to polymer precipitation and NPs formation. (**Figure 1**).

Different families of PLA and PLGA (co)polymers were evaluated for VCM incorporation in NPs. The characteristics of each polymer and the corresponding NP formulation are shown in **Table 1**. Polymers differ in end group, composition and M_w that determine the inherent viscosity and the performance to encapsulate hydrophilic drugs. As shown in **Table 1**, all the polymers formed NPs with PDIs lower than 0.26. The mean hydrodynamic diameters determined by DLS ranged from 300 to 370 nm. The increase in NP size was associated with the increment in the M_w of the employed polymer: PLGA₁₅C (325±25 nm), PLGA₆₁C (350±25 nm) and PLGA₁₁₃C (367±25 nm) (**Table 1**), while drug loading had no significant impact on the NP size. The morphology of the NPs was investigated by

SEM (**Figure S1**) and TEM (**Figure 2**) and the obtained average sizes corroborated with DLS results (**Table 1**). Typical TEM images showed that the NPs were spherical and devoid of aggregates. Sizes ranged in between around 100 and 400 nm.

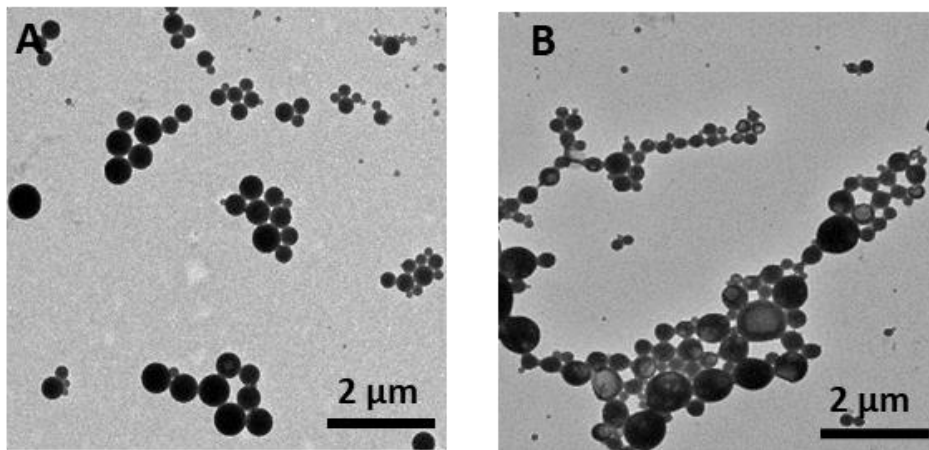


Figure 2. Typical TEM images of NPs prepared by double-emulsion using PLGA₁₅C: **A)** empty and **B)** VCM-loaded.

Table 1. VCM encapsulation in NPs with different polymer compositions, effect on DL, EE, mean diameter, PDI and Zeta potential. PLA and PLGA (co)polymers from EXPANSORB® were used.

Name	M _w Range (kDa)	End Group	Lactic unit (%)	Inherent viscosity range (dL/g)	DL (wt% + SD)	EE (wt% + SD)	Mean diameter*† (nm)	PDI	Zeta potential (mV + SD)
PLA ₈ C	6 - 10	Carboxyl	100	0.05-0.20	7 ± 2	16 ± 5	319	0.18 ± 0.05	-1.6 ± 0.1
PLA ₁₅ C	10 - 20	Carboxyl	100	0.15-0.30	<1	<1	322	0.25 ± 0.07	-1.7 ± 0.1
PLGA ₁₃ C	5 - 20	Carboxyl	75	0.08-0.21	5 ± 1	11 ± 2	312	0.13 ± 0.01	-1.9 ± 0.1
PLGA ₁₅ C	10 - 20	Carboxyl	50	0.15-0.25	14 ± 4	36 ± 2	325	0.19 ± 0.02	-1.9 ± 0.1
PLGA ₂₃ C	15 - 30	Carboxyl	45	0.15-0.30	9 ± 1	24 ± 1	323	0.18 ± 0.03	-1.3 ± 0.1
PLGA ₂₈ C	15 - 40	Carboxyl	50	0.25-0.40	8 ± 1	18 ± 2	326	0.21 ± 0.03	-0.7 ± 0.3
PLGA ₅₄ C	42 - 65	Carboxyl	50	0.40-0.55	<1	<1	324	0.14 ± 0.01	-1.4 ± 0.3
PLGA ₆₁ C	37 - 84	Carboxyl	75	0.38-0.64	<1	<1	350	0.16 ± 0.03	-1.4 ± 0.1
PLGA ₁₀₃ C	76 - 130	Carboxyl	75	0.70-0.90	<1	<1	352	0.14 ± 0.01	-1.3 ± 0.3
PLGA ₁₁₃ C	95 - 130	Carboxyl	50	0.65-0.90	<1	<1	367	0.17 ± 0.03	-1.4 ± 0.1
PLGA ₁₅ E	10 - 20	Ester	50	0.15-0.25	<1	<1	323	0.26 ± 0.04	-0.9 ± 0.1
PLGA ₈₂ E	72 - 91	Ester	50	0.60-0.70	<1	<1	344	0.15 ± 0.04	-1.4 ± 0.2

* Standard deviations (SD) are 25 nm for all the formulations.

† Measured by DLS.

The NPs' Zeta potential was close to zero (**Table 1**), indicating a neutral surface charge which could be attributed to the presence of the non-charged PVA emulsifier. Indeed, PVA can intermingle with the PLA and PLGA chains and stay associated with the NPs' surface despite an extensive washing procedure.⁴¹ Here, the residual PVA amount was 6 ± 1 wt%, whatever the polymer used, confirming that PVA forms a protective steric layer at the NP surfaces shielding the negative charges of the PLGA and PLA polymer end groups.

Drug Loading and Mechanism

Although all the NP formulations presented similar physical properties such as size, PDI and Zeta potential, they differed significantly in terms of DL and EE (**Table 1**). DL ranged from <1 wt% (undetectable) to 14 wt% and EE from <1 wt% to 36 wt%. As a general trend, (co)polymers with the

highest M_w such as PLGA₅₄C and PLGA₁₁₃C did not incorporate VCM, whereas PLGA₁₅C and PLGA₂₃C (co)polymers with the same compositions but lower M_w entrapped a higher amount of drug (14 ± 4 wt% and 9 ± 1 wt% VCM, respectively). Furthermore, ester-terminated polymers failed to incorporate VCM whatever their M_w . Finally, the higher the hydrophilicity of the (co)polymer (i.e. the lower the L content), the higher the VCM DL. For example, at similar M_w , PLGA₁₅C with 50% L units has a DL of 14 wt%, whereas PLGA₁₃C with 75% and PLA₁₅C with 100% L units, have DLs of 5 wt% and <1 wt% respectively.

In conclusion, the DL and EE were related to three properties of PLA and PLGA (co)polymers: i) the M_w ; ii) the terminal groups (C or E) and iii) the percentage of L units. The optimal (co)polymer for VCM incorporation was PLGA₁₅C, with the lowest M_w and a carboxy end group. From the PLA series, PLA₈C was the best with 7 ± 2 wt% DL and 16 ± 5 wt% EE. The NP preparation parameters and optimizations are detailed in **Tables S2 and S3** with the emphasis of using NaCl to form rapidly the NPs.

In a nutshell, the results in **Table 1** supported our hypothesis that VCM is efficiently incorporated if it establishes electrostatic interactions with the carboxyl end group of the polymer. Keeping in mind that the same amount of polymer was used to prepare NPs, the lower the M_w (i.e. the shorter the polymer chains), the higher the number of carboxy end groups, so the higher the possibilities of electrostatic interactions with VCM. More precisely, during the formation of the first emulsion (**Fig. 1**), electrostatic interactions occur depending on the physicochemical properties of the VCM and the (co)polymers used to incorporate it. The VCM solutions have an acidic pH (~ 4) at which it has an overall positive charge arising from its two positively charged alkylamine groups and a negatively charged carboxylic acid group^{53, 54}, while PLA and PLGA, with their carboxyl end groups ($pK_a=3.85$), are slightly deprotonated.⁵⁵ Therefore, charge-charge interactions can be established between the (co)polymers and the VCM at the interface as schematized in **Figure 3**. Drug loading can be ensured as

the VCM will have less tendency to leak out of the droplets. In addition, VCM self-association in the aqueous compartments should also contribute to the formation of bulky structures, favoring their loading.

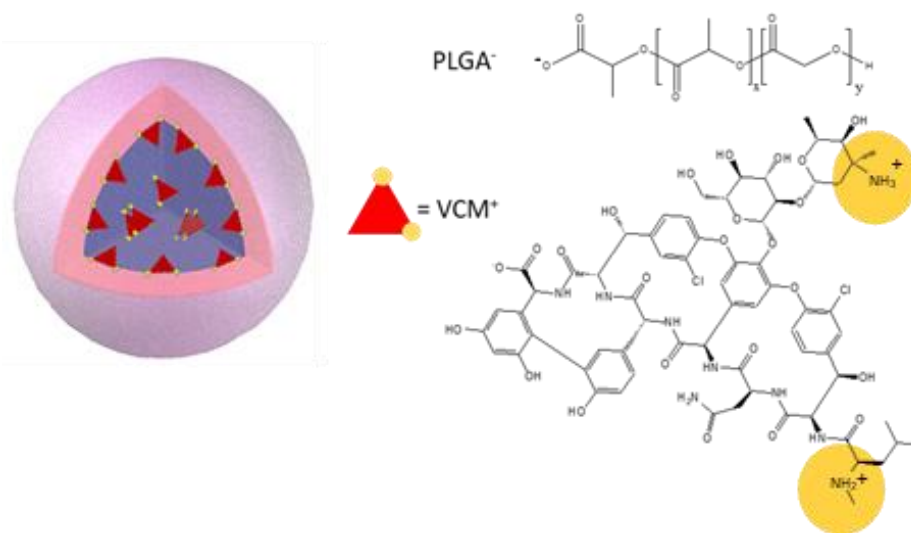


Figure 3. Schematic representation of the hypothesized mechanism of VCM (red triangle) incorporation in a NP compartment (blue) and chemical structures of PLGA (deprotonated form) and VCM (protonated form). x and y are the numbers of L and G units. The VCM protonated amine groups (in orange) interact with deprotonated carboxylic acid groups of the polymer at the interface of aqueous inner compartments.

Solid state NMR spectroscopy was used to provide further information about the mechanism of the VCM encapsulation since it allows a deep characterization of the structure and interactions between the drug and the polymer carrier at an atomic level.⁵⁶ At first, ^1H and ^{13}C MAS NMR spectra of empty and VCM loaded PLGA₁₅C NPs were recorded (**Figure S2**). The presence of the ^{13}C resonances of VCM in the loaded particles confirmed the successful VCM encapsulation. Next, the ^1H - ^1H 2D MAS NMR was performed to investigate the interactions between drug and the polymer. **Figure 4** presents the correlation study including cross peaks between VCM and PLGA. Despite the use of high magnetic field (20 T) and fast-MAS (60 kHz), there was still a strong overlap of the proton NMR

signals of the NPs and VCM. Only a NH proton (8 ppm) and an OH proton (9 ppm) of VCM could clearly be resolved. Cross-correlation peaks obtained between one NH from the VCM and the protons from PLGA indicates close spatial proximity between the drug and the polymer, hence the electrostatic interactions between these two. This assessment is in agreement with NMR studies in the literature that show the strong interactions of NH amide groups of the VCM with the terminal carboxylate of the bacterial cell wall peptide.⁵⁷

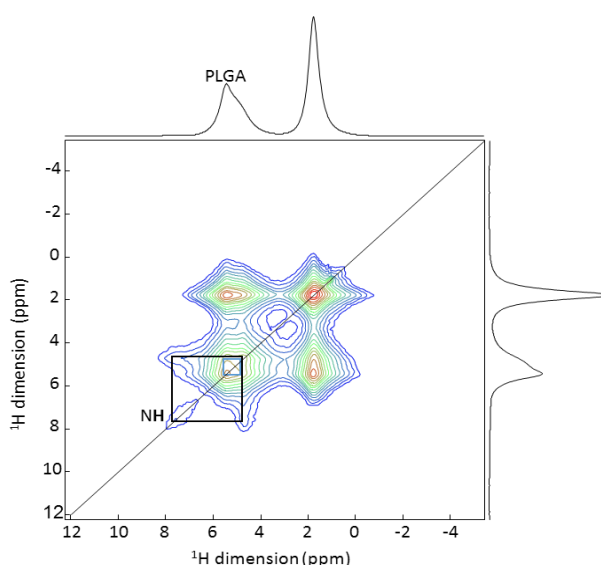


Figure 4. 2D ^1H - ^1H MAS NMR spectrum of PLGA₁₅C NPs loaded with VCM. The black rectangle highlights the cross-correlation peaks between the NH of the VCM and the protons of the PLGA.

To give further proof of the electrostatic interactions, additional experiments were carried out. VCM loaded NPs were prepared by using deuterated water and deuterated VCM in order to shield the electrostatic interactions between VCM-polymer. As awaited, results showed dramatical modifications due to the lack of H bond interactions: DL and EE decreased from 14 ± 4 to 5 ± 1 wt % and from 36 ± 2 to 14 ± 1 wt%, in the case of non-deuterated and deuterated systems, respectively. Eventually, in order to detect the ^1H species by NMR, the deuterated VCM loaded NPs were

submitted to a back exchange from D to H by prolonged contact with water. Results are summarized in **Figure 5**. The deuterated formulation (red spectrum) in the ^1H MAS NMR spectrum presents narrower NH proton resonances of VCM (i.e., they appear more intense, despite the lower DL), indicating weak interactions between the polymer and VCM. As control, VCM loaded NPs prepared in water showed broader NH proton signal (black line in **Figure 5**), which clearly evidences the existence of H bond interactions between VCM and the polymer. These H-bonds indeed result in ^1H chemical shift distribution (distribution of H-bonds) hence broader line in the spectrum. In conclusion, the establishment of VCM-polymer H bonds were shown to be responsible of high DL and EE.

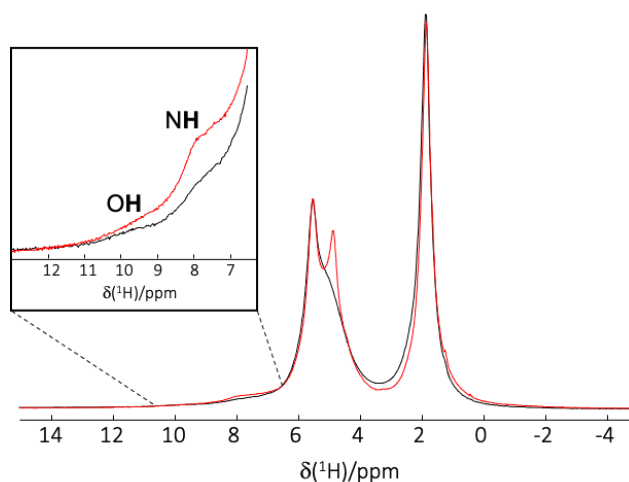


Figure 5. ^1H MAS NMR spectra of VCM loaded PLGA₁₅C NPs prepared in H₂O (black spectrum) and in D₂O by using deuterated VCM (red spectrum). An expansion on OH and NH of VCM is shown in insert.

Knowing that the electrostatic interactions between VCM (monomers or self-associates) and polymer play a major role, and are governed by the pH, a study has been carried on to observe the effect of the pH of the inner and outer aqueous phases used in the 1st and 2nd emulsion respectively during preparation of VCM loaded NPs (**Table 2**). Neither the DL nor the EE depended on the pH of the outer medium in a range from 6.3 to 8.5. On the contrary, when the pH of the inner VCM solution (1st emulsion) was

7.4, both the DL and the EE were increased reaching 25 ± 3 wt% and 53 ± 7 wt% respectively. The viscosity of the VCM solution was increased at pH 7.4 as compared to pH 4.0. Presumably, VCM self-association/ aggregation occurred preventing VCM from leaking out of the inner droplets during NP preparation thus resulting in improved DL and EE (**Table 2**).

Table 2. Effect of the pH of VCM solution (inner aqueous phases, 1st emulsion) and of the suspension medium containing NaCl and the emulsifier PVA (outer aqueous phases, 2nd emulsion) on the incorporation of VCM and PLGA₁₅C NP size and polydispersity.

pH of 1 st emulsion	pH of 2 nd emulsion	DL (wt% \pm SD)	EE (wt% \pm SD)	Mean diameter*† (nm)	PDI
4.0	6.3	14 ± 4	36 ± 2	325	0.16 ± 0.17
	7.4	12 ± 1	36 ± 1	340	0.17 ± 0.04
	8.5	14 ± 4	43 ± 9	353	0.19 ± 0.06
7.4	6.3	22 ± 1	47 ± 2	318	0.15 ± 0.01
	7.4	25 ± 3	53 ± 7	312	0.15 ± 0.03
	8.5	23 ± 3	50 ± 7	319	0.19 ± 0.02

* Standard deviations (SD) are 25 nm for all the formulations.

† Measured by DLS.

In conclusion, from the series of PLA and PLGA (co)polymers studied here, PLA₈C and PLGA₁₅C were the best studied materials for the VCM encapsulation. They had the lowest M_w and carboxyl end groups. The optimization study reported a dramatic enhancement of VCM loading into PLGA₁₅C NPs with DL and EE up to 25 wt% and 53 wt% respectively, which to the best of our knowledge, overcome the DLs and EEs reported so far for VCM incorporation in other NPs or in liposomes.^{8,26,27,39}

Finally, when the NPs were stored at 4°C for three months, their mean diameter remained unchanged (less than 5% variation) and less than 4% of the incorporated VCM was released over this time. These results indicate a good stability upon storage.

NPs' Inner Morphology

Cryogenic TEM (cryo-TEM) investigations were carried on to gain insights into the inner structure of the PLGA and PLA NPs. Interestingly, the VCM-loaded PLGA₁₅A and PLA₈C NPs possessed relatively large inner aqueous compartments (lighter regions) delimited by thin polymer shells (darker regions) of around 10-40 nm as pointed out with red arrows in **Figure 6C** and **6D**. To the best of our knowledge, this is the first time that large compartments inside PLA or PLGA-based NPs are visualized. On the contrary, empty NPs (prepared by the same procedure, but without VCM) were dense and devoid of compartments (**Figure 6A, 6B**). This striking differences in the inner structure between loaded and empty PLGA and PLA NPs reinforces the fact that VCM-polymer interactions happen in the NP inner aqueous compartments that shown to stabilize these compartments favoring the VCM encapsulation.

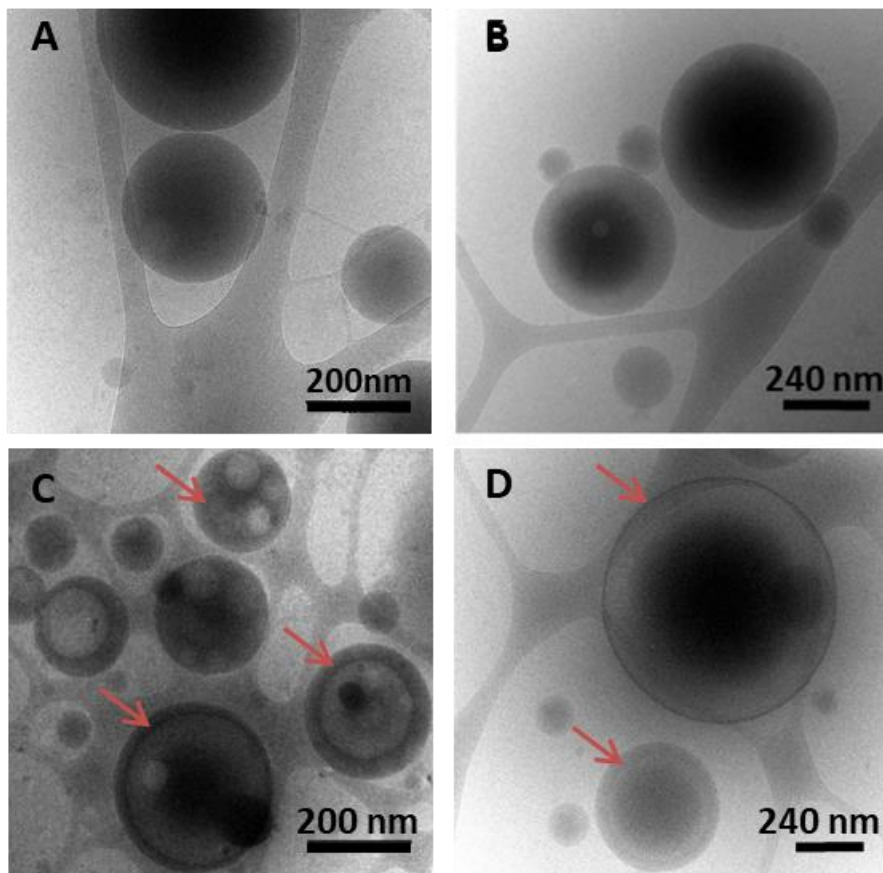


Figure 6. Representative cryo-TEM images of **A)** empty PLGA₁₅C NPs; **B)** empty PLA₈C NPs; **C)** VCM-loaded PLGA₁₅C NPs, and **D)** VCM loaded PLA₈C NPs. Polymer shells are indicated with red arrows.

Individual NP characterization: Localization of VCM SEM-EDX

SEM equipped with EDX is a method of choice to investigate NPs individually, analyzing both their morphology and composition. It commonly identifies the elemental composition on the NPs' top layers (less than 10 nm depth) since the electron beam has energy of only 2 keV, hampering its penetration inside the cores. PLGA and VCM are composed of carbon, hydrogen and oxygen atoms whereas VCM possess also nitrogen atoms. Therefore, nitrogen detection by SEM-EDX gives information on VCM presence in the NPs' top layers.

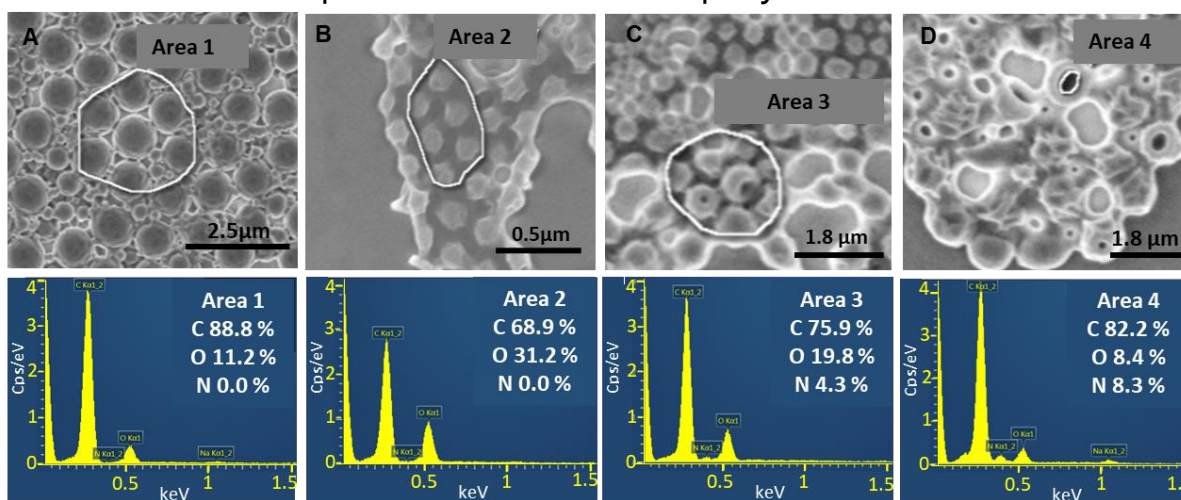


Figure 7. SEM images (top) with EDX analysis (below) of **A)** empty PLGA₁₅C NPs, **B)** VCM loaded PLGA₁₅C NPs. Sample B was continuously analyzed until holes appeared due to polymer melting **C, D)** and EDX analysis was further focused on the inner regions which were thus revealed.

Figure 7 presents the EDX analysis of PLGA₁₅C NPs, loaded or not with VCM. Elemental analysis was performed on the areas indicated in SEM

images. As expected, no trace of nitrogen was detected in empty NPs (**Figure 7A**). This was the case also with VCM-loaded NPs suggesting that VCM was embedded deeper in their cores (**Figure 7B**). The SEM observations were pursued until the formation of holes in their structure (**Figure 7C, 7D**). Interestingly, EDX elemental analysis focused on selected areas of the holes revealed the presence of 4.3% nitrogen (**Figure 7C**) and up to 8.3% when only the hole was analyzed (**Figure 7D**). These investigations of individual NPs rule out the presence of VCM on the NP surface and support VCM loading inside their cores.

STEM-EDX

Further characterization of individual NPs was performed by STEM-EDX that enables qualitative and semi-quantitative measurements of the atomic compositions, as the beam passes throughout the sample. Therefore, in contrast to SEM-EDX, information is accessible also from the core of the NP. A typical STEM image of VCM-loaded PLGA₁₅C NPs (**Figure 8A**) clearly shows the presence of numerous compartments of NPs similar to the Cryo-TEM ones (**Fig 6C**).

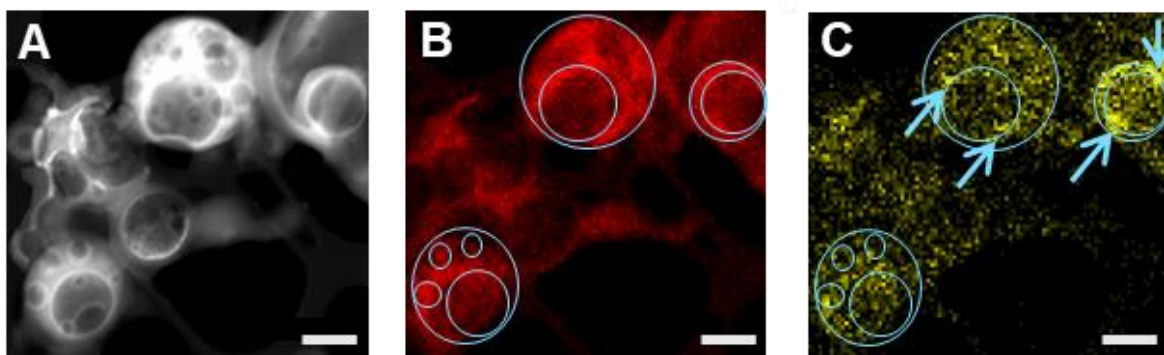


Figure 8. **A)** STEM image of VCM loaded PLGA₁₅C NPs in which inner aqueous compartments are visible. Chemical mapping for elemental analysis of **B)** carbon (red) and **C)** nitrogen (yellow). Blue lines are guides

for the eyes and blue arrow indicates nitrogen-rich regions. Scale bars are 500 nm.

The corresponding EDX maps of chemical elements highlights the repartition of carbon and nitrogen in VCM loaded PLGA₁₅C NPs (**Figure 8B, 8C**). As shown on the elemental mapping of nitrogen in **Figure 8C**, VCM location can be tracked inside the NPs and mainly at the interface of the water inclusions (blue arrows). This observation supported the suggested VCM encapsulation mechanism based on the establishment of electrostatic interactions at the polymer/drug interfaces.

Line-scanning profiles of NPs were also recorded to evaluate by EDX the composition distribution on the cross section of the selected line on a single NP with two large compartments (**Figure 9**). Carbon concentration was significantly lower within the inclusions in line with the presence of less material (**Figure 9C**). No nitrogen signal corresponding to VCM was detected outside the NPs or onto their surface, in agreement with SEM-EDX experiments (**Figure 7**). Noticeably, peaks of nitrogen intensity were observed at the border of the internal compartments (**Figure 9B**). Similar findings were displayed in **Figure S3**. In a nutshell the results suggest the preferential accumulation of VCM at the interface and inside of the inclusions.

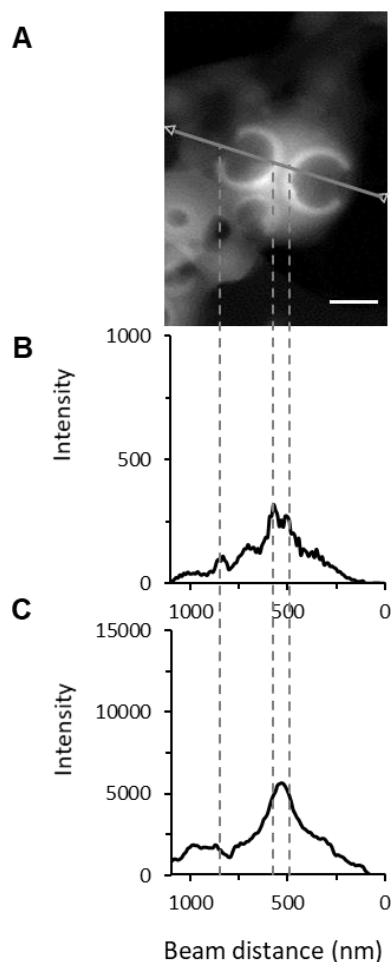


Figure 9. **A)** STEM image of VCM loaded PLGA₁₅C NPs, EDX line scanning profiles on **B)** the elemental mapping of the nitrogen and **C)** of the carbon. The higher values of the nitrogen intensity are indicated by the dashed lines. Scale bar is 250 nm.

AFM-IR

To complete the compartmentalized NP characterization, we used high resolution vibrational spectroscopy AFM-IR which combines the spatial resolution of AFM (down to around 20 nm) with the capability of IR spectroscopy to unambiguously identify the chemical composition of an individual NP.^{58, 59, 60} Recently, our teams used AFM-IR to locate a hydrophobic drug in PLA NPs.⁶¹ Despite the low loading (< 1wt%), the drug could be well detected and it was shown that it was located only in the

NPs' top layers and not within their cores. This sensitive method was used here to study the VCM location within PLA₈C NPs. AFM-IR enabled to acquire either an IR chemical map at a specific wavenumber (IR mapping) or an IR spectrum at one specific location in the sample (local IR spectrum). To do so, firstly, specific wavenumbers were defined as "fingerprints" to unambiguously identify each component of the NP system, the PLA, the VCM and the PVA. The characteristic IR bands of these three components were recorded by FTIR within the 1850-1000 cm⁻¹ range as the accessible IR region in AFM-IR (**Figure 10A**). The PLA has a main characteristic band at 1760 cm⁻¹, corresponding to the stretching of the C=O of carboxyl groups, and other signals at 1068 and 1133 cm⁻¹ (CH₃ groups), 1090 and 1188 cm⁻¹ (C-O-C ester bond stretching) and in the region 1300-1500 cm⁻¹ (C-H bending of CH₂ and CH₃).⁶² The VCM showed a C=O stretching absorption band centered at 1658 cm⁻¹, the band associated to the N-H bending at 1502 cm⁻¹, an absorption at 1228 cm⁻¹ (phenols) and the band associated to the C-N stretching vibrations of amine groups at 1126 and 1060 cm⁻¹.⁶³ To unambiguously detect the VCM within the NP samples, its absorption at 1600 cm⁻¹ was chosen with no interference signal from the other NPs components (PLA, PVA or the residual liquid water) (**Figure 10A**). Reciprocally, the specific band 1760 cm⁻¹ of the PLA₈C polymers where no VCM and PVA absorption occurred was used to locate the NPs.

As an example, **Figure 10C** shows a representative AFM topography image recorded on a single NP and the respective IR mapping of PLA (**Figure 10D**) and VCM (**Figure 10E**). The signal corresponding to PLA overlapped well with the topography images except at the upper part edges of the NP, which corresponds to the previously reported phase shift effect occurring in the case of PLA NPs.⁴³ Remarkably, chemical mappings of VCM showed that the drug was well located within the NP and not at its surface (**Figure 10E**). This result is in contrast with the previously AFM-IR investigations reporting the location of drugs at the PLA NPs' surface and resulting in uncontrolled release.⁴³

The final proof of VCM location was given by acquiring local spectra within the NPs' cores with the excellent AFM resolution. The spectra obtained from the point indicated with orange arrow (**Figure 10B**) looks very similar to the FTIR one of VCM-loaded PLA₈C NPs (**Figure 10A**).

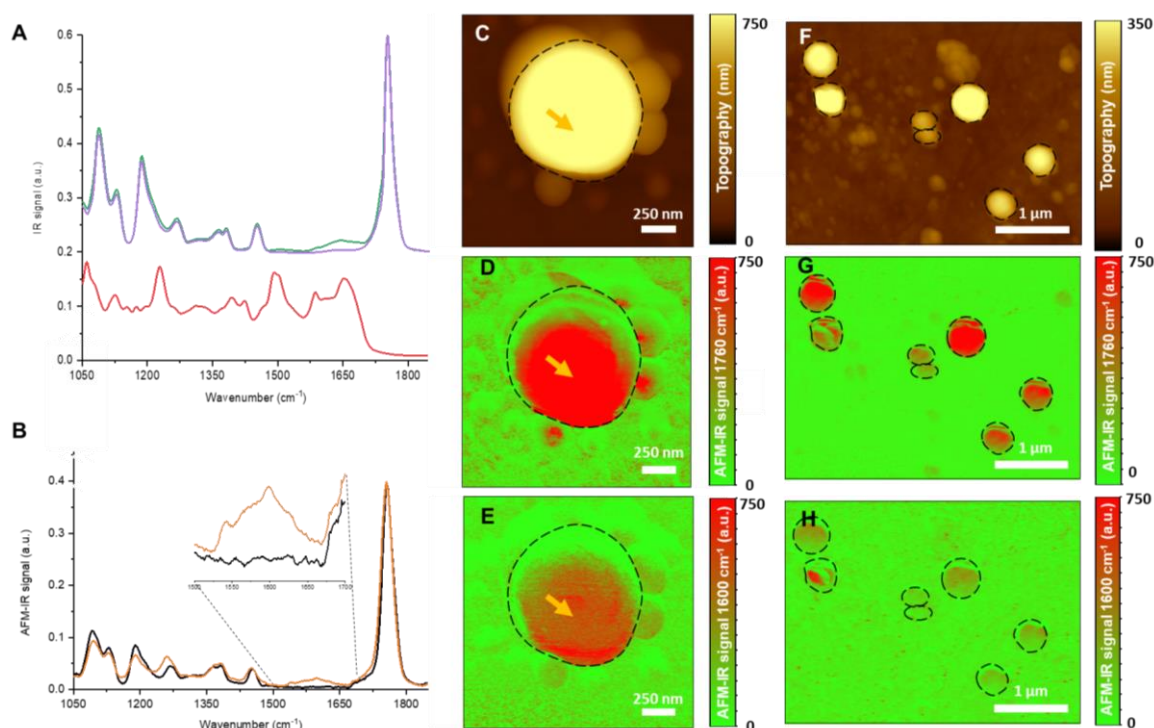


Figure 10. A) ATR-FTIR spectra of VCM (red), empty PLA₈C NPs (purple), VCM-loaded PLA₈C NPs (green). **B)** Local IR spectrum obtained by AFM-IR on empty (black) and VCM-loaded (orange) PLA₈C NPs at the position indicated with an orange arrow in **C-E**. **C), F)** Topography images of PLA NPs. **D), G)** Tapping AFM-IR map at 1760 cm⁻¹ corresponding to the strong absorption of PLA, **E), H)** Tapping AFM-IR map at 1600 cm⁻¹ corresponding to VCM absorption.

To complete the study, a region of interest containing several VCM-loaded NPs was investigated (**Figure 10F-H**). The topography image (**Figure 10F**) showed round-shaped NPs with sizes between 240 and 500 nm. PLA mapping (**Figure 10G**) matches with the topography (**Figure 10F**) showing that even the composition of the smallest NPs (240 nm) could be

investigated by AFM-IR. The signal of the largest NPs was more intense, in agreement with the fact that they contained higher amounts of PLA.

In contrast to PLA, VCM mapping showed an uneven drug distribution within the NPs (**Figure 10H**) and in some cases, a compartmentalized location of VCM. Interestingly, some of the smallest NPs did not contain VCM. It was previously shown that the largest NPs have higher content of inner compartments and some small NPs are dense and not compartmentalized (**Figure 6, Figure 8**). Therefore, it can be hypothesized that the smallest NPs do not entrap VCM because there is no internal interface where electrostatic interaction could take place.

In conclusion, there was a good agreement between AFM-IR, CryoTEM, SEM-EDX and STEM-EDX investigations which showed that VCM was incorporated inside the NPs' cores and that it was mainly localized at the interface between the polymer matrix and the inner compartments.

pH-Controlled Drug Release and Related Mechanism

Drug release from the compartmentalized VCM-loaded NPs was studied as a function of the pH of the release medium (from 5.3 to mimic infection site to 7.4 which correspond to normal physiological conditions) (**Figure 11A**). At pH 7.4, no more than 10% of the VCM cargo was released within 24h. In contrast, at pH 5.3, VCM was rapidly released (60%) within the first minutes upon incubation. A total release was observed after 24h. At pH 6.3, this release shows an intermediate profile.

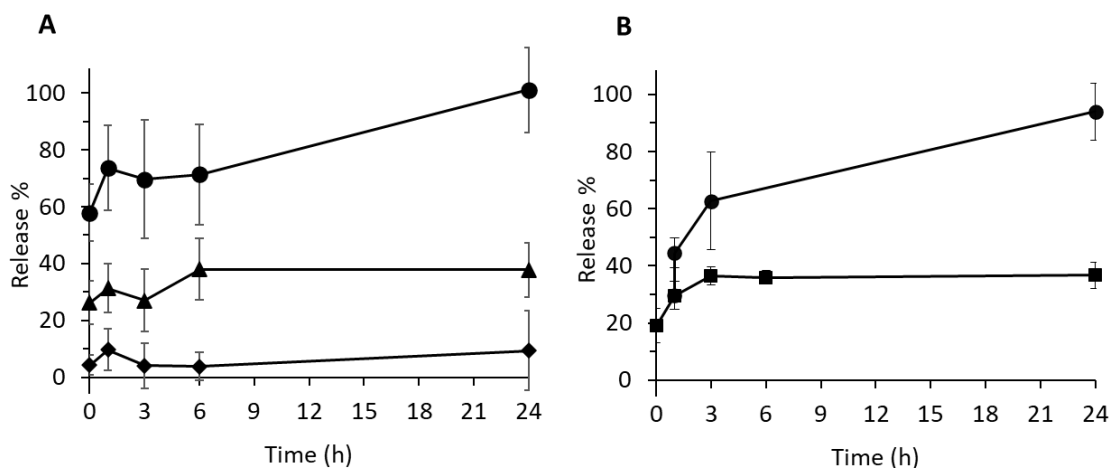


Figure 11. A. pH-dependent VCM release profiles of PLGA₁₅C NPs in 100 mM PB at pH=5.3 (circle), pH=6.3 (triangle) and pH=7.4 (diamond). **B.** VCM release profile of PLGA₁₅C NPs in RPMI cell culture medium containing 10% serum (square) at pH 7.4. In another set of experiments, the pH was changed from 7.4 to 5 (circle). All experiments were performed in triplicate at 37°C.

Furthermore, the VCM release was studied over 24h in cell culture media containing serum (**Figure 11B**). Around 20% of the incorporated drug were released immediately, reaching a plateau at 35% after 3h. This shows that the majority of the drug (65%) remained associated to the NPs. The same experiment was repeated, but one hour after the start of the release, the pH of the cell culture medium was adjusted to 5. It was found that immediately after, 45% of the entrapped VCM was released, followed by a total release within 24h. These data show that VCM release can be triggered by acidic conditions in complex release media.

It's noteworthy that no degradation of the polymers was observed during the timeframe of the release experiments (**Figure S4**). This suggests that VCM release relies on a diffusion process of the VCM and not on the degradation of the NP matrix. In line with these findings, cryo-TEM observations showed that the compartmentalized structure of the NPs was maintained during drug release whatever the pH of the media (**Figure S5**).

Thus, we hypothesize that VCM release mechanism is based on diffusion through the polymeric matrix and the pH-dependent reversible aggregation of VCM.⁶⁴ Indeed, at pH 7.4, VCM self-associates forming bulky structures that diffuse less than the monomeric forms at acidic pH.

The pH-dependent release behavior of the compartmentalized NP system could be an asset to achieve VCM release specifically in acidic conditions corresponding for example to infected sites or to intracellular compartments in infected cells²¹ but not in healthy tissues and organs.

CONCLUSIONS

This study highlights the importance of the choice of the polymeric material to engineer NPs which can allow efficient VCM incorporation by a simple method. Taking advantage of the strongly pH-dependent physico-chemical properties of VCM (charge, reversible aggregation), it was possible to efficiently incorporate it in biodegradable NPs, by establishing electrostatic interactions, as shown by solid state NMR studies. The drug molecules were confined in large inclusions inside the NPs and their loadings reached 25 wt%. The NPs were comprehensively characterized at the single NP level by using a set of complementary methods including electron microscopies coupled with EDX and AFM-IR. The methodology proposed here for NP physicochemical characterization sets up the basis for a deep understanding not only of the morphology, but also of drug location inside polymer matrices, which in turn has a deep impact on drug release mechanism. Furthermore, the release of the VCM was triggered by acidic environment. These characteristics suggest potential therapeutic applications of targeted VCM delivery at an infected or inflammatory site. The developed PLGA and PLA NPs could also offer a platform to (co)encapsulate other hydrophilic molecules or synergic drug combinations.

ASSOCIATED CONTENT

Supporting Information

The supporting information is available free of charge on the ACS Publications website: Experimental details: HPLC method, PVA quantification, effect of preparation parameters on DL, EE and mean diameters, effect of the concentrations of NaCl and PVA on the incorporation of VCM and mean diameters. Figures: SEM image of VCM loaded PLGA₁₅C NPs, ¹H and ¹³C MAS NMR spectra, STEM image, of a VCM-loaded PLGA₁₅C NP, SEC analysis, Cryo-TEM images of VCM-loaded PLGA₁₅C NPs after 48h incubation.

AUTHOR INFORMATION

Corresponding Author

* Corresponding author: Ruxandra Gref, e-mail: ruxandra.gref@universite-paris-saclay.fr

Author Contributions

RG conceived the study. RG, MSU, MMM and GS designed the experiments. MSU, MMM and GS performed the experiments. JM, ECA, ADB and AD contributed to AFM-IR investigations. MP and CMC contributed to solid state NMR investigations. MSU and RG wrote the manuscript. All authors reviewed the manuscript.

Funding Sources

This work was supported by the Paris Ile-de-France Region – DIM Respire and by public grants overseen by the French National Research Agency (ANR) ANR-16-CE18-0018, ANR-10-LABX-0035 and IR-RMN-THC Fr3050 CNRS.

ACKNOWLEDGMENT

We are grateful to Dr K. Salim (Seqens, Longjumeau, France) for kindly donating the Expansorb® polymer samples. We thank Dr F. Laurent and Dr J. Josse from the International Center for Research on Infectious diseases (Lyon, France) for the VCM samples. We acknowledge Institut de Chimie et des Matériaux de Paris Est (Thiais, France) for providing access to the SEM-EDX and STEM-EDX facility, Dr E. Leroy for technical assistance and Dr C. Jain-Beuguel for her kind help. We also thank Pr P. Roger and Dr L. Costa for their help with the SEC experiments. MP thanks the Région Centre-Val de Loire for a PhD fellowship.

ABBREVIATIONS

AFM, atomic force microscopy; AFM-IR, AFM-infrared spectroscopy; ATR, attenuated total reflection; C, carboxylic; CP, cross-polarization; cryo-TEM, cryogenic TEM; DCM, dichloromethane; DL, drug loading; DMSO, dimethyl sulfoxide; DLS, dynamic light scattering; E, ester; EDX, energy-dispersive X-ray; EE, entrapment efficiency; FCS, fetal calf serum; FDA, food and drug administration; FTIR, Fourier transform IR, HAADF, high angle annular dark field; HCl, hydrochloric acid; HPLC-UV-VIS, high performance liquid chromatography-ultraviolet-visible; IR, infrared; KCl, potassium chloride; KH_2PO_4 , potassium phosphate monobasic; MAS, magic-angle spinning; MRSA, methicillin-resistant *S. aureus*; M_w , molecular weights; Na_2HPO_4 , sodium phosphate dibasic; NaCl, sodium chloride; NMR, nuclear magnetic resonance; NPs, nanoparticles; PB, phosphate buffer, PEG, poly(ethylene glycol); PDI, polydispersity index; PLA, polylactic acid; PLGA, poly(lactic-co-glycolic acid); SE, standard error; SEC, size-exclusion chromatography; *S. aureus*, *Staphylococcus aureus* PVA, poly (vinyl alcohol); RF, Radio Frequency; TEM, transmission electron microscopy; TFA, trifluoroacetic acid; TMS, tetramethylsilane; VCM, vancomycin; $w_1/o/w_2$, water-in-oil-in-water; wt, weight.

REFERENCES

- (1) Lehar, S. M.; Pillow, T.; Xu, M.; Staben, L.; Kajihara, K. K.; Vandlen, R.; DePalatis, L.; Raab, H.; Hazenbos, W. L.; Hiroshi Morisaki, J.; Kim, J.; Park, S.; Darwish, M.; Lee, B. C.; Hernandez, H.; Loyet, K. M.; Lupardus, P.; Fong, R.; Yan, D.; Chalouni, C.; Luis, E.; Khalfin, Y.; Plise, E.; Cheong, J.; Lyssikatos, J. P.; Strandh, M.; Koefoed, K.; Andersen, P. S.; Flygare, J. A.; Wah Tan, M.; Brown, E. J.; Mariathasan, S. Novel Antibody-Antibiotic Conjugate Eliminates Intracellular *S. Aureus*. *Nature* **2015**, *527* (7578), 323–328. <https://doi.org/10.1038/nature16057>.
- (2) Guzman Prieto, A. M.; van Schaik, W.; Rogers, M. R. C.; Coque, T. M.; Baquero, F.; Corander, J.; Willems, R. J. L. Global Emergence and Dissemination of Enterococci as Nosocomial Pathogens: Attack of the Clones? *Frontiers in Microbiology*. Frontiers Media S.A. 2016. <https://doi.org/10.3389/fmicb.2016.00788>.
- (3) Daneman, N.; McGeer, A.; Low, D. E.; Tyrrell, G.; Simor, A. E.; McArthur, M.; Schwartz, B.; Jessamine, P.; Croxford, R.; Green, K. A. Hospital-Acquired Invasive Group A Streptococcal Infections in Ontario, Canada, 1992-2000. *Clin. Infect. Dis.* **2005**, *41* (3), 334–342. <https://doi.org/10.1086/431589>.
- (4) Nuzzo, I.; Sanges, M. R.; Folgore, A.; Carratelli, C. R. Apoptosis of Human Keratinocytes after Bacterial Invasion. *FEMS Immunol. Med. Microbiol.* **2000**, *27* (3), 235–240. [https://doi.org/10.1016/S0928-8244\(99\)00190-X](https://doi.org/10.1016/S0928-8244(99)00190-X).
- (5) Fowler, T.; Wann, E. R.; Joh, D.; Johansson, S.; Foster, T. J.; Höök, M. Cellular Invasion by *Staphylococcus Aureus* Involves a Fibronectin

- Bridge between the Bacterial Fibronectin-Binding MSCRAMMs and Host Cell B1 Integrins. *Eur. J. Cell Biol.* **2000**, *79* (10), 672–679. <https://doi.org/10.1078/0171-9335-00104>.
- (6) Hess, D. J.; Henry-Stanley, M. J.; Erickson, E. A.; Wells, C. L. Intracellular Survival of Staphylococcus Aureus within Cultured Enterocytes. *J. Surg. Res.* **2003**, *114* (1), 42–49. [https://doi.org/10.1016/S0022-4804\(03\)00314-7](https://doi.org/10.1016/S0022-4804(03)00314-7).
- (7) Nair, S. P.; Bischoff, M.; Senn, M. M.; Berger-Bächi, B. The Σ B Regulon Influences Internalization of Staphylococcus Aureus by Osteoblasts. *Infect. Immun.* **2003**, *71* (7), 4167–4170. <https://doi.org/10.1128/IAI.71.7.4167-4170.2003>.
- (8) Pumerantz, A.; Muppidi, K.; Agnihotri, S.; Guerra, C.; Venketaraman, V.; Wang, J.; Betageri, G. Preparation of Liposomal Vancomycin and Intracellular Killing of Meticillin-Resistant Staphylococcus Aureus (MRSA). *Int. J. Antimicrob. Agents* **2011**, *37* (2), 140–144. <https://doi.org/10.1016/j.ijantimicag.2010.10.011>.
- (9) Foster, T. J. Immune Evasion by Staphylococci. *Nat. Rev. Microbiol.* **2005**, *3* (12), 948–958. <https://doi.org/10.1038/nrmicro1289>.
- (10) Garzoni, C.; Kelley, W. L. Staphylococcus Aureus: New Evidence for Intracellular Persistence. *Trends Microbiol.* **2009**, *17* (2), 59–65. <https://doi.org/10.1016/j.tim.2008.11.005>.
- (11) Barcia-Macay, M.; Seral, C.; Mingeot-Ledercq, M. P.; Tulkens, P. M.; Van Bambeke, F. Pharmacodynamic Evaluation of the Intracellular Activities of Antibiotics against Staphylococcus Aureus in a Model of THP-1 Macrophages. *Antimicrob. Agents Chemother.* **2006**, *50* (3), 841–851. <https://doi.org/10.1128/AAC.50.3.841-851.2006>.
- (12) Prasad, Y.; Puthli, S. P.; Eaimtrakarn, S.; Ishida, M.; Yoshikawa, Y.; Shibata, N.; Takada, K. Enhanced Intestinal Absorption of Vancomycin

- with Labrasol and D- α -Tocopheryl PEG 1000 Succinate in Rats. *Int. J. Pharm.* **2003**, *250* (1), 181–190. [https://doi.org/10.1016/S0378-5173\(02\)00544-6](https://doi.org/10.1016/S0378-5173(02)00544-6).
- (13) Patel, S.; Preuss, C. V.; Bernice, F. *Vancomycin*; StatPearls Publishing, 2021.
- (14) Roszell, S.; Jones, C. Intravenous Administration Issues. *J. Infus. Nurs.* **2010**, *33* (2), 112–118. <https://doi.org/10.1097/nan.0b013e3181cfcee4>.
- (15) Rybak, M.; Lomaestro, B.; Rotschafer, J. C.; Moellering, R.; Craig, W.; Billeter, M.; Dalovisio, J. R.; Levine, D. P.; Reilly, C. Therapeutic Monitoring of Vancomycin in Adult Patients: A Consensus Review of the American Society of Health-System Pharmacists, the Infectious Diseases Society of America, and the Society of Infectious Diseases Pharmacists. *Am. J. Heal. Pharm.* **2009**, *66* (1), 82–98. <https://doi.org/10.2146/ajhp080434>.
- (16) Sun, H.; Maderazo, E. G.; Krusell, A. R. Serum Protein-Binding Characteristics of Vancomycin. *Antimicrob. Agents Chemother.* **1993**, *37*(5), 1132–1136. <https://doi.org/10.1128/AAC.37.5.1132>.
- (17) Levison, M. E.; Levison, J. H. Pharmacokinetics and Pharmacodynamics of Antibacterial Agents. *Infect. Dis. Clin. North Am.* **2009**, *23* (4), 791–815. <https://doi.org/10.1016/j.idc.2009.06.008>.
- (18) Sorrell, T. C.; Collignon, P. J. A Prospective Study of Adverse Reactions Associated with Vancomycin Therapy. *J. Antimicrob. Chemother.* **1985**, *16* (2), 235–241. <https://doi.org/10.1093/jac/16.2.235>.
- (19) Pei, Y.; Mohamed, M. F.; Seleem, M. N.; Yeo, Y. Particle Engineering for Intracellular Delivery of Vancomycin to Methicillin-Resistant Staphylococcus Aureus (MRSA)-Infected Macrophages. *J. Control. Release* **2017**, *267* (February), 133–143.

- <https://doi.org/10.1016/j.jconrel.2017.08.007>.
- (20) Kollef, M. H. Limitations of Vancomycin in the Management of Resistant Staphylococcal Infections. *Clin. Infect. Dis.* **2007**, *45* (SUPPL. 3), 191–195. <https://doi.org/10.1086/519470>.
- (21) Ladavière, C.; Gref, R. Toward an Optimized Treatment of Intracellular Bacterial Infections: Input of Nanoparticulate Drug Delivery Systems. *Nanomedicine* **2015**, *10* (19), 3033–3055. <https://doi.org/10.2217/nnm.15.128>.
- (22) Si, Y.; Grazon, C.; Clavier, G.; Rieger, J.; Audibert, J. F.; Sclavi, B.; Méallet-Renault, R. Rapid and Accurate Detection of Escherichia Coli Growth by Fluorescent PH-Sensitive Organic Nanoparticles for High-Throughput Screening Applications. *Biosens. Bioelectron.* **2016**, 320–327. <https://doi.org/10.1016/j.bios.2015.08.028>.
- (23) Radovic-Moreno, A. F.; Lu, T. K.; Puscasu, V. A.; Yoon, C. J.; Langer, R.; Farokhzad, O. C. Surface Charge-Switching Polymeric Nanoparticles for Bacterial Cell Wall-Targeted Delivery of Antibiotics. *ACS Nano* **2012**, *6* (5), 4279–4287. <https://doi.org/10.1021/nn3008383>.
- (24) Singh, R.; Lillard, J. W. Nanoparticle-Based Targeted Drug Delivery. *Exp. Mol. Pathol.* **2009**, *86* (3), 215–223. <https://doi.org/10.1016/j.yexmp.2008.12.004>.
- (25) Iqbal, M.; Zafar, N.; Fessi, H.; Elaissari, A. Double Emulsion Solvent Evaporation Techniques Used for Drug Encapsulation. *Int. J. Pharm.* **2015**, *496* (2), 173–190. <https://doi.org/10.1016/j.ijpharm.2015.10.057>.
- (26) Sande, L.; Sanchez, M.; Montes, J.; Wolf, A. J.; Morgan, M. A.; Omri, A.; Liu, G. Y. Liposomal Encapsulation of Vancomycin Improves Killing of Methicillin-Resistant Staphylococcus Aureus in a Murine Infection Model. *J. Antimicrob. Chemother.* **2012**, *67* (9), 2191–2194.

<https://doi.org/10.1093/jac/dks212>.

- (27) Ma, T.; Shang, B. C.; Tang, H.; Zhou, T. H.; Xu, G. L.; Li, H. L.; Chen, Q. H.; Xu, Y. Q. Nano-Hydroxyapatite/Chitosan/Konjac Glucomannan Scaffolds Loaded with Cationic Liposomal Vancomycin: Preparation, in Vitro Release and Activity against Staphylococcus Aureus Biofilms. *J. Biomater. Sci. Polym. Ed.* **2011**, *22* (12), 1669–1681. <https://doi.org/10.1163/092050611X570644>.
- (28) Shahverdi, A. R.; Fakhimi, A.; Shahverdi, H. R.; Minaian, S. Synthesis and Effect of Silver Nanoparticles on the Antibacterial Activity of Different Antibiotics against Staphylococcus Aureus and Escherichia Coli. *Nanomedicine Nanotechnology, Biol. Med.* **2007**, *3*(2), 168–171. <https://doi.org/10.1016/j.nano.2007.02.001>.
- (29) Hur, Y. E.; Park, Y. Vancomycin-Functionalized Gold and Silver Nanoparticles as an Antibacterial Nanoplatfrom against Methicillin-Resistant Staphylococcus Aureus. *J. Nanosci. Nanotechnol.* **2016**, *16* (6), 6393–6399. <https://doi.org/10.1166/jnn.2016.12393>.
- (30) Kaur, A.; Preet, S.; Kumar, V.; Kumar, R.; Kumar, R. Synergetic Effect of Vancomycin Loaded Silver Nanoparticles for Enhanced Antibacterial Activity. *Colloids Surfaces B Biointerfaces* **2019**, *176*, 62–69. <https://doi.org/10.1016/j.colsurfb.2018.12.043>.
- (31) Esmaeillou, M.; Zarrini, G.; Rezaee, M. A.; Mojarrad, J. S.; Bahadori, A. Vancomycin Capped with Silver Nanoparticles as an Antibacterial Agent against Multi-Drug Resistance Bacteria. *Adv. Pharm. Bull.* **2017**, *7*(3), 479–483. <https://doi.org/10.15171/apb.2017.058>.
- (32) Gu, H.; Ho, P. L.; Tong, E.; Wang, L.; Xu, B. Presenting Vancomycin on Nanoparticles to Enhance Antimicrobial Activities. *Nano Lett.* **2003**, *3* (9), 1261–1263. <https://doi.org/10.1021/nl034396z>.
- (33) Singla, R.; Guliani, A.; Kumari, A.; Yadav, S. K. Metallic Nanoparticles,

- Toxicity Issues and Applications in Medicine. In *Nanoscale Materials in Targeted Drug Delivery, Theragnosis and Tissue Regeneration*; Springer Singapore: Singapore, 2016; pp 41–80. https://doi.org/10.1007/978-981-10-0818-4_3.
- (34) Koo, O. M.; Rubinstein, I.; Onyuksel, H. Role of Nanotechnology in Targeted Drug Delivery and Imaging: A Concise Review. *Nanomedicine Nanotechnology, Biol. Med.* **2005**, *1* (3), 193–212. <https://doi.org/10.1016/j.nano.2005.06.004>.
- (35) Sayin, B.; Çalifi, S. Influence of Accelerated Stab Studied on the Storage of Vancomycin Loaded Microspheres. **2005**, 111–116.
- (36) Özalp, Y.; Özdemir, N.; Kocagöz, S.; Hasirci, V. Controlled Release of Vancomycin from Biodegradable Microcapsules. *J. Microencapsul.* **2001**, *18* (1), 89–110. <https://doi.org/10.1080/026520401750038638>.
- (37) Ritsema, J. A. S.; Herschberg, E. M. A.; Borgos, S. E.; Løvmo, C.; Schmid, R.; te Welscher, Y. M.; Storm, G.; van Nostrum, C. F. Relationship between Polarities of Antibiotic and Polymer Matrix on Nanoparticle Formulations Based on Aliphatic Polyesters. *Int. J. Pharm.* **2018**, *548* (2), 730–739. <https://doi.org/10.1016/j.ijpharm.2017.11.017>.
- (38) Posadowska, U.; Brzychczy-Wloch, M.; Pamula, E. Injectable Gellan Gum-Based Nanoparticles-Loaded System for the Local Delivery of Vancomycin in Osteomyelitis Treatment. *J. Mater. Sci. Mater. Med.* **2016**, *27* (1), 1–9. <https://doi.org/10.1007/s10856-015-5604-2>.
- (39) Zakeri-Milani, P.; Loveymi, B. D.; Jelvehgari, M.; Valizadeh, H. The Characteristics and Improved Intestinal Permeability of Vancomycin PLGA-Nanoparticles as Colloidal Drug Delivery System. *Colloids Surfaces B Biointerfaces* **2013**, *103*, 174–181. <https://doi.org/10.1016/j.colsurfb.2012.10.021>.
- (40) Huang, W. F.; Tsui, C. P.; Tang, C. Y.; Yang, M.; Gu, L. Surface Charge

- Switchable and PH-Responsive Chitosan/Polymer Core-Shell Composite Nanoparticles for Drug Delivery Application. *Compos. Part B Eng.* **2017**, *121*, 83–91. <https://doi.org/10.1016/j.compositesb.2017.03.028>.
- (41) Zambaux, M. F.; Bonneaux, F.; Gref, R.; Maincent, P.; Dellacherie, E.; Alonso, M. J.; Labrude, P.; Vigneron, C. Influence of Experimental Parameters on the Characteristics of Poly(Lactic Acid) Nanoparticles Prepared by a Double Emulsion Method. *J. Control. Release* **1998**, *50* (1–3), 31–40. [https://doi.org/10.1016/S0168-3659\(97\)00106-5](https://doi.org/10.1016/S0168-3659(97)00106-5).
- (42) Massiot, D.; Fayon, F.; Capron, M.; King, I.; Le Calvé, S.; Alonso, B.; Durand, J. O.; Bujoli, B.; Gan, Z.; Hoatson, G. Modelling One- and Two-Dimensional Solid-State NMR Spectra. *Magn. Reson. Chem.* **2002**, *40* (1), 70–76. <https://doi.org/10.1002/mrc.984>.
- (43) Mathurin, J.; Pancani, E.; Deniset-Besseau, A.; Kjoller, K.; Prater, C. B.; Gref, R.; Dazzi, A. How to Unravel the Chemical Structure and Component Localization of Individual Drug-Loaded Polymeric Nanoparticles by Using Tapping AFM-IR. *Analyst* **2018**, *143* (24), 5940–5949. <https://doi.org/10.1039/c8an01239c>.
- (44) Xing, B.; Jiang, T.; Wu, X.; Liew, R.; Zhou, J.; Zhang, D.; Yeow, E. K. L. Molecular Interactions between Glycopeptide Vancomycin and Bacterial Cell Wall Peptide Analogues. *Chem. - A Eur. J.* **2011**, *17* (50), 14170–14177. <https://doi.org/10.1002/chem.201102195>.
- (45) Jia, Z.; O'Mara, M. L.; Zuegg, J.; Cooper, M. A.; Mark, A. E. Vancomycin: Ligand Recognition, Dimerization and Super-Complex Formation. *FEBS J.* **2013**, *280* (5), 1294–1307. <https://doi.org/10.1111/febs.12121>.
- (46) Loll, P. J.; Bevivino, A. E.; Korty, B. D.; Axelsen, P. H. Simultaneous Recognition of a Carboxylate-Containing Ligand and an Intramolecular Surrogate Ligand in the Crystal Structure of an Asymmetric Vancomycin Dimer. *J. Am. Chem. Soc.* **1997**, *119* (7),

- 1516–1522. <https://doi.org/10.1021/ja963566p>.
- (47) Loll, P. J.; Miller, R.; Weeks, C. M.; Axelsen, P. H. A Ligand-Mediated Dimerization Mode for Vancomycin. *Chem. Biol.* **1998**, *5*(5), 293–298. [https://doi.org/10.1016/S1074-5521\(98\)90622-6](https://doi.org/10.1016/S1074-5521(98)90622-6).
- (48) Giammarco, J.; Mochalin, V. N.; Haeckel, J.; Gogotsi, Y. The Adsorption of Tetracycline and Vancomycin onto Nanodiamond with Controlled Release. *J. Colloid Interface Sci.* **2016**, *468*, 253–261. <https://doi.org/10.1016/j.jcis.2016.01.062>.
- (49) Quellec, P.; Gref, R.; Perrin, L.; Dellacherie, E.; Sommer, F.; Verbavatz, J. M.; Alonso, M. J. Protein Encapsulation within Polyethylene Glycol-Coated Nanospheres. I. Physicochemical Characterization. *J. Biomed. Mater. Res.* **1998**, *42* (1), 45–54.
- (50) Lotfipour, F.; Abdollahi, S.; Jelvehgari, M.; Valizadeh, H.; Hassan, M.; Milani, M. Study of Antimicrobial Effects of Vancomycin Loaded PLGA Nanoparticles against Enterococcus Clinical Isolates. *Drug Res. (Stuttg)*. **2014**, *64* (7), 348–352. <https://doi.org/10.1055/s-0033-1358747>.
- (51) Kentish, S.; Wooster, T. J.; Ashokkumar, M.; Balachandran, S.; Mawson, R.; Simons, L. The Use of Ultrasonics for Nanoemulsion Preparation. *Innov. Food Sci. Emerg. Technol.* **2008**, *9* (2), 170–175. <https://doi.org/10.1016/j.ifset.2007.07.005>.
- (52) Mahdi Jafari, S.; He, Y.; Bhandari, B. Nano-Emulsion Production by Sonication and Microfluidization - A Comparison. *Int. J. Food Prop.* **2006**, *9* (3), 475–485. <https://doi.org/10.1080/10942910600596464>.
- (53) Takács-Novák, K.; Noszál, B.; Tókés-Kövesdi, M.; Szász, G. Acid-Base Properties and Proton-Speciation of Vancomycin. *Int. J. Pharm.* **1993**, *89* (3), 261–263. [https://doi.org/10.1016/0378-5173\(93\)90252-B](https://doi.org/10.1016/0378-5173(93)90252-B).
- (54) Johnson, J. L. H.; Yalkowsky, S. H. Reformulation of a New Vancomycin

- Analog: An Example of the Importance of Buffer Species and Strength. *AAPS PharmSciTech* **2006**, *7* (1), E1–E5. <https://doi.org/10.1208/pt070105>.
- (55) Yoo, J. W.; Mitragotri, S. Polymer Particles That Switch Shape in Response to a Stimulus. *Proc. Natl. Acad. Sci. U. S. A.* **2010**, *107*(25), 11205–11210. <https://doi.org/10.1073/pnas.1000346107>.
- (56) Shestakova, P.; Martineau, C.; Mavrodinova, V.; Popova, M. Solid State NMR Characterization of Zeolite Beta Based Drug Formulations Containing Ag and Sulfadiazine. *RSC Adv.* **2015**, *5* (100), 81957–81964. <https://doi.org/10.1039/c5ra15097c>.
- (57) Knox, J. R.; Pratt, R. F. Different Modes of Vancomycin and D-Alanyl-D-Alanine Peptidase Binding to Cell Wall Peptide and a Possible Role for the Vancomycin Resistance Protein. *Antimicrob. Agents Chemother.* **1990**, *34* (7), 1342–1347. <https://doi.org/10.1128/AAC.34.7.1342>.
- (58) Dazzi, A.; Prater, C. B. AFM-IR: Technology and Applications in Nanoscale Infrared Spectroscopy and Chemical Imaging. *Chem. Rev.* **2017**, *117* (7), 5146–5173. <https://doi.org/10.1021/acs.chemrev.6b00448>.
- (59) Lu, F.; Jin, M.; Belkin, M. A. Tip-Enhanced Infrared Nanospectroscopy via Molecular Expansion Force Detection. *Nat. Photonics* **2014**, *8* (4), 307–312. <https://doi.org/10.1038/nphoton.2013.373>.
- (60) Pancani, E.; Mathurin, J.; Bilent, S.; Bernet-Camard, M. F.; Dazzi, A.; Deniset-Besseau, A.; Gref, R. High-Resolution Label-Free Detection of Biocompatible Polymeric Nanoparticles in Cells. *Part. Part. Syst. Charact.* **2018**, *35* (3). <https://doi.org/10.1002/ppsc.201700457>.
- (61) Mathurin, J.; Pancani, E.; Deniset-Besseau, A.; Kjoller, K.; Prater, C. B.; Gref, R.; Dazzi, A. How to Unravel the Chemical Structure and

- Component Localization of Individual Drug-Loaded Polymeric Nanoparticles by Using Tapping AFM-IR. *Analyst* **2018**, *143* (24), 5940–5949. <https://doi.org/10.1039/c8an01239c>.
- (62) Yuniarto, K.; Aris Purwanto, Y.; Purwanto, S.; Welt, B. A.; Karia Purwadaria, H.; Candra Sunarti, T. Infrared and Raman Studies on Polylactide Acid and Polyethylene Glycol-400 Blend. **2016**, *1725*, 20101. <https://doi.org/10.1063/1.4945555>.
- (63) Salter, C. J.; Mitchell, R. C.; Drake, A. F. Infrared Spectroscopic Studies of Vancomycin and Its Interactions with N-Acetyl-D-Ala-D-Ala and N,N'-Diacetyl-L-Lys-D-Ala-D-Ala. *J. Chem. Soc. Perkin Trans. 2* **1995**, No. 12, 2203–2211. <https://doi.org/10.1039/p29950002203>.
- (64) Phillips-Jones, M. K.; Lithgo, R.; DInu, V.; Gillis, R. B.; Harding, J. E.; Adams, G. G.; Harding, S. E. Full Hydrodynamic Reversibility of the Weak Dimerization of Vancomycin and Elucidation of Its Interaction with VanS Monomers at Clinical Concentration. *Sci. Rep.* **2017**, *7*(1), 1–10. <https://doi.org/10.1038/s41598-017-12620-z>.

SUPPLEMENTARY INFORMATION

Compartmentalized Polymeric Nanoparticles Deliver Vancomycin in a pH-Responsive manner

*M. Seray Ural, Mario Menéndez-Miranda, Giuseppina Salzano, Jérémie Mathurin, Ece N. Aybeke, Ariane Deniset-Besseau, Alexandre Dazzi, Marianna Porcino, Charlotte Martineau-Corcos, Ruxandra Gref **

HPLC method

The mobile A phase was water and the mobile B phase was acetonitrile, both containing 0.1% TFA. Chromatographic separation of VCM was performed at room temperature and elution was performed at a rate of 1 mL/min in gradient elution mode (**Table S1**). The injection volume was 10 μ L.

Table S1. HPLC gradient elution program

Time (min)	A (%)	B (%)
0	90	10
6	55	45
10	90	10

PVA quantification

1.3 g of NP suspension containing around 20 mg of PLGA₁₅C or PLG₈C NPs was centrifuged at 17,000 x g for 15 min and the supernatant was discarded. The NP pellet was hydrolyzed overnight in 5 mL of 1N KOH and then neutralized with 1N HCl. To 0.1 mL of neutralized sample, 0.375 mL of 3.7% w/v boric acid solution, 0.01 mL of iodine solution (1.66% potassium iodide and 1.27% iodine in distilled water) w/v and 0.7 mL of 1N HCl were added. The absorbance of this solution was further measured in UV spectrometer at 620 nm. All samples were analyzed in triplicate.

SEM

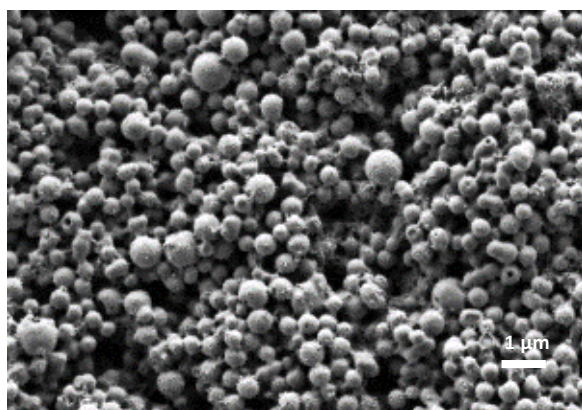


Figure S1. Typical SEM image of PLGA₁₅C NPs loaded with 14 wt% VCM.

Effect of preparation parameters on DL, EE and mean diameters

The influence of drug to polymer ratio on the DL and EE was investigated (**Table S2**). DL and EE increased with the drug/polymer ratio until reaching a plateau at the ratio of 0.4/1 (DL=14±4 wt%). In contrast, the drug/polymer ratio had no effect on the size of the NPs.

Table S2. Effect of drug/polymer mass ratio on DL, EE and mean diameter on VCM loaded PLGA₁₅C NPs

Formulations (drug/polymer ratio)	DL (wt% ± SD)	EE (wt% ± SD)	Mean diameter*† (nm)
0.2/1	9 ± 2	50 ± 11	324
0.3/1	10 ± 1	37 ± 4	330
0.4/1	14 ± 4	36 ± 2	320
0.5/1	14 ± 2	33 ± 3	327

* Standard deviations (SD) are 25 nm for all the formulations.

† Measured by DLS.

In complementary studies, it was found that the addition of NaCl during NP preparation had a high impact on VCM incorporation (**Table S3**). For example, DL increased from 9 ± 1 wt% to 14 ± 4 wt% in the presence of 1% NaCl and EE increased from 23 ± 1 % to 36 ± 2 %, without having a significant effect on the NP size. Indeed, salts were reported to facilitate polymer precipitation and enhance DL.^{1, 2} However, higher salt contents did not improve DL nor EE but led to much larger NPs (up to 460 nm).

Additionally, neither the use of more concentrated PVA solutions nor other emulsifiers lead to an improvement in DL. As presented in **Table S3**, doubling the concentration of PVA slightly affects the DL (from 12 ± 2 wt% to 14 ± 4 wt%). Noteworthy, the use of anionic surfactants such as sodium cholate instead of PVA failed to stabilize the emulsions, leading to phase separation.

Table S3. Effect of the concentrations of NaCl and PVA on the incorporation of VCM and mean diameters. NPs were prepared using PLGA₁₅C (co)polymer.

STEM-EDX

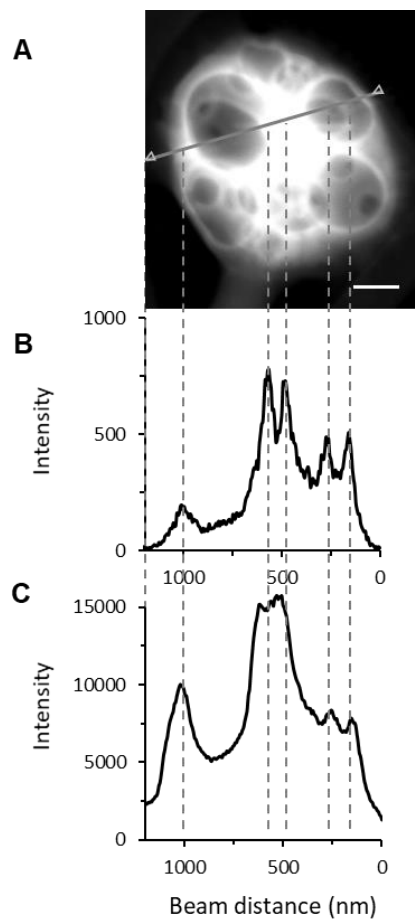


Figure S3. **A)** STEM image of a VCM-loaded PLGA₁₅C NP. EDX line scanning profiles of **B)** Nitrogen and **C)** Carbon. Nitrogen intensity at its peak values can be followed by the dashed lines. Scale bar is 250 nm.

Degradation studies

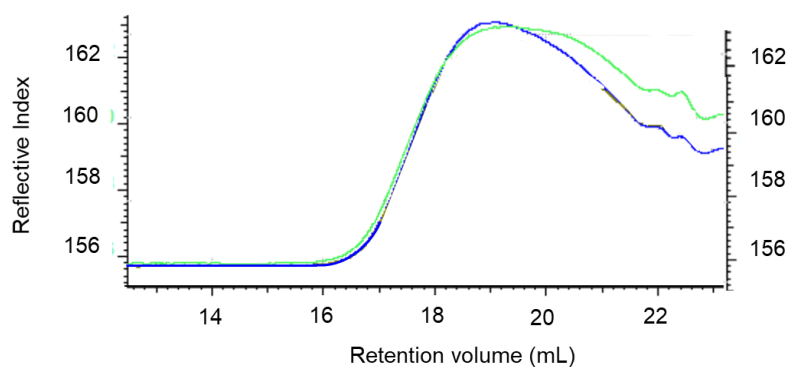


Figure S4. SEC analysis of loaded PLGA₁₅C NPs incubated in phosphate buffer at pH 5.3 during 5 min (light green) and 4 days (blue). No significant polymer degradation was observed.

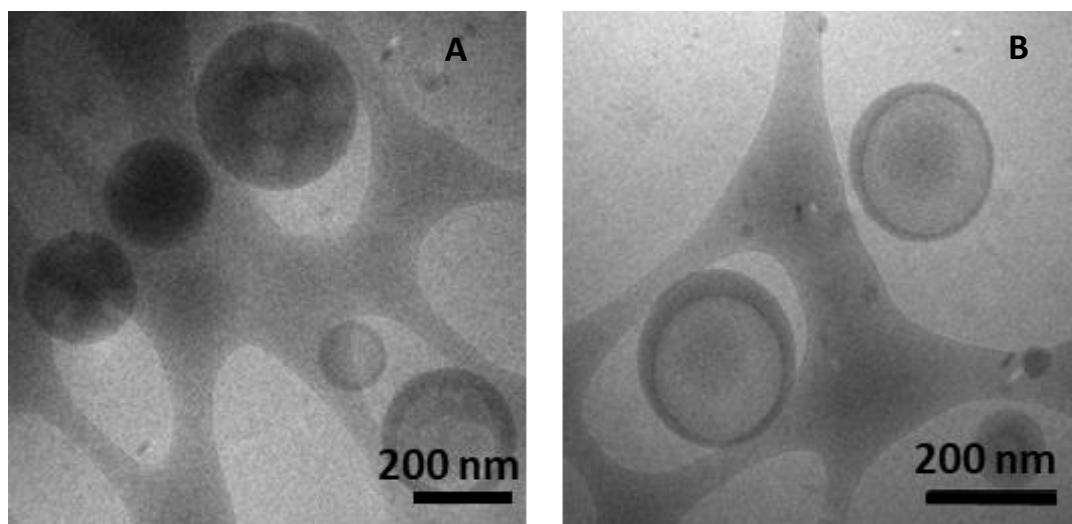


Figure S5. Typical Cryo-TEM images of VCM-loaded PLGA₁₅C NPs after 48h incubation at 37°C: **A)** in phosphate buffer at pH 5 and **B)** in water.

References

- (1) Tu, F.; Lee, D. Controlling the Stability and Size of Double-Emulsion-Templated Poly(Lactic- Co -Glycolic) Acid Microcapsules. *Langmuir* **2012**, *28* (26), 9944–9952. <https://doi.org/10.1021/la301498f>.
- (2) Gorrepati, E. A.; Wongthahan, P.; Raha, S.; Fogler, H. S. Silica Precipitation in Acidic Solutions: Mechanism, PH Effect, and Salt Effect. *Langmuir* **2010**, *26* (13), 10467–10474. <https://doi.org/10.1021/la904685x>.

Chapter III

Quantify drug loading at the single nanoparticles level using AFM-IR technique: a convenient method to map and evaluate the drug distribution

Quantify drug loading at the single nanoparticles level using AFM-IR technique: a convenient method to map and evaluate the drug distribution

Merve Seray Ural, Emmanuel Dartois, Jérémie Mathurin, Didier Desmaële, Philippe Collery, Alexandre Dazzi, Ariane Deniset-Besseau, Ruxandra Gref*

[*] Dr. R. Gref, Dr. M.S. Ural, Dr. E. Dartois

Institut de Sciences Moléculaires d'Orsay (ISMO), CNRS UMR 8214, Université Paris-Sud, Université Paris-Saclay, 91405 Orsay, France
E-mail : ruxandra.gref@universite-paris-saclay.fr

Dr. A. Deniset-Besseau, Dr. J Mathurin, Dr. A. Dazzi
Institut de Chimie Physique (ICP), CNRS UMR 8000, Université Paris Sud, Université Paris-Saclay, 91405 Orsay, France
E-mail : ariane.deniset@universite-paris-saclay.fr

Dr. D. Desmaële
Institut Galien (IGPS), CNRS UMR 8612, Université Paris-Sud, Université Paris-Saclay, 91405 Orsay, France
E-mail :

P. Collery M.D.
Society for the Coordination of Therapeutic Research, 2B010 Algajola, France

Keywords: nanoparticle, AFM-IR, polylactic acid, quantification, drug loading, nanoscale maps, IR microspectroscopy.

Quantify drug loading at the single nanoparticles level using AFM-IR technique: a convenient method to map and evaluate the drug distribution

Abstract

Researchers are increasingly thinking smaller to solve some of the biggest challenges in nanomedicine: the control of drug encapsulation. Although recent years have witnessed a significant increase in the development and characterization of polymeric drug nanocarriers, several key features are still to be addressed: Where is the drug located within each nanoparticle (NP)? How much drug each NP contains? Is the drug loading homogeneous on an individual NP basis? To answer these questions, individual NP characterization was achieved here by using atomic force microscopy-infrared spectroscopy (AFM-IR). A label-free quantification methodology was proposed to estimate with a nanoscale resolution the drug loadings of individual poly(lactic acid) (PLA) NPs loaded with an anticancer drug. First, a drug loading calibration curve was established using conventional IR microspectroscopy employing PLA/drug homogeneous films of well-known compositions. Then, single NPs were investigated by AFM-IR acquiring both IR mappings of PLA and drug as well as local IR spectra. Besides, drug location within single NPs was unravelled. The measured drug loadings were drastically different (0 to 21 wt%) from one NP to another, emphasizing the particular interest of this methodology in providing a simple quantification method for the quality control of nanomedicines.

Quantify drug loading at the single nanoparticles level using AFM-IR technique: a convenient method to map and evaluate the drug distribution

1. Introduction

Nanotechnology provides the opportunity to organize matter at the nanometer scale, building supramolecular constructs with particular interest for healthcare. Drug nanocarriers are able to protect and ferry the active molecules from their administration site to the targeted tissues, organs or cells.^[1] Poly(lactic acid) (PLA) and poly(lactic-co-glycolic acid) (PLGA) (co)polymers remain among the most employed biomaterials to engineer nanocarriers, due to their well-established safety profiles, biocompatibility and biodegradability.^[2] However, to date only few PLA and PLGA nanoparticle (NP) formulations reached the clinical trials stage.^[3,4] Indeed, on the journey from bench to bedside, the quality control of NP formulations, encompassing accurate estimations of size distributions and drug incorporation is a challenging step.

Drug loading (DL) is one of the key parameters that determines the therapeutic efficacy of NPs. It has to be carefully optimized as an important pre-requisite for a preclinical development.^[5] In the majority of the studies, DL was determined by separating the NPs from their suspension media, in which the non-encapsulated drug was quantified by chromatographic or spectroscopic methods. These measurements provide average values on large populations of NPs but cannot monitor individually their heterogeneities in composition. Indeed, individual drug-loaded NPs might drastically differ in terms of DL and/or drug location.^[6] These factors are not only important for quality control, but they also play a major role on the drug release mechanism and the interplay with biological media. Significant DL variations could render only a fraction of the NPs therapeutically active.^[7,8] To the best of our knowledge, today, there is no available method able to assess DL and the molecular integrity of the drug when inserted in the NPs, on an individual NP basis.

Quantify drug loading at the single nanoparticles level using AFM-IR technique: a convenient method to map and evaluate the drug distribution

There is a clear need to develop a characterization methodology that would enable investigating polymeric NPs to: i) map the location of the drug with high resolution and ii) perform quantitative analysis of the drug content at the nanoscale level.^[9]

Only a few techniques including high-angle annular dark-field scanning transmission electron microscopy (HAADF-STEM) enable mapping the constitutive elements of the NPs. However, STEM-HAADF is not adapted to the detection of carbon, hydrogen and oxygen (main components of drug-loaded polymeric NPs) because of the presence of carbon in the grids, trace water, and impurities in the NPs. Besides, this method only tracks elements, but not whole molecules, therefore cannot ascertain drug location. Single particle inductively coupled plasma mass spectrometry (spICP-MS) could provide element mass concentration on single NP but it excludes carbon based nanomaterials due to the intrinsic low sensitivity of carbon in ICP-MS.^[10]

Electron microscopies (EMs) coupled with energy-dispersive X-ray spectroscopy were also used for chemical mappings, but sensitive polymeric NPs often suffer significant damages under the electron beam.^[9] In addition, EMs often require cumbersome sample preparation and do not allow three-dimensional imaging. Raman microspectroscopy imaging coupled with chemical analysis is an interesting alternative, but the method remains restricted by the diffraction limit, and its spatial resolution is too low to explore the loading of NPs smaller than 300 nm.^[11]

Our study aims at mapping the location of a drug within its polymeric NP matrix with high spatial resolution (around 15 nm), and determining the individual drug loading of a NP batch. These goals were achieved here in the case of PLA NPs loaded with an anticancer drug by using atomic force microscopy (AFM) coupled to infrared spectroscopy (AFM-IR). AFM-IR is a method of choice, which combines the chemical sensitivity of infrared

Quantify drug loading at the single nanoparticles level using AFM-IR technique: a convenient method to map and evaluate the drug distribution

spectroscopy with the spatial resolution of scanning probe microscopy AFM. It is based on the detection of photo-thermal process that occurs within the sample after its illumination via tuneable pulsed IR laser.^[12–14] Indeed, when molecules absorb at the tuned wavenumber of the IR laser, this results in a fast and highly localized heating leading to a rapid thermal expansion of the sample, detected by the AFM tip in contact with the surface.^[15] Noteworthy, the AFM-IR signal is proportional to the local IR absorption^[12,13] Overall, AFM-IR allows chemical analysis overcoming the classical IR diffraction-limit, achieving a nanometer-size resolution (~15 nm).^[16,17] Noteworthy, AFM-IR can be operated either in top-down illumination^[18] where the laser shines directly on the sample, or in bottom-up configuration^[19], where the specimen is illuminated *via* an evanescent field wave through an IR transparent prism. Furthermore, the AFMIR measurements can be performed using the contact^[14], the tapping^[20]) or the peak force mode^[21] of the AFM. AFM-IR appears *a priori* as a versatile technique to be used on almost any organic material under ambient conditions with a high resolution that is promising to quantify the composition of individual drug-loaded NPs.

Pioneering studies in our groups demonstrated that AFM-IR is a reliable, non-destructive and direct method able to precisely locate and chemically characterize PLA NPs of about 150 nm in diameter inside cells without the need of labelling.^[22] This was a great advantage, as previous studies reported that labelling with fluorescent dyes or other molecules can significantly alters the physicochemical properties of the NPs and their interactions with biological systems.^[23] In another study, the location of the drug incorporated in PLA NPs could be precisely assessed despite the very low loadings (< 1 wt%).^[24] Surprisingly, it was found that the majority of the drug was in the NP shell consisting of poly(vinyl alcohol) (PVA) chains intermingled with the PLA cores. This location correlated well with the fast (“burst”) release of the drug. In our investigations, AFM IR was

Quantify drug loading at the single nanoparticles level using AFM-IR technique: a convenient method to map and evaluate the drug distribution

used in the tapping mode, which is less invasive than the contact mode, and thus better adapted for the loosely adhesive PLA NPs.^[20]

Scarce attempts have been made so far to use AFM-IR for quantification purposes. In 2016, Tang et al.^[25] investigated the distribution of polyethylene components in high impact polypropylene alloys by using AFM-IR in contact mode, using a set up with bottom up illumination that necessitates the preparation of thin specimens on prisms and requires perfect sample to prism adhesion. This study pointed out the necessity of an external calibration to lead to a quantitative analysis by AFM-IR. However, the proposed calibration by ATR-FTIR has the inconvenience of the dependence of the analysed depth with the wavelength (the penetration depth of the evanescent wave increases at lower wavenumbers, and it must be adequately taken into account). This semiquantitative method is therefore challenging to be adapted for calibration purposes. More recently, Ramer et al. conducted measurements using AFM-IR in contact mode, once again with a bottom up illumination and analysed the sample parameters (thickness, homogeneity, intensity of absorption bands) in an attempt to achieve a rigorous quantitative measurement on poly(methyl methacrylate) films of 43 to 1243 nm thick. They suggested that thin samples (< 500 nm) should be used to maintain a linear behaviour of signal intensity with the amount of analysed sample.^[26]

To the best of our knowledge, no study has considered yet local component quantification on NP systems by using AFM-IR, neither in top-down nor in bottom-up configuration. Top-down approach in comparison to bottom up, simplifies the sample preparation and is less constrained by the physical properties of the sample (size, shape, transparency etc.) therefore it is adapted to routine analysis. One of the other advantages of this approach is the availability of AFM tapping mode that is ideal for loosely adhesive and soft NPs.

Quantify drug loading at the single nanoparticles level using AFM-IR technique: a convenient method to map and evaluate the drug distribution

In this work AFM-IR was in top-down configuration and operated in the tapping mode as the best configuration to avoid crushes or displacements of PLA NPs.^[24] We present the quantification of the DL on single PLA NPs together with the precise mapping of the drug inside the NPs. The quantification methodology by employing AFM-IR was established by using a series of PLA NPs (size range of 200-300 nm) loaded with a Re-based anticancer drug. Re(I) tricarbonyl-diselenium complex with the ability to modulate the redox status of cancer cells was used as it has been involved in the most advanced preclinical studies up to date and showed remarkable anticancer activity, efficacy at low doses and low toxicity.^[27] The administration of this newly emerging anticancer agent *via* NPs could be a great step forward its targeted delivery to cancer cells.

The methodology proposed here establishes a precise calibration of the infrared band intensities combining conventional IR microspectroscopy and AFM-IR measurements using reference thin films with well-known PLA and drug compositions. Drug loading was assessed on an individual NP basis through the local AFM-IR spectral analysis. A fast local quantification method was established by the use of IR maps that paves the way to perform statistical analysis on numerous individual NPs within the same batch overcoming the slowness of spectral analysis. Unexpectedly, it allowed determining large differences in NP composition not correlated to their sizes.

2. Results and Discussion

2.1. Preparation of NPs and films

The NPs were prepared with precise drug:PLA mass ratios, from 0 (pure PLA) to 0.20. Empty NP(0), and drug-loaded PLA NPs were successfully obtained by nanoprecipitation using PVA as emulsifier. They were named according to the drug:PLA mass ratios used in their preparation, as

Quantify drug loading at the single nanoparticles level using AFM-IR technique: a convenient method to map and evaluate the drug distribution

NP(0.03); NP(0.10); NP(0.15) and NP(0.20). After removing aggregates by filtration, the NPs were characterized (**Table 1**). Mean hydrodynamic diameters of the NPs ranged from 249 to 264 nm, and polydispersities from 0.1 to 0.3. Noteworthy, the drug content in the formulations had no significant impact on the NP size. The NPs suspensions were stable for 3 months after their preparation, with less than 5% size variations.

Table 1. Characteristics of empty and drug-loaded NPs as a function of the drug amount used in their preparation (drug:PLA mass ratio).

Name	drug:PLA mass ratio	Mean hydrodynamic diameter [nm]	PDI
NP(0)	0	255±10	0.32±0.01
NP(0.03)	0.03	249±10	0.21±0.09
NP(0.10)	0.10	264±12	0.09±0.04
NP(0.15)	0.15	250±18	0.30±0.05
NP(0.20)	0.20	255±10	0.29±0.05

TEM images showed that the NPs had spherical shapes, with sizes in the range of around 200-400 nm (**Figure 1**), in agreement with DLS data (**Table 1**). The NP morphology was unaffected by the loaded drug.

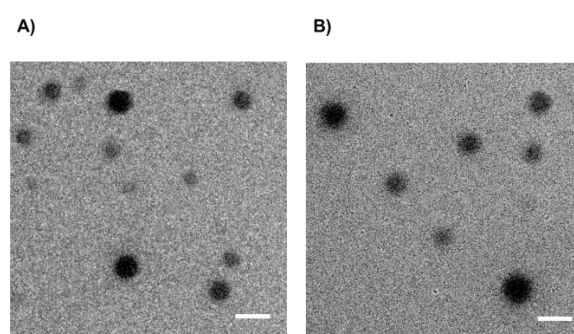


Figure 1. Typical TEM images of PLA NPs: A) NP(0) and B) NP(0.20). Scale bars are 500 nm.

Quantify drug loading at the single nanoparticles level using AFM-IR technique: a convenient method to map and evaluate the drug distribution

To complement the study, films were casted using exactly the same drug:polymer solutions which were used for NP preparation. The use of physical mixtures of drug and PLA with well-known drug:polymer mass ratios enabled to obtain the signal of bulk materials, avoiding the issue of aggregate formation as it was the case with NPs. The films were named according to their drug:PLA mass ratios as F(0); F(0.03); F(0.10); F(0.15) and F(0.20). All the films were translucent with a homogenous aspect.

2.2. AFM-IR methodology

The films and NPs were characterized by AFM-IR which is schematically represented in **Figure 2**. In the top-down configuration used here, the AFM laser light is focussed on the oscillating cantilever, whereas a photodiode detects the deflected light. In addition, a tuneable IR radiation is shed onto the sample (**Figure 2A**). When a compound absorbs the radiation an immediate expansion occurs in a small volume, and is detected by changes in the cantilever deflections (**Figure 2C, D**). The main idea here was to irradiate the sample with specific wavelengths at which only one of the NP components (either drug or polymer) will respond. In this way, maps of both drug and polymer can be recorded. To do so, it was necessary in a first step to investigate the IR vibrational spectra of each component of the NP to identify its "fingerprint".

Quantify drug loading at the single nanoparticles level using AFM-IR technique: a convenient method to map and evaluate the drug distribution

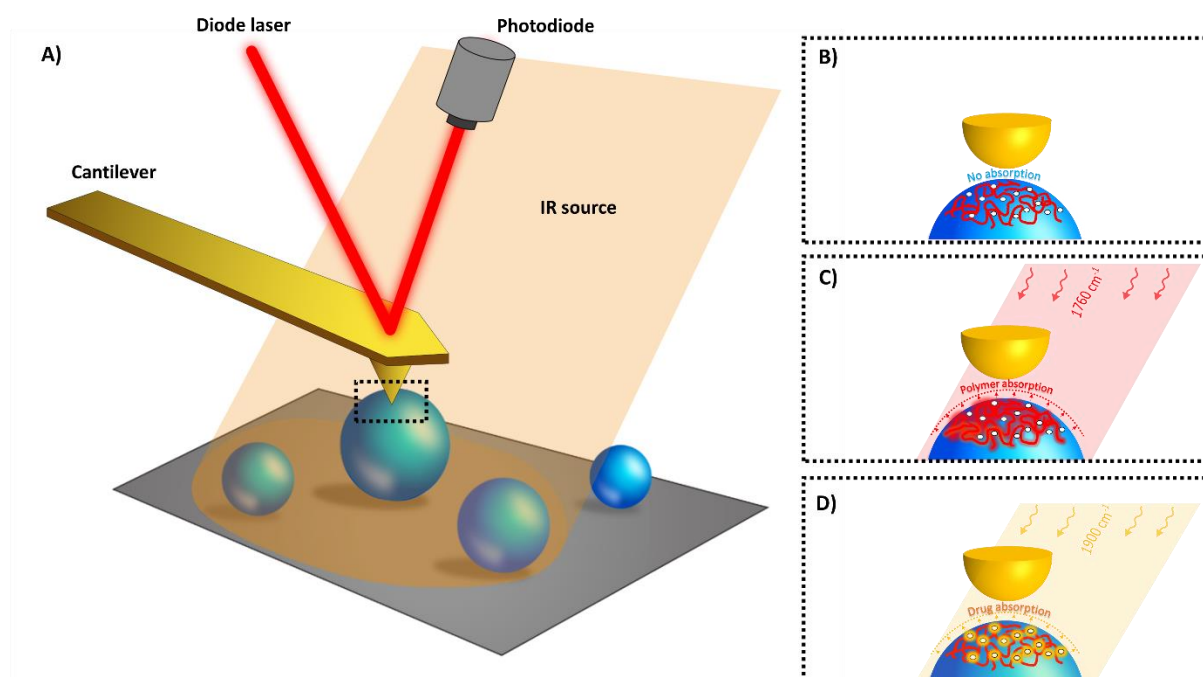


Figure 2. In AFM-IR with top-down configuration pulsed, tuneable laser light is focused onto the sample at the AFM tip location **(A)** enabling to analyse the surface of individual NPs **(B)**. When the IR matches the drug **(C)** or the polymer **(D)** absorption band (« fingerprint ») a rapid thermal expansion occurs due to heating (few kelvins ^[24,28]). The picometric expansion affects the cantilever oscillations, which are measured with the photodiode. IR maps at specific wavelengths corresponding to the polymer and/or the drug absorptions can be acquired.

2.3. IR Vibrational characterization

To specifically map each element constitutive of the films and NPs, isolated IR bands are needed, to avoid overlapping/mixing of the response with contributions from other components. The serie of films and NPs mixtures were characterized by ATR-FTIR to determine their vibrational absorption frequencies, focusing in particular on the carbonyl bands. To begin with, the IR absorptions of each component (PLA, drug and PVA)

Quantify drug loading at the single nanoparticles level using AFM-IR technique: a convenient method to map and evaluate the drug distribution

were recorded separately and their corresponding IR bands were attributed (**Figure SI2**).

Figure 3 presents the IR absorption bands in the region $1675\text{--}1908\text{ cm}^{-1}$ in which the AFM-IR experiments are carried on. The optimal bands selected to discriminate the PLA from the drug are located at 1760 cm^{-1} for PLA and 1900 cm^{-1} for the drug. The former band correspond to the CO stretching of the carbonyl of the ester function of PLA while the later correspond to the $A' C_s$ stretching mode of the octahedral *fac*- $\text{Re}(\text{CO})_3$ moiety^[29]. In addition, this choice ascertains that the presence of eventual residual PVA in the NPs formulations do not interfere with the detection of the PLA matrix and that of the incorporated drug, as PVA presents in the selected region a C=O stretching absorption around 1724 cm^{-1} (**Figure 3**).

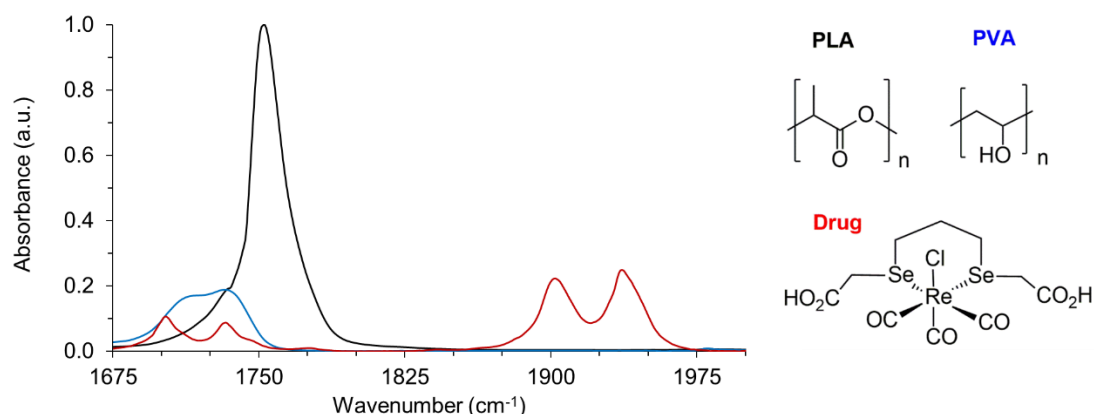


Figure 3. ATR-FTIR spectra of PLA (black), PVA (blue) and drug (red) that were used to prepare films and/or NPs. Chemical structures of each NP component are presented on the right.

2.4. Calibration by IR microspectroscopy

Quantify drug loading at the single nanoparticles level using AFM-IR technique: a convenient method to map and evaluate the drug distribution

After determining the drug and PLA fingerprints the next goal was to establish the relationship between the intensities of the respective IR signals of drug and polymer and their concentration inside the analysed samples, films and NPs, in view of establishing a calibration curve to be used throughout the study, for the proof of concept and drug quantification by AFM-IR.

To do so, IR microspectroscopy was employed as an accurate analytical tool to gain spatially resolved chemical information. It allowed investigating films and NP samples which were gently compressed and flattened to a fine and uniform thickness ($\sim 1\mu\text{m}$) ensuring non saturated absorptions.

First, PLA-drug films were prepared with known respective concentrations of each component. Analysed by IR microspectroscopy, the casted films exhibited typical Fabry-Perot interference fringes. The fringes appeared as sinusoidal waves that are characteristic of thin non-scattering samples with uniform thicknesses.^[30] Chemical analysis of at least 5 independent domains of $50 \times 50 \mu\text{m}$ or $75 \times 75 \mu\text{m}$ (rectangular aperture) on each film preparation was performed to gain insights into the homogeneity of bulk samples at the spatial scale typically probed by classical infrared microspectroscopy, ie of a few tens of microns. The domains analysed showed reproducible spectra demonstrating that the samples were homogeneous at such analysis scale.

Figure 4A shows typical spectral features of drug-PLA films, F(0)-F(0.20), which were normalized to the PLA band intensity at 1760 cm^{-1} (I_{1760}). Information in this region was comparable to ATR-FTIR data (**Figure 3**). Band intensity at 1900 cm^{-1} (I_{1900}) steadily increased with the amount of drug incorporated in the film (**Figure 4A**). A linear relationship ($R^2=0.98$) was found by plotting the ratios of the intensities of the specific carbonyl bands of drug and polymer (I_{1900} / I_{1760}) against the drug:polymer mass

Quantify drug loading at the single nanoparticles level using AFM-IR technique: a convenient method to map and evaluate the drug distribution

ratios ($m_{\text{drug}} / m_{\text{PLA}}$ **Figure 4B**). As the amount of PLA (m_{PLA}) was kept constant throughout the experiments, this means that I_{1900} / I_{1760} is proportional to the drug content in this explored drug concentration range. This linear relationship was further used as a calibration curve.

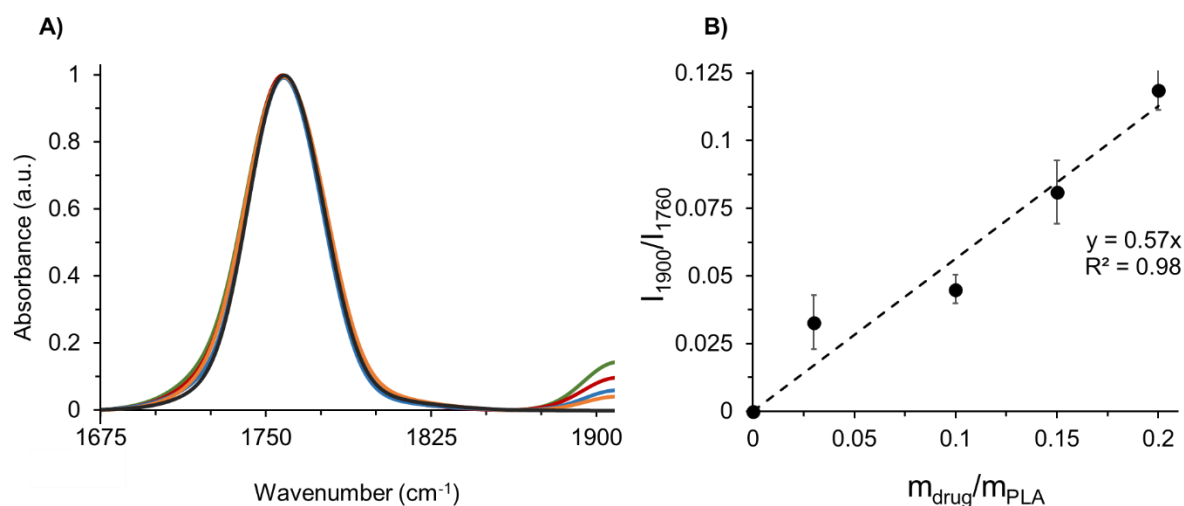


Figure 4. A) Absorbance spectra of F(0) (black), F(0.03) (orange), F(0.10) (blue), F(0.15) (red) and F(0.20) (green) films recorded by IR microspectroscopy, normalised to the PLA carbonyl intensity. B) Calibration curve and its respective calibration line. Drug:polymer mass ratios in the films were represented as $m_{\text{drug}}/m_{\text{PLA}}$. Intensity ratios of carbonyl band of drug to polymer were represented as I_{1900} / I_{1760} .—The AFM-IR working range was in between 1675 and 1908 cm^{-1} as detailed in materials and methods (section 4.8).

In addition, bulk analysis of drug-loaded NPs was performed by IR microspectroscopy. **Figure 5A** represents the absorbance spectra of six NPs formulations prepared with different drug:polymer mass ratios. Carbonyl band intensity ratios of drug and polymer (I_{1900}/I_{1760}) were plotted as a function of drug:polymer mass ratios ($m_{\text{drug}} / m_{\text{PLA}}$) (**Figure 5B**), The increase in the intensity of the drug fingerprint (1900 cm^{-1}) was

Quantify drug loading at the single nanoparticles level using AFM-IR technique: a convenient method to map and evaluate the drug distribution

evident upon the increase in its mass ratio. This indicates the successful loading of the drug into the NPs. The presence of residual PVA in the formulation was detected at around 1712 cm^{-1} as a shoulder contribution to the main PLA carbonyl band.

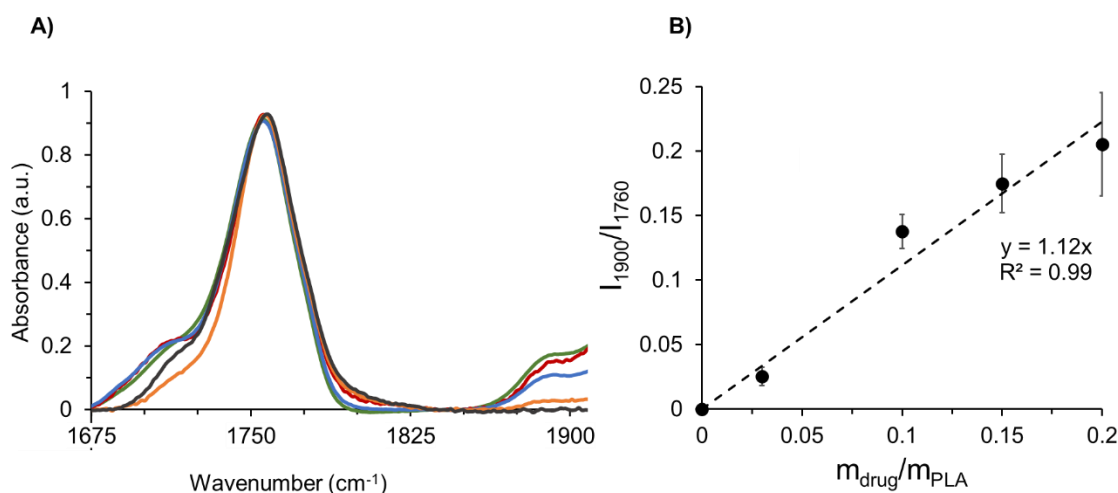


Figure 5. A) Absorbance spectra of NPs prepared with initial drug concentration of NP(0) (black), NP(0.03) (orange), NP(0.10) (blue), NP(0.15) (red) and NP(0.20) (green). B) Intensity ratios of carbonyl bands (I_{1900} / I_{1760}) as a function of drug:polymer mass ratios used in the NP preparation and calibration curve obtained with films of known $m_{\text{drug}}/m_{\text{PLA}}$ ratios (**Figure 4B**)

The I_{1900} / I_{1760} values were used to calculate the drug:polymer mass ratios for each NP, i.e. NP(0)-NP(0.20), by using the calibration curve established above (**Figure 4B**). **Table 2** presents the drug:polymer mass ratios, measured as 0.05 ± 0.02 ; 0.14 ± 0.03 ; 0.17 ± 0.04 ; 0.34 ± 0.04 and 0.35 ± 0.04 for NP(0); NP(0.03); NP(0.10); NP(0.15) and NP(0.20), respectively. The AFM-IR working range was in between 1675 and 1908 cm^{-1} as detailed in materials and methods (section 4.8).

Quantify drug loading at the single nanoparticles level using AFM-IR technique: a convenient method to map and evaluate the drug distribution

Table 2. Drug:polymer mass ratios used in the preparation procedure ($m_{\text{drug}}/m_{\text{PLA}}$), measured drug:polymer mass ratios and measured DLs of NPs : NP(0)-NP(0.20).

	NP(0)	NP(0.03)	NP(0.10)	NP(0.15)	NP(0.20)
($m_{\text{drug}}/m_{\text{PLA}}$)	0	0.03	0.10	0.15	0.20
($m_{\text{drug}}/m_{\text{PLA}}$)m eas.	0	0.04±0.01	0.24±0.02	0.31±0.04	0.36±0.07
DL (wt%)	0	4.3 ± 1.2	19.5 ± 2.3	23.5 ± 3.8	26.5 ± 6.6

Table 2 shows that the measured drug:polymer mass ratios in the NPs are higher than the ones used for their preparation. This could be explained by the fact that during NP formation part of the polymer precipitated without forming NPs and did not entrap the drug. Whereas the precipitates were easily removed, because of polymer loss, the measured drug:polymer mass ratios in the NPs were higher than the ones used in the preparation step. The “bulk” DLs of the NP formulations, calculated according to **equation 2**, increased from 4.3 to 26.5 wt% with the drug:PLA mass ratio used for their preparation (**Table 2**). Noteworthy, as precipitates were formed during NP formation, the data altogether question about the homogeneity of the NPs and point out the interest to investigate and determine the drug loading of individual NPs within a formulation, using AFM-IR. Before achieving this goal, the proof of concept of quantification from AFM-IR measurements was established on drug-PLA films with known compositions and proven to be homogeneous by IR microspectroscopy.

2.5. AFM-IR calibration curve using drug-PLA films

Quantify drug loading at the single nanoparticles level using AFM-IR technique: a convenient method to map and evaluate the drug distribution

The aim here was to establish the comparability between quantitative conventional IR microspectroscopy and AFM-IR, using the drug-PLA films; F(0); F(0.03); F(0.10); F(0.15) and F(0.20).

Two main goals were pursued. First, the homogeneity of films was probed with the nanometric AFM resolution, to check if the analysed regions of interest are representative of the whole sample. To do so, 150 local absorption spectra were recorded in three different locations on each of the five investigated films. The IR intensities of both PLA and drug fingerprints were analysed and compared. Second, it was important to determine the sample thickness range in which quantification could be carried on by AFM-IR. For too thin samples, the information could be at the limit of detection due to a low signal-to-noise, thus not allowing an accurate analysis. On the other hand, if the sample is too thick, the AFM-IR information might arise only from the part of the sample probed and not the whole sample due to the penetration depth of the detection, and this can lead to misinterpretations of the sample overall composition.

Previous quantifications of film compositions by AFM-IR were all carried on in contact mode with a bottom up configuration^[25,26], and the AFM-IR signal was proven to be linear up to about 1 μm sample thickness.^[26,31,32] However, contact mode and bottom up illumination were shown to be inadequate for NP investigation.^[20] It was of main interest to investigate here for the first time the possibility to quantify sample composition by AFM-IR in the tapping mode and using the top down illumination.

Films were casted with thicknesses lower than 500 nm, in order to cover the range of NP's thickness. Special attention was given to the analysis of regions of the film which offered an extended range of thicknesses, increasing progressively but not sharply. In addition, films with a wide range of compositions were analyzed in order to study the relationship between the AFM-IR signal and the relative concentration of each of their

Quantify drug loading at the single nanoparticles level using AFM-IR technique: a convenient method to map and evaluate the drug distribution

components. Indeed, a linear relationship is a requirement for quantitative analysis by AFM-IR.

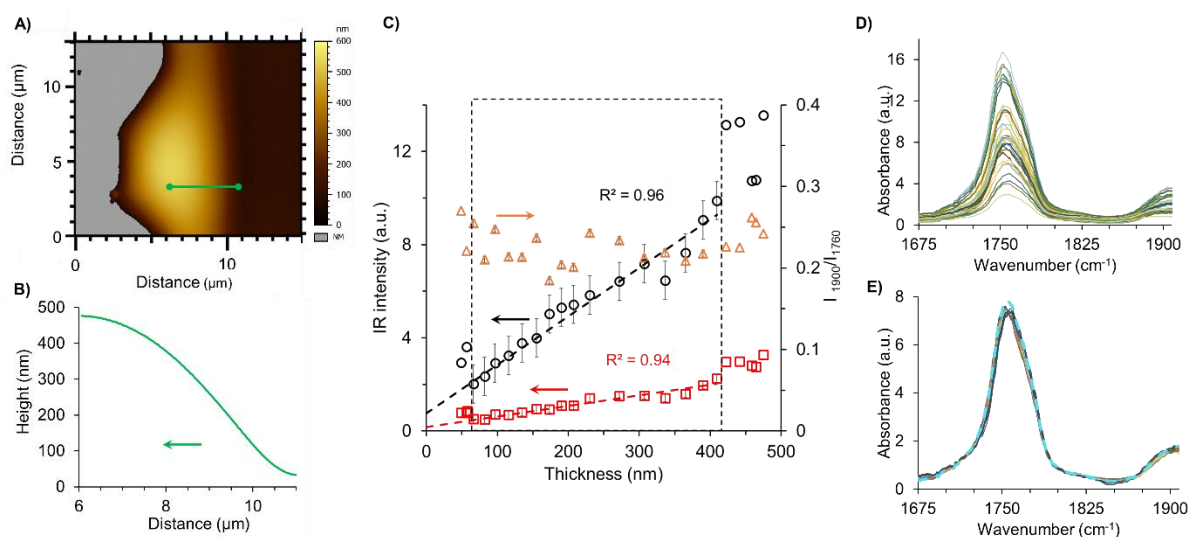


Figure 6. A) AFM topography image of F(0.15). Green line shows the measured spectral line map of 5 μm length. Grey regions represent the substrate (signal below the threshold). B) Height profile of the studied region. C) IR intensities at 1760 (black) and 1900 cm^{-1} (red) collected from 23 local spectra on the green line with spatial intervals of 200 nm, and plotted as a function of film thickness. Intensity ratios (1900 to 1760 cm^{-1} ie I_{1900}/I_{1760}) are plotted on the secondary Y axis (orange). D) 23 local IR spectra recorded on the film in the topography image shown in **A** across the 5 μm region with 200 nm steps. E) Normalized local IR spectra and mean spectrum of spectra (blue dashed line). The AFM-IR working range was in between 1675 and 1908 cm^{-1} as detailed in materials and methods (section 4.8).

Figure 6 summarizes the strategy pursued for the analysis of films focussing on the example of F(0.15). The AFM topography image was recorded at the edge of the film to study the IR signal as a function of the thickness (**Figure 6A**). Local spectra acquisition was performed on a region of 5 μm length represented by the green line on the topography.

Quantify drug loading at the single nanoparticles level using AFM-IR technique: a convenient method to map and evaluate the drug distribution

The corresponding analysed height profile shown in **Figure 6B** shows that the minimum and maximum film thickness were 35 nm and 425 nm, respectively. The IR intensity values of PLA (1760 cm^{-1}) and drug (1900 cm^{-1}) were plotted in function of the film thickness in **Figure 6C, D**, revealing that the intensity values increase linearly with the sample thickness in the region from 60 to 420 nm sample thickness. The deviation from the linearity below 60 nm was related with the electromagnetic enhancement induced by gold-coated cantilevers (tip) which may prevail for the lowest thickness. Gold tips is mandatory in the top-down illumination to limit self-absorption of the AFM probe and the induced enhancement is not critical for sample which thickness above 100 nm. However the use of thin samples has been shown to lead to non-linearity in the signal intensity as well as possible artefacts during the analysis. ^[33,34] The ratio of the two carbonyl intensities (PLA and drug) plotted in a secondary axis (orange circles) in function of the thickness (**Figure 6C, D**), showed constant values at around 0.22 ± 0.02 . This clearly indicates the homogenous distribution of both drug and PLA within the film.

In a nutshell, these investigations allowed to keep track on the linearity of the IR intensities of both drug and polymer as a function of the sample thickness up to 420 nm, thus setting the ground of our approach.

Typical local spectra collected along the studied film (**Figure 6A**) were plotted in **Figure 6D**, showing as expected, characteristic peaks of both PLA and the drug, at 1760 cm^{-1} and 1900 cm^{-1} , respectively. Normalization of the spectral profiles as shown in **Figure 6E** reveals the self-similar nature of these curves that is also a signature of the homogeneity of each analysed region. When the mean spectrum was plotted, as shown in **Figure 6E**, it was observed that the mean peak intensity corresponding to the polymer was roughly 5 times that of the drug. This further corroborates our previous observation of the ratio of intensity profiles plateauing at a value of 0.22 ± 0.02 (**Figure 6C**).

Quantify drug loading at the single nanoparticles level using AFM-IR technique: a convenient method to map and evaluate the drug distribution

The same methodology was applied for all the films. **Figure 7A** shows mean spectra of the five films F0-F0.20, normalized to the PLA carbonyl band. The intensity of the drug carbonyl band at 1900 cm^{-1} increases with the drug concentration. For each studied film, the ratio of the intensities of the carbonyl bands of the drug peaking at 1900 cm^{-1} and the PLA one at 1760 cm^{-1} was plotted against the $m_{\text{drug}}/m_{\text{PLA}}$ mass ratio (**Figure 7B**). A linear fit was obtained with a correlation coefficient $R^2 = 0.98$. Nevertheless, the most significant inference from **Figure 7B** is the observed linearity between intensity ratios and the concentration, thereby enabling us to perform a quantitative analysis based on intensity ratio measurements, in the sample thickness range from 60 to 420 nm.

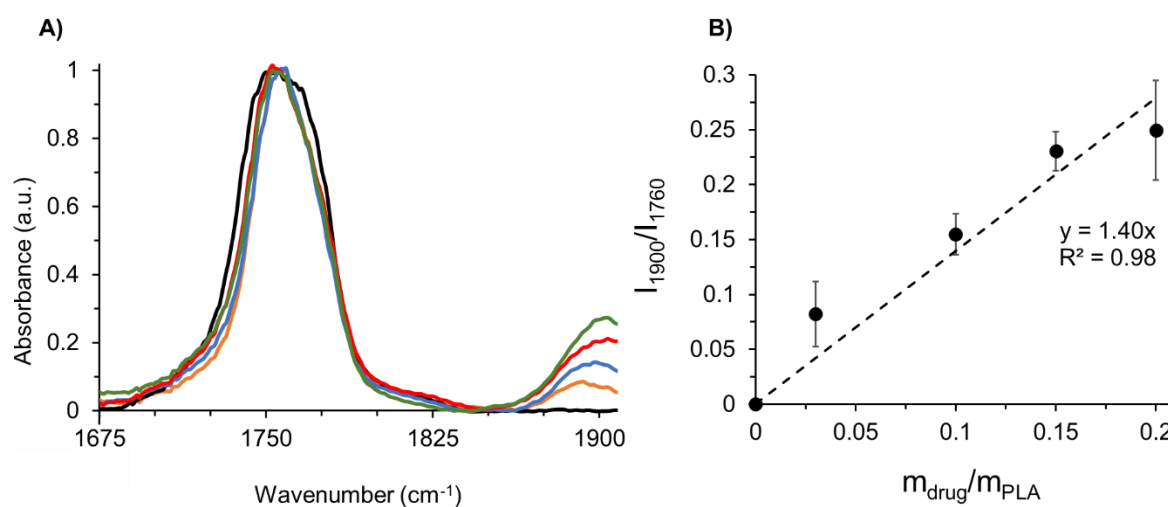


Figure 7. A) Normalized mean spectra of films analysed by AFM-IR; F0 (black), F(0.03) (orange), F(0.10) (blue), F(0.15) (red) and F(0.20) (green). **B)** A linear curve was derived by the ratiometric analysis of the respective PLA and drug band intensities obtained by AFM-IR as a function of the $m_{\text{drug}}/m_{\text{PLA}}$ mass ratio. The AFM-IR working range was in between 1675 and 1908 cm^{-1} as detailed in materials and methods (section 4.8).

Quantify drug loading at the single nanoparticles level using AFM-IR technique: a convenient method to map and evaluate the drug distribution

The proof of concept can now be completed with a comparative analysis of the two techniques (quantitative IR-microspectroscopy and AFM-IR) with respect to their calibration curves (**Figure 4B** and **Figure 7B**). As listed in **Table SI1**, the ratio of the drug:PLA areas in IR-microspectroscopy were 0, 0.03, 0.05, 0.08 and 0.12 for F(0); F(0.03); F(0.10); F(0.15) and F(0.20), respectively with a slope of 0.57. In the case of AFM-IR, the slope of the fitting curve equals to 1.40, and the drug:PLA areas values for the same films were 0.08, 0.15, 0.23, 0.25 respectively. This reveals a scale factor of 2.7 ± 0.5 between the two techniques, where the AFM-IR values are larger than ones of IR-microspectroscopy. Same scale factor was driven as well from the comparison of slopes of the two calibration curves obtained by AFM-IR and IR microspectroscopy (**Table SI1**).

This scale factor was subsequently implemented to rescale AFM-IR spectra of each film. The rescaled AFM-IR spectra were overlaid with those of IR-microspectroscopy. This comparison was represented in **Figure 8A** for the case of F(0.15) and in **Figure SI3** for each film. Remarkably, the spectra from the two techniques could be well superimposed. (**Figure 8E**). Taking into account this scaling factor, the IR microspectroscopy calibration curve (**Figure 4B**) can be used for quantification by AFM-IR.

On the ground of good agreement between the AFM-IR and IR microspectroscopy investigations, the next step was to perform the quantitative analysis on the NPs.

Quantify drug loading at the single nanoparticles level using AFM-IR technique: a convenient method to map and evaluate the drug distribution

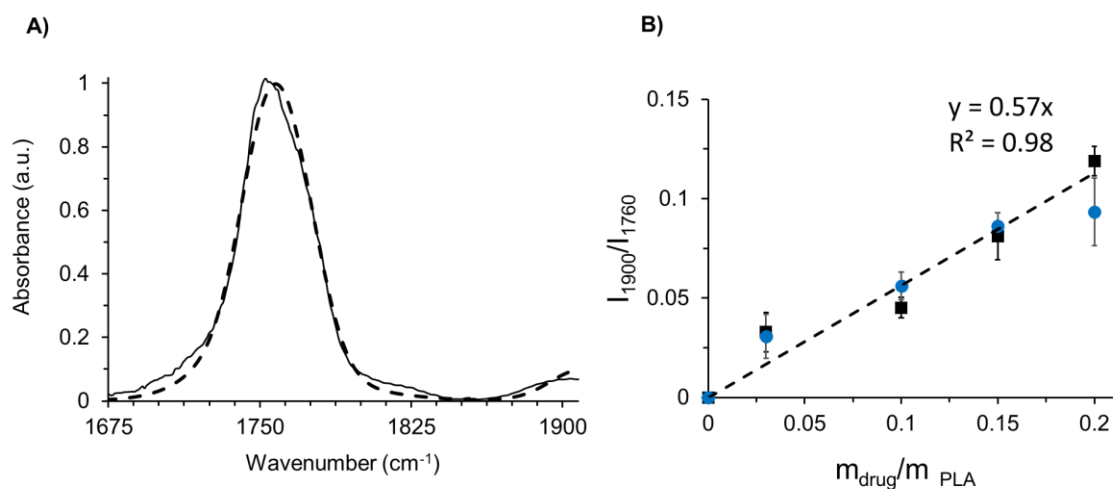


Figure 8. Comparison of A) AFM-IR spectra (solid line) to IR-microspectroscopy spectra (dashed lines) of F(0.15) B) data set and calibration curve obtained from IR microspectroscopy (black) in comparison to AFM-IR (blue) data set of the same films. A scaling factor of 2.7 was applied to AFM-IR data. The AFM-IR working range was in between 1675 and 1908 cm⁻¹ as detailed in materials and methods (section 4.8).

2.6. Methodology for quantitative analysis of individual NPs by AFM-IR in tapping mode

Following the demonstrated proof of concept and the correlation between the two techniques, IR microspectroscopy and tapping AFM-IR, we present here the methodology to perform quantitative analysis of the local DL on individual NPs by using any of the two acquisition modes in AFM-IR: local IR absorption spectra or IR map.

As an example, **Figure 9** shows the case of the NP formulation NP(0.20). The topography image (**Figure 9A**) was recorded on a 5 μm x 5 μm area. The NPs sizes ranged from 200 to 500 nm, in agreement with DLS and TEM investigations. **Figure 9B** presents the local IR spectra on different individual NPs. The absence of signal on the support (orange arrow,

Quantify drug loading at the single nanoparticles level using AFM-IR technique: a convenient method to map and evaluate the drug distribution

Figure 9B) clearly shows that the drug was only associated to the NPs and that no residual polymer was on the support.

The ratio of the intensities of the drug and PLA IR bands (I_{1900}/I_{1760}) were calculated from the NPs' local IR spectra (**Figure 9B**). The drug:PLA mass ratios were calculated from the calibration curve equation established by IR microspectroscopy (**Figure 4B**). Mass ratios were then converted to DLs by using **equation (2)**. For the four randomly chosen NPs, the DL were 4 % (violet arrow, NP of around 390 nm), 10 % (grey arrow, NP of 300 nm), 21 % (red or green arrows; NP of 425 nm) and 10% (black arrow; NP of 570 nm). The DL differed strikingly from one NP to another (4; 10; 21 %). However, the DLs measured on the same NP in two points were consistent (21 %, red and green arrows).

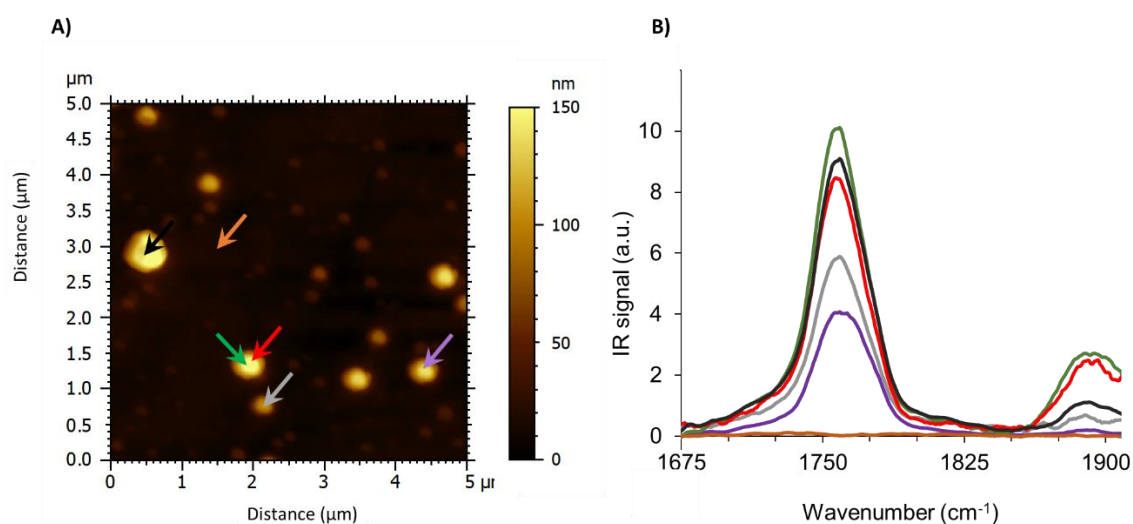


Figure 9. A) Topography image of NPs. B) Local IR absorption spectra of NPs and background recorded on the regions of interest indicated with arrows in A. Orange arrow presents the analysis on the region without NP. The AFM-IR working range was in between 1675 and 1908 cm^{-1} as detailed in materials and methods (section 4.8).

Quantify drug loading at the single nanoparticles level using AFM-IR technique: a convenient method to map and evaluate the drug distribution

Interestingly, the NP size and the DL do not correlate. It can be hypothesized that the large heterogeneities in DLs (factor of 5) are due to a random segregation between the drug and the polymer occurring in the process of NP formation. Indeed, the NP preparation involves a dispersion step, consisting in pouring a drug-polymer organic solution in water. Immediately after, the common solvent of the drug and the polymer diffuse in the aqueous dispersion medium. As a consequence, the polymer precipitates under the form of NPs, while aggregates are also formed. This nanoprecipitation process has been deeply studied and it was found that NP and aggregate formation is strongly correlated to the experimental conditions and the physicochemical properties of both the drug and polymer.^[35] Possibly, the large DL heterogeneities observed here are related to affinity differences between the drug and the polymer, leading to phase separation at the nanoscale during the rapid nanoprecipitation process. To the best of our knowledge, this is the first report of large discrepancies in terms of individual NP composition. Moreover, these differences are not related to the NP diameters.

Drug quantification using the IR absorbance spectra provides very precise, local quantitative analysis on a region of around 10-15 nm depending on the AFM tip. However, the investigation of a large number of NPs to provide statistically relevant data is time consuming. Therefore, an alternative method was developed here, based on the capability of AFM-IR to perform IR maps of both drug and PLA, at the wavenumbers corresponding to the "fingerprints" of these compounds. AFM-IR provides access to the IR intensity in any point on the maps. Then, by dividing the maps or by performing ratiometric analysis of the displayed IR intensities on specific regions, DL can be assessed in any point. The method has the advantage of providing information over large regions, thus allowing analysing simultaneously a large number of NPs.

Quantify drug loading at the single nanoparticles level using AFM-IR technique: a convenient method to map and evaluate the drug distribution

To validate this approach, a direct transposition from local spectrum to map was needed. Therefore, the strategy was to compare the initial local AFM-IR spectra at a specific point with the reconstructed IR spectra from a series of IR maps. To do so, at first, local IR spectra were recorded on 11 different points on an individual NP (**Figure 10A**). When normalized, all the 11 local spectra were well overlapped and their average spectra (represented in red curve in **Figure 10C**) was further used. Then, a series of 23 IR maps (in the spectral range between 1670 and 1920 cm^{-1} details see method section) was recorded on the region containing the same NP. These studies allowed measuring the IR intensities of randomly chosen points on the NP.

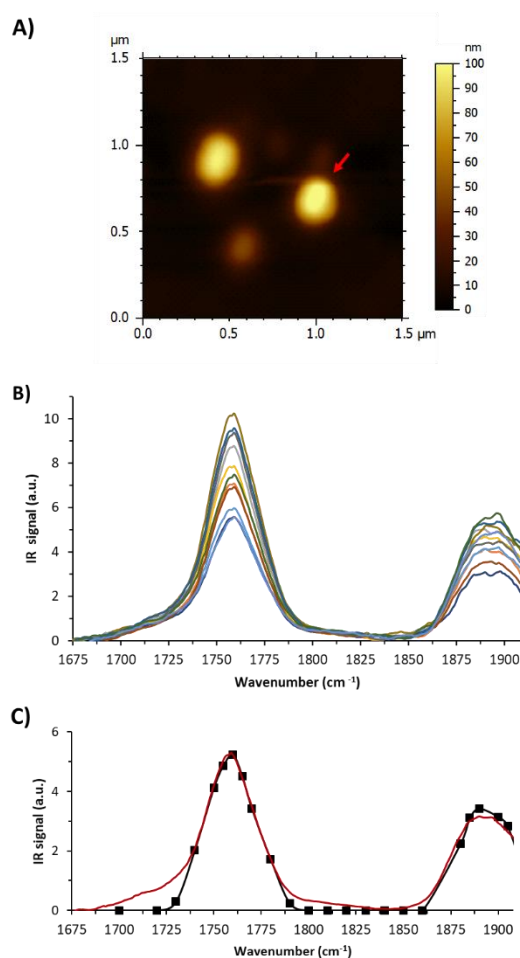


Figure 10. A) Topography image of drug-loaded NPs. One NP (indicated with an arrow) was chosen. B) Local IR spectra recorded by AFM-IR on 11

Quantify drug loading at the single nanoparticles level using AFM-IR technique: a convenient method to map and evaluate the drug distribution

randomly chosen positions on this NP. C) Overlay of the average spectrum of the 11 local IR spectra recorded by AFM-IR (red line) and the reconstructed IR profile (black line) from the 23 IR maps series (precisely at 1700, 1720, 1730, 1740, 1750, 1755, 1760, 1765, 1770, 1780, 1790, 1800, 1810, 1820, 1830, 1840, 1850, 1860, 1880, 1885, 1890, 1900 and 1905 cm^{-1}). 3 reconstructed spectra were obtained from randomly chosen locations (on the chosen NP) and averaged. The AFM-IR working range was in between 1675 and 1908 cm^{-1} as detailed in materials and methods (section 4.8).

From each IR map recorded, the IR intensities of a selected point were retrieved. Then, the local IR spectra were obtained by plotting the intensity values against their corresponding wavenumbers. After recording the local spectra of three different points on the same NP, average data for each wavenumber are shown as black squares in **Figure 10C**.

The resulting average local spectrum extracted from the maps (black line in **Figure 10C**) was well superimposed to the high resolution measured spectra at specific positions (red line in **Figure 10C**), which validates that a quantitative study can be made simply by recording a series of IR map. Eventually, from these average local spectra, intensities of the carbonyl bands were determined to calculate the drug:PLA mass ratio from the calibration curve equation (scale factor was used). The DL was calculated as 28 ± 6 wt%.

The same NP was further analysed focusing on IR maps. Its topography image represented in **Figure 11A** reveals the NP size of around 320 nm and height of 90 nm (**Figure 11B**). IR maps recorded at 1760 cm^{-1} and 1900 cm^{-1} (**Figure 11C, D**) revealed the location of both the polymer and the drug, although a lack of intensity with a crescent shape was observed in the upper part of the NP. This phenomenon, previously reported for PLA

Quantify drug loading at the single nanoparticles level using AFM-IR technique: a convenient method to map and evaluate the drug distribution

NPs, was associated with a phase shift during the contact between the tip and the NPs in tapping AFM [24,36].

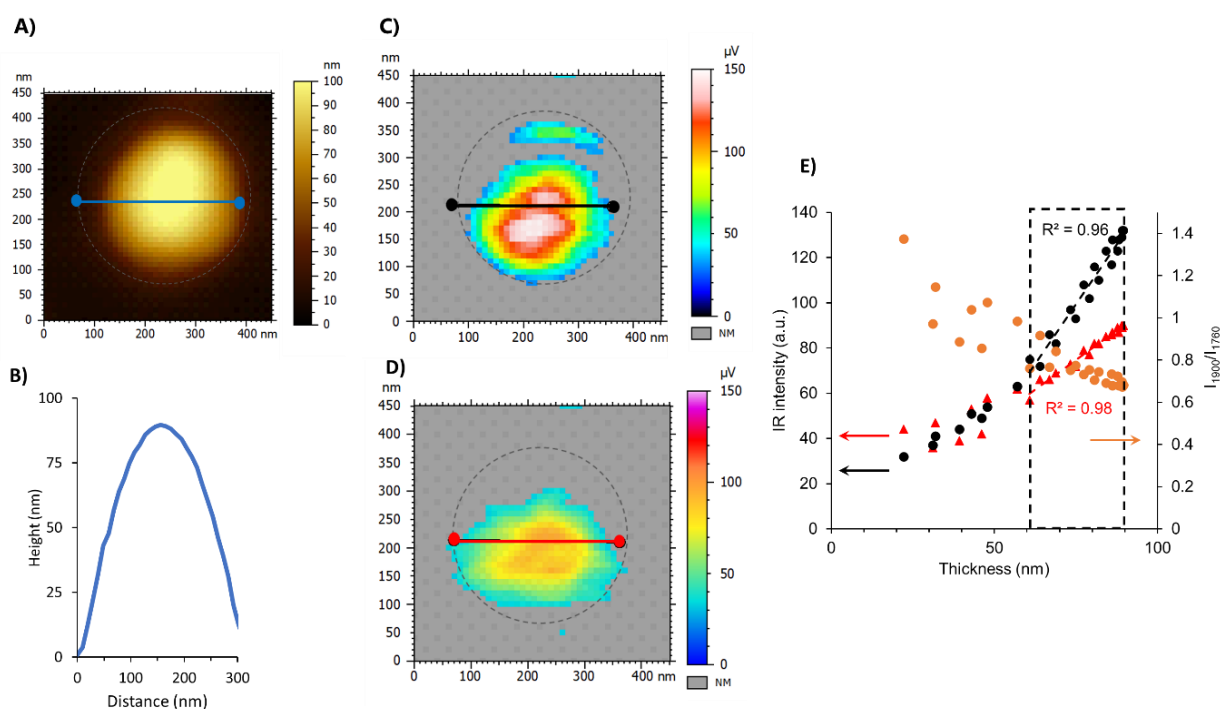


Figure 11. A) AFM topography image of a single NP. B) Height profile of the NP recorded on the blue line C) IR map recorded at 1760 cm^{-1} and D) 1900 cm^{-1} to detect PLA and the drug, respectively. E) IR intensity profile at 1760 cm^{-1} (PLA, black) and 1900 cm^{-1} (drug, red) and the ratios of IR intensities ($1900\text{ to }1760\text{ cm}^{-1}$) (orange) recorded on the line as a function of thickness of NP and plotted on the secondary Y axis. Grey regions represent the AFM support (signal below the threshold). The AFM-IR working range was in between $1675\text{ and }1908\text{ cm}^{-1}$ as detailed in materials and methods (section 4.8).

Intensity profiles were extracted through the line scan on the NP (black and red line **Figure 11C-D**) and plotted against thickness (**Figure 11E**). The evolutions of the intensity profiles at 1760 cm^{-1} (black) and 1900 cm^{-1}

Quantify drug loading at the single nanoparticles level using AFM-IR technique: a convenient method to map and evaluate the drug distribution

(red) suggested the proportionality of IR intensity with thickness. Both intensities were linear ($R^2 \geq 0.96$) when the thickness was above 60 nm, in good agreement with the lower limits found in the proof of concept. The ratios of the intensities at 1908 to 1760 cm^{-1} were calculated showing a constant value of 0.74 ± 0.06 except at the borders of the NP (orange dots **Figure 11E**). This is an indication of the good homogeneity of the NP in terms of composition. The deviations observed at the edges of the NP are most probably due to reaching the limits of AFM-IR detection, as shown in proof of concept. Noteworthy, the constant value of 0.74 ± 0.06 was the average of 17 measurements, above the thickness threshold of 60 nm. The corresponding DL was then calculated and obtained as $32 \pm 6\%$. This value is in line with the DL calculated by local IR spectra ($28 \pm 6\text{ wt\%}$, **Figure 10**) emphasizing the accuracy of the proposed quantification method.

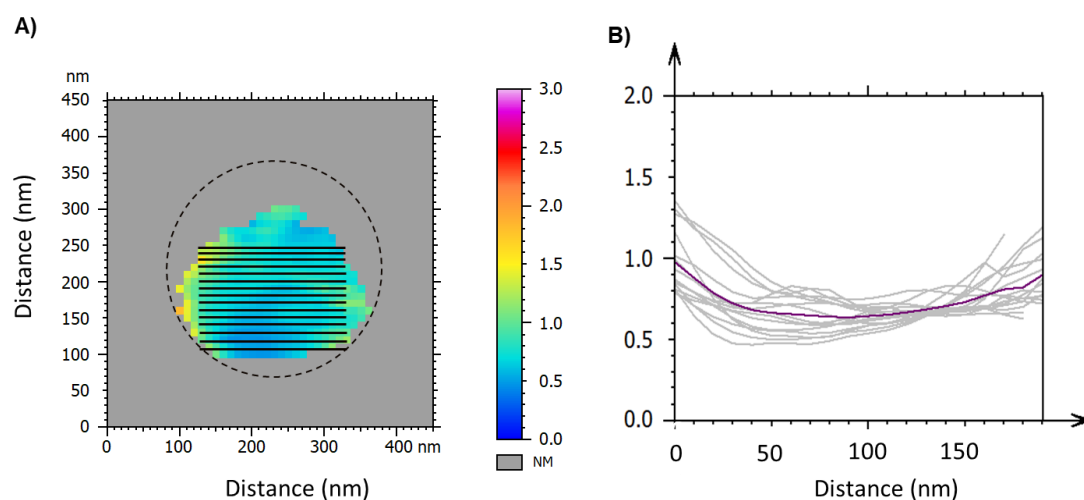


Figure 12. A) Ratio of the IR maps recorded at 1900 cm^{-1} (drug) to the one at 1760 cm^{-1} (polymer) as shown in Figure 11D and 11C, respectively. Detailed profile analyses were performed along a distance of 200 nm on 15 different regions represented in black lines on the NP. B) The ratio of intensities (1900/1760) was recorded from the 15 profile analysis (A), as a function of distance. Each grey curve represents one profile analysis and the average curve is shown in purple.

Quantify drug loading at the single nanoparticles level using AFM-IR technique: a convenient method to map and evaluate the drug distribution

The next step consisted of a complementary study, where 15 profile analyses were carried on the NP' ratio map (1900/1760) as shown in **Figure 12A**. The ratio map appeared to be almost constant. The ratios of intensity profiles were recorded on the black lines and plotted as a function of distance (200 nm) in **Figure 12B**. A linear trend was obtained for each analysed profile, which suggests the NP's overall homogeneity. Noticeably, the calculated ratios of intensities were around 0.7, as the violet line represents the average profile that is in close agreement with the above findings (average of 0.74 ± 0.06 , **Figure 11E**).

Finally, here we show the simple protocol proposed in this study for the local quantitative analysis of a large set of individual NPs. Topography image was recorded (**Figure 13A**) while simultaneously acquiring chemical maps by illuminating the sample with the laser at 1760 cm^{-1} (**Figure 13B**) and at 1900 cm^{-1} (**Figure 13C**), to detect the PLA polymer and the drug, respectively.

Quantify drug loading at the single nanoparticles level using AFM-IR technique: a convenient method to map and evaluate the drug distribution

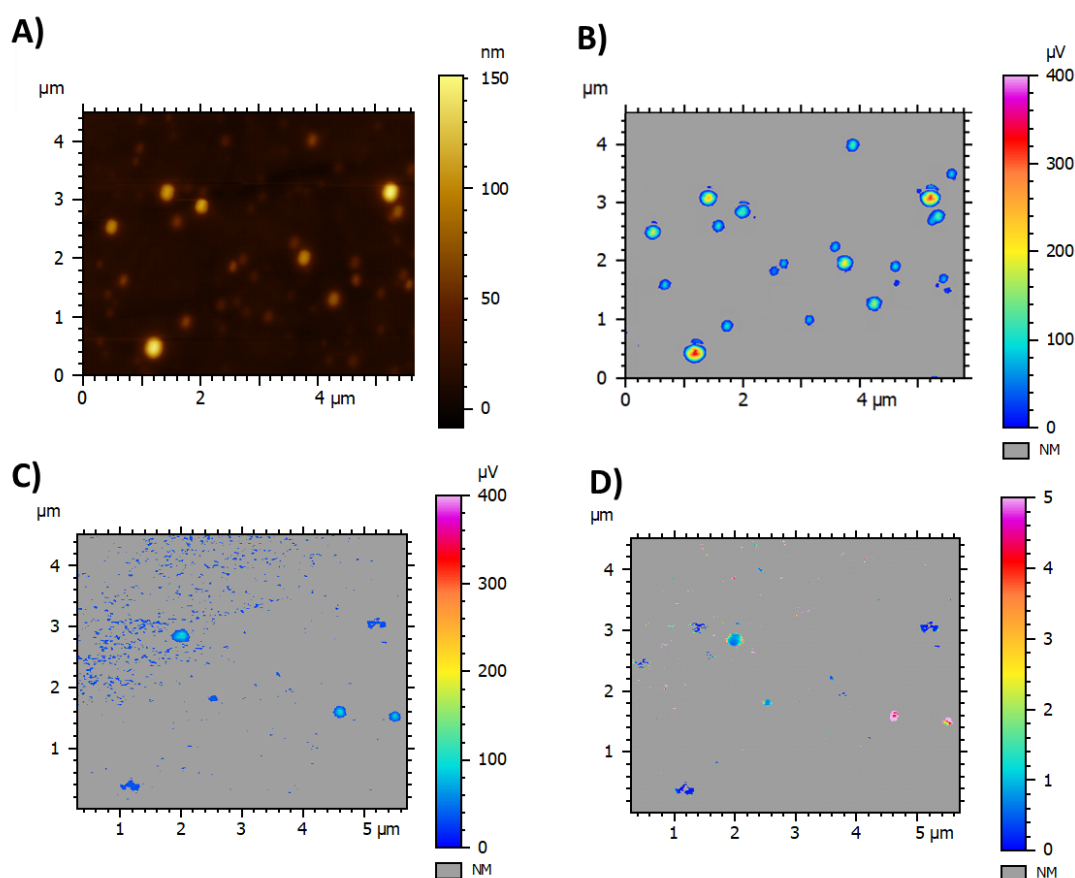


Figure 13. A) AFM topography image of NP(0.20). IR maps recorded by AFM-IR at B) 1760 cm⁻¹ and C) 1900 cm⁻¹ to detect the polymer and the drug, respectively. D) Ratio of the IR maps recorded at 1900 cm⁻¹ (drug) to the one at 1760 cm⁻¹ (polymer).

The IR map at 1760 cm⁻¹ displays the location of the polymer, thus the NPs. While the NPs appear to vary in size (80 to 370 nm), even the tiniest ones could be detected in the IR PLA map (**Figure 13B**) with regard to the topography image (**Figure 13A**). Map at 1900 cm⁻¹ revealed however, that only few of the NPs contain the drug (**Figure 13C**). This clearly points out the chemical heterogeneity among the NPs arising during the NP formulation and emphasizes the interest of performing NP characterization individually. Simply by the ratio of two IR maps, a statistical analysis on over 20 individual NPs was performed overcoming

Quantify drug loading at the single nanoparticles level using AFM-IR technique: a convenient method to map and evaluate the drug distribution

the slowness of the spectral analysis. Results showed that only 9 of the NPs were loaded, in which the DLs varied from 10 to 90 wt% with no dependence on the NP size. We hypothesized that the discrepancies in terms of NP DLs were due to their fast precipitation in the preparation process, inducing drug/polymer segregation. Since NP function is tightly regulated by the physicochemical properties bestowed by their composition, such significant DL variations could render only a low fraction of the NPs therapeutically active. While heterogeneities in terms of sizes of NPs obtained by nanoprecipitation were widely reported, up to our knowledge, this study presents for the first time large heterogeneities in terms of drug content in individual polymeric NPs.

3. Conclusion

A stringent correlation was proven between IR microspectroscopy and AFM-IR in tapping mode with a top-down illumination. A correlation between these two techniques was shown, enabling to perform quantitative chemical analysis by AFM-IR in tapping mode with a top down illumination at a specific location with AFM resolution. The method was shown to be robust, as calibrations of IR intensities of both components of the studied NPs (drug and polymer), determined by two different methods, showed no statistical differences. By performing local AFM-IR on an individual NP, it was possible to investigate its chemical homogeneity at nanoscale (10-20 nm) and to calculate its drug mass fraction within 60 to 420 nm sample thickness.

An important finding here was to evidence huge heterogeneities in terms of individual NP composition, by contrast to films prepared using the same components which were found to be homogeneous.

These studies proved the usefulness of AFM-IR in nanomedicine, by enabling a precise chemical analysis and quantification at the nanoscale. We believe that these findings go steps beyond the commonly used

Quantify drug loading at the single nanoparticles level using AFM-IR technique: a convenient method to map and evaluate the drug distribution

characterization methods, by affording new tools to better understand the supramolecular organization of NPs and their composition with a nanometric resolution. The methodology proposed here can set up the ground towards quality assessment of drug nanocarriers. Moreover, it could also help understanding the NP formation process and help optimizing the formulations protocols.

Further studies will comprise AFM-IR investigations of other type of NPs such as hybrid organic-inorganic ones and more complex hybrid structures resulting from the association of polymeric and metal NPs. It is worth investigating the limits of the methods in terms of minimal NP size that can be analysed as a function of the nature of the materials that are used. Furthermore, the analysis spectral domain of AFM-IR could be enlarged given that novel lasers can be employed, opening the way to study a larger set of available drugs and polymers.

4. Materials and methods

4.1. Chemicals

PLA acid terminated (MW: 6-10 KDa, EXPANSORB® 10P006) was kindly donated by Sequens (Expansorb, Aramon, France). Poly (vinyl alcohol) (PVA) (30000-70000 g/mol, 88% hydrolyzed), $\text{Re}(\text{CO})_5\text{Cl}$, cyclohexane and acetone were purchased from Sigma-Aldrich and used as received.

Calcium fluoride (CaF_2) optical windows used as AFM-IR substrates were purchased from Crystal GmbH (Germany). AFM-IR cantilevers (Multi75GB-G, $f=75$ kHz 3N/m) were supplied from Budget Sensors (Germany). Eppendorf™ membrane filters (0.45 μm) were used to remove precipitates from NP suspensions.

4.2. Drug synthesis and characterization

Quantify drug loading at the single nanoparticles level using AFM-IR technique: a convenient method to map and evaluate the drug distribution

The Re(I) tricarbonyl-diselenium drug was synthesized, as previously reported, by reacting the commercially available $\text{Re}(\text{CO})_5\text{Cl}$ with a selenium containing ligand.^[37] Briefly, $\text{Re}(\text{CO})_5\text{Cl}$ (0.154 g, 0.43 mmol) was added to the solution of 3,7-diselena-nonanedioic acid (0.135 g, 0.43 mmol) in 15 ml of THF. After stirring at reflux overnight THF was removed under reduced pressure, and the drug was recovered as a white powder. Yield: 0.240 g (90%); MS (positive mode): 589 ($[\text{M} - \text{Cl}]^+$); IR: 3330-2340 (m), 2029 (s), 1935 (s), 1895 (s), 1731 (s), 1699 (s), 1415 (m), 1351 (m), 1282 (m), 1249 (m), 1206 (s), 1186 (m), 1092 (m), 834 (m), 785 (m), 752 (m), 670 (m), 637 (m), 624 (s), 605 (m) cm^{-1} ; ^1H NMR (CD_3OD): δ 2.6-3.9 (m, 10 H); *Anal.* Calc. for $\text{C}_{10}\text{H}_{12}\text{O}_7\text{ClSe}_2\text{Re}$: C, 19.25; H, 1.94. Found: C, 19.46; H, 1.97.

4.3. Preparation of drug loaded PLA films

The physical mixtures of PLA and (Re)-based drug were prepared in acetone with drug:PLA mass ratios 0; 0.03; 0.05; 0.10; 0.15 and 0.20. The PLA concentration was 100 mg/mL for all the solutions. The PLA-drug mixtures were vigorously stirred overnight at room temperature to achieve complete dissolution. Then, 15 μL of each solution were casted onto glass plates and the solvent was allowed to evaporate overnight at room temperature. Translucent, homogeneous films were thus obtained and named according to their drug:PLA mass ratios as F(0); F(0.03); F(0.10); F(0.15) and F(0.20). They were further analysed in IR microspectroscopy. For AFM-IR studies, films were prepared and analysed directly on CaF_2 windows. To do so, the previous PLA-drug mixtures were diluted ten times in acetone and 5 μL of these solutions were casted and spread on the CaF_2 windows, followed by complete solvent evaporation.

4.4. Preparation and characterization of drug loaded PLA NPs

Drug-loaded PLA NPs were prepared by nanoprecipitation. Briefly, 0.5 mL of drug-PLA mixtures (drug:PLA mass ratios of 0; 0.03; 0.05; 0.10; 0.15 and 0.20) was added drop-wisely into 5 mL of 0.5% PVA aqueous solution

Quantify drug loading at the single nanoparticles level using AFM-IR technique: a convenient method to map and evaluate the drug distribution

under continuous vigorous magnetic stirring. The rapid solvent diffusion in the aqueous phase led to instantaneous precipitation of the polymer to form NPs. The organic solvent was evaporated at room temperature under gentle magnetic stirring. Control NPs were prepared under the same conditions except that no drug was added. Resulting NPs were named as NP(0); NP(0.03); NP(0.10); NP(0.15) and NP(0.20), according to the drug:PLA mass ratios used in their preparation. NP suspensions were filtrated through a cellulose 0.45 μm membrane to remove precipitates. These NPs were stored at 4°C. All formulations were prepared at least in triplicate.

DL, a commonly used term to describe drug quantity in drug delivery systems, was defined as the mass fraction of NPs that is composed of drug and was determined according to following equation **(1)**:

$$DL (\text{wt}\%) = \frac{\text{mass of drug in the NP}}{\text{mass of NP}} * 100 \quad (1)$$

where *mass of NP* refers to sum of the masses of drug and PLA. Therefore, if *m* is the drug:PLA mass ratio in the NPs, DL was represented as **(2)**:

$$DL (\text{wt}\%) = \frac{m}{m+1} * 100 \quad (2)$$

The NP average hydrodynamic diameter was determined by DLS at 25 °C with an equilibration time of 60 s using a Zetasizer® (Nano ZS90, Malvern Instruments, Worcestershire, UK). All formulations were measured at least in triplicate. Mean diameters were reported as Z Average (nm) \pm SE (Standard Error) with the polydispersity index (PdI). The NPs mean diameters were monitored during three months of storage at 25 °C.

4.5. TEM

TEM images of NPs were acquired using a JEOL electron microscope (JEM 100 CX II, operating at 120 kV) equipped with an US1000 2kx2k camera

Quantify drug loading at the single nanoparticles level using AFM-IR technique: a convenient method to map and evaluate the drug distribution

(Gatan). To do so, 5 μ L of samples were deposited onto a 400 mesh carbon-coated copper grid beforehand treated with a glow discharge (easiGlow, Ted Pella Inc).

4.6. ATR-FTIR spectroscopy

ATR-FTIR spectra of pure drug, PLA and PVA were obtained by using a Fourier Transform Bruker Vertex 70 spectrometer (MCT detector, cooled down using liquid nitrogen) and an ATR module (PIKE MIRacle crystal plate diamond ZnSe). Spectra were recorded in the 4000–600 cm^{-1} range with an accumulation of 100 scans and a spectral resolution of 4 cm^{-1} .

4.7. IR microspectroscopy

IR microspectroscopy measurements were recorded on a Nicolet Continuum infrared microscope (Thermo Fisher Scientific) equipped with a liquid nitrogen cooled MCT detector, with a x32 objective. Spectra were recorded in transmission mode covering the 4000 to 650 cm^{-1} energy range. Spectra were acquired by averaging 128 scans and were recorded at 2 cm^{-1} spectral resolution. The aperture dimension on the sample was set to 50 x 50 or 75 x 75 μm , depending on the local homogeneity of the area.

Films and NPs were analysed as bulk. For a reliable quantitative analysis, the thickness of the analyzed samples was carefully optimized and controlled using a diamond compression cell. Smooth and flat samples in the μm thickness range were obtained.

For each sample, at least five independent areas were analysed. Before each analysis, a background spectrum was collected in a clean region of the diamond substrate without sample. The transmittance spectrum was obtained by dividing the sample spectrum by this background. The spectra were extracted in transmittance, and samples thin film interference

Quantify drug loading at the single nanoparticles level using AFM-IR technique: a convenient method to map and evaluate the drug distribution

fringes were baseline-corrected through a spline function generated in the software Origin Pro 8. Then spectra were converted to absorbance.

4.8. AFM-IR

NanoIR-2 (Anasys Instruments, Santa Barbara) in top-down configuration coupled with a multichip QCL source (MIRcat, Daylight Solutions; tuneable repetition rate range of 0–2 MHz; maximal spectral resolution of 0.1 cm^{-1}) covering the range from 890 cm^{-1} to 1945 cm^{-1} of the mid-IR region with a tuneable repetition rate was used in tapping mode. The setup was described previously in details.^[20] The QCL beam was focused onto the gold-coated silicon probe (tapping AFM-IR cantilever, Multi75GB-G, $f=75\text{ kHz}$ 3N/m , Budget Budget Sensors) that avoids the effects linked to IR absorption of the silicon cantilever. Measurements were carried out with the tapping oscillation at the fundamental mode of cantilever and IR absorption was detected using the second mode^[24]. AFM tip was fixed at a specific location to acquire local IR spectra (also line or matrix spectra) by tuning the laser wavenumber with a spectral resolution of 1 cm^{-1} . Topographic images were acquired simultaneously with IR absorption maps at the specific wavenumbers. IR map of single NP was performed at 23 different wavenumbers, precisely at 1700, 1720, 1730, 1740, 1750, 1755, 1760, 1765, 1770, 1780, 1790, 1800, 1810, 1820, 1830, 1840, 1850, 1860, 1880, 1885, 1890, 1900 and 1905 cm^{-1} . They were then analysed using the MountainMap 7.3 software. To each recorded image, a background correction was applied, followed by a Gaussian filtering of 3×3 pixels. Threshold was performed by setting non-measured points to grey. Gold palette was then applied to the final images.

150 local IR spectra were taken for each film in three different locations and were analysed on Orange 3.27.1. Spectra were filtered using the Savitzky–Golay algorithm (2^{nd} order polynomial using 15 points), followed by pre-processing with extended multiplicative signal correction (EMSC)

Quantify drug loading at the single nanoparticles level using AFM-IR technique: a convenient method to map and evaluate the drug distribution

since it deals with variations in the vertical scale and offsets^[38]. Resulting spectra were baseline subtracted on the y-axis in order to set the baseline at zero outside the absorption regions, prior to calculate the intensity band ratios.

4.9. IR Microspectroscopy and AFM-IR data treatment

In order to establish comparability between classical IR-microspectroscopy and AFM-IR spectra, we took into consideration two factors. The first is that the measured AFM-IR bands appeared slightly broader than the FTIR microspectroscopy. A simple broadening correction could enable to superimpose the two carbonyl bands of PLA from both measurements. The C=O band of PLA (at 1760 cm^{-1}) of each measured film was then normalized to unity.

The second consideration was related to the spectral analysis range in AFM-IR. The Quantum Cascade Laser (QCL) used in AFM-IR limits the measurements to about 1908 cm^{-1} , where the laser power starts dropping significantly (**Figure SI1**). The useful spectral acquisition range was thus ended at 1908 cm^{-1} .

To obtain a calibration curve, the intensity ratio I_{1900} / I_{1760} (the intensity of the peaks corresponding to the drug (1900 cm^{-1}) and to the PLA (1760 cm^{-1})) was plotted as a function of drug:PLA mass ratios ($m_{\text{drug}} / m_{\text{PLA}}$).

IR spectra of NP (as bulk) were measured and ratios were evaluated using the intensities of the carbonyl absorption in selected peaks corresponding to PLA and the drug. In this way, the drug:PLA mass ratios in each NP formulation was calculated from the calibration curve, and then converted to the DL (wt%).

Supporting information

Quantify drug loading at the single nanoparticles level using AFM-IR technique: a convenient method to map and evaluate the drug distribution

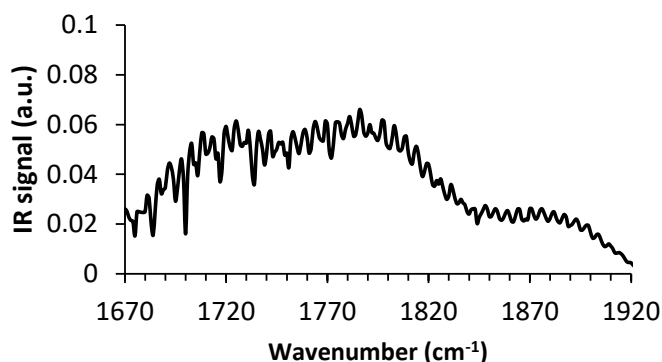


Figure SI 1. Power of QCL laser in function of the wavenumber recorded with a power meter and used as background for the local spectra recorded in AFM-IR

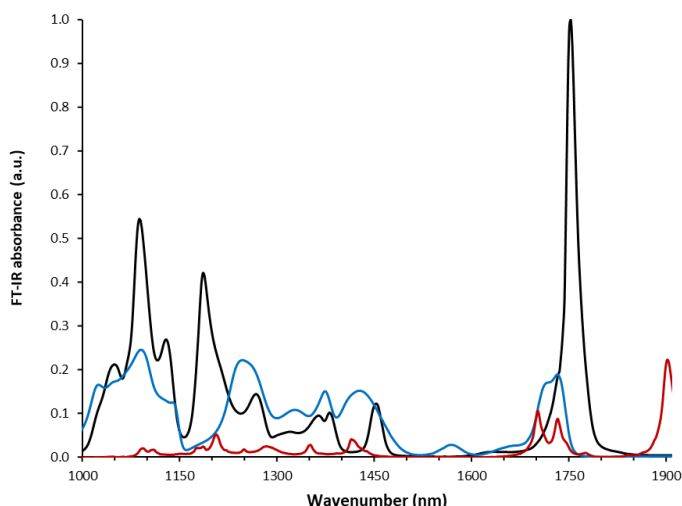


Figure SI 2. ATR-FTIR spectra of the compounds used to prepare films and/or NPs; PLA (black), PVA (blue), drug (red).

PLA has a characteristic CH_3 group appearing at 1068 and 1133 cm^{-1} . The bands at 1090 and 1188 cm^{-1} correspond to the C-O-C ester bond stretching. Furthermore, C-H bending bands are found in the region 1300 - 1500 cm^{-1} . The band at 1760 cm^{-1} was attributed to stretching of the C=O of carboxylic acid group. For PVA, the characteristic absorption bands are

Quantify drug loading at the single nanoparticles level using AFM-IR technique: a convenient method to map and evaluate the drug distribution

identified for C=O at 1724 cm^{-1} , and for CH bending at 1415 cm^{-1} CH₂ wagging was at 1390 cm^{-1} , CH wagging at 1268 cm^{-1} , C-C and C-O-C stretching at 1151 cm^{-1} , C=O stretching at 1106 cm^{-1} and C-O stretching at 1045 cm^{-1} . In addition, C=O of carboxylic acid group of the drug was at 1699 and 1729 cm^{-1} and strong CO stretching bands were found in the region at 1900 cm^{-1} .

Table SI1. Comparison of calibration curves performed with AFM-IR and IR microscopy on the films prepared with known concentrations. Standard deviations are less than 0.01.

Calibration technique	Ratio of intensities (I_{1900}/I_{1760})					Slope
	F(0)	F(0.03)	F(0.10)	F(0.15)	F(0.20)	
IR micro-spectroscopy	0	0.03	0.05	0.08	0.12	0.57
AFM-IR	0	0.08	0.15	0.23	0.25	1.40

Quantify drug loading at the single nanoparticles level using AFM-IR technique: a convenient method to map and evaluate the drug distribution

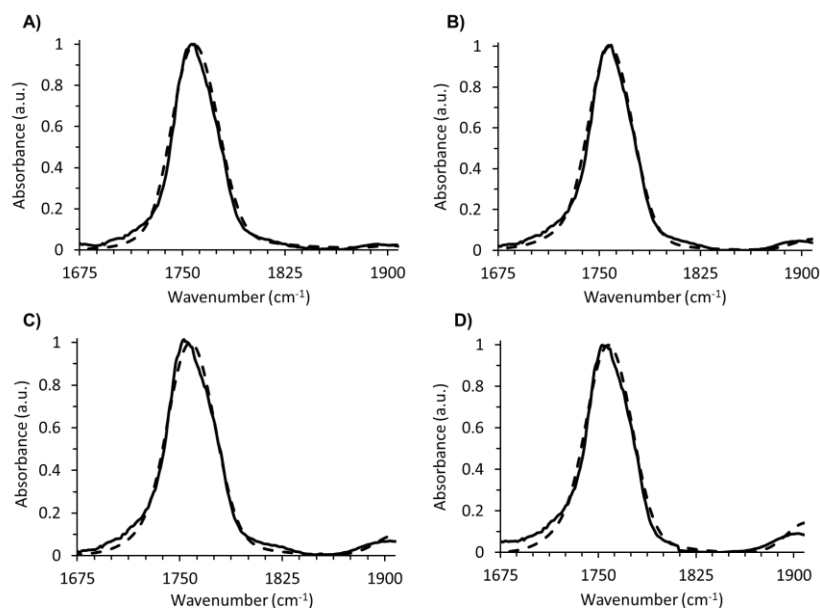


Figure S13. Comparison of AFM-IR spectra (solid line) to IR-Mic spectra (dashed lines) of films A) F(0.03), B) F(0.10), C) F(0.15) and D) F(0.20). A scaling factor of 2.7 was applied to AFM-IR.

Acknowledgements

This research received support from the French National Research Agency (ANR-14-CE08-0017 and ANR-20-CE19-0020) and by Labex NanoSaclay (ANR-10-LABX-0035). The present work has benefited from Imagerie-Gif core facility supported by ANR (ANR-11-EQPX-0029/Morphoscope, ANR-10-INBS-04/FranceBioImaging; ANR-11-IDEX-0003-02/ Saclay Plant Sciences).

Received: ((will be filled in by the editorial staff))

Revised: ((will be filled in by the editorial staff))

Published online: ((will be filled in by the editorial staff))

Quantify drug loading at the single nanoparticles level using AFM-IR technique: a convenient method to map and evaluate the drug distribution

References

- [1] M. J. Mitchell, M. M. Billingsley, R. M. Haley, M. E. Wechsler, N. A. Peppas, R. Langer, *Engineering precision nanoparticles for drug delivery*, Vol. 20, Nature Research, **2020**, pp. 101–124.
- [2] D. Essa, P. P. D. Kondiah, Y. E. Choonara, V. Pillay, *Front. Bioeng. Biotechnol.* **2020**, *8*, 1.
- [3] Z. Li, S. Tan, S. Li, Q. Shen, K. Wang, *Cancer drug delivery in the nano era: An overview and perspectives (Review)*, Vol. 38, Spandidos Publications, **2017**, pp. 611–624.
- [4] Y. Wang, *Am. Pharm. Rev.* **2016**, *20*.
- [5] S. Rezvantalab, N. I. Drude, M. K. Moraveji, N. Güvener, E. K. Koons, Y. Shi, T. Lammers, F. Kiessling, *Front. Pharmacol.* **2018**, *9*, 1260.
- [6] T. L. Andresen, J. B. Larsen, *Acta Biomater.* **2020**, *118*, 207.
- [7] S. M. Stavis, J. A. Fagan, M. Stopa, J. A. Liddle, *ACS Appl. Nano Mater.* **2018**, *1*, 4358.
- [8] J. M. Rabanel, V. Adibnia, S. F. Tehrani, S. Sanche, P. Hildgen, X. Banquy, C. Ramassamy, *Nanoparticle heterogeneity: An emerging structural parameter influencing particle fate in biological media?*, Vol. 11, Royal Society of Chemistry, **2019**, pp. 383–406.
- [9] M. Chaupard, M. de Frutos, R. Gref, *Part. Part. Syst. Charact. Syst. Charact.* **2021**.
- [10] F. Laborda, E. Bolea, J. Jiménezjiménez-Lamana, F. Laborda, **2013**.
- [11] D. Kurouski, A. Dazzi, R. Zenobi, A. Centrone, .
- [12] A. Dazzi, F. Glotin, R. Carminati, *J. Appl. Phys.* **2010**, *107*, 124519.

Quantify drug loading at the single nanoparticles level using AFM-IR technique: a convenient method to map and evaluate the drug distribution

- [13] A. Dazzi, C. B. Prater, Q. Hu, D. B. Chase, J. F. Rabolt, C. Marcott, *Appl. Spectrosc.* **2012**, *66*, 1365.
- [14] A. Dazzi, R. Prazeres, F. Glotin, J. M. Ortega, *Opt. Lett.* **2005**, *30*, 2388.
- [15] A. Dazzi, C. B. Prater, *Chem. Rev.* **2017**, *117*, 5146.
- [16] F. Lu, M. A. Belkin, *Opt. Express, Vol. 19, Issue 21, pp. 19942-19947* **2011**, *19*, 19942.
- [17] M. R. Rosenberger, M. C. Wang, X. Xie, J. A. Rogers, S. Nam, W. P. King, *Nanotechnology* **2017**, *28*, 355707.
- [18] D. Q. M. Craig, G. A. Hill, J. H. Rice, K. Vodopyanov, M. Reading, P. Kuo, S. R. Meech, *Opt. Lett. Vol. 34, Issue 4, pp. 431-433* **2009**, *34*, 431.
- [19] A. Dazzi, R. Prazeres, F. Glotin, J. M. Ortega, *Ultramicroscopy* **2007**, *107*, 1194.
- [20] J. Mathurin, E. Pancani, A. Deniset-Besseau, K. Kjoller, C. B. Prater, R. Gref, A. Dazzi, *Analyst* **2018**, *143*, 5940.
- [21] L. Wang, H. Wang, M. Wagner, Y. Yan, D. S. Jakob, X. G. Xu, *Sci. Adv.* **2017**, *3*, e1700255.
- [22] E. Pancani, J. Mathurin, S. Bilent, M. F. Bernet-Camard, A. Dazzi, A. Deniset-Besseau, R. Gref, *Part. Part. Syst. Charact.* **2018**, *35*.
- [23] P. Álamo, V. Pallarès, M. V. Céspedes, A. Falgàs, J. M. Sanchez, N. Serna, L. Sánchez-garcía, E. Voltà-duràn, G. A. Morris, A. Sánchez-chardi, I. Casanova, R. Mangues, E. Vazquez, A. Villaverde, U. Unzueta, *Pharmaceutics* **2020**, *12*, 1.
- [24] J. Mathurin, E. Pancani, A. Deniset-Besseau, K. Kjoller, C. B. Prater, R. Gref, A. Dazzi, *Analyst* **2018**, *143*, 5940.

Quantify drug loading at the single nanoparticles level using AFM-IR technique: a convenient method to map and evaluate the drug distribution

- [25] F. Tang, P. Bao, Z. Su, *Anal. Chem.* **2016**, *88*, 4926.
- [26] G. Ramer, V. A. Aksyuk, A. Centrone, *Anal. Chem.* **2017**, *89*, 13524.
- [27] P. Collery, D. Desmaele, V. Vijaykumar, *Curr. Pharm. Des.* **2019**, *25*, 3306.
- [28] A. Mancini, V. Giliberti, A. Alabastri, E. Calandrini, F. De Angelis, D. Garoli, M. Ortolani, *J. Phys. Chem. C* **2018**, *122*, 13072.
- [29] B. S. Ault, T. M. Becker, G. Q. Li, M. Orchin, *Spectrochim. Acta Part A Mol. Biomol. Spectrosc.* **2004**, *60*, 2567.
- [30] J. M. Chalmers, In *Handbook of Vibrational Spectroscopy* (Ed.: Chalmers, J. M.), John Wiley & Sons, Ltd, Chichester, UK, **2006**.
- [31] P. Nguyen-Tri, P. Ghassemi, P. Carriere, S. Nanda, A. A. Assadi, D. D. Nguyen, *Recent applications of advanced atomic force microscopy in polymer science: A review*, Vol. 12, MDPI AG, **2020**.
- [32] B. Lahiri, G. Holland, A. Centrone, *Small* **2013**, *9*, 439.
- [33] F. Lu, M. Jin, M. A. Belkin, *Nat. Photonics* **2014**, *8*, 307.
- [34] J. Waeytens, J. Mathurin, A. Deniset-besseau, V. Arluison, L. Bousset, H. Rezaei, V. Raussens, A. Dazzi, *Analyst* **2020**.
- [35] P. Legrand, S. Lesieur, A. Bochot, R. Gref, W. Raatjes, G. Barratt, C. Vauthier, *Int. J. Pharm.* **2007**, *344*, 33.
- [36] M. S. Ural, M. Menéndez-Miranda, G. Salzano, J. Mathurin, E. N. Aybeke, A. Deniset-Besseau, A. Dazzi, P. Marianna, C. Martineau-Corcos, R. Gref, *ACS Appl. Mater. Interfaces* **2021**.
- [37] A. Kermagoret, G. Morgant, J. D'Angelo, A. Tomas, P. Roussel, G. Bastian, P. Collery, D. Desmaële, *Polyhedron* **2011**, *30*, 347.
- [38] J. Skogholt, K. H. Liland, U. G. Indahl, *J. Raman Spectrosc.* **2019**, *50*, 407.

A comprehensive investigation of the interactions of human serum albumin with polymeric and hybrid nanoparticles

Merve Seray Ural ^{a,b}, Joice Maria Joseph ^{a,b}, Frank Wien ^c, Xue Li ^a, My-An Tran ^a, Myriam Taverna, Claire Smadja ^{b*}, Ruxandra Gref ^{a*}

^a Université Paris-Saclay, Institute of Molecular Sciences of Orsay, French National Center for Scientific Research, Orsay, France

^b Université Paris-Saclay, Institute Galien, French National Center for Scientific Research, Châtenay-Malabry, France

^c Université Paris-Saclay, Synchrotron Soleil, 91190 Saint-Aubin, France

Corresponding authors : Dr. Ruxandra Gref: ruxandra.gref@universite-paris-saclay.fr and Prof. Claire Smadja: claire.smadja@universite-paris-saclay.fr

Key words: Protein stability; nanoparticle; PLGA; metal-organic frameworks; Synchrotron Radiation Circular Dichroism; capillary electrophoresis.

Abstract

Nanoparticles (NPs) engineered as delivery systems continue to make breakthroughs as they offer numerous advantages over free therapeutics. Although an intensive research is dedicated to the development of NPs for nanomedicine, their translation into clinics is hindered by the lack of a deep understanding of their interaction with biological media and in particular with proteins. Interactions with blood proteins, determine the NPs in vivo fate, the efficacy and the immunological toxicity of NPs. Moreover, blood protein function and structure can be altered by contact with NPs. In order to fulfill the growing need of investigating nano-bio interactions, this study provides a systematic understanding considering the two main aspects of nano-bio interactions: i) protein adsorption on the surface of NPs so called protein corona and ii) modifications on protein's structure and stability after being in contact with NPs. A methodology was developed by combining orthogonal techniques that takes advantage of analyzing the quantitative aspects of protein corona formation and qualitative aspect of NP effect on protein structure and stability with a model protein, human serum albumin (HSA). A protein kit together and capillary electrophoresis provided quantitative information on the adsorbed protein while a comparative quantitative analysis was performed on LC-MS. Capillary electrophoresis, remarkably allowed the separation of HSA forms (cysteinylation, native and glycation) that gave insights on the qualitative aspects of nano-bio interactions. SR-CD was the method of choice for the secondary structure analysis and thermal stability of HSA. A comparative study was designed with NPs comprising different cores and shells. This includes two different type of NPs (organic vs hybrid), prepared with or without polyethylene glycol (PEG) that is a hydrophilic polymer chain, modifies the surface properties of NPs, known as shielding nano-bio interactions and increase NP blood circulation. This

strategy allowed a deep understanding of the contributing factors for nano-bio interactions. Polymeric and hybrid organic-inorganic NPs of similar sizes presented distinct HSA adsorption profiles quantitatively. PLGA NPs showed protein repelling properties however they induced structural modifications on HSA. On the other side, HSA showed a significant affinity to nanoMOFs and protein corona was formed affecting also the protein structure. The shielding impact was gained through PEGylation for both NPs avoiding both the protein corona formation and modifications on unbound HSA.

Introduction

Engineered nanoparticles (NPs) developed with the advent of nanotechnology hold a great promise for revolutionizing medicine owing to their unique physicochemical properties that are different from those of bulk materials. NPs were employed as drug delivery vehicles with targeting and theranostic abilities ¹. Although a significant amount of work has been dedicated to the development of novel NPs and their physicochemical characterization, the insufficient understanding of NPs' interaction with biological molecules, so called nano-bio interactions, is an obstacle for their transition into clinics. ²

Immediately after the NP are administered into the bloodstream, a dynamic interplay takes place between their surface and plasma proteins, leading to the formation of a protein corona ^{3 4}. The PC composition depends mainly on the physicochemical properties of the NPs (surface hydrophilicity and charge) and on their size and shape ⁵. PC governs the biological identity of the NPs and determines their *in vivo* fate, stability and toxicity ^{6 7 8}. Once adsorbed onto the NPs' surfaces, certain proteins act as opsonins, triggering the recognition and removal of the NPs by the immune system ⁹.

In most of the reported studies, the PC formation resulted in a consequent conformational and functional change of the adsorbed proteins.^{10 11} Thus, the nano-bio interactions induced protein structural rearrangements^{12 13} aggregation, inappropriate signaling and other functional alterations.^{5 14 15} Protein misfolding diseases were reported as a result of protein unfolding upon nano-bio interactions¹⁶.

Proteins can also interact with NPs, without adsorbing onto their surface, but the contacts due to Brownian motions can lead to alterations in their structures. However, few studies dealt yet with these important aspects. For example, silver nanoparticles of around 15 nm precipitated lysozymes, modified the secondary structure of transthyretin and affected the stability of human serum albumin (HSA)¹⁷. Gold NPs denatured bovine serum albumin (BSA)¹⁸ in contrast to Gadolinium-based NPs, which were shown to increase the stability of HSA¹⁹. Silica NPs of around 26 nm increased the affinity of haemoglobin for oxygen²⁰. It was emphasized that the thermodynamic stability and the secondary structure of blood proteins may vary in the presence of NPs¹⁷.

In this context, an intensive research was dedicated to engineering the NPs' surfaces to modulate their interactions with proteins, and more particularly, opsonins⁹. NPs with protein-repelling surfaces such as those made of poly(ethylene glycol) (PEG) had long blood circulation abilities ("stealth" properties)¹.

PEG remains nowadays one of the most employed coating materials to reduce protein adsorption onto the NPs. At the same time, polylactide-co-glycolide (PLGA), a biodegradable polymer approved by food and drug administration (FDA), has been widely used to elaborate the NPs' cores and to incorporate a variety of active molecules. Several microparticles based on

PLGA are on the market²¹ but only one NP formulation based on PLGA-PEG (BIND-014) made up the way to clinical trials²². More recently, highly porous NPs made of metal-organic frameworks (nanoMOFs) attracted growing interest in nanomedicine in reason of their “green” (organic solvent free) preparation, drug loading and surface functionalization²³. Iron carboxylate-based nanoMOFs (MIL-100, stands for material of Institute Lavoisier) were non-toxic *in vivo*²⁴. Their surface was successfully engineered with PEG shells by various strategies^{25 26}.

The development of nanoparticulate drug carriers is in need of a methodology for the deep understanding of their interactions with blood proteins, crucial to predict their *in vivo* fate and possible toxic side-effects. The large majority of analytical methods proposed so far relied on the analysis of the PC: i) sodium dodecyl sulphate–polyacrylamide gel electrophoresis (SDS-PAGE) and mass spectroscopy (MS) allowed protein identification²⁷; ii) adsorbed proteins were visualized using optical, electron and atomic force microscopies²⁸; iii) the kinetics of protein adsorption were studied by isothermal titration calorimetry (ITC)^{16 29} and surface plasmon resonance^{30 31}. These techniques give valuable information about the thickness and density of the protein layer on the NPs, on the affinity of various proteins for the NPs and on the adsorption kinetics. However, they lack structural information on the PC.

In this context, fluorescence spectroscopy has been employed to study protein structure and conformation³² as well as protein binding affinity for the NPs^{33 34 35}. However, protein labeling with fluorescent dyes might change their conformation, structure and affinity for the NPs³⁶. Therefore, analytical techniques which do not require labelling are of main interest. Moreover, the strategic combination of different analytical techniques enables gaining both

qualitative and quantitative aspects on the PC and a better understanding of NP-protein interactions¹⁴.

In this study we provide a comprehensive analysis on protein interactions of two important types of NPs (PLGA and nanoMOF) and their PEGylated counterparts by using human serum albumin (HSA) as a model protein. Considering NP-serum protein interactions, HSA is typically the first protein to undergo adsorption due to its extraordinary ligand-binding capacity and predominant abundance in blood³⁷. The orthogonal methodology proposed here combines both quantitative and qualitative assessments of the amounts of adsorbed HSA, as well as an evaluation of the integrity of the non-adsorbed protein.

The experiments were designed with the aim of avoiding the need of desorbing HSA from the NPs' surfaces without any sample pretreatment, in order to avoid misleading results³⁸. First, the amounts of adsorbed HSA were determined with a protein kit. Then, capillary electrophoresis (CE) allowed both an accurate protein quantification and gaining valuable qualitative data on the HSA forms (native, cysteinated and glycated) once in contact with NPs. LC-MS investigations completed the studies, providing quantitative data on the amount of adsorbed protein. Finally, state-of-the-art Synchrotron radiation circular dichroism (SR-CD) gave complementary insights on the stability of the protein in contact with the NPs.

It was discovered that the two types of NPs studied here (PLGA and nanoMOFs) behaved differently regarding protein adsorption. The complementary experiments showed that no surface is completely inert with regard to protein interactions. Surprisingly, in the case of PLGA NPs, despite an undetectable HSA adsorption, important changes occurred in protein structure and stability upon prolonged contact with the NPs. On the opposite,

nanoMOFs adsorbed high amounts of HSA but the protein remaining in the supernatants was practically unaffected. Finally, PEG coating provided efficient shielding effects towards protein adsorption and structural modification in both cases.

Materials & Methods

Chemicals

PLGA 50:50 acid terminated (MW: 10–20 KDa, Expansorb® 10P019) and PLGA 50:50 PEG terminated ($M_w=32-70$ KDa, Expansorb® 10P037) were kindly donated by Sequens (Expansorb®, Aramon, France). Poly (vinyl alcohol) (PVA) (30000-70000 g/mol, 88% hydrolyzed), anhydrous dichloromethane (DCM), sodium chloride (NaCl), sodium phosphate dibasic (Na_2HPO_4), potassium phosphate monobasic (KH_2PO_4), formic acid, 1,3,5-benzenetricarboxylic acid (BTC) and acetonitrile were all purchased from Sigma-Aldrich (Saint-Quentin-Fallavier, France). Iron (III) chloride hexahydrate (98%) was from Alfa Aesar (Schiltigheim, France). Deionized water was obtained from a Direct-QR 3 Water Purification System from Merck Millipore (Billerica, MA, USA). All buffers were prepared using deionized water and filtered through a 0.22 μm nylon (VWR) before use. In particular, phosphate buffer at pH 7.4 (10mM) was prepared by mixing stock solutions of KH_2PO_4 and Na_2HPO_4 in deionized water.

Plasma derived Human Serum Albumin (HSA) (lyophilized powder, essentially globulin free, $\geq 99\%$), 4-(2-hydroxyethyl)-1-piperazineethanesulfonic acid (HEPES), sodium phosphate monobasic and sodium dodecyl sulfate (SDS) were obtained from Thermo Fisher Scientific (Les Ulis, France). The background electrolyte (BGE) used in capillary electrophoresis was 75 mM HEPES, containing 0.5 mM SDS at pH 8.0 adjusted with 1 M NaOH before

adding water to a final volume of 50 mL. Pierce™ BCA protein assay kit was purchased from Thermo Fisher Scientific.

Preparation of PLGA and PLGA-PEG NPs

PLGA NPs were prepared as previously reported using PVA as emulsifier and using DCM solutions of PLGA or PLGA-PEG (75 mg/mL)³⁹. Briefly, aqueous and organic phases were mixed using a sonic probe (Sonopuls HD 2070, BANDELIN electronic GmbH & Co, 270 Berlin, Germany) at 40% of power for 15 sec. The dispersion medium was 5 mL of 0.5% w/v PVA solution containing 1% w/v NaCl and was sonicated for 30 seconds at 40% of power in an ice bath to avoid overheating. The resulting emulsion was left at room temperature under gentle magnetic stirring overnight to allow the organic solvent to evaporate.

Synthesis of CD-PEG derivative

CD-PEG was synthesized as previously described (Cutrone et al) using phosphorylated β -cyclodextrin (β -CD) building-blocks to bind to the metallic sites on the nanoMOF surface. β -CD was chosen because its dimensions are, as needed, large enough to avoid penetration within the MIL-100(Fe) nanoMOFs pores and their numerous free OH groups are very suitable for introducing functional groups in the primary or/and secondary rims.

Synthesis of MIL-100(Fe) nanoMOF and PEG coating

Iron trimesate nanoMOFs were synthesized using a microwave-assisted hydrothermal method described elsewhere.^{40 41} Briefly, 30 mL of an aqueous mixture containing 6.0 mM iron chloride hexahydrate and 4.0 mM of BTC was

heated at 130°C under stirring for 6 min and under microwave irradiation at 1600 W (Mars-5, CEM Corporation, Matthews, NC, USA). The synthesized nanoMOFs were recovered by centrifugation at 10000 g for 15 min and purified by six times washing with absolute ethanol. They were stored as ethanolic suspensions at room temperature until further use. Before the experiments, ethanol was removed by centrifugation and nanoMOFs were redispersed in aqueous media by vortex.

PEG-coated nanoMOFs (nanoMOFs-PEG) were prepared as previously reported^{40 26 42} by incubating overnight at room temperature the nanoMOFs suspensions in water (2mg/mL) with CD-PEG solutions (0.2 mg/mL).

NP characterization

Morphology of NPs was visualized by transmission electron microscopy (TEM) with a JEOL electron microscope (JEM 100 CX II, operating at 120 kV) equipped with an US1000 2kx2k Gatan camera. 5uL of samples were deposited onto a carbon-coated copper grid treated beforehand with a glow discharge (easiGlow, Ted Pella Inc), and excess liquid was removed with a filter paper after 30 sec.

Mean hydrodynamic diameters and size distributions were determined by dynamic light scattering (DLS) at 25°C with an equilibration time of 60 sec using a Zetasizer® (Nano ZS90, Malvern Instruments, Worcestershire, UK). All formulations were measured at least in triplicate. Mean diameters were reported as Z Average (nm) ± SE (Standard Error) with the polydispersity index (PdI). Zeta potential (ZP) was measured by in KCl 1 mM at 25°C with a Zetasizer®. Additionally, nanoMOFs were characterized by nitrogen sorption measurements performed on a Micromeritics Instruments ASAP 2020 at 77 K. Samples were degassed at 100 °C for 15 h. BET surface area of 1690 ± 80

A comprehensive investigation of the interactions of human serum albumin with polymeric and hybrid nanoparticles

$\text{m}^2 \text{g}^{-1}$ was calculated in the partial pressure range of 0.05 – 0.20 P/P_0 . NanoMOF-PEG were prepared as previously described by incubation with an aqueous solution of CD-PEG overnight²⁶. After surface functionalization, the nanoMOF-PEG were recovered by centrifugation (10 min, 10000 g). The crystallinity of the nanoMOFs, was preserved before after surface modification with CD-PEG, as assessed by X-ray powder diffraction (XRPD) in agreement with previous investigations²⁶.

Human serum albumin (HSA) adsorption studies

PLGA and PLGA-PEG NPs (3 and 10 mg/mL) were put into contact with an HSA solution (1mg/mL) in phosphate buffer (0.01M, pH 7.4). NanoMOF and nanoMOF-CD-PEG (1.5 or 3 mg/mL) were incubated with HSA solutions (0.5 or 1mg/mL). In all cases, the HSA:nanoMOF weight ratio was 1:3. All NPs were dispersed in 300 mL phosphate buffer (0.01 M, pH 7.4) and were incubated at RT up to 72 h using a vertical rotating shaker. In all cases, the unbound HSA was assessed in the supernatants obtained after NP centrifugation at 10000 g for 15 min. HSA reference incubated without NPs with respect to time intervals and centrifuged before analysis (except SR-CD study).

Quantification of protein adsorption at the surface of nanoparticles : Bicinchoninic acid (BCA) assay

The HSA adsorption kinetics were studied by monitoring the unbound HSA concentration as a function of time. The unbound protein concentration was determined colorimetrically with a Pierce™ BCA protein assay kit. To do so, 25 μL of supernatants containing the unbound proteins were recovered after

NP centrifugation and were mixed with 200 μ L of the BCA reagent in a 96-well microplate. The samples were well shaken and incubated at 37 °C for 30 minutes. After cooling for 15 minutes, the absorbance was read at 562 nm using a microplate reader (Infinite 200, Tecan Inc., Switzerland). The amount of unbound protein was calculated by interpolation of a calibration curve by using HSA standards with known concentrations. Controls were aqueous solutions and NP suspensions without HSA. The results were reported as the mean value of at least three separate determinations.

Capillary zone electrophoresis coupled to UV detection (CZE-UV)

CE experiments were performed on a P/ACE MDQ Instrument (Sciex, Framingham, MA, USA), coupled to a diode array detection UV-vis detector that was set at 214 nm. The 32 Karat™ software version 7.0 (Sciex) was used to collect the data. The analysis were carried out by using PVA-coated capillaries, purchased from Sciex, with an internal diameter of 50 μ m and a total length of 60.2 cm (effective length of 50 cm). Before the first use, the PVA capillaries were rinsed at 30 psi during 10 min with water and freshly prepared BGE (75 mM HEPES containing 0.5 mM SDS at pH 8). The sample was hydrodynamically injected from the inlet by applying a pressure of 0.5 psi for 15 s. The separation was then conducted at -25 kV at 25 °C. Between each analysis, the capillary was flushed at 20 psi during 15 min with water and 15 min with BGE. At the end of the day, the capillary was rinsed with water (15 min, 20 psi) and BGE (15 min, 20 psi) and stored at 4 °C with the ends in water as previously described⁴³.

Liquid Chromatography-Tandem Mass Spectrometry (LC-MS/MS)

Unbound HSA was analyzed with a Waters Xevo G2-XS QToF/Tof - ACQUITY UPLC M-Class system run by Masslynx v4.1 (Waters) after dilution in water with 0.1% (v/v) formic acid to reach a final concentration of 0.01 mg/mL. 1 μ L of samples were loaded onto a C18 trap column (NanoE MZ Sym C18 5 μ m 180 μ m x 20 mm, Waters), at 20 μ L min⁻¹ and desalted with 0.1% (v/v) formic acid and 5% (v/v) acetonitrile. After 4 min, the precolumn was connected to C18 Nanocolumn (NanoE MZ PST CSH130, 1.7 μ 75 μ m x 150 mm, Waters).

Electrospray ionization was performed at 2.5 kV, with a source temperature of 120°C, desolvation temperature of 250°C and 80 L/h cone gas flow. Buffers were 0.1% formic acid in water (A) and 0.1% formic acid in acetonitrile (B). Peptides were separated using a linear gradient from 5 to 95% buffer B for 80 min at 300 nL min⁻¹. One run was performed in 90 min, including the regeneration step at 95% buffer B and the equilibration step at 95% buffer A.

Mass spectrometric data were investigated with the Masslynx v4.1 software (Waters). Background subtraction was applied to mass spectrum with polynomial order at 25, below curve at 5%, tolerance at 0.01. Deconvolution was run on the 6 most intense peaks by Max Ent1 function by iteration to convergence with the following parameters: output mass ranges 60000-70000 Da with resolution 1.00 Da/channel, damage model as uniform Gaussian with at half height of 1.00 Da.

SRCD

The SRCD measurements were performed at the DISCO-beamline, SOLEIL Synchrotron (Saint-Aubin, France). Thanks to the photon flux and beam size at the Synchrotron facility, the measurements were performed with a good

signal to noise ratio (200) down to 175 nm, which is difficult to reach with a conventional CD set up . Thus, the UV CD region (175–250 nm), which corresponds to peptide bond absorption, was analyzed using the DISCO SRCD set up. Spectra were acquired every nanometer using a 1 nm bandwidth and 1.2 s integration time. Raw data (θ) was measured in millidegrees (mdeg), which were converted to molar circular dichroism values ($\Delta\epsilon$), after averaging, baseline subtraction and calibration with (+)-camphor-10-sulfonic acid (CSA). Data treatment including average, baseline subtraction, smoothing, scaling and standardization were performed with the CDtool software ⁴⁴.

For the molar circular dichroism values or $\Delta\epsilon$, the following equation was applied:

$$\Delta\epsilon = \theta \times (0.1 \times \text{MRW}) / [(P \times C) \times 3298] \quad \text{(I)}$$

The MRW (mean residue weight) of HSA is 113.8 Da ($\text{g}\cdot\text{mol}^{-1}$), P (pathlength) is 0.00234 cm (measured by interferometry) ⁴⁴ and C (protein concentration) is 1 mg/mL.

The secondary structure content was determined by using ContinLL and SELCON3 programs ⁴⁴ and additionally BeStSel server ⁴⁵. Normalized root-mean-square deviation (NRMDS) indicated the most accurate fit for each spectrum.

The NP suspensions after their incubation with HSA were analyzed directly without separation of the unbound protein. To do so, 4 μL samples were loaded in circular demountable calcium fluoride cells with a path length of 50 μm ⁴⁶. Baselines were collected in triplicate for all samples, corresponding to buffer solutions, suspension media or NP suspensions without protein.

Thermal denaturation experiments were carried out by collecting SRCD spectra at temperatures ranging from 23 to 98 °C using a 3 °C step and a 5

min settling time. Three spectra were collected for each temperature with a total measurement time of 3 h. Spectral cut-off at 180nm was used, based on the high tension of the PMT (Photomultiplier Tube) corresponding to an absorbance below 1. As controls, spectra were also recorded for 3 h without changing the temperature to ensure that over this time no additional phenomena (radiation damage or drying) affected the spectral amplitude. These controls showed that HSA was not susceptible to radiation damage and that the photon flux and beam size were appropriate for the investigations^{47 48}.

Results and discussion

Preparation of the NPs

Firstly, PLGA and PLGA-PEG NPs were prepared using commercially available biodegradable polymers³⁹. While the hydrophobic PLGA polymer possess carboxyl end groups, the PLGA-PEG diblock copolymer is uncharged. The hydrophilic PEG units covalently attached to the PLGA block dispose in a "brush" conformation at the NPs' surface leading to protein-repellent surface properties⁴⁹. Both PLGA and PLGA-PEG NPs were prepared by using an emulsifier, PVA, that forms a neutral, hydrophilic shell on the surface of the NPs, as it has been previously emphasized^{50 39}. Since more than 25 years, the versatile PLGA and PLGA-PEG NPs were used to incorporate and deliver in a controlled manner a variety of hydrophilic and hydrophobic drugs⁵¹.

Secondly, biodegradable MIL-100(Fe) nanoMOFs were synthesized by a "green" (organic solvent-free) microwave-assisted hydrothermal method generating an open 3D porous crystalline architecture. The nanoMOFs possess mesoporous windows (5.6 and 8.6 Å) and internal cages of around 24 and 29 Å in diameter²³. Discovered more recently than the polymeric PLGA

and PLGA-PEG NPs, they have the advantage to incorporate a variety of drugs without using organic solvents, reaching payloads up to 20–70 wt%²³ and were well tolerated *in vivo*⁵².

Aiming to develop biomedical applications of nanoMOFs, we have set up strategies to modify the nanoMOFs' surfaces with PEG chains by mild, one-step procedures devoid of reactants and organic solvents^{26,40}. The coating was based on cyclodextrin (CD) derivatives that are large enough to avoid their penetration within the nanoMOF's pores, not to interfere and displace the loaded drugs²⁵. The CD scaffolds displaying grafted PEG moieties (average MW ~2000 g/mole) spontaneously adsorbed onto the nanoMOFs, where they firmly anchored by coordination with the available metal sites at the surface²⁶. Advantageously, the procedure was carried out in a one-step procedure in water and without using any toxic additives and led to stable coatings without altering the nanoMOFs' crystalline structure.

Morphology and characteristics of NPs

PLGA and nanoMOF NPs, PEGylated or not, were successfully prepared with similar sizes to allow a comparative study of their nano-bio interactions as a function of both their core and surface properties (**Figure 1A-D**). Whereas the PLGA NPs appeared round-shaped, the nanoMOFs were crystalline with faceted structures in agreement with previous studies^{26,42}. In all cases, the average diameters ranged from 80 to 370 nm. These sizes were in agreement with DLS measurements, which showed that the PLGA and nanoMOFs NPs had mean hydrodynamic diameters of 310 ± 15 and 234 ± 16 nm, respectively (Table 1, SI). Polydispersities (PDIs) were 0.1 and 0.2, respectively, indicating that the NPs were monodisperse. PLGA-PEG and nanoMOF-PEG NPs had

larger diameters of 418 ± 30 , and 286 ± 20 nm, respectively, possibly because the presence of a PEG shell and differences in molecular weights.

Zeta potential for PLGA and PLGA-PEG NPs were around 0 mV, which was attributed to their neutral PVA shell, as previously reported^{50,39}. This protective steric layer shields the negatively charges of the carboxyl end group of PLGA. The nanoMOFs, coated or not, had Zeta potentials of -17 ± 3 mV, in good agreement with previously published data^{26,42}.

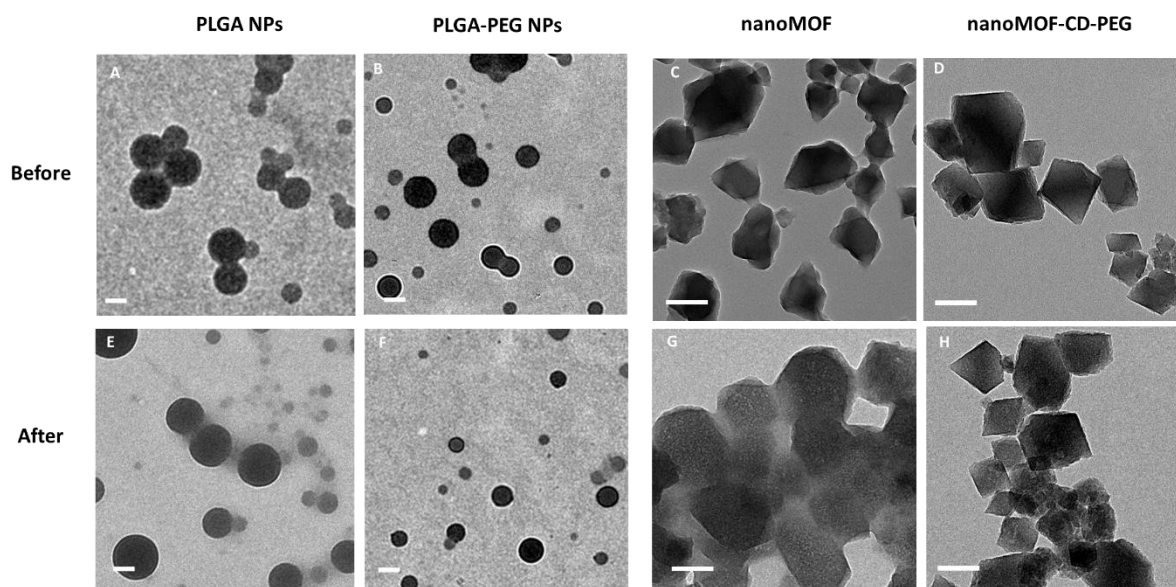


Figure 1. Representative TEM images of: A) PLGA NPs; B) PLGA-PEG NPs; C) nanoMOF and D) nanoMOF-PEG. TEM images obtained after incubation with HSA: E) and F) PLGA and PLGA-PEG NPs, after three days (1:10, HSA:NP); G) and H) nanoMOF and nanoMOF- PEG after 2h (1:3, HSA:NP). Scale bars: 100 nm.

Nano-bio interactions

Kinetics of protein adsorption

The kinetics of HSA adsorption onto the two types of NPs, hybrid and polymeric, with different core and shells, were comparatively studied. The NPs were incubated with HSA solutions up to 24 h. The unbound HSA was quantified using a BCA colorimetric assay at different time intervals (**Figure 2**).

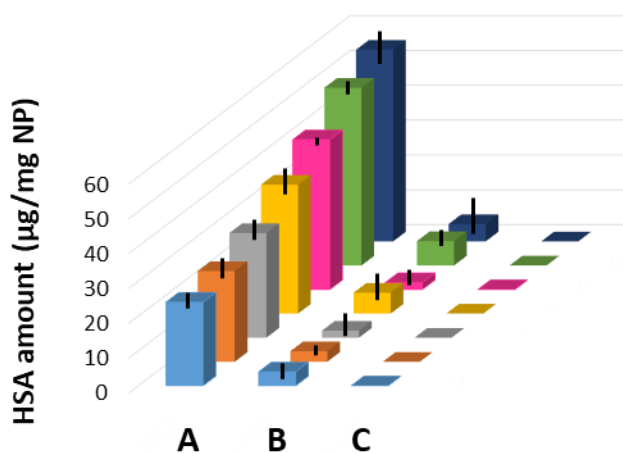


Figure 2: Amounts of HSA ($\mu\text{g}/\text{mg}$ of NPs) adsorbed on nanoMOFs (A), nanoMOFs-PEG (B), and PLGA NPs coated or not with PEG. (C) The HSA:NP weight ratio was 1:3 for the nanoMOFs and nanoMOFs-PEG, and 1:3, 1:10 and 1:100 for the PLGA and PLGA-PEG NPs. Different time points were studied: 5 min (light blue); 1 h (orange); 2 h (grey); 4 h (yellow); 6 h (pink); 8 h (green) and 24 h dark blue).

In the case of nanoMOFs, HSA adsorption occurred as soon as they were in contact with HSA ($24 \pm 2 \mu\text{g}/\text{mg}$). Then, HSA adsorption gradually increased

in a time dependent manner up to around 55 $\mu\text{g}/\text{mg}$ where it reached a plateau at 8th hour of incubation (**Figure 2**). In contrast, the amount of adsorbed HSA was very low in the case of nanoMOF-PEG (less than 7 ± 2 $\mu\text{g}/\text{mg}$) regardless the incubation time. This suggests that the affinity of HSA for the nanoMOF surface decreased while they gained “stealth” properties through PEGylation.

Surprisingly, neither the PLGA nor the PLGA-PEG NPs did adsorb any significant protein amounts. Even within three days incubation, the adsorbed amounts were undetectable by the BCA assay. This was the case also when increasing the HSA-NP contact area (i.e. decreasing the HSA:NP ratio to 1:10 and 1:100). Taking into account the surface area developed by the NPs, it was calculated that less than 0.15 mg/m^2 HSA was adsorbed. Therefore, it was concluded that the affinity of HSA for both PLGA and PLGA-PEG NPs was very low as compared to bare and PEGylated nanoMOFs.

The striking differences in protein adsorption between the two types of analyzed NPs could be explained based on their composition and physicochemical properties such as surface charge and hydrophilicity. PLGA NPs possess a neutral and hydrophilic surface in reason of their PVA coatings¹⁴. In contrast, the bare surface of the nanoMOFs is negatively charged and display numerous accessible iron sites prone to bind large molecules such as proteins⁵³. Whatever the NPs (PLGA or nanoMOF) the PEG shells protected them against protein adsorption.

Finally, the kinetic studies performed here provided the incubation conditions to be carried on for the following protein corona investigations in phosphate buffer. In the case of nanoMOFs, two hours were sufficient to form a large protein corona without NP degradation⁵⁴. However, nanoMOFs progressively degraded in phosphate buffer after longer incubation times^{54 55}. On the

opposite, PLGA formulations were stable in phosphate buffer, so they were studied over three days in this medium.

NP morphology upon contact with protein

NP morphologies were investigated after incubation with HSA by TEM (**Figures 1E-H**). The micrographs revealed that both PLGA and PLGA-PEG NPs maintained their uniform and spherical shapes and the images were similar to the as prepared NPs ((**Figures 1A-B**). Both PLGA and PLGA-PEG NPs preserved their morphology after contact with HSA for 3 days with no evidence of protein corona formation (**Figure 1 E-F**), in line with the HSA kinetic findings (**Figure. 2**), which demonstrated no HSA adsorption onto the polymeric NPs.

On the other hand, TEM images showed that the faceted morphology of nanoMOFs and nanoMOF-PEG were preserved after interaction with HSA (**Figure 1G-H**). Noticeably, only uncoated nanoMOFs after incubation with HSA presented a blurry aspect (**Figure 1G**), not observed with PEG-coated ones (**Figure 1H**). Therefore, taking into account the high HSA adsorption onto these NPs (**Figure. 2**), it can be hypothesized that the blurry aspect is due to a protein corona formation.

CE was further used to investigate the corona formation on the nanoMOFs. This versatile technique also brings insights on the possible alterations of the unbound HSA after contact with the different NPs studied here.

Capillary zone electrophoresis

CE is a versatile method allowing to investigate protein corona on NPs by both quantitative and qualitative approaches⁵⁶. One of the advantages of CE is to avoid using any stationary phase that might cause unwanted interactions and allow analysis of unbound HSA without any sample pretreatment⁵⁷. The

method was optimized to avoid any electroosmotic flow (EOF) and to suppress unwanted HSA interactions with the capillary wall. To do so, PVA-coated capillaries were used, as they afford obtaining highly hydrophilic, neutral and inert coatings⁵⁸. Indeed, our previous findings showed that the PVA-coated PLGA NPs adsorbed negligible amounts of HSA (**Figure. 2**).

Another advantage of PVA-coated capillaries is their excellent ability to separate different forms of HSA: native, glycosylated and cysteinylated⁵⁹. Indeed, HSA exists as a mixture of different proteoforms (native, cysteinylated, glycosylated) that could bind nanoparticles with different affinities. In previous studies, the analysis of the protein peak area gave quantitative information on protein adsorption. In addition, the modifications on the relative amounts of HSA forms can be evaluated qualitatively to gain understanding on the HSA interaction with NP surfaces⁶⁰. Therefore, CE was a method of choice here to investigate nano-bio interactions combining both quantitative and qualitative aspects.

CE experiments were performed firstly on HSA solutions (without NPs) in order to investigate the stability of the protein in the experimental conditions employed here for adsorption studies. Thus, the HSA solutions incubated up to three days at RT or 37°C and were submitted to the centrifugation conditions employed to sediment the NPs. The CE electropherograms were compared to those of fresh HSA solutions (**Figure SI1**). The electrophoretic profiles of the HSA solutions remained unaltered whatever the experimental conditions, pointing out the stability of HSA under the experimental conditions used here to study its interaction with the NPs.

On the basis of this proof of concept, the NP series (MOF and PLGA) were incubated with HSA and their supernatants were recovered to investigate the aforementioned two aspects: i) quantitative by analysing the peak areas of

unbound HSA and ii) qualitative by analysing the transformation/modification of the three HSA forms. **Figure 4** presents the CE-UV profiles of HSA recovered from NP supernatants after the incubation studies.

Reference HSA incubated without NPs presents three reproducible peaks at 12.4, 12.5 and 12.7 min. These data are in close agreement with published studies using the same type of capillaries⁵⁹ which showed three HSA peaks assigned to glycosylated (Gly), native and cysteinylated (Cys) forms, respectively.

CE profiles of unbound HSA were obtained after incubation with PLGA and PLGA-PEG NPs at a HSA:NP ratio of 1:3 (**Figure 4A**, blue and orange lines). The obtained electropherograms were almost identical to the incubated HSA reference. However, an increase in the NP concentration from 3 to 10 mg/mL (ratio 1 :10) resulted in a significant decrease of the peak at 12.7 min corresponding to the Cys HSA. Moreover, a new peak appeared at 11.8 min for this ratio. Interestingly, the total area of all the HSA peaks was preserved as compared to the reference (less than 5% differences). It is worth to mention that the same CE profiles were obtained when PLGA and PLGA-PEG NPs were incubated with HSA during one (**Figure SI2**) or three days (**Figure 4A**). In contrast, when incubation time was set to 2h, there was not any significant modifications on HSA even at the HSA:NP ratio of 1:10 (**Figure SI3**). This shows the dependence of the qualitative aspect of nano-bio interactions both on concentration and also incubation time.

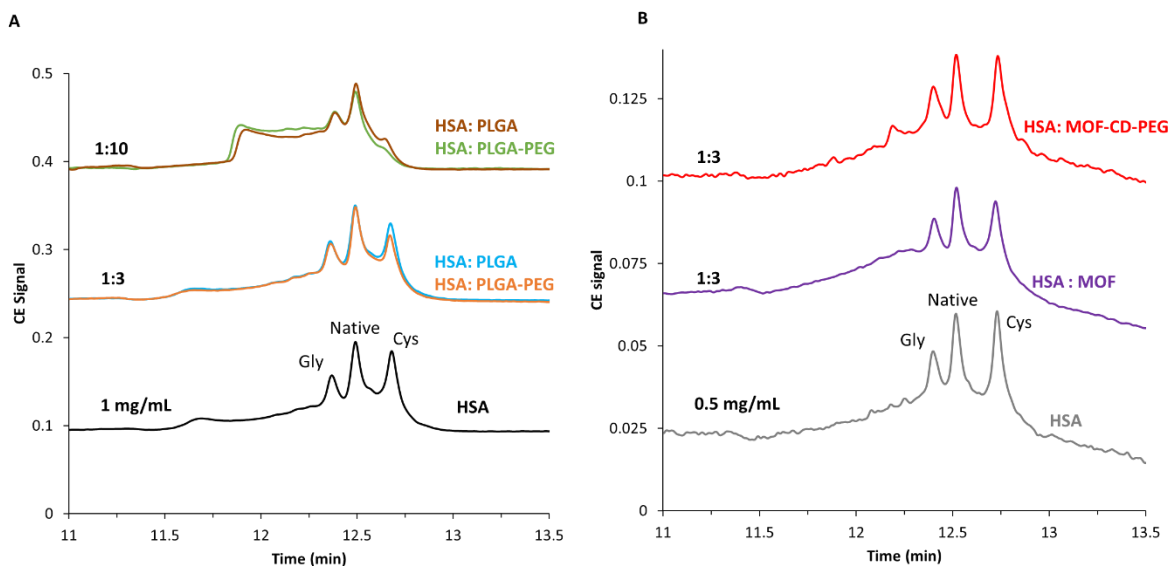


Figure 4: CE-UV electropherograms of unbounded HSA recovered from supernatants after incubation with A) PLGA-PEG (green, orange) and PLGA (brown, blue) NPs during 3 days with HSA: NP ratio of 1:3 and 1:10. B) nanoMOF-PEG (red) and nanoMOF (purple) during 2h with HSA: NP ratio of 1:3. Black and grey lines are the reference HSA solutions at 1 and 0.5 mg/mL, respectively.

Thus, we speculate that the shift in Cys position might correspond to a structural alteration of the protein, although it did not adsorb onto the NPs' surfaces (**Figure 2**). These findings suggest that HSA in contact with PLGA based NPs might undergo modifications despite of having a low affinity towards them. As shown here, these modifications could be observed for both contact time and NPs concentration (ie developed surface areas). It was then interesting to investigate if structural changes occur with HSA upon incubation with nanoMOFs, where important amounts ($30 \pm 2 \mu\text{g}/\text{mg}$) were adsorbed within 2h (**Figure 2**).

In the case of nanoMOF with higher affinity for HSA as compared to PLGA NPs, there was no qualitative modification (ie. no change of the retention

times) on the unbound HSA species after incubation (**Figure 4B**). However, the $11 \pm 3\%$ decrease in the peak area after incubation with the nanoMOF are an indication that around $37 \pm 9 \mu\text{g}$ of the HSA was adsorbed per mg of nanoMOF, which is in a good agreement with the BCA protein assay ($30 \pm 2 \mu\text{g}/\text{mg}$ adsorption, **Figure 2**). Moreover, the shielding effect gained through PEGylation was demonstrated as the area of unbound HSA was preserved after incubation with nanoMOF-PEG (less than 5% changes). To the best of our knowledge, no studies described yet the modifications of HSA forms upon incubation with NPs, without adsorption. However, more details investigations would be needed to decipher the specific alterations of the Cys forms.

In complement to the CE studies, LC-MS investigations were carried on in an attempt to resolve the HSA forms in the NP supernatants.

LC-MS investigations

Total ion count (TIC) chromatograms provided in **Figure 5** represent the ion intensities displayed as a sum of the individual HSA fragments as function of incubation time with the PLGA and nanoMOF NPs, PEGylated or not. TIC chromatograms of unbound HSA after incubation with or without NPs revealed similar shapes and same retention time (75.2 min) in all the studied cases (**Figure 5**). When HSA was incubated with PLGA and PLGA-PEG NPs, an additional small peak appeared at 74.7 min. It corresponds to free PVA emulsifier in the NP suspensions and it induced no effect on the main peak (**Figure 5B-C**).

Values derived from the areas under the intensity curves give insights about the abundance of the protein thus relative protein quantity between samples. As indicated next to the chromatograms in **Figure 5A-B**, areas under the

A comprehensive investigation of the interactions of human serum albumin with polymeric and hybrid nanoparticles

curves values did not vary between incubated HSA reference and HSA in contact with PLGA (<14% deviations in the areas). Therefore, it is in an agreement with the quantitative BCA assays findings, which showed that HSA was not adsorbed on the PLGA NPs. In contrast, a dramatic change was recorded when HSA was in contact with nanoMOFs (non-PEGylated): 50% of reduction occurred in comparison to incubated HSA reference (**Figure 5D-E**). This result is also in line with the findings above suggesting a decrease in the unbound HSA in the supernatant and thereby formation of protein corona. Noticeably, PEGylated NPs, PLGA-PEG and the nanoMOF-PEG, clearly resisted to protein adsorption as only 12 and 4% differences were found respectively as compared to HSA reference (**Figure 5E-F**).

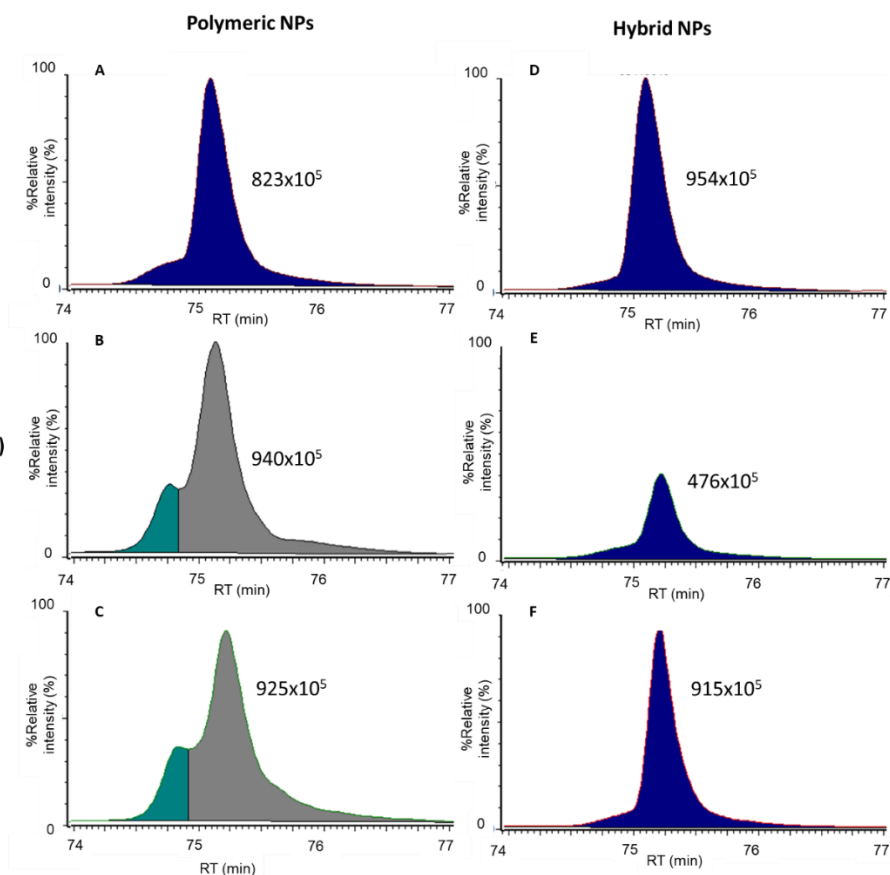


Figure 5. TIC chromatograms of unbound HSA recovered after the incubation A) without NPs, for 3 days B) with PLGA NPs, for 3 days, C) with PLGA-PEG NPs, for 3 days, D) without NPs, for 2h E) with nanoMOF for 2h, F) with nanoMOF-PEG for 2h.

SR-CD investigations

To complete these studies, SR-CD was a method of choice to investigate the changes in the secondary structure of the HSA protein due to its interaction with the NPs. CD provides access to the relative content of the secondary structure components of HSA (alpha-helix, beta-sheet, beta-turns, and random coil). The extended spectral range (175-250 nm) accessible at DISCO beamline made a more accurate analysis on the entire protein peak at 192 nm possible (**Figure 6A-B**). This range is of interest regarding the singlet electron transitions in the HSA peptide backbone. As presented in **Figure 6**, HSA exhibited a typical spectrum of a predominantly α -helical protein with two minimums at 224 and 208 nm and a maximum at 192 nm. These data were in agreement with the literature. The peak at 224 nm was attributed to $\pi\pi^*$ transition from the lone pair of oxygen to a π^* anti-bonding orbital. The peak observed at 208 nm was due to the $\pi\pi^*$ electronic transitions of the peptide bond, whereas a positive band at 192 nm was due to the transition of non-bonding π orbital to the π^* orbital.⁶¹ The region around 180 nm is known as a charge transfer region. Unlike other transitions, the transitions in this region occur intramolecularly from one peptide bond to another⁶².

The amount of α -helical secondary structure of HSA was obtained by deconvolution of the CD spectra. Fresh HSA reference used here presented a 70% helix content which was in agreement with the literature⁶³. This helicity

content was preserved 2h after incubation (70%), whereas it dropped to 61% after three days of incubation. **(Figure 6A)**, The decrease in the HSA helicity upon incubation has been shown in various studies based on CD spectroscopy, confirming the results found here. ^{64 65}

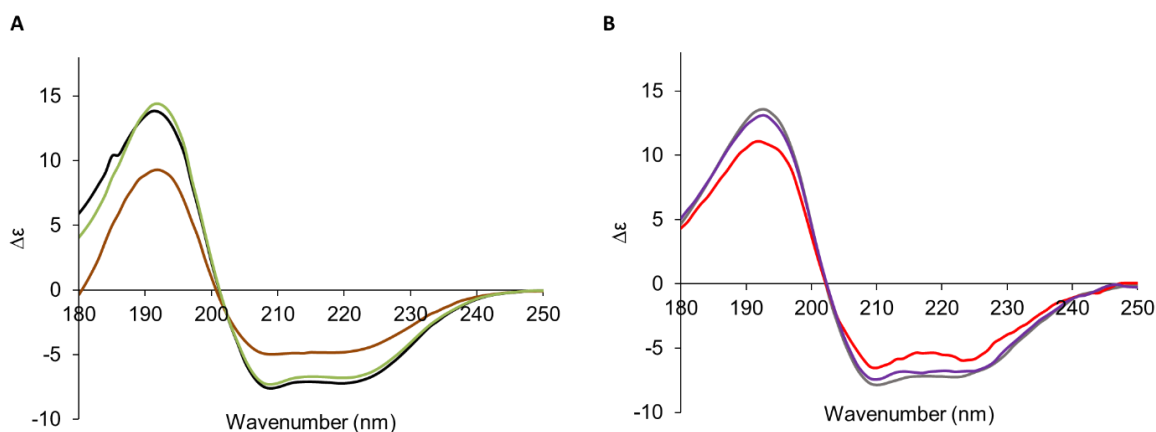


Figure 6 Far UV SR-CD spectra of : HSA incubated without NPs during 2h (grey) and 3 days (black); PLGA (brown) and PLGA-PEG (green) NPs incubated with HSA during 3 days at a HSA: NP ratio of 1:10; nanoMOF (purple) and nanoMOF-PEG (red) incubated with HSA during 2h at a HSA: NP ratio of 1:3. The spectra were taken directly on the NP suspensions and the concentration of HSA was 1 mg/mL in all studies.

The interactions of bare and PEGylated NPs with HSA were analyzed by SR-CD directly on the NP suspensions as the NPs did not interfere with the experiments **(Figure 6)**. A special attention was given to HSA secondary structure differences between the reference (HSA incubated without NPs) and HSA in the presence of the four types on NPs. Firstly, the contact of HSA with the PLGA NPs during 3 days (1:10, HSA:PLGA NP) resulted in a dramatic loss in α -helix content (from 61 to 27%) with visible signs of modifications that

affected the bands at 224 nm ($n\pi^*$ parallel transitions), 208 nm ($\pi\pi^*$ parallel transitions) as well as at 192 nm ($\pi\pi^*$ perpendicular transitions) (**Figure 6A**). A significant change observed around 180 nm indicated that HSA was subjected to intramolecular charge-charge transitions. On the other hand, the increase recorded on HSA's parallel β -strand (from 0 to 4%) and antiparallel β -strand (from 0 to 12%) signified the increase in β -sheet populations. Moreover, the amount of turns were slightly modified (from 10 to 8 %). Given the fact that turns are inherently linked to the number of alpha helices. it can be hypothesized that the HSA interactions with the PLGA NPs disturbed the secondary structure. Possibly, a minor denaturing or reorganisation with formation of β -strands of took place during collisions at the NPs' surfaces, without leading to adsorption as it was previously established (**Figure 2**). Noticeably, when lower amount of PLGA and PLGA-PEG NPs in contact with the same amount of HSA, the α -helix structure of the protein was not modified (**Figure SI4**).

HSA incubated (2h) with nanoMOF was then analyzed and compared with incubated (2h) HSA reference (**Figure 6B**). After contact with NPs, a loss in α -helix content of HSA was observed, from 70% to 52 %. This decrease was remarkable taking into account the short incubation time of only 2h. Further analysis of the SR-CD data showed only a slight increase in antiparallel β -strands (from 0 to 2%) and in beta-turns (from 9 to 14%). Besides, the percentage of other secondary structure components (unordered) increased from 21 to 32%.

On the opposite, the CD spectra in the case of HSA incubated with PLGA-PEG NPs and nanoMOF-PEG were similar to their reference HSA spectra (**Figure. 6A-B**). The α -helix content was preserved with less than 5% differences (within the detection limit of the method) as compared to control HSA.

In a nutshell, these results suggest that the PEGylated surfaces preserve the α -helix structure of the protein, whereas uncoated surfaces disturb it, independently if adsorption occurred or not.

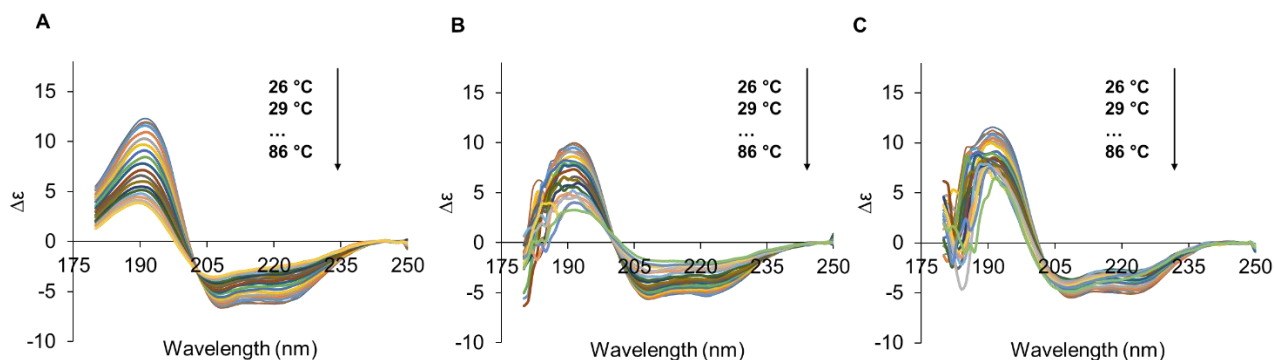


Figure 7. Thermal unfolding of A) HSA (1mg/mL), HSA incubated with B) PLGA and C) PLGA-PEG NPs followed by SR-CD spectroscopy as a function of temperature over a range from 26 to 86 °C at intervals of 3 °C. Weight ratio of HSA:NP was 1:10. The samples were analyzed after 3 days incubation.

To go a step further, protein unfolding was analyzed through thermal denaturation studies that give insights about the effect of NPs on protein's thermal stability. Far-UV SRC-D spectra were collected over a wide temperature range, from 26 to 86 °C. **Figure 7A** shows a typical spectrum of HSA unfolding upon increase in temperature. All the thermal unfolding spectra intersected at 203 nm which corresponds to the isobestic point. The HSA thermal unfolding was then assessed after incubation with the NPs. The changes on the unfolding behavior of HSA due to interactions with the PLGA NPs are presented in **Figure 7B**. The isobestic point was shifted from 203 nm to 201 nm, which is a clear indication of a reduction in HSA's stability¹⁹.

In addition, changes in other spectral features were also noted. Spectra appeared less compact state from the first scan. as compared to HSA reference. This was in line with the results shown in **Figure 6A** where same NP induced helicity decrease on HSA. The unfolding behavior characterized by the peak at 208 nm (**Figure 7B**) was strikingly different as compared to control HSA solutions. This could be attributed to NP-induced modifications on the HSA secondary structure, particularly on the $\pi\pi^*$ parallel transitions. The disappearance of the band at 208 nm at high temperatures (>70 °C) can be taken as evidence for the modifications of the melting behavior of HSA resulting from structural changes due to their contact with the NPs.

On the opposite, the thermal behavior of HSA has not been affected by the incubation with PLGA-PEG NPs, as the characteristic bands were fully maintained (**Figure 7C**). A more compact HSA structure was observed, suggesting that the protein has gained thermal stability. It is worth mentioning that HSA denaturation depend on its concentration and experimental conditions^{17 66}. Thus, in this study, given that all the experimental conditions were the same, qualitative comparisons could be made between HSA samples incubated or not with NPs. The main finding was the modifications on HSA stability upon contact with PLGA NPs despite the fact that they didn't adsorb onto their surfaces (**Figure. 2**).

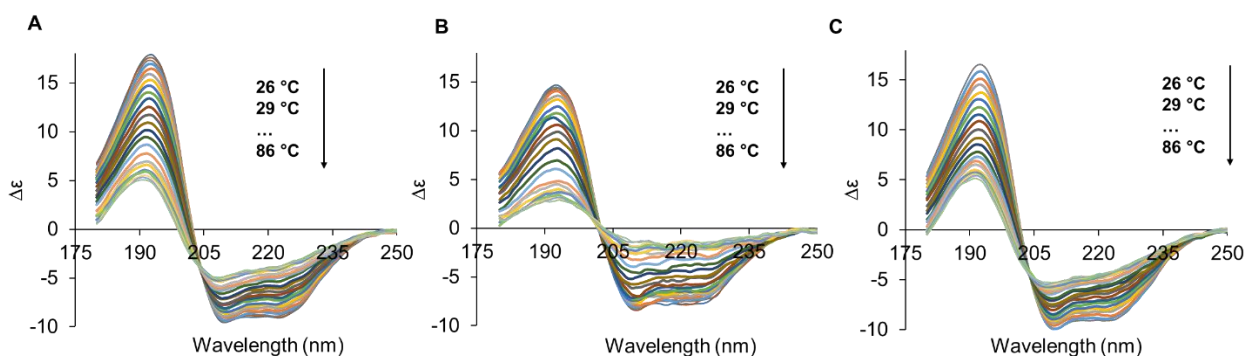


Figure 8. Thermal unfolding of HSA followed by SRCD spectroscopy studied as a function of temperature over a range from 26 to 86 °C with intervals of 3 °C. A) control HSA (1mg/mL), B) HSA:nanoMOF (1:3), C) HSA:nanoMOF-PEG (1:3). All samples were analyzed after 2h of incubation.

Thermal denaturation profiles of HSA incubated with nanoMOF and nanoMOF-PEG were represented in **Figure 8**. Results were similar to the ones of PLGA and PLGA-PEG NPs. HSA was in a more unfolded state after incubation with the nanoMOF, and in particular, its characteristic band at 208 nm was diminished when increasing the temperature (**Figure 8B**). Moreover, HSA unfolding occurred, as the isobestic point shifted from 204 nm (HSA reference) to 202 nm (HSA in contact with the nanoMOFs). However, in the case of nanoMOF-PEG, there were no significant modifications neither on the characteristic band at 208 nm nor on the isobestic point. The protein was maintained in a more folded state upon heating and remarkably preserved its compact form throughout the temperature increase. It can be therefore concluded that the PEG-based coating conferred thermal stabilization to the HSA molecules. The protective effect of the PEG coatings on both PLGA and nanoMOFs is in line with the previous CE findings. This is also clearly shown in **Figure 9**, presenting the melting curves of reference HSA, and HSA after contact with each NP. Differences among HSA melting behavior after contact with bare NPs, PLGA (brown) NPs and nanoMOFs (red) were shown whereas PEGylated NPs avoided modifications on melting profile suggesting that HSA preserved its thermal stability in contact with PEGylated NPs.

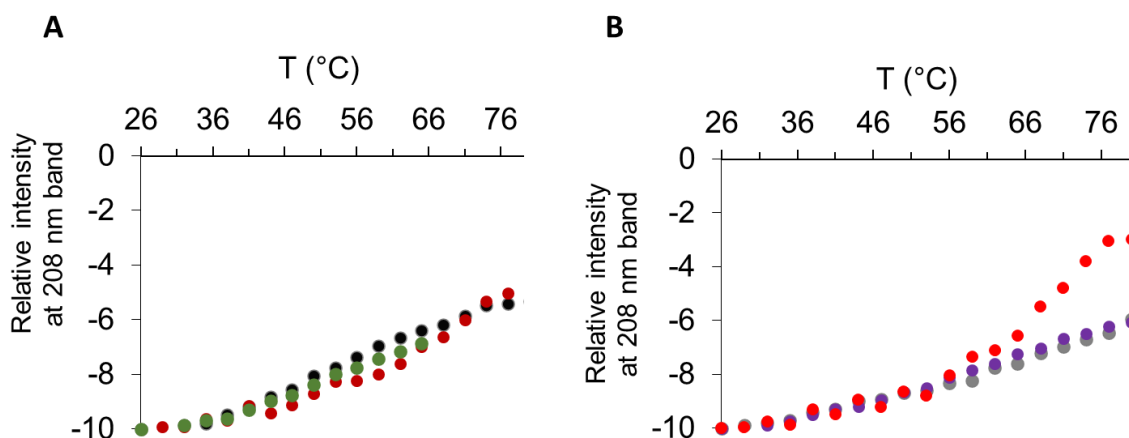


Figure 9. Melting curves of control HSA incubated during 2h (grey) and 3 days (black); A) PLGA (brown) and PLGA-PEG (green) NPs incubated with HSA during 3 days at a HSA: NP ratio of 1:10 B) nanoMOF (purple) and nanoMOF-PEG (red) incubated with HSA during 2h at a HSA: NP ratio of 1:3.

Conclusion

A set of orthogonal techniques was used here to investigate the interactions between HSA, the most abundant protein in the blood, and a series of NPs of similar mean diameters, surface-modified with PEG shells or not. Quantitative insights were gained using LC-MS and a protein assay kit. We discovered that despite the fact that HSA didn't adsorb onto PLGA NPs, it underwent dramatic structural changes upon contact with these NPs. Indeed, the Cys form of HSA was particularly affected and our studies revealed the appearance of new forms, yet to be identified. In contrast to PLGA NPs, nanoMOFs adsorbed rapidly high amounts of HSA, but the protein forms were unaffected by these interactions. Secondary structures of HSA and melting curves were also investigated by SR-CD. In all cases, the PEG protective layers avoided protein unfolding.

As biocompatible NPs are gaining increasing interest for biomedical applications, a thorough understanding of their effects on the structure and functions of proteins is essential. The methodology proposed here could be applied to other types of NPs, loaded or not with drugs, as well as to other proteins known to interact with NPs in the bloodstream, such as immunoglobulins, complement, fibronectin etc. Moreover, in line with ethical issues, *in vitro* orthogonal methodologies to study NP-protein interactions are essential prior to *in vivo* experiments. In a wider view, the methodology developed in this work may be applied to evaluate the impact and risk of a variety of NPs engineered for intravenous administration.

Acknowledgements

We thank Stéphanie Yen-Nicolaÿ from the Plateforme de Protéomique (Ingénierie et Plateformes au Service de l'Innovation Thérapeutique, Chatenay Malabry, France) for help with LC-MS investigations and fruitful discussions. SR-CD measurements on DISCO beamline at SOLEIL Synchrotron light source were performed under the proposals 20180883 and 20171494. We thank Matthieu REFREGIERS and Frank WIEN for welcoming us to the DISCO beamline. This work is supported by a public grant overseen by the French National Research Agency (ANR) as part of the "Investissements d'Avenir" program (Labex NanoSaclay, reference: ANR-10-LABX-0035).

Author contribution

Conceived the study: RG, CS. Performed the experiments: MSU, JMJ, XL, MAT. Data treatment: MSU, JMJ, MAT, FW, MT, CS, RG. Wrote the manuscript: MSU,

RG. Funding acquisition: RG, CS. All authors have read and agreed to the published version of the manuscript.

References

1. Mitchell, M. J. *et al.* Engineering precision nanoparticles for drug delivery. *Nature Reviews Drug Discovery* vol. 20 101–124 (2021).
2. Ventola, C. L. Progress in nanomedicine: Approved and investigational nanodrugs. *P T* **42**, 742–755 (2017).
3. Nakanishi, K., Sakiyama, T. & Imamura, K. On the adsorption of proteins on solid surfaces, a common but very complicated phenomenon. *Journal of Bioscience and Bioengineering* vol. 91 233–244 (2001).
4. Lundqvist, M. *et al.* Nanoparticle size and surface properties determine the protein corona with possible implications for biological impacts. *Proc. Natl. Acad. Sci. U. S. A.* **105**, 14265–14270 (2008).
5. Nel, A. E. *et al.* Understanding biophysicochemical interactions at the nano-bio interface. *Nature Materials* vol. 8 543–557 (2009).
6. Tenzer, S. *et al.* Rapid formation of plasma protein corona critically affects nanoparticle pathophysiology. *Nat. Nanotechnol.* **8**, 772–781 (2013).
7. Schöttler, S., Landfester, K. & Mailänder, V. Controlling the Stealth Effect of Nanocarriers through Understanding the Protein Corona. *Angew. Chemie - Int. Ed.* **55**, 8806–8815 (2016).
8. Rampado, R., Crotti, S., Caliceti, P., Pucciarelli, S. & Agostini, M. Recent

- Advances in Understanding the Protein Corona of Nanoparticles and in the Formulation of “Stealthy” Nanomaterials. *Frontiers in Bioengineering and Biotechnology* vol. 8 (2020).
9. Papini, E., Tavano, R. & Mancin, F. Opsonins and Dysopsonins of Nanoparticles: Facts, Concepts, and Methodological Guidelines. *Frontiers in Immunology* vol. 11 2343 (2020).
 10. Mariam, J., Sivakami, S. & Dongre, P. M. Albumin corona on nanoparticles—a strategic approach in drug delivery. *Drug Deliv.* **23**, 2668–2676 (2016).
 11. Lu, X. *et al.* Tailoring the component of protein corona via simple chemistry. *Nat. Commun.* **10**, (2019).
 12. Lundqvist, M., Sethson, I. & Jonsson, B. H. Protein adsorption onto silica nanoparticles: Conformational changes depend on the particles' curvature and the protein stability. *Langmuir* **20**, 10639–10647 (2004).
 13. Satzer, P., Svec, F., Sekot, G. & Jungbauer, A. Protein adsorption onto nanoparticles induces conformational changes: Particle size dependency, kinetics, and mechanisms. *Eng. Life Sci.* **16**, 238–246 (2016).
 14. Saptarshi, S. R., Duschl, A. & Lopata, A. L. Interaction of nanoparticles with proteins: Relation to bio-reactivity of the nanoparticle. *J. Nanobiotechnology* **11**, 1 (2013).
 15. Shemetov, A. A., Nabiev, I. & Sukhanova, A. Molecular interaction of proteins and peptides with nanoparticles. *ACS Nano* vol. 6 4585–4602 (2012).
 16. Lindman, S. *et al.* Systematic investigation of the thermodynamics of

- HSA adsorption to N-iso-propylacrylamide/N-tert-butylacrylamide copolymer nanoparticles. Effects of particle size and hydrophobicity. *Nano Lett.* **7**, 914–920 (2007).
17. Laera, S. *et al.* Measuring protein structure and stability of protein-nanoparticle systems with synchrotron radiation circular dichroism. *Nano Lett.* **11**, 4480–4484 (2011).
 18. Teichroeb, J. H., Forrest, J. A. & Jones, L. W. Size-dependent denaturing kinetics of bovine serum albumin adsorbed onto gold nanospheres. *Eur. Phys. J. E* **26**, 411–415 (2008).
 19. Yang, X. *et al.* Human serum albumin in the presence of aquix nanoagents: Structure stabilisation without direct interaction. *Int. J. Mol. Sci.* **21**, 1–17 (2020).
 20. Devineau, S. *et al.* Manipulating hemoglobin oxygenation using silica nanoparticles: A novel prospect for artificial oxygen carriers. *Blood Adv.* **2**, 90–94 (2018).
 21. Rezvantalab, S. *et al.* PLGA-based nanoparticles in cancer treatment. *Front. Pharmacol.* **9**, 1260 (2018).
 22. Li, Z., Tan, S., Li, S., Shen, Q. & Wang, K. Cancer drug delivery in the nano era: An overview and perspectives (Review). *Oncology Reports* vol. 38 611–624 (2017).
 23. Horcajada, P. *et al.* Porous metal-organic-framework nanoscale carriers as a potential platform for drug delivery and imaging. *Nat. Mater.* **9**, 172–178 (2010).
 24. Baati, T. *et al.* In depth analysis of the in vivo toxicity of nanoparticles of porous iron(III) metal-organic frameworks. *Chem. Sci.* **4**, 1597–1607

- (2013).
25. Agostoni, V. *et al.* A "green" strategy to construct non-covalent, stable and bioactive coatings on porous MOF nanoparticles. doi:10.1038/srep07925.
 26. Cutrone, G. *et al.* Design of engineered cyclodextrin derivatives for spontaneous coating of highly porous metal-organic framework nanoparticles in aqueous media. *Nanomaterials* **9**, (2019).
 27. Cedervall, T. *et al.* Understanding the nanoparticle-protein corona using methods to quantify exchange rates and affinities of proteins for nanoparticles. *Proc. Natl. Acad. Sci. U. S. A.* **104**, 2050–2055 (2007).
 28. Fornaguera, C. *et al.* Interactions of PLGA nanoparticles with blood components: Protein adsorption, coagulation, activation of the complement system and hemolysis studies. *Nanoscale* **7**, 6045–6058 (2015).
 29. Aguilar-Castillo, B. A. *et al.* Nanoparticle stability in biologically relevant media: influence of polymer architecture. *Soft Matter* **11**, 7296–7307 (2015).
 30. Linse, S. *et al.* Nucleation of protein fibrillation by nanoparticles. *Proc. Natl. Acad. Sci. U. S. A.* **104**, 8691–8696 (2007).
 31. Hühn, J. *et al.* Dissociation coefficients of protein adsorption to nanoparticles as quantitative metrics for description of the protein corona: A comparison of experimental techniques and methodological relevance. *International Journal of Biochemistry and Cell Biology* vol. 75 148–161 (2016).
 32. Duan, Y., Liu, Y., Shen, W. & Zhong, W. Fluorescamine Labeling for

- Assessment of Protein Conformational Change and Binding Affinity in Protein-Nanoparticle Interaction. *Anal. Chem.* **89**, 12160–12167 (2017).
33. De Paoli Lacerda, S. H. *et al.* Interaction of gold nanoparticles with common human blood proteins. *ACS Nano* **4**, 365–379 (2010).
 34. Röcker, C., Pötzl, M., Zhang, F., Parak, W. J. & Nienhaus, G. U. A quantitative fluorescence study of protein monolayer formation on colloidal nanoparticles. *Nat. Nanotechnol.* **4**, 577–580 (2009).
 35. Welsch, N., Dzubiella, J., Graebert, A. & Ballauff, M. Protein binding to soft polymeric layers: A quantitative study by fluorescence spectroscopy. *Soft Matter* **8**, 12043–12052 (2012).
 36. Kharazian, B., Hadipour, N. L. & Ejtehad, M. R. Understanding the nanoparticle-protein corona complexes using computational and experimental methods. *International Journal of Biochemistry and Cell Biology* vol. 75 162–174 (2016).
 37. Lee, H. Effects of Nanoparticle Electrostatics and Protein–Protein Interactions on Corona Formation: Conformation and Hydrodynamics. *Small* **16**, 1906598 (2020).
 38. Böhmert, L. *et al.* Isolation methods for particle protein corona complexes from protein-rich matrices. *Nanoscale Adv.* **2**, 563–582 (2020).
 39. Ural, M. S. *et al.* Compartmentalized Polymeric Nanoparticles Deliver Vancomycin in a pH-Responsive manner. *ACS Appl. Mater. Interfaces* (2021).
 40. Agostoni, V. *et al.* A 'green' strategy to construct non-covalent, stable and bioactive coatings on porous MOF nanoparticles. *Sci. Rep.* **5**, 1–7

(2015).

41. Agostoni, V. *et al.* Towards an Improved anti-HIV Activity of NRTI via Metal-Organic Frameworks Nanoparticles. *Adv. Healthc. Mater.* **2**, 1630–1637 (2013).
42. Qiu, J. *et al.* Self-assembled multifunctional core–shell highly porous metal–organic framework nanoparticles. *Int. J. Pharm.* **581**, (2020).
43. Rossi, E., Tran, N. T., Hirtz, C., Lehmann, S. & Taverna, M. Efficient extraction of intact HSA-A β peptide complexes from sera: Toward albuminome biomarker identification. *Talanta* **216**, 121002 (2020).
44. Lees, J. G., Smith, B. R., Wien, F., Miles, A. J. & Wallace, B. A. CDtool - An integrated software package for circular dichroism spectroscopic data processing, analysis, and archiving. *Anal. Biochem.* **332**, 285–289 (2004).
45. Micsonai, A. *et al.* Accurate secondary structure prediction and fold recognition for circular dichroism spectroscopy. *Proc. Natl. Acad. Sci. U. S. A.* **112**, E3095–E3103 (2015).
46. Wien, F. & Wallace, B. A. Calcium fluoride micro cells for synchrotron radiation circular dichroism spectroscopy. *Appl. Spectrosc.* **59**, 1109–1113 (2005).
47. Miles, A. J. *et al.* Light flux density threshold at which protein denaturation is induced by synchrotron radiation circular dichroism beamlines. *J. Synchrotron Radiat.* **15**, 420–422 (2008).
48. Wien, F., Miles, A. J., Lees, J. G., Vrønning Hoffmann, S. & Wallace, B. A. VUV irradiation effects on proteins in high-flux synchrotron radiation circular dichroism spectroscopy. in *Journal of Synchrotron Radiation*

- vol. 12 517–523 (International Union of Crystallography, 2005).
49. Gref, R. *et al.* Biodegradable long-circulating polymeric nanospheres. *Science (80-.)*. **263**, 1600–1603 (1994).
 50. Zambaux, M. F. *et al.* Influence of experimental parameters on the characteristics of poly(lactic acid) nanoparticles prepared by a double emulsion method. *J. Control. Release* **50**, 31–40 (1998).
 51. Tobío, M., Gref, R., Sánchez, A., Langer, R. & Alonso, M. J. Stealth PLA-PEG nanoparticles as protein carriers for nasal administration. *Pharm. Res.* **15**, 270–275 (1998).
 52. Baati, T. *et al.* In depth analysis of the in vivo toxicity of nanoparticles of porous iron(iii) metal–organic frameworks. *Chem. Sci.* **4**, 1597–1607 (2013).
 53. Li, X. *et al.* Drug-Loaded Lipid-Coated Hybrid Organic-Inorganic “Stealth” Nanoparticles for Cancer Therapy. *Front. Bioeng. Biotechnol.* **8**, 1027 (2020).
 54. Li, X. *et al.* New insights into the degradation mechanism of metal-organic frameworks drug carriers OPEN. doi:10.1038/s41598-017-13323-1.
 55. Christodoulou, I., Serre, C. & Gref, R. Metal-organic frameworks for drug delivery: Degradation mechanism and in vivo fate. in *Metal-Organic Frameworks for Biomedical Applications* 467–489 (Elsevier, 2020). doi:10.1016/b978-0-12-816984-1.00023-8.
 56. *Capillary Electrophoresis of Proteins and Peptides*. vol. 1466 (Springer New York, 2016).
 57. Coty, J. B. *et al.* Characterization of nanomedicines’ surface coverage

- using molecular probes and capillary electrophoresis. *Eur. J. Pharm. Biopharm.* **130**, 48–58 (2018).
58. Belder, D., Deege, A., Husmann, H., Kohler, F. & Ludwig, M. Cross-linked poly(vinyl alcohol) as permanent hydrophilic column coating for capillary electrophoresis. *Electrophoresis* **22**, 3813–3818 (2001).
 59. Rossi, E., Tran, N. T., Hirtz, C., Lehmann, S. & Taverna, M. Efficient extraction of intact HSA-A β peptide complexes from sera: Toward albuminome biomarker identification. *Talanta* **216**, 121002 (2020).
 60. Marie, A. L. *et al.* Capillary zone electrophoresis and capillary electrophoresis-mass spectrometry for analyzing qualitative and quantitative variations in therapeutic albumin. *Anal. Chim. Acta* **800**, 103–110 (2013).
 61. Rogers, D. M. *et al.* Electronic Circular Dichroism Spectroscopy of Proteins. *Chem* vol. 5 2751–2774 (2019).
 62. Bulheller, B. M., Miles, A. J., Wallace, B. A. & Hirst, J. D. Charge-transfer transitions in the vacuum-ultraviolet of protein circular dichroism spectra. *J. Phys. Chem. B* **112**, 1866–1874 (2008).
 63. Kamal, J. K. A., Zhao, L. & Zewail, A. H. Ultrafast hydration dynamics in protein unfolding: Human serum albumin. *Proc. Natl. Acad. Sci. U. S. A.* **101**, 13411–13416 (2004).
 64. Maciążek-Jurczyk, M. *et al.* Human serum albumin aggregation/fibrillation and its abilities to drugs binding. *Molecules* **25**, (2020).
 65. Bhattacharya, M., Jain, N. & Mukhopadhyay, S. Insights into the mechanism of aggregation and fibril formation from bovine serum

A comprehensive investigation of the interactions of human serum albumin with polymeric and hybrid nanoparticles

albumin. *J. Phys. Chem. B* **115**, 4195–4205 (2011).

66. WETZEL, R. *et al.* Temperature Behaviour of Human Serum Albumin. *Eur. J. Biochem.* **104**, 469–478 (1980).

Supporting Information

Table SI1. Characteristics of the NPs; surfactant, hydrodynamic size, PDI and surface charge.

NP	PLGA	PLGA-PEG	nanoMOF	nanoMOF-PEG
Surfactant	PVA	PVA	-	-
Hydrodynamic size (nm)	310 ± 15	418 ± 30	234 ± 16	286 ± 20
PDI	0.1	0.4	0.2	0.2
Surface Charge (mV)	-0	-0	-18	-16

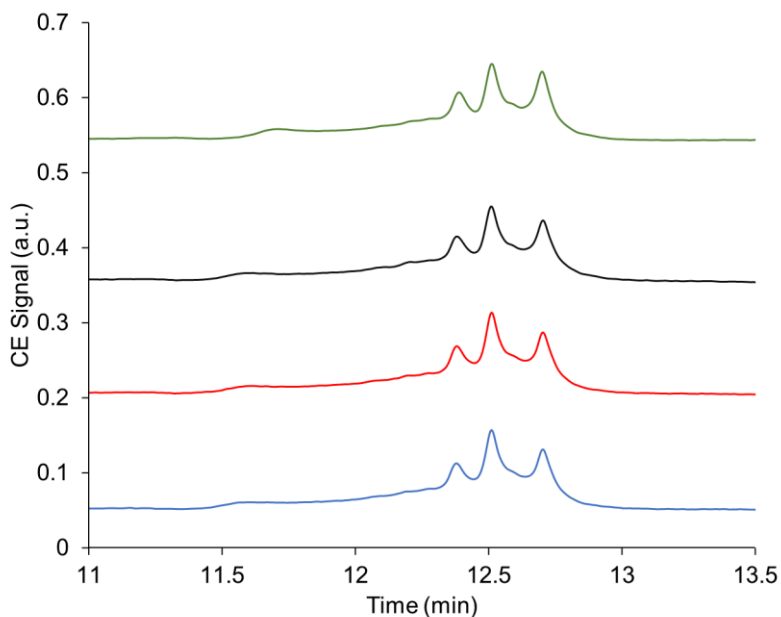


Figure SI1. HSA stability study carried on with 1 mg/mL HSA analysed by CE-UV without centrifugation and incubation (blue); after centrifugation without

A comprehensive investigation of the interactions of human serum albumin with polymeric and hybrid nanoparticles

incubation (red); after centrifugation after 1 day incubation (black); after centrifugation after 3 days incubation (green).

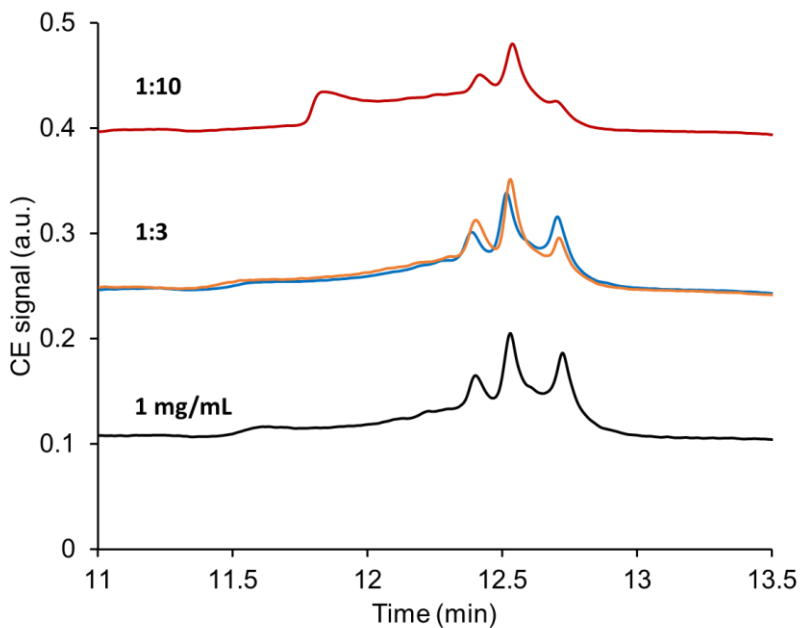


Figure SI2. CE-UV electropherograms of unbounded HSA recovered from supernatants after incubation with PLGA-PEG (orange) and PLGA (red, blue) and NPs during 1 day with a HSA: NP ratio of 1:3 and 1:10. Black line is the reference HSA solutions of 1 mg/mL.

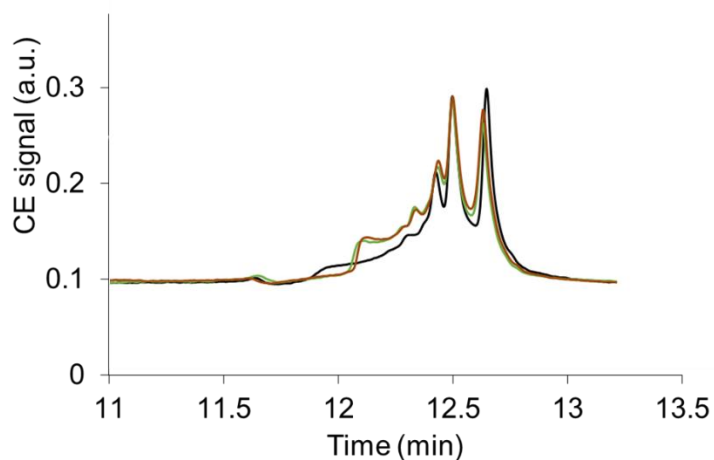
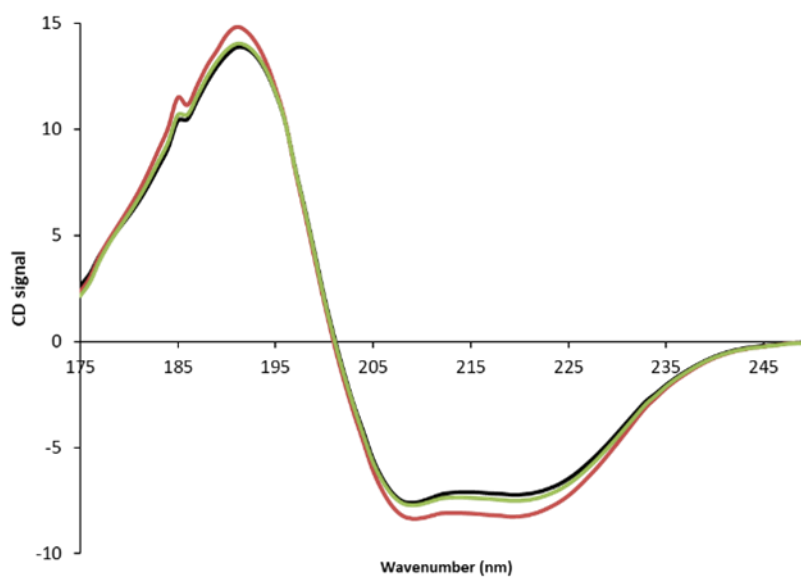


Figure SI3. CE-UV electropherograms of unbounded HSA recovered from supernatants after incubation with PLGA (green) and PLGA-PEG (orange) and NPs during 2h with a HSA: NP ratio of 1:3 and 1:10. Black line is the reference HSA solutions of 1 mg/mL.



A comprehensive investigation of the interactions of human serum albumin with polymeric and hybrid nanoparticles

Figure SI4: The SR-CD spectra of the PLGA (red) and PLGA-PEG (green) NPs incubated with HSA with 1:3 (HSA:NPs) ratio during 3 days. Black line is the reference HSA solutions of 1 mg/mL incubated without NPs during 3 days.

General Discussion and Perspectives



General discussion and perspectives

Nanomedicine offers unique opportunities to improve the current therapies and to develop new treatments for diseases previously thought difficult or impossible to treat. The clever use of NPs as nanomedicines has revolutionized how therapeutics are formulated and delivered. With the development of NP-delivered COVID-19 vaccines, they are now becoming a life-saving strategy while controlling the spread of coronavirus. Polymeric NPs are among the most applied nanoparticulate drug delivery vehicles according to their well-known safety profiles, stability, biodegradability and tuneable physicochemical properties. The **chapter I** of this thesis summarizes the principal types of nanoparticulate systems used in the drug delivery field. Among them, special emphasis was put on PLA and PLGA-based polymers which have a potential use as controlled release systems with the great ability to protect therapeutic agents and to improve their bioavailability.¹ They can be prepared through a wide range of techniques according to need of the application and enables encapsulation of both hydrophilic and hydrophobic drugs. By modulating the composition of the polymers, it was possible to precisely control some of the NPs features such as surface charge, stability, responsivity to external stimuli, drug loading efficiencies, and drug release kinetics. The surface functionalization of PLA and PLGA NPs has also been extensively studied to optimize their pharmacokinetics and biodistribution.

Although remarkable advances have been achieved through an extensive research and development on PLA and PLGA based NPs, a breakthrough of NPs from bench to bedside has not occurred so far. While more than 15 PLA and PLGA based microparticles have been approved² up to date, only few NP formulation have reached to a clinical trial stage^{3,4}. This clearly shows that one main challenge here is related to the size of the NPs which develop tremendous surface areas as compared to microparticles. As it was stated earlier, nanoparticulate systems develop

unique properties and nano-size indeed bears advantageous properties and favour biological responses as compared to microparticles.

We concluded the chapter by indicating that the nano-size also induces novel challenges in terms of characterization, insufficient drug loadings (especially for hydrophilic molecules) and studies of the nano-bio interactions. The aim of the thesis was to address these challenges by using up to date methodologies.

This thesis focused on the development and advanced characterisation of NPs based on PLA and PLGA as novel drug delivery systems. **Chapter II** deals first with the encapsulation of a last resort antibiotic, VCM, into a series of PLA and PLGA NPs. While VCM's instability, tendency to aggregate and acidic pH is one of the main reasons for the difficulties related to its administration, it also generates a challenge for its encapsulation into organic, hydrophobic, polymer matrices⁵. Therefore, a double emulsion solvent evaporation method was adopted here, in an attempt to locate the drug in the inner water compartments inside the NPs. Emulsion methods are simple, the parameters are easy to tune according to the need of NP's application and the resulting NPs are known to be stable.⁶ In order to have control/understanding on VCM loading into PLA and PLGA NP thus achieve high DLs, several parameters were tested. This included i) the effect of physicochemical properties of the polymer on DLs using a series of PLA and PLGA (co)polymers differing in Mw, end groups and lactic acid percentages, ii) the effect of physicochemical properties of the VCM that has been observed considering its charge-charge interactions and H-bonding capacity depending on the pH iii) NP preparation parameters such as drug to polymer ratio, concentration of emulsifier, addition of salt.

All tested (co)polymers formed successfully NPs with low polydispersity index and Zeta potential close to zero, which was an indication of the association of the emulsifier on the NP surface. This lead to a shielding

effect of the negatively charged end groups of the PLA and PLGA (co)polymers. Indeed, the residual amount of the emulsifier (PVA) was calculated as 6 ± 1 wt% and was not affected by the type of (co)polymer. The good stability of NPs (at least up to 3 months) was also associated with this protective steric layer at the NP surface. The size of NP was obtained between 320 and 370 nm and it was shown to be depended on the Mw of the (co)polymer and the concentration of salts in the outer emulsion phase. NPs were larger in case of using polymers with high Mw. Neither the concentration of the emulsifier nor the increase in the drug to polymer ratio had significant effect on NP size.

On the other side, NPs displayed significant differences in the VCM loadings. This complex picture was resolved by a detailed analysis of the parameters (i, ii and iii) as mentioned above. From the (co)polymers standpoint, the significant impact of Mw, terminal group (carboxyl or ester) and lactic content of (co)polymers on DL was noticed individually. Altogether, low Mw, carboxyl ended (co)polymers with lower percentage of lactic unit showed the highest VCM loadings. Among the PLA and PLGA series, short chain PLA₈C and PLGA₁₅C were the best performing (co)polymers. In the light of these findings, electrostatic interactions (charge-charge) between VCM and the (co)polymers were suggested, as the capacity of VCM to build such interactions with similar functional groups was shown already in the literature ⁷. Moreover H-bonding interactions between drug and the polymer was also proven by carefully replacing VCM's hydrogen atoms with deuterium that resulted in significant drops of the drug loading. Visible signs of decrease in H-bonding interactions were highlighted by solid-NMR studies. Therefore, the mechanism of drug loading was proposed, suggesting charge-charge and H-bonding interactions between polymer and drug that indeed depend on the pH. Therefore, to achieve high DLs, a study was carried on by adapting the pH of the inner and outer mediums when the double emulsion was performed. Remarkably, increasing the pH of the inner

emulsion (the mixture of drug and the polymer) contributed to the increase of DL from 14 ± 4 wt% up to 25 ± 3 wt%, which to the best of our knowledge is the highest VCM loading ever reported^{8,9,10,11}.

The images collected by cryo-TEM for the VCM loaded particles appeared remarkably different than their non-loaded counterparts. While empty NPs were plain with no sign of water inclusions/inner compartments, compartmentalised inner structure was obtained on VCM loaded NPs. This strongly suggested the VCM stabilization in the water inclusions.

Bearing in mind the common drawbacks of the available polymeric NP preparation methods as the heterogeneity among NPs especially on their size and chemical compositions, a second aspect of the study in **chapter II** was to characterize the developed NPs in an individual NP basis with a special interest on the chemical composition and VCM location. The challenge here was the need of visualization the NPs in parallel to their chemical analysis that has been limited by the number of available techniques that combine high resolution microscopy with spectroscopy. While electron microscopy coupled with EDX spectroscopy could address this challenge; working on different EMs; SEM-EDX and STEM-EDX, allowed to analyse NPs through different optical depths, namely the surface and the whole NP. By this way, one of the greatest concerns, whether the drug was adsorbed on the surface or it was encapsulated inside the NP, was addressed. SEM-EDX showed no trace of VCM on the NP surface, whereas VCM was detected in the NP's holes which appeared after NPs investigations under the electron beam. Such degradation/melting effect of polymeric NPs in contact with electron beam have been often reported in the literature¹². On the other side, STEM allowed to visualize the compartmentalized inner structure of individual NPs and simultaneous chemical analysis allowed to map the distribution of VCM on each NP, in detail. Noticeably, VCM was identified inside and at the interface of the inner compartments, which supports the

hypothesis of VCM stabilization in the water inclusions, as well as the interactions between drug and polymer.

Moreover, a label free, state-of-the-art characterization technique called AFM-IR was used that combines the spatial resolution of AFM (down to 10-20 nm) with precise chemical identification of IR. Recently developed tapping mode of AFM, demonstrated the particular success of this technique on the chemical characterization of individual PLA NPs¹³¹⁴. Here we were able to apply both acquisition modes in AFM-IR to show: i) local IR spectra on a single NP where the fingerprints of drug and polymer were used, and ii) the mapping of the IR absorptions at the selected wavenumbers that allowed to identify the drug in the NP core and the polymer matrix, simultaneously with the NP's topography.

The characterization conducted here paved the way to engineer the drug release of VCM from polymeric NPs. Indeed, a pH-controlled release was established *in vitro*. Moreover, the NPs were stable and preserved their VCM payloads at physiological pH up to 24h with less than 10% release. A rapid VCM release was observed in case of a slight decrease in pH to 5.3. This interesting pH dependence in VCM release could be potentially applied to controlled release at the infected site characterized by the local slightly acidic pH.

As perspective, the identified mechanism for the encapsulation and release of VCM into PLA and PLGA NPs, paves the way to engineer the encapsulation of different hydrophilic drug(s) presenting similar physicochemical characteristics with VCM. Amikacin, an aminoglycoside antibiotic is one of the candidates for this purpose. Co-encapsulation strategies together with VCM can also be developed with amikacin or with another hydrophilic drug(s). It is also possible to develop co-encapsulation strategies of VCM with a hydrophobic drug into PLA and PLGA NPs. Moreover, it was possible to show in the NanoCage team in ISMO that metal NPs could be also associated to the antibiotic-loaded NPs, crating

thus multifunctional supramolecular constructs to fight severe infections in a synergic manner. A patent was filed in 2020. These studies will be pursued in vitro on infected cells and on biofilms, as well as in vivo with selected formulations.

In order to go a step further on NP quality control, the next objective of this thesis was to achieve quantitative analysis on individual NPs with a great interest to obtain DLs locally. It is worth to mention that there was not any available method to achieve this objective for PLA and PLGA NPs up to our knowledge. AFM-IR gave us the inspiration to initiate the groundworks for quantification of drug-loaded NPs, regarding its high lateral resolution and its high chemical specificity together with an excellent resolution.^{15,16} In order to meet the needs of a reliable chemical analysis to be used in quantitative aspects, an anticancer drug with a strong IR absorption was chosen. While the potential anticancer properties of Rhenium based drugs were shown in the literature, Re(I) tricarbonyl-diselenium derivative, being the most preclinically studied Re based drug, was loaded into PLA NPs by nanoprecipitation. NPs were prepared with different drug contents and were fully characterized to determine their size distribution, polydispersity and morphology. NPs presented similar sizes in between 248 to 264 nm whatever their composition. They had spherical shapes, with no signs of NP aggregation, according to the TEM investigations.

The study presented in **Chapter III** focuses on a proof of concept on the use of AFM-IR for quantification purposes. The strategy was to establish a correlation between AFM-IR and a conventional quantitative technique through its bulk calibration. Evidently, an IR based technique can provide the greatest comparability with AFM-IR and its local IR spectra. However, the conventional FTIR is not adapted for quantitative analysis due to the limitations related to the thickness dependency, light scattering and well known optical losses. Therefore, we proposed to use IR microspectroscopy for calibration purposes.

Calibration samples were drug-PLA films with different and well-known drug contents. The resulting IR spectra were analysed focusing on the intensities of the fingerprint bands of PLA (1760 cm^{-1}) and drug (1900 cm^{-1}). Good calibration curves were obtained. Linearity of this curve ($R^2=0.99$) satisfied the important criteria to perform quantitative analysis, based on a linear correlation between the IR signal and the concentration of the sample.

Thus, the proof of concept was obtained by analysing the same films by tapping AFM-IR and by comparison with the quantitative IR microspectroscopy. For the reliability of the AFM-IR analysis, the important parameters to verify for each sample were identified as i) homogeneity of the film, ii) thickness dependence of IR intensity, iii) concentration dependence of the IR intensity. This led to establish a good correlation between two techniques simply by using a scale factor that was inserted on the spectral data collected from AFM-IR. Quantitative information was then driven from the calibration equation established by IR microspectroscopy.

We then presented a methodology to perform quantitative analysis on individual NPs by using any of the two acquisition modes in AFM-IR: local IR absorption spectra or IR cartography. Drug quantification from local IR spectra recorded by AFM-IR on single NP, provided precise quantitative analysis on a region of around 10-15 nm. While DLs calculated by analysing two points on same NP were same, DLs were strikingly different from one NP to another. Heterogeneities among NPs were recorded as DLs varied between 4-21%. Such information on nanoscale has not been provided in the literature for polymeric NPs up to our knowledge. However, to provide statistically relevant data, one should investigate a large number of NPs and such analysis with this method is very time consuming,

Therefore, an alternative method has been developed based on IR cartographies. The aim was to perform quantitative analysis from IR cartographies recorded on the wavenumbers corresponding to the "fingerprints". This enables to reach intensities from any point on the cartographs and thus to analyse large regions in short time. To do so, a direct transposition from local IR spectra to IR mapping intensities were proven.

The usefulness of AFM-IR has been proven in the nano world, enabling precise chemical analysis at nanoscale. We believe that our study has gone steps beyond the typical characterization methods, by affording new tools to better understand the supramolecular organization of the NPs and their composition with a nanometric resolution. Besides, these studies enrich the capabilities of the technique.

So, the study conducted here was not only capable to detect small molecules in NPs of around 250 nm in diameter, it also provided an understanding on the sample heterogeneities quantitatively with nanoscale resolution. The promising strategy developed here could be revolutionary in nanomedicine. Preparation of NPs with the capacity to determine DLs on a particle by particle basis could help to identify the NP preparation parameters which result in heterogeneities. Consequently, it could allow engineering more homogenous NPs and potentially develop NPs with highest DLs. Besides, the knowledge of drug location is crucial, as it determines the release patterns.

The quantification method developed here should be further validated on other drug-loaded NPs. Indeed, we have already initiated the study to test a similar system: PLA NPs loaded with another Re-based drug. Further studies could be based not only on polymeric systems but also other type of NPs (liposomes, inorganic, hybrid organic-inorganic, lipid nanoparticles, etc.). Indeed, the detection limits provided here could be confirmed and further tested on other types of nanoparticulate systems.

The local quantitative analysis strategies could be developed considering heterogenous individual particles.

Another innovative aspect of this thesis presented in **Chapter IV** was the study of the interactions of the developed NPs with biological fluids. NPs possess surfaces that are commonly reactive toward biological molecules. Nano-bio interactions that refers to the continuous interplay between NPs and biological molecules present in the biofluid is one of the key obstacles towards a successful transition of NPs from bench to clinic. Adsorption of proteins on the NP surface is a common phenomenon called protein corona formation. It leads to a dramatic change in NP surface properties, eventually redefines NP's *in vivo* fate. Not only NP but also proteins might be affected from this interaction that might induce significant modifications on the stability and the function of proteins. Protein corona formation is of value to identify NPs' immunological toxicity thus the clinical efficiency of a formulation. "Stealth" NPs have emerged to reduce these interactions and provide long blood circulation times to reach the targets (tumours, infected sites).

A comparative study was carried on by using two different type of NPs (organic vs hybrid), with their PEGylated counterparts, allowing a deep understanding and the contributing factors of nano-bio interactions. The methodology described in **Chapter IV** aimed to characterize NP-protein interactions by combining different techniques. The novelty of this study was the strategic combination of the complementary techniques that revealed different aspects of the NP-protein interactions; quantitative (protein corona) and qualitative (modifications on unbound protein).

NP-protein interactions were initiated by incubating NPs and protein at physiological pH over a time interval and concentrations. A protein kit was used to quantify unbound protein that allowed to estimate the formation of protein corona quantitatively. CE was then method of choice as it provides information on both protein quantity and also its forms. Model

protein, HSA, presented three main peak that are identified as three forms of HSA (native, cysteinated and glycated)¹⁷. Regarding to these forms, the modifications on unbound HSA, incubated with NPs, was analysed qualitatively. It was observed that polymer NPs and hybrid particles had very different affinity towards HSA. While there was no significant HSA adsorption of PLGA NPs, high amount of HSA was adsorbed on nanoMOFs. On the other hand, qualitative analysis on the unbound HSA showed that cysteine form of HSA was modified remarkably upon incubation with PLGA NPs. In case of nanoMOF, no important change was observed on HSA forms. PEGylated NPs exhibited protein repelling profiles. These interesting findings were further supported through LC-MS analysis of unbound HSA that allowed a comparative quantitative analysis between reference HSA and HSA incubated with NPs. Finally, a more detailed qualitative analysis were performed by SR-CD focusing on secondary structural rearrangements on HSA and also on its stability as shown in thermal denaturation study.

This study successfully established an orthogonal methodology for reliable protein corona investigations. It could represent a model study analysing interactions of empty NPs with a model protein. Future work will concentrate to apply this methodology into VCM loaded PLGA and PLGA-PEG NPs. Similar outcomes of nano-bio interactions of loaded NPs are expected owing to similar surface properties of both systems gained by the surfactant as well as the absence of VCM on the NP surface as shown above. On the other hand, nanoMOF and nanoMOF-PEG are more likely to have different surface properties upon drug loadings due to their porosity and morphology and absence of surfactant.

References

1. Essa, D., Kondiah, P. P. D., Choonara, Y. E. & Pillay, V. The Design of Poly(lactide-co-glycolide) Nanocarriers for Medical Applications.

- Front. Bioeng. Biotechnol.* **8**, 1–20 (2020).
2. Blasi, P. Poly(lactic acid)/poly(lactic-co-glycolic acid)-based microparticles: an overview. *Journal of Pharmaceutical Investigation* vol. 49 337–346 (2019).
 3. Li, Z., Tan, S., Li, S., Shen, Q. & Wang, K. Cancer drug delivery in the nano era: An overview and perspectives (Review). *Oncology Reports* vol. 38 611–624 (2017).
 4. Wang, Y. FDA's regulatory science program for generic PLA/PLGA-based drug products | Request PDF. *Am. Pharm. Rev.* **20**, (2016).
 5. Jia, Z., O'Mara, M. L., Zuegg, J., Cooper, M. A. & Mark, A. E. Vancomycin: Ligand recognition, dimerization and super-complex formation. *FEBS J.* **280**, 1294–1307 (2013).
 6. Astete, C. E. & Sabliov, C. M. Synthesis and characterization of PLGA nanoparticles. *J. Biomater. Sci. Polym. Ed.* **17**, 247–289 (2006).
 7. Giammarco, J., Mochalin, V. N., Haeckel, J. & Gogotsi, Y. The adsorption of tetracycline and vancomycin onto nanodiamond with controlled release. *J. Colloid Interface Sci.* **468**, 253–261 (2016).
 8. Pumerantz, A. *et al.* Preparation of liposomal vancomycin and intracellular killing of methicillin-resistant *Staphylococcus aureus* (MRSA). *Int. J. Antimicrob. Agents* **37**, 140–144 (2011).
 9. Sande, L. *et al.* Liposomal encapsulation of vancomycin improves killing of methicillin-resistant *Staphylococcus aureus* in a murine infection model. *J. Antimicrob. Chemother.* **67**, 2191–2194 (2012).
 10. Ma, T. *et al.* Nano-hydroxyapatite/chitosan/konjac glucomannan scaffolds loaded with cationic liposomal vancomycin: Preparation, in vitro release and activity against *staphylococcus aureus* biofilms. *J. Biomater. Sci. Polym. Ed.* **22**, 1669–1681 (2011).
 11. Zakeri-Milani, P., Loveymi, B. D., Jelvehgari, M. & Valizadeh, H. The characteristics and improved intestinal permeability of vancomycin PLGA-nanoparticles as colloidal drug delivery system. *Colloids Surfaces B Biointerfaces* **103**, 174–181 (2013).
 12. Chye Joachim Loo, S., Ping Ooi, C. & Chiang Freddy Boey, Y.

- Influence of electron-beam radiation on the hydrolytic degradation behaviour of poly(lactide-co-glycolide) (PLGA). *Biomaterials* **26**, 3809–3817 (2005).
13. Pancani, E. *et al.* High-Resolution Label-Free Detection of Biocompatible Polymeric Nanoparticles in Cells. *Part. Part. Syst. Charact.* **35**, (2018).
 14. Mathurin, J. *et al.* How to unravel the chemical structure and component localization of individual drug-loaded polymeric nanoparticles by using tapping AFM-IR. *Analyst* **143**, 5940–5949 (2018).
 15. Dazzi, A., Glotin, F. & Carminati, R. Theory of infrared nanospectroscopy by photothermal induced resonance. *J. Appl. Phys.* **107**, 124519 (2010).
 16. Dazzi, A., Prazeres, R., Glotin, F. & Ortega, J. M. Analysis of nano-chemical mapping performed by an AFM-based ('AFMIR') acousto-optic technique. *Ultramicroscopy* **107**, 1194–1200 (2007).
 17. Rossi, E., Tran, N. T., Hirtz, C., Lehmann, S. & Taverna, M. Efficient extraction of intact HSA-A β peptide complexes from sera: Toward albuminome biomarker identification. *Talanta* **216**, 121002 (2020).

General Conclusion



General conclusion

In this research work, a series of PLA and PLGA NPs were engineered as drug delivery systems by focusing on their preparation and in-depth characterization designed to meet the needs of their translation from bench to bedside. Challenges associated with drug loadings and NP quality control methods were addressed throughout the thesis as follows;

1. A series of PLA and PLGA (co)polymers were used to prepare NPs to encapsulate a hydrophilic drug, VCM using an optimized double emulsion solvent evaporation method. Striking differences in DLs were observed for each NP formulation and appeared to be influenced strongly by the physicochemical properties of both the polymer (M_w , end group and hydrophilicity) and the drug (pH-dependent net charge and self-association). By taking advantage of these parameters, NPs were engineered to enhance VCM loading that reached up to 25 wt%, the highest values to the best of our knowledge.

These findings together with solid NMR investigations, allowed us to identify the drug encapsulation mechanism which is based on non-covalent interactions between drug and the polymer. Consequently, a pH-controlled release was shown. This is indeed an important achievement to potentially apply controlled VCM release at an infected site, playing with pH differences in pathological conditions, or in an intracellular compartment such as endosomes. Developed formulations were stable up to at least three months and preserved their drug payload in physiological pH with less than 10% drug release.

2. In-depth NP characterization was performed through various advanced techniques. First, Cryo-TEM studies revealed the compartmentalized structure of VCM-loaded PLGA NPs whereas non-loaded NPs were devoid of inner compartments, suggesting VCM stabilization in the inner NP compartments. Furthermore, NPs were characterized individually with the ambitious aim of

performing chemical analysis. Electron microscopies coupled to EDX and also AFM coupled to IR were chosen to perform this chemical analysis, as both have high resolution offering different detection methods for the verification of the results. Definitively, VCM was detected inside and at the interface of the PLA NP's inner compartments with no signs of drug adsorbed on the external surface of the NPs.

3. In another study we went a step further and developed a proof of concept to quantify the drug localized on an individual PLA NP. A Re-based anticancer drug was loaded into PLA NPs by nanoprecipitation. To establish a correlation between quantitative IR microspectroscopy and AFM-IR, drug-PLA films were prepared with known composition and were deeply studied. To succeed quantitative analysis, some important parameters were verified on AFM-IR including homogeneity of the sample, linearity of the IR signal against sample thickness and linearity of concentration against thickness. A proof of concept was carried by comparing the calibration curves obtained from both IR microspectroscopy and AFM-IR. A good correlation was achieved and the scaling factor of 3.2 between the techniques was determined. These studies paved the way to correlate AFM-IR data with the quantitative aspect of IR microspectroscopy. The methodology was then used to calculate DLs on NPs simply by recording a local IR spectrum by AFM-IR. Dramatic heterogeneities in terms of composition between individual NPs were shown, highlighting the interest of our approach. To go a step further, we developed a method that enables to conduct quantitative measurements on numerous individual NPs simultaneously. This was achieved through IR cartographies recorded on wavenumbers corresponding to IR "fingerprints" of the drug and the NP.

4. Finally yet importantly, nano-bio interactions were studied with the a novel methodology. Considering the protein corona phenomenon, a comprehensive study was carried on by comparing the protein interactions of PLGA NPs with hybrid NPs (nanoMOFs). Surface modified counterparts, PLGA-PEG NPs and nanoMOF-PEG were also explored. By this way, the effect of core and also the shell of NPs was investigated. HSA was used as a model protein. The methodology consisted of strategic combination of orthogonal methods that allowed to estimate the nano-bio interactions in a deep and reliable manner. First, quantitative analysis was performed using a protein assay to estimate the amount of HSA adsorbed on the NPs' surface. Then, capillary electrophoresis analysis generated both quantitative and qualitative data. Qualitative aspects of protein corona, signifying the effect of nano-bio interactions on free protein, were further investigated by LC-MS and SR-CD. While LC-MS allowed to make comparative quantitative analysis among HSA samples incubated with or without NPs, SR-CD enabled deciphering the secondary structure modifications strongly correlated with the stability of the free protein. Results showed significant differences among the NPs. PLGA NPs remarkably avoided the protein absorption on their surface, while nanoMOF were prone to protein adsorption as soon as they were put in contact with. This absorption trend was not observed in nanoMOF-PEG, indicating their "stealth" properties due to their PEG shell. One main finding were the qualitative investigations which showed modifications, in several aspects, on the unbounded (free) protein.

